AD-A163 482 RESEARCH INVESTIGATION DIRECTED TOWARD EXTENDING THE USEFUL RANGE OF THE ELECTROMAGNETIC SPECTRUM(U) COLUMBIA RADIATION LAB NEW YORK G W FLYNN ET AL. 1/4

UNCLASSIFIED 31 DEC 85 DAAG29-85-K-0049 F/G 20/6 NL

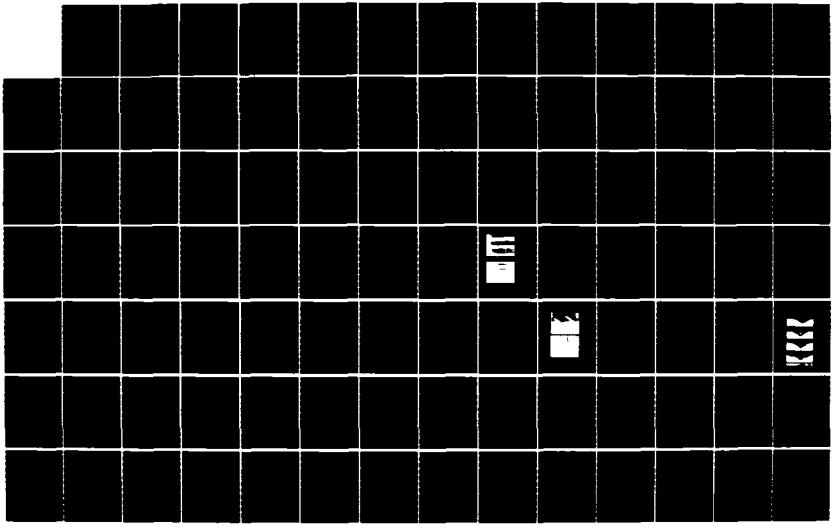

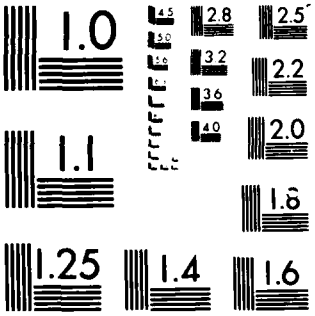

MICROCOPY RESOLUTION TEST CHART
NATIONAL BUREAU OF STANDARDS 1963 A

(1)

CRL

COLUMBIA UNIVERSITY

DEPARTMENTS OF PHYSICS,
CHEMISTRY, ELECTRICAL ENGINEERING

AD-A163 482

★ PROGRESS REPORT NO. 35

April 1, 1984–September 30, 1985

CONTRACT DAAG29-85-K-0049

APPROVED FOR PUBLIC RELEASE: DISTRIBUTION UNLIMITED

DTIC
ELECTE
JAN 30 1986
S D
B

TO:

THE JOINT SERVICES TECHNICAL ADVISORY COMMITTEE

REPRESENTING: THE U.S. ARMY RESEARCH OFFICE
THE OFFICE OF NAVAL RESEARCH
THE AIR FORCE OFFICE OF SCIENTIFIC RESEARCH

DTIC FILE COPY

COLUMBIA RADIATION LABORATORY, NEW YORK, NEW YORK 10027

★ December 31, 1985

86 1 30 039

COLUMBIA RADIATION LABORATORY

RESEARCH INVESTIGATION DIRECTED TOWARD EXTENDING THE USEFUL RANGE OF THE ELECTROMAGNETIC SPECTRUM

Progress Report No. 35

April 1, 1984 through September 30, 1985

Contract DAAG29-85-K-0049

Object of the Research:

Basic research in the fields of quantum electronics; electromagnetic propagation, detection and sensing; and solid state electronics.

The research reported in this document was made possible through support extended the Columbia Radiation Laboratory, Columbia University, by the Joint Services Electronics Program (U.S. Army Research Office, Office of Naval Research, and the Air Force Office of Scientific Research) under Contract DAAG29-85-K-0049.

Submitted By: George W. Flynn and Richard M. Osgood, Jr., Co-Directors

Coordinated By: Karen Wingate, Departmental Administrator

DTIC
ELECTE
JAN 30 1986
S D
B

COLUMBIA UNIVERSITY
Columbia Radiation Laboratory
Department of Physics
New York, New York 10027

December 31, 1985

Approved for public release; distribution unlimited

The research reported in this document was made possible through support extended to the columbia Radiation Laboratory, Columbia University by the Joint Services Electronics Program (U.S. Army Research Office, Office of Naval Research, and the Air Force Office of Scientific Research) under Contract DAAG29-85-K-0049.

Portions of this work were also supported by:

Air Force Office of Scientific Research

AFOSR-84-0013

AFOSR/DARPA

F-49620-84-K-0022

Army Research Office

Contract DAAG29-85-K-0210

National Science Foundation

Grant NSF-CHE 82-11593
Grant NSF-DMR 80-06966
Grant NSF-CHE 80-23747
Grant NSF-ECS 82-17677
Grant NSF-ECS 82-19636
Grant NSF-CDR 84-21402

Office of Naval Research

Contract N00014-78-C-0517

Department of Energy

Contract DE-AC02-78-ER-04940

QUALITY INSPECTED 9

Accession For
NTIS GRA&I
DTIC TAB
Unannounced
Justification
By
Distribution/
Availability Codes
Dist | Avail and/or Special
A-1

The support of these agencies is acknowledged in footnotes in the text.

SECURITY CLASSIFICATION OF THIS PAGE (When Data Entered)

REPORT DOCUMENTATION PAGE

READ INSTRUCTIONS BEFORE COMPLETING FORM

1. REPORT NUMBER
Progress Report No. 35

2. GOVT ACCESSION NO.
AD-A163 482

3. RECIPIENT'S CATALOG NUMBER

4. TITLE (and Subtitle)
RESEARCH INVESTIGATION DIRECTED TOWARD EXTENDING THE USEFUL RANGE OF THE ELECTROMAGNETIC SPECTRUM

5. TYPE OF REPORT & PERIOD COVERED
1 April 1984 through 30 September 1985

6. PERFORMING ORG. REPORT NUMBER

7. AUTHOR(s)
George W. Flynn
Richard M. Osgood, Jr.

8. CONTRACT OR GRANT NUMBER(s)
DAAG29-85-K-0049

9. PERFORMING ORGANIZATION NAME AND ADDRESS
Columbia Radiation Laboratory
Columbia University
New York, New York 10027

10. PROGRAM ELEMENT, PROJECT, TASK AREA & WORK UNIT NUMBERS

11. CONTROLLING OFFICE NAME AND ADDRESS
Department of the Army
U.S. Army Research Office
Research Triangle Park, NC 27709

12. REPORT DATE
December 31, 1985

13. NUMBER OF PAGES
277

14. MONITORING AGENCY NAME & ADDRESS(if different from Controlling Office)

15. SECURITY CLASS. (of this report)
Unclassified

15a. DECLASSIFICATION/DOWNGRADING SCHEDULE

16. DISTRIBUTION STATEMENT (of this Report)
Approved for public release; distribution unlimited.

17. DISTRIBUTION STATEMENT (of the abstract entered in Block 20, if different from Report)

18. SUPPLEMENTARY NOTES
Portions of this work were also supported by the Air Force Office of Scientific Research, the Army Research Office, the National Science Foundation, the Office of Navel Research, the Department of Energy, AFOSR/DARPA and NIH.

19. KEY WORDS (Continue on reverse side if necessary and identify by block number)
Adsorption
Barrier crossing
Carbenes
Charge-transfer
(continued)

20. ABSTRACT (Continue on reverse side if necessary and identify by block number)
The characteristics of light generated by distinctly non-Poisson processes have been studied with particular interest in sub-Poisson light (light whose photon-number fluctuations are lower than those of lasers). The use of such quiet light can be beneficial, e.g., it could possibly increase the distance between repeaters in a fiber-optic communications system

DD FORM 1 JAN 73 1473 EDITION OF 1 NOV 65 IS OBSOLETE

unclassified

SECURITY CLASSIFICATION OF THIS PAGE (When Data Entered)

Block 20 continued - Abstract

As an example of a mechanism for producing such light, a Franck-Hertz apparatus excited by a space-charge-limited electron beam has been studied. Extensive theoretical calculations of the properties of such a source of light have been carried out. Under suitable conditions this device can produce antibunched and sub-Poisson photon emissions. Initial experiments were carried out which produced a photon-counting distribution that was indeed sub-Poisson, thereby providing the first cw source of nonclassical quiet light. A quantum analog of the Burgess variance theorem has also been proven. This confirmed that the sub-Poisson nature of a light beam is conserved in the presence of absorptive media and additive (Poisson) background light. Thus the light can be used once it is generated. Two other ways of producing nonclassical light have been investigated: (1) the generation of sub-Poisson light by selective deletion from cascaded atomic emissions and (2) the generation of binomial states of the quantized radiation field and an exploration of their properties.

Variance-stabilizing transforms for families of exponential and Rayleigh random variables have been derived and shown to be exact. These transforms, when applied to appropriate noisy images, render signal-dependent noise signal-independent. Their utility is that, after applying the transforms, classical estimation procedures devised for additive, signal-independent noise can be brought to bear. The results are expected to find use in image filtering, in the analysis of failure times and particle sizes, and in the processing of optical field magnitudes and intensities generated by chaotic sources.

A technique has been developed to determine the forward bias capacitance of metal semiconductor contacts. The method is based on accurately setting the phase of the measuring circuit and is termed accurate phase capacitance spectroscopy. Measuring the forward bias capacitance enables us to determine the interface state distribution at the junction and its evolution with

Block 20 continued - Abstract

device formation. Our results have been obtained on transition metal silicon diodes both prior to and after silicide formation. Silicide formation leads to a more perfect interface with a corresponding reduction in interface state density. In addition, observation of the epitaxial and nonepitaxial $NiSi_2$-Si leads us to conclude that the characteristics of the interface states are controlled by the degree of structural perfection of the interface rather than by the specific epitaxy.

Experimental observation of the photovoltaic effect of a semiconductor grain boundary with a scanning laser spot has been analyzed assuming a single trap energy level. The current is calculated from the recombination velocity and the concentration of the minority carriers at the grain boundary which was derived from the continuity equation. The open-circuit voltage across the sample is obtained from equating this recombination current to the compensating current using the thermionic emission model. Using the recombination velocity and the diffusion length as variables, the calculated open-circuit voltage is compared with the experimental data.

A tunneling junction has been developed that is easily produced at room temperature. The junction characteristics are controllable, and it does not appear to be difficult to make in integrated form. The basic idea is to modify a metal-semiconductor contact by introducing a thin near-intrinsic semiconductor layer between the metal and the bulk semiconductor. The result is a tunneling junction for majority carriers under forward bias. The reverse saturation current is small but not negligible, and the breakdown voltage is quite high. It is shown that a good ohmic contact can be converted into a tunneling rectifier with this technique. Potential applications include MESFETs, tunnel transistors, detectors and integrated circuits. A physical model is presented and some useful device parameters are obtained for an Al-aSi-nSi diode. Experimental data are presented to demonstrate the basic features of majority carrier tunneling.

Block 20 continued - Abstract

Analog charge-coupled computing is being investigated. Two silicon surface-channel charge-coupled computers have been designed and fabricated at Columbia. Buried-channel gallium arsenide charge-coupled computing structures have been modelled.

A low energy-ion beam has been used to oxidize silicon. The gate of oxide of a metal-oxide-semiconductor field-effect transistor (MOSFET) has been successfully fabricated at room temperature using this technique.

Novel photodetector devices formed in a laser-etched cavity for optical fiber interconnects have been fabricated and tested as part of a collaborative research effort.

Projection dry-etching of GaAs using an ArF excimer laser and HBr precursor gas has been demonstrated for the first time. Line-width resolution down to the optical limit (4 μm) was achieved through the addition of the buffer gases (H_2, Ar, and C_2H_4). The line-resolution and the etch-rate dependencies as a function of buffer gas pressure reveal that the mechanism is related to nonlinear gas-surface reaction kinetics, together with the pulsed-photochemistry produced by the excimer laser.

A surface analysis apparatus for analyzing chemical reactions has been set up. The system is equipped with ESCA, Auger, and ISS and a sample loadlock. This apparatus has been used to measure the oxidation of GaAs by ultraviolet light and ion-beam oxidation of silicon.

A time-of-flight mass spectrometer system has been designed and constructed for the purpose of analyzing the fundamental chemistry of laser-induced reactions. The apparatus has a pulsed molecular beam and an extensive signal processing capability.

Block 20 continued - Abstract

The basic physics of the light-guided etching in semiconductors have been investigated. This technique, which uses an ultraviolet laser to effect wet etching, can form ultrahigh aspect ratio features in the semiconductor surface. The recent work has shown that the highly verticle features produced can be explained by the incident-angle-dependent etching rates which are established with a nonuniform intensity laser beam.

Ultraviolet laser radiation is being used to control and modify the chemical species in the plasma discharge environment of a semiconductor processing reactor. This technique provides for separate control of the production of desired gas-phase chemical species and the ion bombardment parameters in the plasma chamber.

A capillaritron supersonic nozzle discharge source has been used to produce beams of chemically reactive species with a characteristic rotational and translational temperature of $7^{o}K$. Ions produced by the capillaritron discharge are highly energetic and are characterized by a high temperature corresponding to energy spreads of 1-2 eV.

A sophisticated, extraordinarily powerful diode laser probe technique has been developed for following dynamic high energy collision and chemical reaction processes. This method has been used to measure the final "bath" states of CO_2 molecules produced by collisions with electronically excited mercury atoms. These processes are prototypes for catalytic metal-molecule interactions. This same technique has been used to study collisions between high energy (approximately 2 eV) hydrogen or deuterium atoms and CO_2. The final states of CO_2 molecules produced by these translationally energetic collision events have been determined. These processes serve as prototypes for high temperature chemical reactions and energy transfer events.

A gas discharge method and a collisional energy transfer technique have

Block 20 continued - Abstract

been developed to mark or "tag" high energy vibrational states of molecules. These experimental methods allow us to follow high energy states produced by chemical reactions or collision events.

A molecular beam/bolometer technique has been used to study clusters formed in supersonic expansions of C_4F_8, CO_2 and SF_6. A sensitive laser dissociation experiment was employed to set upper and lower limits on the percentage of clusters in a molecular beam.

Picosecond laser studies have established several key factors that control the intramolecular dynamics of excited singlet to ground triplet transformation in diaryl carbenes. A significant solvent polarity effect is observed on the rate of intersystem crossing as well as on the singlet-triplet energy splitting for several carbenes which were characterized for the first time. By changing the structure of the carbene, the energy splitting can be varied from less than 300 cm^{-1} to greater than 2400 cm^{-1}. Exploiting the fact that the energy splitting depends on structure as well as on the nature of the environment, two limiting energy regimes, which define the relaxation dynamics of the carbene, were identified experimentally for the first time . Carbenes possessing small singlet-triplet energy gaps (< 2000 cm^{-1}) exhibit an inverse isotope effect as well as an "inverse" gap effect, i.e. intersystem crossing time increases as the gap decreases. An off resonance coupling model is used to explain the behavior. Carbenes can also be forced into a high energy gap limit, as exemplified by dimesitylcarbene, where the rate of singlet to triplet state relaxation is found to be an inversely varying function of the energy splitting.

Picosecond measurements provided for the first time the direct measurement of the intramolecular and intermolecular energy decay dynamics of excited singlet diphenylcarbene in the presence of reactive molecules. It is shown that reactants provide not only a chemical decay channel but also an

Block 20 continued - Abstract

intramolecular decay channel which is due to a solvent polarity effect. The chemical and physical effects can act in opposite directions leading to the important result that a significant increase in the low lying excited singlet state lifetime can be achieved upon addition of reacting molecules.

Picosecond time-resolved fluorescence was used to study solvent effects on the dynamics of intramolecular charge-transfer in p-dimethylamino-benzonitrile (DMABN) in n-alcohols. As in the case of n-nitriles, the rate of charge-transfer depends on the solvent polarity. In addition, DMABN undergoes significant hydrogen bonding in the alcohol solvents which slows down the charge-transfer process. Dynamical properties of the solvent, such as dielectric relaxation and viscosity, are shown to be non-rate-limiting.

The direct study of the structure of surfaces of neat liquids and solutions has been achieved using a new application of second harmonic generation techniques . New information has been obtained about the orientation of adsorbates in the liquid surface for coverages as low as 5% of a monolayer. Phenol molecules adsorbed at the water/air interface are found to be orientated with their long axis titled 60° from the surface normal.

Time-delayed four-wave mixing (TDFWM) on the 3S-3P transition in Na vapor has been studied using intense 7-nsec pulses from a broadband laser. Large-scale 1.9 psec modulation associated with the fine structure of the 3P state is observed throughout. At low buffer-gas pressures and low Na vapor temperatures, pulse-induced relaxation effects are observed while at higher Na-vapor temperatures an anomalous response develops. In the normal region the TDFWM signal is interpreted in terms of either accumulated free decays or photon echoes. We estimate the relaxation induced by the excitation pulses.

Photon Echo Modulation Spectroscopy (PEMS) has been extended into a new regime to study coherences between states that are widely separated in

Block 20 continued - Abstract

frequency compared to the bandwidth of the exciting laser pulses. Time Delayed Four Wave Mixing (TDFWM) is observed on the Na D line transitions. As the two, double frequency, 7 nsec, light pulses are delayed with respect to each other a 1.9 psec beating of the integrated TDFWM signal is observed. It persists throughout the region where the excitation pulses overlap and into the normal photon echo region where they are separated by several excitation pulse widths.

The Photon echo technique was used to investigate the $^3P_0$ - $^3H_6$ (5985 Å) and the two $^3P_0$ - $^3H_5$ (5333 Å, 5333.5 Å) transitions in Pr^{3+}:LaF_3. Echo intensity as a function of excitation pulse separation was recorded on all three of these transitions at 4.6 °K. On the $^3P_0$ - $^3H_6$ transition, the echo signal spans a dynamic range of nine decades in intensity. The data displays modulation and decayed exponentially with a time constant of 250 nsec. Fourier analysis of the data yields the nuclear hyperfine splittings of the $^3H_6$ level used (4222 cm^{-1}). An even faster decay was observed on the echo data obtained on the transitions connecting $^3P_0$ to each of the two lowest levels of $^3H_5$ manifold. The time constant for both of these transitions reduced from our data is about 100 nsec, however no modulation is apparent. Stimulated echo data was also obtained on all three of these transitions. The data indictaes that the fast decay rates observed are due to a population decay out of the $^3H_6$ and $^3H_5$ levels. The fast decay rates are anomalous in view of previous experiments in this sample. Some preliminary results presented here indicate that the population decay out of these levels is due to energy transfer between the Pr ions and other existing impurity ions (possibly Nd ions). Temperature relaxation studies on these transitions reveal the existence of a residual homogeneous linewidth for all three levels studied. Phonon transition rates from the levels studied here to other levels in the $^3H_5$ and $^3H_6$ manifolds were obtained from our temperature relaxation data.

Block 20 continued - Abstract

At high excitation pulse powers, laser action was observed on the $^3P_0$ - $^3H_6$ transition at 5985 Å. Laser action was also observed at 77 ^oK on two of the $^3P_0$ - $^3H_6$ transitions (5985 Å, 6000 Å) and the $^3P_0$ - $^3F_4$ transition at 7195 Å while pumping with a 7 nsec excitation pulse at the $^3P_0$ - $^3H_4$ and $^3P_1(^1I_6)$-$^3H_4$ (4633 Å) transitions. The observed emission is a narrow 3 nsec pulse followed by an exponential tail with approximately 300 nsec time constant. Stimulated emission was observed on all the three lasing tarnsitions by detecting amplification of a weak probe pulse on these transitions.

'Satellite Echoes' have been observed on the satellite lines of the $^3P_0$ - $^3H_4$ transition at 4778 Å in a .1% sample of Pr^{3+}:LaF_3. Photon echo data was obtained for the first time on the satellite line at 4768 Å. The modulation character of the data is different from that of the central line and the decay rate observed is more than two times faster than that of the central line.

Collisional relaxation of 2S-nS and 2S-nD superposition states in atomic Li vapor is measured with the trilevel photon echo technique. Principal quantum numbers range from n = 4 to well into the Rydberg regime with n = 30. For the rare gas perturbers (He, Ne, Ar, Kr and Xe) the variation of collisional cross section with n is considerably weaker than previously found with Na vapor.

A photon echo from the allowed 3D-3P transition in Na vapor is spontaneously emitted after a single-pulse, one-photon excitation of the 3P state is followed by a single-pulse, two-photon excitation of the 3D state. The collisional relaxation cross section of the excited 3D-3P superposition states of Na in Ar has been measured.

Block 19 continued - Key Words

Chemical Intermediates
Chemical Reactions
Dielectric Relaxation
Dimethylaminobenzonitrile
Energy Relaxation
Excited State Structural Change
Hydrogen Bonding
Intersystem Crossing
Isotope Effects
Liquid-Air Interface
Picosecond Lasers
Solvent Effects
Surface Second Harmonic Generation
Twisted Internal Charge-Transfer
Vibronic Level Structure
Plasma
U.V.
Etching
HBr
CO_2
C_4F_8
H_2S
Hot atoms
Collisions
Chemistry
Discharge
Energy transfer
Capillaritron
Supersonic expansion
Translational cooling
Diode laser
Dynamic
Charge-coupled devices,
CCD
Analog computer
Gallium arsenide
GaAs
Ion beam
Oxidation
Low temperature processing
Optical interconnect
Photodetector
Optical coherent transients
Photon echoes
Incoherent excitations
Incoherent light
Four-wave mixing
Time-delayed four-wave mixing (TDFWM)
Accumulated photon echo
Accumulated free decay
Pulse induced relaxation
Optical noise
Ultrafast modulation spectroscopy
Photon echo modulation spectroscopy (PEMS)
$LaF_3:Pr^{3+}$
Lithium vapor
Rydberg states
Trilevel echo
Collisional line broadening
Two-photon-excited-state trilevel photon echo
Two photon excitation
Sodium vapor
Stimulated echo
Temperature relaxation
Laser action
Spectroscopy
Hyperfine interaction
Relaxation
Homogeneous linewidth
Excimer laser
Dry processing
Laser etching
HBr
Projection chemical etching
Surface reactions
Surface analysis
Time of flight mass spectroscopy
Semiconductor oxidation
GaAs
Ultraviolet lasers
Image-processing
Photon-counting
Variance-stabilizing transforms
Fiber-optic communications
Coherence
Photon statistics,
Sub-Poisson light
Antibunched light
Thin films
Photovoltaic effects
Grain boundary
Traps
Tunneling rectifier
Interface states
Silicides
Accurate phase capacitance spectroscopy
Barrier height
Schottky barrier
Amorhous silicon
Scanning laser beam

III. GENERATION AND DYNAMIC PROPERTIES OF METASTABLE SPECIES FOR QUANTUM ELECTRONICS AND LASER MICROPROCESSING 83

A. UV Laser Enhanced Chemistry In Plasma Etching Of GaAs 83

B. Translational Energy Characteristics Of Radicals And Ions In A Capillaritron Supersonic Nozzle Discharge 98

C. Diode Laser Probing Of Vibrational Product State Distributions In Metal-Molecule Collisions: $Hg(6^3p_1)-CO_2(mn^1p)$ 101

D. Dynamics Of High Energy Collision Processes 112

E. Marking Vibrational States By Their Kinetic Behavior 122

F. Probing High Energy Overtone States Of Molecules With Diode Lasers 134

G. Diode Laser Probing Of High Energy Molecular States Using A Discharge Reference Cell For Level In The Electron Volt Range 140

H. Bolometric Evidence For Cluster Formation In Supersonic Molecular Beams Of CO_2 And C_4F_8 144

I. Vibration Predissociation Of SF_6 Clusters In A Supersonic Molecular Beam 149

IV. PICOSECOND ENERGY TRANSFER AND PHOTOFRAGMENTATION SPECTROSCOPY 152

A. Photophysics And Photochemistry Of Divalent Carbon Intermediates 152

B. Twisted Internal Charge Transfer Phenomena 171

C. Second Harmonic Generation From Liquid Surfaces 181

TABLE OF CONTENTS

PUBLICATIONS AND REPORTS xiii

FACTUAL DATA, CONCLUSIONS, AND PROGRAM
FOR THE NEXT INVERVAL

I. QUANTUM DETECTION AND SENSING OF RADIATION 1

A. Noise In The Generation, Partition And Detection Of Light 1

B. Exact Variance Stabilizing Transformations For Image-Signal-Dependent Exponential And Raleigh Noise 7

II. PHYSICAL AND PHOTOCHEMICAL PROPERTIES OF ELECTRONIC MATERIALS 16

A. Maskless Projection Of Etching Of GaAs Using Excimer Laser Photochemistry 16

B. Chemical Physics Of Interface Reactions 26

C. Electronic States At Silicide-Silicon Interfaces 42

D. Tunneling In A metal-Semiconductor-Semi-Conductor Thin Film Structure 57

E. A Study Of The Photovoltaic Effect Of A Semiconduction Grain Boundary By A Scanning Laser Beam 68

F. Device Fabrication Facility 81

G. Analog Charge-Coupled Computing 81

H. Room Temperature Oxidation Of Silicon 82

I. Optical Fiber Interconnect Photodetector 82

V. OPTICAL TRANSIENT SPECTROSCOPY 185

A. Introduction 185

B. Time-Delayed Four-Wave Mixing Using Intense Incoherent Light 187

C. Ultrafast Photon Echo Modulation Spectroscopy 210

D. Spectroscopy, Relaxation, And Laser Action In LaF_3: Pr^{3+} 221

E. Noble Gas-Induced Collisional Line Broadening Atomic Ll Rydberg Superposition States 2S-nS and 2S-nD (n = 4 to 30) Measured By Trilevel Echoes 244

F. Observation And Relaxation Of The Two-Photon-Excited State Trilevel Echo In Sodium Vapor 259

G. Conclusions And Future Directions Of Research 268

SIGNIFICANT ACCOMPLISHMENTS 270

PERSONNEL 274

JSEP REPORTS DISTRIBUTION LIST 276

PUBLICATIONS AND REPORTS

Publications

E.V. Sitzmann and K.B. Eisenthal, "Studies of the Chemical Intermediate Diphenylcarbene," in Applications of Picosecond Spectroscopy in Chemistry, K.B. Eisenthal, ed., D. Reidel Publishing Co., Dordrecht, Holland, 1984. (AFOSR, NSF, JSEP)

E.V. Sitzmann, J. Langan and K.B. Eisenthal, "Intermolecular Effects on Intersystem Crossing Studied on the Picosecond Time Scale," J. Am. Chem. Soc., 10, 1868 (1984). (AFOSR, NSF, JSEP)

K.B. Eisenthal, R.A. Moss, and N.J. Turro, "Divalent Carbon (Carbene) Chemistry, Time Resolved Laser Photolysis and Spectroscopy in the Investigation of Reactive Organic Intermediates," Science, 225, 1439 (1984). (AFOSR, NSF, JSEP)

K.B. Eisenthal, N.J. Turro, E.V. Sitzmann, I.R. Gould, G. Hefferon, J. Langan, and Y. Cha, "Singlet-Triplet Interconversion of Diphenylmethylene, Energetics, Dynamics and Reactivities of Different Spin States," Tetrahedron, 41, 1543 (1985). (AFOSR, NSF, JSEP)

K.B. Eisenthal, J. Hicks, M. Vandersall, and Z. Babarogic, "The Dynamics of Barrier Crossing in Solution: The Effect of a Solvent Polarity-Dependent Barrier," Chem. Phys. Lett., 116, 18 (1985). (AFOSR, NSF, JSEP)

K.B. Eisenthal, D.P. Millar, "Picosecond Dynamics of Barrier Crossing in Solutions: A Study of the Conformational Change of Excited State 1,1'-Binaphthyl," J. Chem. Phys., J. Chem. Phys. 83. 5076 (1985). (AFOSR, NSF, JSEP)

K.B. Eisenthal, E.V. Sitzmann, J.G. Langan,and Z.Z. Ho., "Picosecond Laser Studies on the Effects of Structure ad Environment on Intersystem Crossing in Aromatic Carbenes," in Ultrafast Phenomena IV, D.H. Auston and K.B. Eisenthal, eds., Springer-Verlag, Berlin, 1984. (AFOSR, NSF, JSEP)

K.B. Eisenthal, S. Palfrey and T. Heinz, "Coherence Effects in Pump-Probe Measurements with Colinear, Copropagating Beams," in Ultrafast Phenomena IV, D.H. Auston and K.B. Eisenthal, eds., Springer-Verlag, Berlin, 1984. (AFOSR, NSF, JSEP)

K.B. Eisenthal, E.V. Sitzmann,and J.G. Langan, "Picosecond Laser Studies of the Effects of Reactants on Intramolecular Energy Relaxation of Diphenylcarbene: Reaction of Diphenylcarbene with Alcohols," Chem. Phys. Lett., 112, 111 (1984). (AFOSR, NSF, JSEP)

K.B. Eisenthal, T.F. Heinz, and S.L. Palfrey, "Coherent Coupling Effects in Pump-Probe Measurements with Colinear Copropagating Beams," Optic Letters, 9, 359 (1984). (AFOSR, NSF, JSEP)

K.B. Eisenthal, J.G. Langan, and E.V. Sitzmann, "Picosecond Laser Studies on the Effect of Structure and Environment on Intersystem Crossing in Aromatic Carbenes," Chem. Phys. Lett., 110, 521 (1984). (AFOSR, NSF, JSEP)

K.B. Eisenthal, J.G. Langan, and E.V. Sitzmann, "Inverse Deuterium Isotope Effect on the Intersystem Crossing of Diphenylcarbene," Chem. Phys. Lett., in press. (AFOSR, NSF, JSEP)

K.B. Eisenthal, J. Hicks, and M. Vandersall, "Hydrogen Bonding and Polarity Effects on Barrier Crossing in Solution," in preparation. (AFOSR, NSF, JSEP)

K.B. Eisenthal, E.V. Sitzmann, J. Langan, and D. Griller, "Effect of Solvent Polarity and Structure on Intersystem Crossing in Arylcarbenes: A Picosecond Laser Study of Dimesitylcarbene," in preparation. (AFOSR, NSF, JSEP)

K.B. Eisenthal, C. Dupuy, D. Hrovat, J. Langan, E.V. Sitzmann, T.A. Jenny and N.J. Turro, "Wavelength Dependence and Dissociation Kinetics of the Photolysis of the Endoperoxides of 1,4-Dimethyl-9, 10-Diphenylanthracene," in preparation. (AFOSR, NSF, JSEP)

S. Datta, R.E. Weston, Jr., and G.W. Flynn, "Vibrational Excitation of CH_3F Excited by Collisions with "Hot" Hydrogen Atoms," J. Chem. Phys. 80, 4071 (1984). (DOE)

T. H. Allik, B. B. Brady, G. W. Flynn, and G. B. Spector, "Translational Energy Characteristics of Radicals and Ions in a Capillaritron Supersonic Nozzle Discharge," J. Phys. Chem. 88, 3204 (1984). (JSEP, NSF, DOE)

C. F. Wood, J. A. O'Neill, and G. W. Flynn, "Infrared Diode Laser Probes of Photofragmentation Products: Bending Excitation in CO_2 Produced by Excimer Laser Photolysis of Pyruvic Acid," Chem. Phys. Lett., 109, 317 (1984). (JSEP, NSF, DOE)

S. R. Goates, J. O. Chu, and G. W. Flynn, "Observation of High Vibrational Excitation in HCN Molecules Produced from 193 nm Photolysis of 1,3,5-Triazine," J. Chem. Phys. 81, 4521 (1984). (JSEP, NSF, DOE)

Etienne Pochon, Ralph E. Weston, Jr., and G.W. Flynn, "Infrared Multiphoton Dissociation of Octafluorocyclobutane with a Two-Frequency Q-switched CO_2 Laser," J. Phys. Chem. 89, 86 (1985). (DOE)

J. O. Chu, G. W. Flynn, C. J. Chen, and R. M. Osgood, "Infrared Emission Studies of Vibrational Excitation in CH_3 Fragments Produced from ArF and KrF Laser Photolysis of $Cd(CH_3)_2$ and $Zn(CH_3)_2$," Chem. Phys. Lett., 119, 206 (1985). (JSEP, NSF, DOE)

W. E. Hollingsworth, J. Subbiah, G. W. Flynn, and R. E. Weston, Jr., "Laser-Induced-Fluorescence Study of the Reaction of N_2O with Hot Hydrogen Atoms from 248nm Excimer Laser Photolysis of HI," J. Chem. Phys. 82, 2295 (1985). (JSEP, NSF, DOE)

J. Subbiah and G. W. Flynn, "Dynamics of Intermolecule Vibrational Energy Transfer Between COF_2 and NO," J. Phys. Chem., 89, 2533 (1985). (JSEP, NSF, DOE)

T.H. McGee, R.E. Weston, Jr., and G.W. Flynn, "Effects of Translational Energy and Moderators on Vibrational Excitation of Carbon Dioxide by Hot Hydrogen Atoms," J. Chem. Phys. 82, 3605 (1985). (DOE)

G. B. Spector, B. B. Brady, and G. W. Flynn, "Bolometric Evidence for Cluster Formation in Supersonic Molecular Beams of CO_2 and C_4F_8," J. Phys. Chem., 89, 1875 (1985). (JSEP, NSF, DOE)

T.H. McGee, R.E. Weston, Jr. and G.W. Flynn, "Vibrational Excitation of CH_3F by Collisions with Hot H and D Atoms," J. Chem. Phys. 83, 145 (1985). (DOE)

B.B. Brady, G.B. Spector, and G.W. Flynn, "Vibrational Predissociation of SF_6 Clusters in a Supersonic Molecular Beam," J. Phys. Chem, accepted for publication. (JSEP, NSF, DOE)

J.A. O'Neill, Ji Ye Cai, G.W. Flynn, and R.E. Weston, Jr., "Diode Laser Probing of Bending and Stretching Vibrational Excitation in CO_2 Caused by Collisions with Hot Deuterium Atoms," J. Chem. Phys. 84, 0000 (1986). (JSEP, NSF, DOE)

J. A. O'Neill and G.W. Flynn, "Molecular Studies with Tunable Diode Lasers," Laser Focus, (June 1985) p. 136. (JSEP, NSF, DOE)

W. Jalenak, R. Weston, T. Sears, and G.W. Flynn, "V-V Energy Transfer from Highly Vibrationally Excited Azulene to CO_2," J. Chem. Phys. 83, 0000 (1985). (DOE)

R. Kinchinski, R. Beach, F. Moshary and S.R. Hartmann, "Spectroscopic and Relaxation Study of the $^3H_6$ State in $Pr^{3+}:LaF_3$," Optics Communication 54 (3) 147, (1985). (JSEP, NSF)

R. Beach, D. DeBeer, and S.R. Hartmann, "Time Delayed Four Wave Mixing Using Intense Incoherent Light," Phys. Rev. A 32 4367 (1985). (ONR, JSEP)

D. DeBeer, L.G. VanWagenen, R. Beach, and S.R. Hartmann, "Ultrafast Modulation Spectroscopy," Phys. Rev. Lett., submitted for publication. (ONR, JSEP)

T.J. Chen, D. DeBeer and S.R. Hartmann, "Observations and Relaxation of the Two-Photon-Excited-State Trilevel Echo in Sodium Vapor," JOSA B, in press. (ONR, JSEP)

E.X. Xu, F. Moshary and S.R. Hartmann, "Noble Gas Induced Collisional Line Broadening of Atomic Li Rydberg Superposition States 2S-Ms and Measured by 2S-Md (m = 4 to 30) Trilevel Echoes," JOSA B, in press.

D. Podlesnik, H.H. Gilgen, R.M. Osgood, "Deep-Ultraviolet Wet Eching of GaAs," Appl. Phys. Lett. 45, 563 (1984). (DARPA, AFOSR)

W. Holber, G. Reksten, R.M. Osgood, "Laser-Assisted Dry Etching of Materials," Proc. of SPIE 459, 129 (1984). (JSEP, NSF)

P. Brewer, S. Halle, R.M. Osgood, "Photon-Assisted Dry Etching of GaAs," Appl. Phys. Lett. 45, 475 (1984). (JSEP)

H.H. Gilgen, C.J. Chen, R.R. Krchnavek, R.M. Osgood, "The Physics of Ultraviolet Photodeposition," Laser Processing and Diagnostics, ed., D. Bauerle, Springer Series on Chemical Physics, Berlin, 1984 39, 225. (DARPA, AFOSR, ARO, JSEP)

P. Brewer, G. Reksten, R.M. Osgood, Solid-State Science and Technology 28, 273 (1984). (JSEP)

C.J. Chen and R.M. Osgood, "A Spectroscopic Study of the Excited States of Dimethylcadimium, Dimethylzinc, and Dimethylmercury," J. Chem. Phys. 81, 327 (1984). (ARO, JSEP)

C.J. Chen and R.M. Osgood, "An Analytic Theory of Photodissociation of Linear Symmetric Polyatomic Molecules," J. Chem. Phys. 81, 318 (1984). (ARO, JSEP)

R.R. Krchnavek, H.H. Gilgen, R.M. Osgood, "Maskless Laser Writing of Silicon Dioxide," J. Vac. Sci. Tech. B, 641 (1984). (DARPA, NSF, AFOSR)

W. Holber, G. Reksten, R.M. Osgood, "Laser Enhanced Plasma Etching of Silicon," Appl. Phys. Lett. 46, 201 (1985). (AFOSR, NSF, DARPA)

R.M. Osgood and T.F. Deutsch, "Laser-Induced Chemistry for Microelectronics," Science 227, 709 (1985). (NSF, AFOSR, ARO)

C.J. Chen, H.H. Gilgen, and R.M. Osgood, "Resonant Optical Growth of Submicrometer Metal Gratings," Opt. Lett. 10. 173 (1985). (ARO, DARPA, AFOSR)

P. Brewer, D. McClure, R.M. Osgood, "Dry Laser-Assisted, Rapid HBr Etching of GaAs," Appl. Phys. Lett. 47, 310 (1985). (JSEP)

R.M. Osgood and H.H. Gilgen, "Laser Directed Writing of Materials," Materials Science Review of Ann. Rev. Mater. Sci. 15, 549 (1985). (AFOSR, DARPA, ARO, JSEP)

P.R. Prucnal, American Scientist; May 1984.

P.R. Prucnal, M.A. Santoro, and T.R. Fan, "Orthogonal Modulation in fiber-optic communications," Proc IEEE, December (in press). (JSEP)

P.R. Prucnal, M.A. Santoro, "Spread Spectrum Fiber Optic Local Area Network Using Optical Processing," IEEE J. Lightwave Tech, in press. (NSF)

P.R. Prucnal, M.A. Santoro, "Asynchronous Fiber Optic LAN Using CDMA and Optical Correlation," Elec. Lett., submitted. (NSF)

P.R. Prucnal, P.A. Perrier, "Self-clocking, Low DC, Bandwidth Compaction Code for Multiplexed Optical Channels," IEEE Trans. Communic., submitted. (NASA)

P.R. Prucnal, P.A. Perrier, and C. Brandmaier, "A Low DC Self-locking, Two-Color Transmission Code for Optical Communications," Elec. Lett, submitted. (NASA)

P.R. Prucnal, E.R. Fossum and R.M. Osgood, "Integrated Fiber Opic Coupler for VLSI/VHSIC Interconnects," Opt. Lett., in press. (DARPA)

P.R. Prucnal, "Optical Interconnections for VLSI Local Area Networks, IEEE Electrotech. Rev., in press. (DARPA)

P.R. Prucnal and E. Goldstein, "Exact Variance-Stabilizing Transformations for Signal-Dependent Exponential Rayleigh Noise," J. Opt. Soc. Am., submitted. (JSEP)

P.R. Prucnal and E. Goldstein, "Variance Stabilizing Transforms for Signal Dependent Noise," Proc. IEEE, submitted. (JSEP)

P.R. Prucnal, M.A. Santoro (1985), "Spread Spectrum Fiber Optic Local Area Network Using Optical Processing," Proc. International Tirennia Workshop on Digital Communic., in press. (NSF)

P.R. Prucnal, "Laser Phase Noise in FM Interferometric Demodulation," GTE, 1984. (JSEP)

P.R. Prucnal, "Multiple Access Indoor Wireless Communications," AT T Bell Labs, 1985. (JSEP)

P.R. Prucnal, "Orthogonal Modulation formats for Fiber-Optic Communications," J. Opt. Soc. Am. 73, 1936. (JSEP)

P.R. Prucnal and M.A. Santoro, "Local Area Network with Spread Spectrum Processing," Opt. News 11 9, 102. (NSF)

P.R. Prucnal, E.R. Fossum and R.M. Osgood, "Integrated Fiber Optic Coupler for VLSI Interconnects," Opt. News 11 9, 102, 1985. (DARPA)

P.R. Prucnal, M.A. Santoro and T. Lockwood, "Local Area Network with Optical Spread Spectrum Processing," International Tirennia Workshop on Digital Communic. 5, 2, 1985. (NSF)

P.R. Prucnal and M.A. Santoro, "Local Area Network with Spread Spectrum Processing," J. Opt. Soc. Am., in press. (NSF)

P.R. Prucnal, E.R. Fossum and R.M. Osgood, "Integrated Fiber Optic Coupler for VLSI Interconnects," J. Opt. Soc. Am., in press. (DARPA)

K. Matsuo, M.C. Teich, and B.E.A. Saleh, "Poisson Branching Point Processes," J. Math. Phys. 24, 2174-2185 (1984). (JSEP and NSF)

M.C. Teich, B.E.A. Saleh, and J. Perina, "Role of Primary Excitation Statistics in the Generation of Antibunched and Sub-Poisson Light," J. Opt. Soc. Am. B 1, 366-389 (1984). (JSEP and NSF)

G. Lachs, R. Al-Shaikh, Q. Bi, R.A. Saia, and M.C. Teich, "A Neural- Counting Model Based on Physiological Characteristics of the Peripheral Auditory System. V. Application to Loudness Estimation and Intensity Discrimination," IEEE Trans. Syst. Man Cybern. SMC-14, 819-836 (1984). (NSF)

M.C. Teich, B.E.A. Saleh, and J. Perina, "Role of Statistics of Primary Excitations in Optical Coherence," in Coherence and Quantum Optics V, Proc. 5th Rochester Conference on Coherence and Quantum Optics, June 13-15, 1983, L. Mandel and E. Wolf, eds., Plenum, New York, 1984, pp. 409-410. (JSEP and NSF)

M.C. Teich, B.E.A. Saleh, and K. Matsuo, "Reduced-Noise Direct-Detection Optical Communications," in Proc. XVIth Grantee-User Meeting, W.S.C. Chang and T. Hartwick, eds., University of California at San Diego, 1984, Optical Communications Systems, pp. 5-8. (NSF)

M.C. Teich, "Quiet Light," Columbia Eng. Res. 29, 1-3 (1984) (JSEP)

M.C. Teich and S.M. Khanna, "Pulse-number Distribution for the Neural Spike Train in the Cat's Auditory Nerve," J. Acoust. Soc. Am. 77, 1110-1128 (1985). (NIH and NSF)

B.E.A. Saleh and M.C. Teich, "Multiplication and Refractoriness in the Cat's Retinal-Ganglion-Cell Discharge at Low Light Levels," Biol. Cybern. 52, 101-107 (1985). (NSF)

M.C. Teich, Review of J. Perina's book entitled, Quantum Statistics of Linear and Nonlinear Optical Phenomena, J. Opt. Soc. Am. B 2, 1123 (1985). (JSEP and NSF)

W.J. McGill and M.C. Teich, "Exact Psychometric Functions for a Wideband Envelope Detector," J. Acoust. Soc. Am. 77, S48 (1985). (NSF)

B.E.A. Saleh and M.C. Teich, "Sub-Poisson Light Generation by Selective Deletion from Cascaded Atomic Emissions," Opt. Commun. 52, 429-432 (1985). (JSEP and NSF)

M.C. Teich and B.E.A. Saleh, "Observation of Sub-Poisson Franck-Hertz Light at 253.7 nm," J. Opt. Soc. Am. B 2, 275-282 (1985). (JSEP and NSF)

D. Stoler, B.E.A. Saleh, and M.C. Teich, "Binomial States of the Quantized Radiation Field," Opt. Acta 32 345-355 (1985). (JSEP and NSF)

E. S. Yang, Q. Hua, D.K. Yang, G.S. Yang, and P.S. Ho, "A Metal-Amorphous Silicon-Silicon Tunnel Rectifier," Applied Phys. Lett. 44, 1144, 1984. (NSF, JSEP)

L. M. Chen, H. Y. Li, K.B. Sarachik, W. Hwang, and E.S. Yang, "Spray Deposition Process Study of SnO_2 Solar Cells using Orthogonal Experimental Design," Solar Cells, 34, 73 (1985). (U.S. DOE/SERI)

E. Poon, W. Hwang, E.S. Yang and H.L. Evans, "Photoconductivity Transient Response in Polycrystalline Silicon," J. Appl. Phys. 57, 338 (1985). (NSF, JSEP)

H. L. Evans, X. Wu, and E. S. Yang, P. S. Ho, "Accurate Phase Capacitance Spectroscopy of Transition Metal Silicon Diodes," Appl. Phys. Lett. 46(5), 1 March 1985, 486-489. (NSF, JSEP)

X. Wu, H. L. Evans, and E.S. Yang, M. Liehr, and P. S. Ho, "Summary Abstract: Interface State Measurement of Epitaxial and Nonepitaxial Nickel Silicide Schottky Barriers," Journal of Vacuum Science and Technilogy B, 3(4), 1151-1152 (1985). (ONR at IBM, NSF, JSEP)

E.S. Yang, D.K. Yang, Q.H. Hua and G.S. Yang, "Tunneling in a Metal-Semi-conductor-Semiconductor Thin Film Diode," Solid State Electronics 29 (1986). (NSF, JSEP)

J.S. Song and E.S. Yang, "A Study of the Photovoltaic Effect of a Semiconductor Grain Boundary by a Scanning Laser Beam," J. Appl. Phys. 58 3129 (1985). (NSF, IBM, JSEP)

P.S. Ho, W.S. Yang, H.L. Evans, and X. Wu, "Electronic States at Silicide-Silicon Interfaces," Phys. Rev. Lett. (to be published). (ONR at IBM, NSF, JSEP)

Lectures and Presentations

K. B. Eisenthal, "Intermolecular and Intramolecular Excited State Charge Transfer," Internal Conference on Photochemistry and Photobiology, Alexandria, Egypt, January 1983.

K. B. Eisenthal, "Picosecond Laser Studies of Intramolecular Motions in Liquids," Structure and Dynamics in Liquids Symposium, Am. Chem. Soc. Symposium, Seattle, Washington, March 1983.

K. B. Eisenthal, "Chemistry on the Picosecond Timescale," Laser Spectroscopy and Photochemistry Symposium, Am. Chem. Soc. Meeting, Hershey Resort, Pennsylvania, April 1983.

K. B. Eisenthal, "Chemistry on the Picosecond Timescale," University of Toronto Laser Seminar, Toronto, Canada, April 1983.

K. B. Eisenthal, "Picosecond Laser Studies of Chemical Intermediates," NATO Workshop on Application of Picosecond Spectroscopy to Chemistry, Acquafredda Di Maratea, Italy, June 1983.

K. B. Eisenthal, "Picosecond Laser Studies on Intramolecular Motions in Liquids," Gordan Research Conference on Liquids, Plymouth, New Hampshire, August 1983.

K. B. Eisenthal, "Picosecond Laser Studies of Chemical Intermediates," Princeton University, Princeton, New Jersey, November 1983.

K. B. Eisenthal, "Chemistry on the Picosecond Time Scale," Radiationless Transitions Conference, Newport Beach, California, January 1984.

K. B. Eisenthal, "Chemistry on the Picosecond Time Scale," University of South Florida, Tampa, Florida, February 1984.

K. B. Eisenthal, "Chemistry on the Picosecond Time Scale," University of Miami, Miami, Florida, February 1984.

K. B. Eisenthal, "Chemistry on the Picosecond Time Scale," Rutgers University, New Brunswick, New Jersey, April 1984.

K. B. Eisenthal, "Chemistry on the Picosecond Time Scale: Ground and Excited State Dynamics of Carbenes," New York University, New York, New York, April 1984.

K. B. Eisenthal and E.V. Sitzmann, "Studies of the Chemical Intermediate Diphenylcarbene," NATO Workshop on Application of Picosecond Spectroscopy to Chemistry, Acquafredda Di Maratea, Italy, June 1983.

K. B. Eisenthal, "Ultarfast Photochemistry," University of Wisconsin, Madison, Wisocnsin, October 1984.

K. B. Eisenthal, "Ultrafast Photochemistry," University of Minnesota, Minneapolis, Minnesota, October 1984.

K. B. Eisenthal, "Picosecond Laser Studies of Carbenes," California Institute of Technology, Pasadena, California, December 1984.

K. B. Eisenthal, "Picosecond Laser Studies of Carbenes," University of California at Berkeley, California, March 1985.

K. B. Eisenthal, "Picosecond Laser Studies of Carbenes," U.C.L.A., Los Angeles, California, May 1985.

K. B. Eisenthal, "Advances in Molecular Reaction Dynamics," Aussois, France, June 1985.

G. W. Flynn, "Diode Laser Probes of Dynamic Processes in Molecules," Jackson State University, Jackson, Mississippi, April 1984.

G. W. Flynn, "Diode Laser Probes of Dynamic Processes in Molecules," Massachusetts Institute of Technology, Cambridge, Mass., May 1984.

G. W. Flynn, "Diode Laser Probes of Dynamic Processes in Molecules," Harvard University, Cambridge, Mass., May, 1984.

G. W. Flynn, "Lasers in Chemistry and Physics," American Association for Adv. of Science, New York, New York, May 1984.

G. W. Flynn, "Diode Laser Probes of Dynamic Processes in Molecules," Wayne State University, Detroit, Michigan, December 1984.

G. W. Flynn, "Diode Laser Probes of Dynamic Processes in Molecules," University of Chicago, Chicago, Illinois, January 1985.

G. W. Flynn, "Diode Probes of High Energy Collision and Photofragmentation Processes in Molecules," Wesleyan University, Middletown, Connecticut, February 1985.

G. W. Flynn, "Diode Probes of High Energy Collision and Photofragmentation Processes in Molecules," University of Michigan, Ann Arbor, Michigan, March 1985.

G. W. Flynn, "Diode Probes of High Energy Collision and Photofragmentation Processes in Molecules," University of Arizona, Tucson, Arizona, April 1985.

G. W. Flynn, "Recent Advances in Studies of High Energy Molecular Processes," Columbia University, Arden House, New York, May 1985.

G. W. Flynn "Diode Probes of High Energy Collision and Photofragmentation Processes in Molecules," Stanford University, Stanford, California, April 1985.

G. W. Flynn, "Diode Probes of High Energy Collision and Photofragmentation Processes in Molecules," Gordon Conference on Molecular Energy Transfer, Wolfboro New Hampshire, July 1985.

G. W. Flynn, "Diode Probes of High Energy Collision and Photofragmentation Processes in Molecules," Johns Hopkins University, Baltimore, Maryland, September 1985.

E. R. Fossum, "Charge-Coupled Computing," Army Night Vision and Electro-Optics Laboratory, Ft. Belvoir, Virginia, December 1984.

E. R. Fossum, "Charge-Coupled Computing," Naval Research Laboratory, Washington, D.C., February 1984.

E. R. Fossum, "Microelectronics Research at Columbia," Honeywell Systems and Research Center, Minneapolis, Minnesota, June 1985.

S. R. Hartmann, "Incoherent Photon Echoes," Colloquium at Lehigh, Cornell University, New York, February 1985.

S. R. Hartmann, "Photon Echoes with Incoherent Light, Cornell University, New York, November 1984.

R. M. Osgood, "Laser Chemical Processing," Workshop on Lightwave Technology, Los Angeles, California, January 1984.

R. M. Osgood, "Laser-Assisted Dry Etching," SPIE Symposium on Laser Chemical Processing, Los Angeles, California, January 1984

R. M. Osgood, "Surface Physics of Photodeposition," General Electric Research Labs, Schenectady, New York, February 1984.

R. M. Osgood, "Microelectronics Research at Columbia," IT&T Research, Shelton, February 1984.

R. M. Osgood, "Laser Deposition and Its Physics - for Electronic Packaging," APS Annual Meeting, Detroit, Michigan, March 1984.

R. M. Osgood, "Laser Chemical Processing," (Keynote Address) Rank Prize Minisymposium on Laser Writing, Malvern, April 1984.

R. M. Osgood, "Microelectronics Research at Columbia," Philips Research Laboratory, Briarcliff, April 1984.

R. M. Osgood, "Microelectronics Research at Columbia," Motorola, Special Presentation, New York, New York, June 1984.

H. H. Gilgen, "Resistivity of Photodeposited Metal Lines," CLEO 85, Los Angeles, June 1984.

J. R. Chen, "Collective Enhancement of Surface Reactions," International Quantum Electronics Conference, Los Angeles, California, June 1984.

H. H. Gilgen, "The Physics of Photodeposition," Conference on Laser Processing and Diagnostics, Linz, July 1984.

P. D. Brewer, "Laser-Assisted Dry Etching," Gordon Conference on Plasma Processing in Microelectronics, New Hampshire, July 1984.

R. M. Osgood, "Laser Writing," Conference on Solid-State Devices and Materials, Kobe, September 1984.

R. M. Osgood, "Surface-Enhanced Laser Chemistry," ACS Meeting, Philadelphia, September 1984.

P. D. Brewer, "Excimer Laser Projection Etching of GaAs," Materials Research Society Meeting, November 1984.

D. V. Podlesnik, "The Use of Ultraviolet Lasers in Wet Processing of Semiconductors," Materials Research Society Meeting, November 1984.

H. H. Gilgen, "Electrical Properties of Photodeposited Metal Conductors," Materials Research Society Meeting, November 1984.

G. Reksten, "Doping and Wavelength Dependence in Laser-Enhanced Plasma Etching," Materials Research Society Meeting, November 1984.

R. M. Osgood, "Laser Direct Writing," SRC Presentation, New York, New York, January 1985.

R. M. Osgood, "Microelectronic Processing with Lasers," Perkin-Elmer, Danbury, Connecticut, February 1985.

R. M. Osgood, "UV Surface Reactions in an Aqueous Solution," Symposium on Laser and Ion Beam Surface Microphysics, Santa Fe, California, February 1985.

R. M. Osgood, "Laser Chemistry for Microelectronics," Gordon Conference, Santa Barbara, California, February 1985.

R. M. Osgood, "Optical Physical Phenomena in Laser Processing," University of Toronto, Laser Colloquium, Toronto, March 1985.

R. M. Osgood, "Laser-Assisted Dry Etching," IBM - Plasma Symposium, Burlington, Vermont, May 1985.

R. M. Osgood, "Light-Guided Etching," GE-Whitney Symposium, Schenectady, New York, June 1985.

R. M. Osgood, "Laser Direct Writing for Maskless Processing," SRC-*In Situ* Processing Symposium, Research Triangle, June 1985.

R. M. Osgood, "Laser Chemistry for Microelectronics," NSF-Symposium on Processing Electronics Materials, Newark, Delaware, June 1985.

D. R. Podlesnik, "Direct Fabrication of Diffraction Gratings Using Light-Enhanced Wet Etching," SPIE Conference on Diffraction Phenomena in Optical Engineering Applications, San Diego, California, August 1985.

R. M. Osgood, "Laser Surface Chemistry for Microelectronics," IBM Special School on Lasers and Applications, Lech, August 1985.

A. E. Willner, "Laser Process for Integrated Optics," NATO ASI Conference, Eriche, July 1985.

P. R. Prucnal, "Integated Fiber Optic Coupler for VHSIC/VLSI Interconnections," Workshop on Optical Interconnects, MCC, Austin, Texas, November 1985.

P. R. Prucnal, "Transmission Codes for Optical Communications," NASA Review, November 1985.

P. R. Prucnal, "Optical Interconnects," Optical Processing Annual Review, DARPA, November 1985.

P. R. Prucnal, (1) "Local Area Network with Spread Spectrum Processing," (2) "Integrated Fiber Optic Coupler for VLSI Interconnects," Optical Society of America Annual Meeting, Washington, D.C., October 1985.

P. R. Prucnal, "Spread Spectrum Fiber Optic Local Area Network Using Optical Processing," International Tirennia Workshop on Digital Communications, Tirennia, Italy, September 1985.

P. R. Prucnal, "Ultra High Speed Optical Signal Processing," NSF Industry-University Workshop, Columbia, June 1985.

P. R. Prucnal, "Ultra High Speed Optical Processing," NSF Site Visit, Columbia, January 1985.

P. R. Prucnal, "Telecommunications Research at Columbia: Fiber Optics," Center for Telecommunications Research Opening, Columbia, December 1984.

P. R. Prucnal, "Ultra High Speed Circular Hollow Waveguide Modulator," Joint Services Electronics Program Review Meeting, Columbia, October 1984.

P. R. Prucnal, AT&T Bell Labs, Crawford Hill, June 1984.

P. R. Prucnal, Bell Communications Research, Murray hill, February 1985.

P. R. Prucnal, AT&T Bell Labs, Crawford Hill, July 1985.

M. C. Teich, with B.E.A. Saleh and T Larchuk, "Observation of sub-Poisson Franck-Hertz Light at 253.7 nm," Postdeadline Paper PD-A6, XIIIth International Quantum Electronics Conference, Anaheim, California, June 1984.

M. C. Teich, with K. Matsuo and B.E.A. Saleh, "Excess Noise Factor for Staircase Avalanche Photodiodes," Meeting of the NSF Grantee-User Group in Optical Communication Systems, La Jolla, California, June 1984.

M. C. Teich, "Generation of Quiet (sub-Poisson) Light in Hg Vapor," Optics and Quantum Electronics Seminar, M.I.T. Department of Electrical Engineering and Computer Science, Cambridge, Massachusetts, October 1984.

M. C. Teich, "Optical Communications with Quiet Light," Quantum Electronics Seminar, U.S.C. Center for Laser Studies, Los Angeles, California, January 1985.

M. C. Teich, "Quiet Light Generation and Detection for Fiber-Optic Communications," Electrical Engineering Colloquium, University of California at San Diego, La Jolla, California, January 1985.

M. C. Teich, "The Hecht-Shlaer-Pirenne Experiment Revisited," Department of Psychology Vision Talk, University of California at San Diego, La Jolla, California, February 1985.

M. C. Teich, with W.J. McGill, "Exact Psychometric Functions for a Wideband Envelope Detector," Annual Meeting of the Acoustical Society of America, Austin, Texas, April 1985.

M. C. Teich, "Quiet Light Generation and Detection for Fiber-Optic Communications," Quantum and Superconductive Electronics Seminar, University of California at Berkeley, Berkeley, California, April 1985.

M. C. Teich, "Quiet Light Generation and Detection for Fiber-Optic Communications," Quantum Electronics and Fourier Optics Seminar, Stanford University, Stanford, California, April 1985.

M. C. Teich, with K. Matsuo and B.E.A. Saleh, "Avalanche Multiplication in Photodiodes," Meeting of the NSF Grantee-User Group in Optical Communication Systems, Ithaca, New York, June 1985.

E. S. Yang, "Understanding the Metal-Polysilicon-Silicon Contacts," IBM East Fishkill, March 1984.

E. S. Yang, "Physics of the Schottky Barrier," "Ohmic Contacts and Interconnects," "MOS Transistors: Theory and Practices," "Bipolar Device Physics and Technology," Lectures given at the 1984 Semiconductor Colloquium of Silicon Physics, Materials, Devices and Applications, Academia Sinica, Peking, May 1984.

E. S. Yang, with Q.H. Hua, D.K. Yang and G.S. Yang, "Amorphous Silicon as a Tunneling Barrier," 42nd Device Research Conference, Santa Barbara, CA, June 1984.

E. S. Yang, with P.S. Ho, P.E. Schmid, and M. Liehr, "Interface States and Formation of Schottky Barrier at Silicide- Silicon Interfaces," Int. Chemical Congress, Honolulu, December 1984.

E. S. Yang, with W. Wu, H.L. Evans, M. Liehr, and P.S. Ho, "Interface State Measurement of Epitaxial and Non-epitaxial Ni/Si Schottky Barriers," Phys. & Chem. of Semicon. Interfaces, Phoenix, AZ, January 1985.

E. S. Yang, "Interface State in Silicide-Silicon Schottky Barriers," IBM Yorktown Heights, May 1985.

E. S. Yang, with P.S. Ho, M. Liehr, P.E. Schmio, F.K. LeGoves, H.L. Evans, and X. Wu, "Schottky Barrier, Electronic States and Microstructure at Ni Silicide Silicon Interfaces," Conf. on the Formation of Semiconductor Interfaces, Marseilles, France, June 1985.

E. S. Yang, with X. Wu, H.L. Evans, and P.S. Ho, "Silicide Silicon Interface States," MRS Thin Film Symposium, Boston, MA, December 1985.

E. S. Yang, "Photovoltaic Effect at Grain Boundary," MRS Thin-Film Symposium, Boston, MA, December 1985.

Resonance Seminars

Meetings are held periodically at Columbia University, New York, New York during the academic year and are open to all members of the New York scientific community. Guest speakers are invited to discuss work in the general area of the research in the Columbia Radiation Laboratory.

Daniel Prober, Yale University, "Electron Transport in 1-D and 2-D Systems," March 20, 1985.

Richard R. Freeman, AT&T Bell Laboratories, "Measurements on Mass-Resolved Clusters of Si," April 3, 1985.

Vincent M. Donnelly, AT&T Bell Laboratories, "Laser Induced Deposition and Expitaxy," April 17, 1985.

Cynthis M. Friend, Harvard University, "Chemistry of Modified Tungsten Surfaces," May 8, 1985.

Warren S. Warren, Princeton University, "Elucidating State-to-State Collisional Dynamics by Laser Pulse Shaping," September 13, 1985.

Eric Weitz, Northwestern University, "Spectroscopy and Reaction Kinetics of Coordinatively Unsaturated Metal Carbonyls," September 20, 1985.

Dr. John Reintjes, Naval Research Laboratory, "Beam Clean-Up with Stimulated Raman Scattering," September 27, 1985.

Steven Bernasek, Princeton University, "The Precursor to CO Dissociation on Fe "100"," October 22, 1985.

John Bjorkholm, AT&T Bell Labs, "Resonance Radiation Pressure and Cold Atoms: Optical Molasses," November 1, 1985.

T.P. Ma, Yale University, "Radiation Effects in MOS Device Structures," November 12, 1985.

Robert Hellwarth, Columbia University, "Optical Measurements of Densities, Lifetimes, Cross Sections, and Species of Charge Carriers in Insulators and Semiconductors," November 15, 1985.

William Hellwarth, Columbia University, "Th Photorefractive Effect: Physics and Applications," November 26, 1985.

Richard Fork, AT&T Bell Labs, "Femtosecond Pulse Spectroscopy," December 6, 1985.

Paul S. Henry, AT&T Bell Labs, "Coherent Lightwave Communication," December 10, 1985.

I. QUANTUM DETECTION AND SENSING OF RADIATION

A. NOISE IN THE GENERATION, PARTITION, AND DETECTION OF LIGHT

(M. Teich, P. Prucnal, B. Saleh, D. Stoler, K. Matsuo)
(JSEP Work unit 1, 1985 - 1988)
(Principal Investigator: M.C. Teich (212) 280-3117)

We have continued work on the generation, partition, and detection of light. Our earlier work permitted us to understand the theoretical underpinnings of generating low-noise sub-Poisson (quiet) light, the significance of unavoidable partition noise (such as occurs at a beamsplitter or arises from the finite quantum efficiency of optical devices), and the character of multiplication noise in avalanche photodiodes.[1]

In this last period, we have successfully generated sub-Poisson light at 253.7 nm in the laboratory using a space-charge-limited electron beam to excite the Franck-Hertz effect.[2,3] We believe that this is a significant breakthrough inasmuch as it is the first time that cw quiet light has been generated.

There have been only a few cases in which nonclassical light has been produced. Recently, Short and Mandel[4] demonstrated that laser-excited resonance fluorescence radiation from isolated Na atoms takes the form of conditionally sub-Poisson (or nonstationary) individual emissions. Constructing an unconditionally sub-Poisson light source from a collection of such emissions is a difficult task, however, because the excitation statistics must also be made sub-Poisson.[5] In their experiment the excitation statistics are determined by the number of atoms in the field of view of the apparatus, and there is no clear way in which this number can be regulated. If the excitation statistics are Poisson, as expected, then the photon emissions can be Poisson at best.[5]

In a recent theoretical study we showed that under proper circumstances, sub-Poisson light will be generated by a system consisting of sub-Poisson

excitations cascaded with independent sub-Poisson nonstationary individual emissions.[5] As a specific method for constructing such a source, we proposed that a collection of atoms be excited by a low-energy space-charge-limited (sub-Poisson) electron beam.[6] In this scheme, the reduction of the usual Poisson randomness of the excitation arises from space-charge effects. The quieting can be quite large. After excitation, each atom emits a (sub-Poisson) single photon via the Franck-Hertz (FH) effect. The technique is seen to operate by transferring the anticlustering properties of the electrons, resulting from Coulomb repulsion, to the photons. The direction of transfer is the inverse of that encountered in the usual photodetection process, where the statistical character of the photons is imparted to the photoelectrons (see Fig. 1). Since this mechanism involves ordinary spontaneous emission, it is a first-order optical process and can be expected to produce a strong effect. In the same study, it was shown that such sub-Poisson behavior need not necessarily be accompanied by antibunching. Indeed, mathematical conditions were derived to indicate when each of these attributes of nonclassical light implies the other.[6]

We have carried out an experiment of this kind and observed the generation of ultraviolet (253.7-nm) sub-Poisson light from Hg vapor excited by a space-charge-limited electron beam. The experimental arrangement is shown in Fig. 2. This first sub-Poisson light source is only weakly so, principally because of optical losses in the experimental apparatus. From a theoretical point of view, however, there do not appear to be any fundamental barriers to producing an arbitrarily quiet cw intense source by using this method. Quiet light may find use in applications such as optical signal processing and optical communications.

The representative set of data shown in Fig. 3 shows the average photon-count variance-to-mean ratio (Fano factor) $F_n(T)$ plotted against the detected photon count rate μ (kcnts/sec). Data are presented for Poisson filament light, Poisson laser light, and sub-Poisson Franck-Hertz light. In the range $\mu < 30$ kcnts/sec $\langle n \rangle < 0.03$), values of the Fano factor for the Franck-Hertz light lie below those for the Poisson light by between 2 and 3 standard deviations (depending on the details of how the estimates are made). Absolute values of $F_n(T)$ mean little because of afterpulsing in the

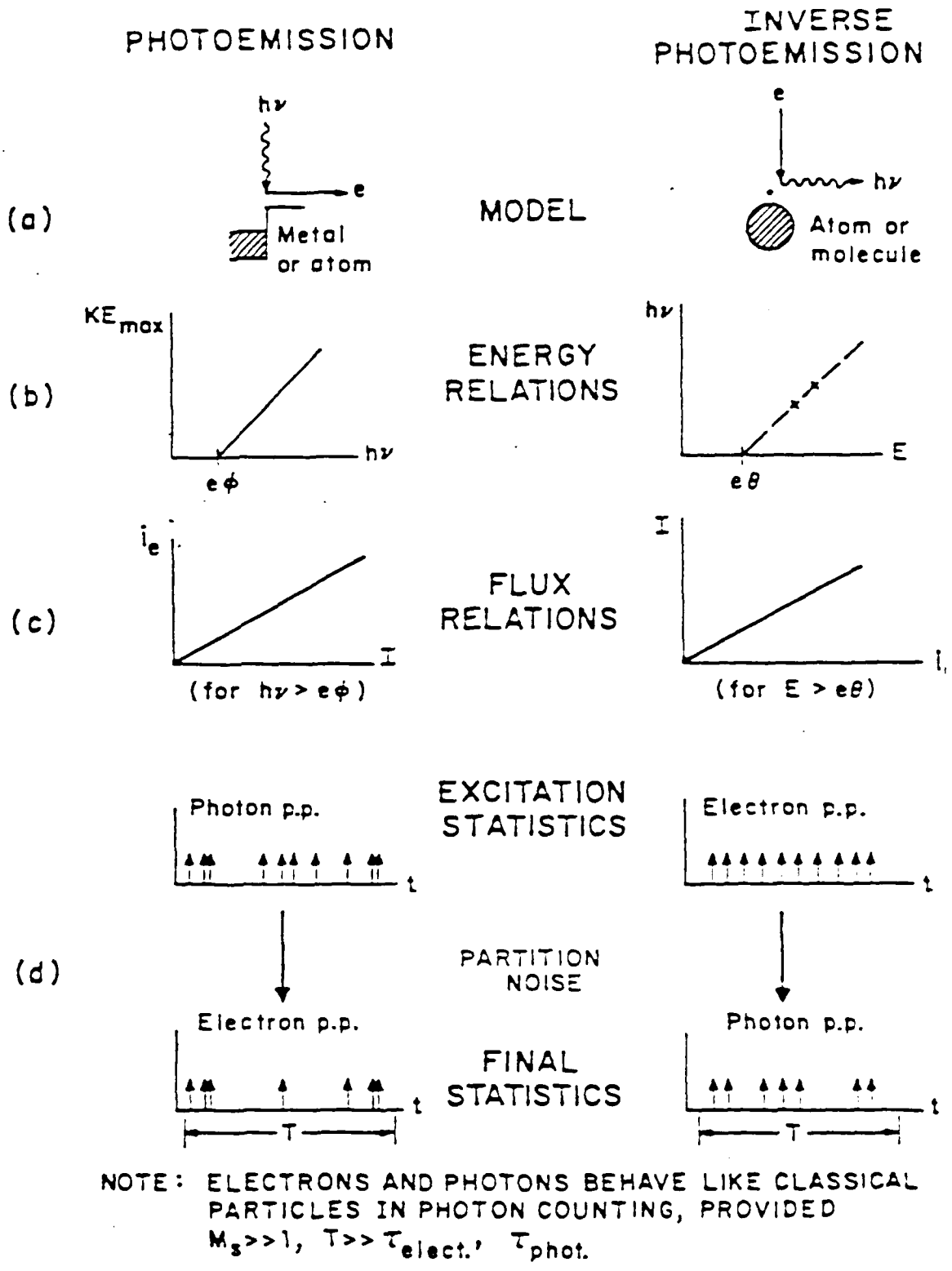

NOTE: ELECTRONS AND PHOTONS BEHAVE LIKE CLASSICAL PARTICLES IN PHOTON COUNTING, PROVIDED $M_s >> 1$, $T >> \tau_{elect.}$, $\tau_{phot.}$

Figure 1: Schematic representation of photoemission and inverse photoemission (Franck-Hertz effect). Electrons and photons behave like classical particles under conditions of multimode spatial and temporal detection.

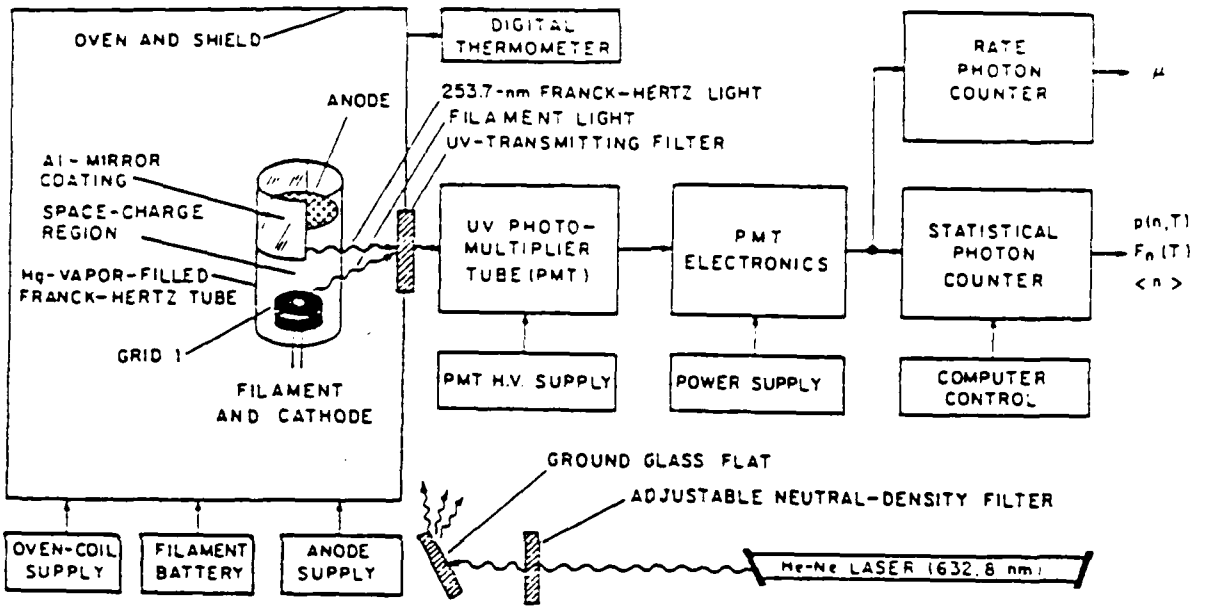

Figure 2: Block diagram of the experimental arrangement.

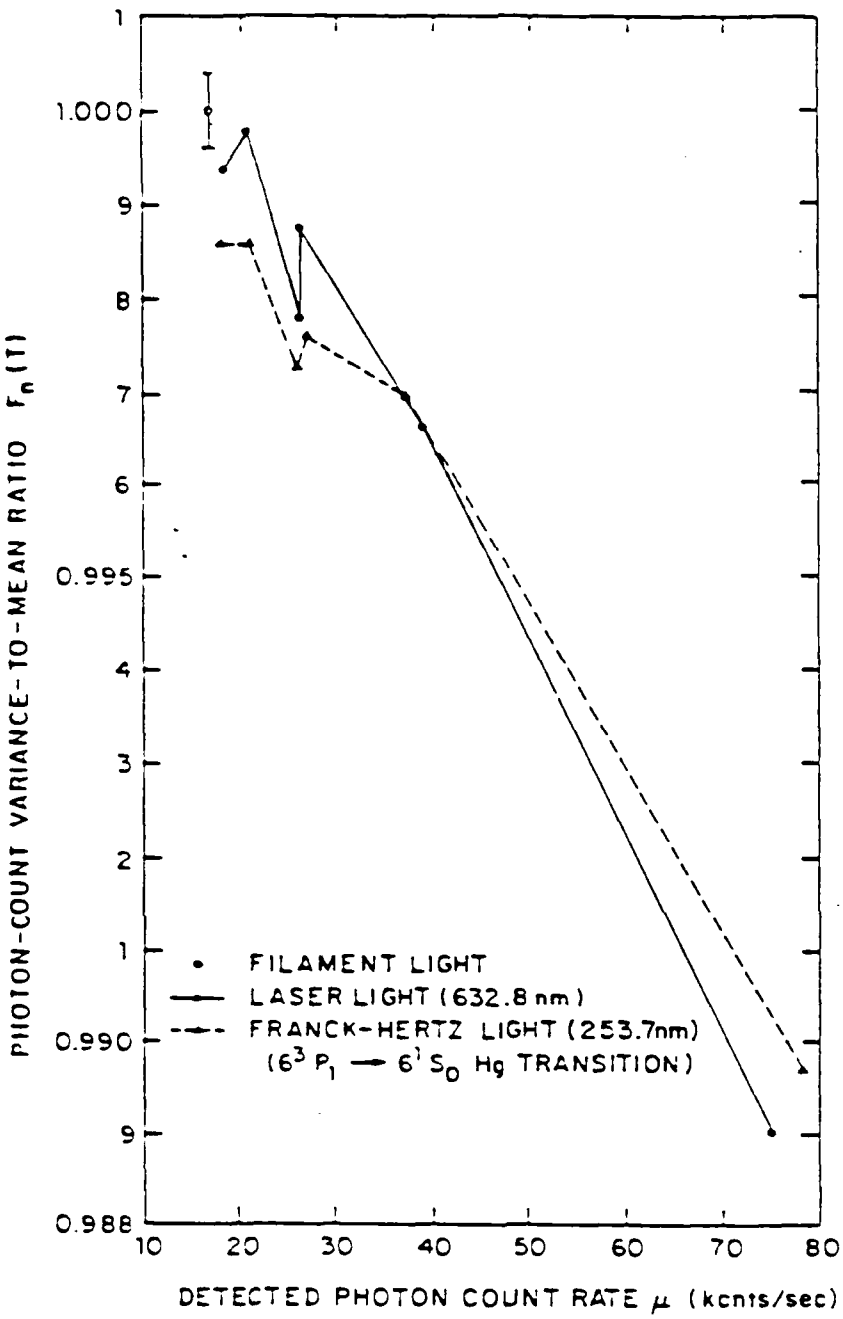

Figure 3: Average photon-count variance-to-mean ratio $F_n(T)$ versus detected photon count rate μ (kcnt/sec) for experiment 0323:3-15. Raw data are shown for Poisson filament light (open circle), Poisson laser-plus-filament light (solid circles and solid line segments), and sub-Poisson Franck-Hertz-plus-filament light (triangles and dashed line segments). Each data point is based on approximately 10^7 samples. The error bracket is the same for all data points. The Fano factors for Franck-Hertz light are seen to lie below those for Poisson light at sufficiently small values of the count rate. The overall negative slope of the data arises from dead time in the photon-counting apparatus.

photomultiplier tube (the afterpulse probability $q \simeq 1.6 \times 10^{-3}$ for any given pulse in T = 1 μsec), dead time in the counting system ($\tau_d \simeq 93$ nsec), and the presence of background filament light ($\mu_{Fil} \simeq 16.6$ kcnts/sec). If we do not bother to correct for background, q provides us with an effective Fano factor F_n' (sub-Poiss) $\simeq 0.9984$ for the FH/filament light in the absence of afterpulsing and dead time.

We have therefore shown that the Franck-Hertz effect stimulated by a space-charge-limited electron beam provides a source of sub-Poisson light, within the statistical uncertainties of the experiment. The agreement with theory [5, 7] is reasonable. There appear to be no fundamental obstacles preventing such a source from being arbitrarily strong and sub-Poisson. Indeed the intensity of our source was very carefully controlled so that the photon-counting equipment would measure the nonclassical nature of the light with a minimum of saturation and dead-time effects. A small increase in the anode voltage produces a virtual flood of sub-Poisson photons.

Studies are underway for enhancing the sub-Poisson nature of the Franck-Hertz source and for developing other means for producing nonclassical light.

This research was also supported by the National Science Foundation under Grant NSF-82-19636.

(1) M.C. Teich, CRL Prog. Rept. No. 34, March 31, 1984, pp. 1-8.

(2) M.C. Teich, B. Saleh, and T. Larchuk, Postdeadline Paper PD-A6, XIIIth International Quantum Electronics Conference, Anaheim, California, June 1984.

(3) M.C. Teich and B. Saleh, J. Opt. Soc. Am. B 2, 275 (1985).

(4) R. Short and L. Mandel, Phys. Rev. Lett. 51, 384 (1983).

(5) M. Teich, B. Saleh and J. Perina, J. Opt. Soc. Am. B 1, 366 (1984).

(6) M. Teich, B. Saleh and D. Stoler, Opt. Commun. 46, 244 (1983).

(7) J. Perina, B. Saleh and M. Teich, Opt. Commun. 48, 212 (1983).

B. EXACT VARIANCE STABILIZING TRANSFORMATIONS FOR IMAGE-SIGNAL- DEPENDENT EXPONENTIAL AND RAYLEIGH NOISE

(P. Prucnal, E. Goldstein)
(JSEP work unit 1, 1985 - 1988)
(Principal Investigator: P. R. Prucnal (212) 280-3119)

1. Technical Report -- One problem presented by the processing of optical signals is that the noise encountered tends to be signal-dependent. Coherent sources, for example, generate photon noise characterized by variance that is proportional to the signal value.(1) Sources emitting chaotic or superposed coherent and chaotic radiation exhibit photon noise variance that is quadratic in the signal value.(2) For film-grain noise, the variance is often proportional to some power of the signal.(3-6) Other imaging devices such as optical disks exhibit noise having a similar signal-dependence.(7)

The problem in processing such noisy images is that classical estimation procedures devised for additive, signal-independent noise do not readily apply. Nonclassical procedures, on the other hand, devised for noise with some given signal dependency, are not only laborious to develop; they also have restricted applicability and are usually computationally complex.(8-10) It is therefore useful to find invertible transformations that render signal-dependent noise signal-independent. The resulting signals can then be subjected to classical estimation procedures, followed by an inverse transformation.

Efforts aimed at finding such transformations have yielded mixed results. Approximate solutions (i.e. transforms yielding approximately variance-stabilized random processes) have turned out to be plentiful.(11-22) But since the notion of the "quality" or "degree" of such approximations has resisted quantitative measure, it is not clear how useful they actually are.

Exact variance-stabilizing transforms, on the other hand, have been scarce; they are known only for random processes comprised of families of log normal,(23) chi-squared, and noncentral chi-squared[1] random variables.

Adding the transforms developed here enlarges this list considerably.

Exact variance-stabilizing transforms have been developed for the exponential and Rayleigh processes. The utility of this for optical processing results from the importance of both exponential and Rayleigh-distributed optical quantities. Coherent sources (e.g. ideal amplitude-stabilized lasers well above threshold) generate photon inter-arrival times that are exponentially distributed. Single-mode chaotic sources (e.g. single-mode lasers below threshold and narrow spectral line sources such as Hg^{198}) produce field intensities that are also exponential processes. The field magnitudes, in the latter case, are Rayleigh. Transforms developed here permit each of these signal-dependent noise processes to be rendered constant in variance. The full variety of processing techniques for additive, signal- independent noise then applies.

2. Integral Expression for Approximate Variance-Stabilizing Transforms — The new exact transforms are suggested by an argument that first appeared in the statistics literature several decades ago[11-14] and has more recently been revived by writers on image processing.[18-23] Consider a random process comprised of a family of random variables X having means μ_x, representing signal values, and variances σ_x^2 representing noise. We wish to transform this family into a new family $Y = g(X)$, where $g(\cdot)$ is chosen so that all members of Y have approximately the same variance.

This expression can be derived as

$$g(X) = \int^X dr/D(r) \qquad (1)$$

for values of X in the range of μ_x, where the notation denotes any anti-derivative of $1/D(r)$, evaluated at X.

3. Exact Variance-Stabilizing Transforms for Exponential and Rayleigh Variables — Equation (1) supplies an approximate, though rather general, solution to the problem. For exponential and Rayleigh families, the variance is proportional to the mean squared, so that Eq. (1) yields a scaled logarithmic transform. The above argument thus implies that if the natural

logarithm can be approximated over the interval $(0, \infty)$ by a two-term Taylor series-- obviously a poor approximation-- then log-transformed exponential and Rayleigh families will exhibit approximately stabilized variance.

As it turns out, the variance in these two cases is exactly stabilized, notwithstanding the argument's poor approximation. This can be shown by applying standard statistical manipulations, yielding several less standard integrals.

As a check of these calculations, probability densities for representative random variables belonging to the families discussed above are plotted. Densities of six exponential random variables, having an evident diversity of variances, are plotted in Fig. 1(a). These six, when transformed by $Y = \ln X$, yield the densities of Fig. 1(b). Similarly, densities of six Rayleigh random variables are plotted in Fig. 2(a). Applying the transformation $Y = (\pi/(4-\pi))^{1/2} \ln X$ yields the densities of Fig. 2(b). Visual inspection leads to the same conclusion in each case: both transforms, so far as the eye can discern, exactly stabilize variance. This is in agreement with the analytical results we have obtained.

4. Conclusion -- With the aid of variance-stabilizing transforms, images degraded by signal-dependent noise can be processed using techniques devised for the more familiar case of additive, signal-independent noise. However, few exact variance-stabilizing transforms are known. For the exponential and Rayleigh processes, the logarithmic transform was shown to exactly stabilize variance. In image processing, these two special cases alone have important applications. Outside optics, variance-stabilization of the Weibull family is expected to find use in analyses of waiting times, particle dimensions, and weakest-link failure times.

This research was supported also by the National Science Foundation ERC under contract CDR-84-21402.

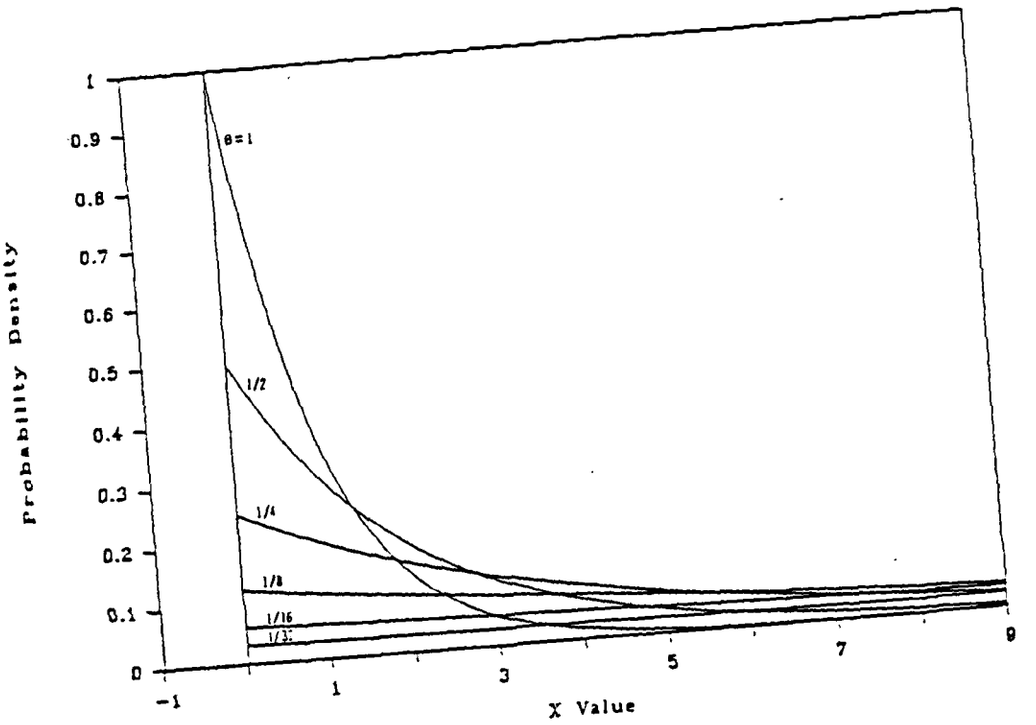

Fig. 1(a).

Fig. 1. Probability Density Functions of (a) Exponential and (b) Transformed Exponential Random Variables.

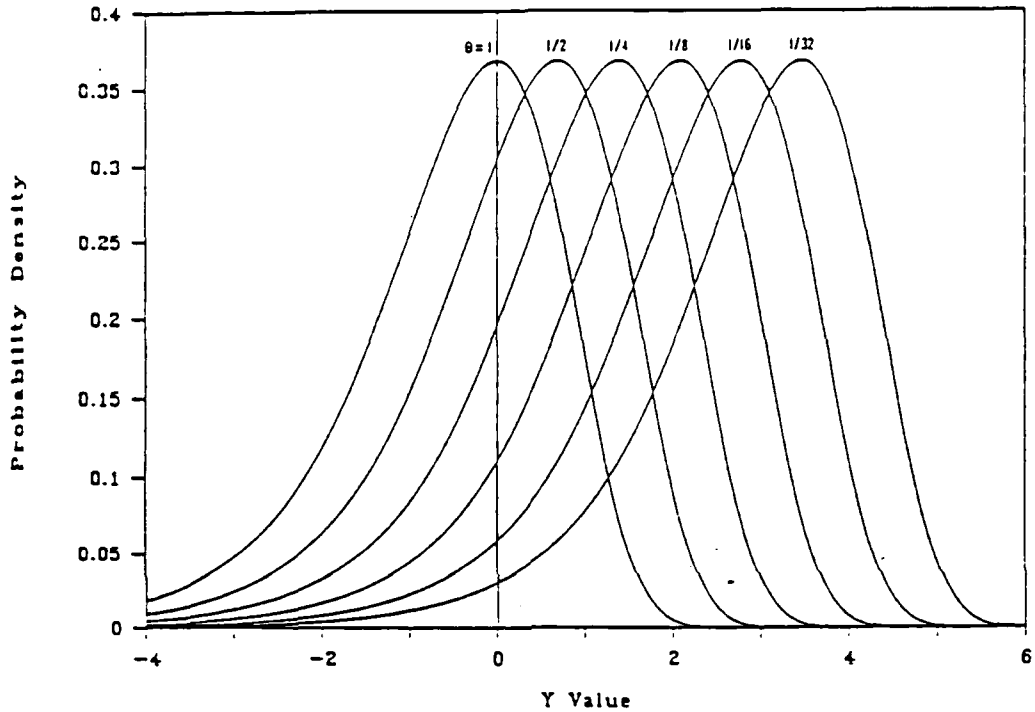

Fig. 1(b).

Fig. 1. Probability Density Functions of (a) Exponential and (b) Transformed Exponential Random Variables.

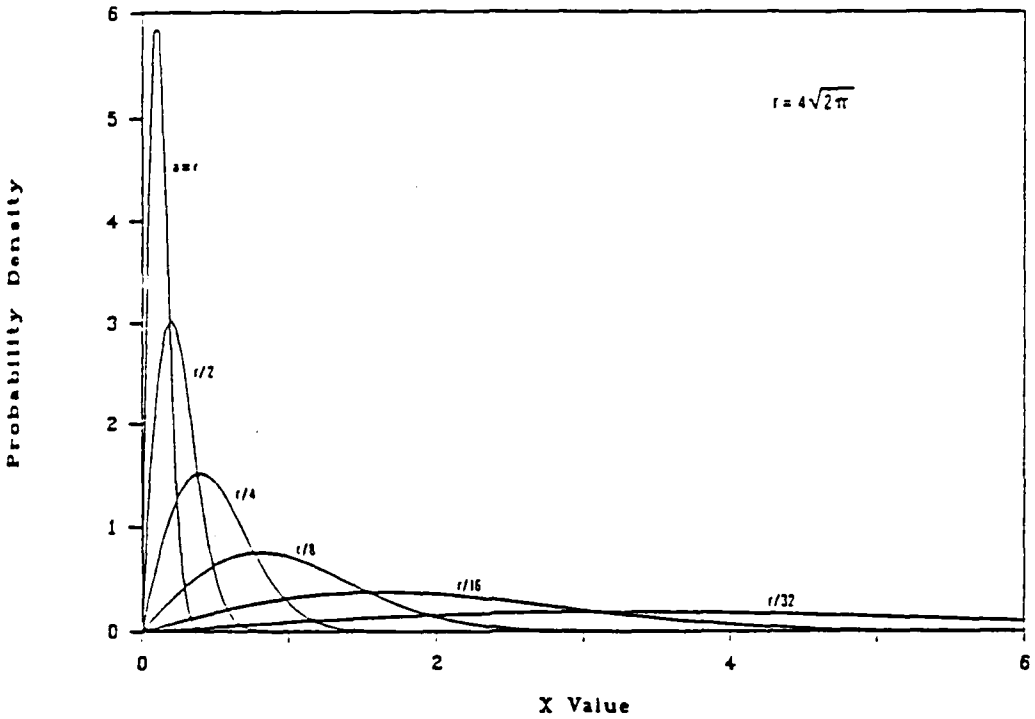

Fig. 2(a).

Fig. 2. Probability Density Functions of (a) Rayleigh and (b) Transformed Rayleigh Random Variables.

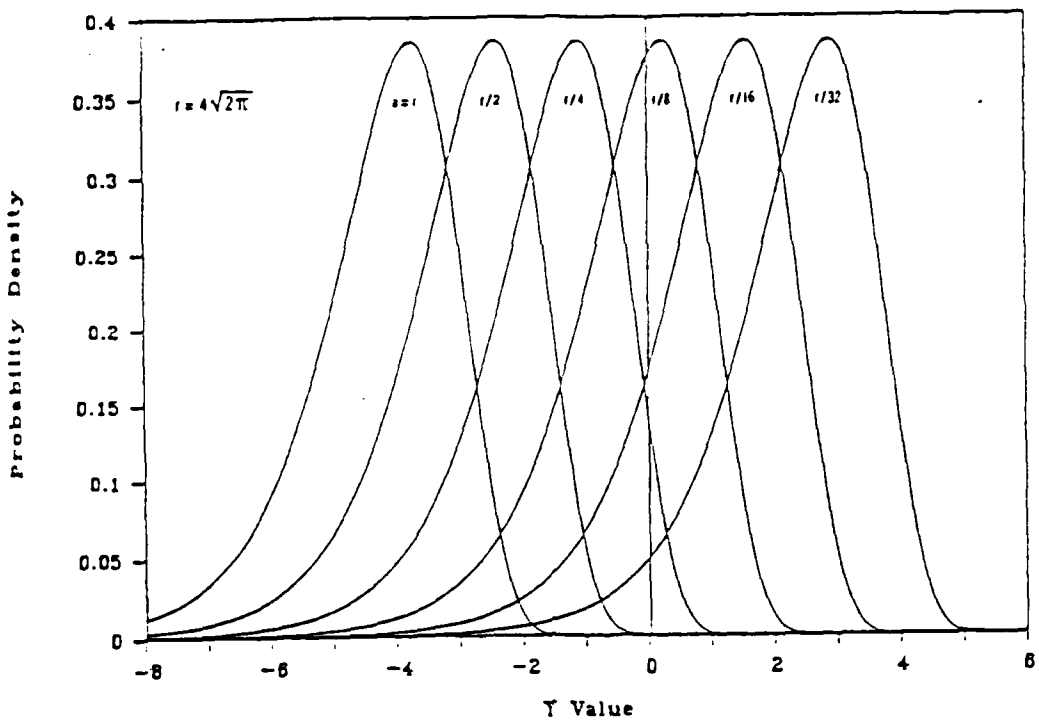

Fig. 2(b).

Fig. 2. Probability Density Functions of (a) Rayleigh and (b) Transformed Rayleigh Random Variables.

(1) B.E.A. Saleh, Photoelectron Statistics (Springer-Verlag, New York, 1978).

(2) P. R. Prucnal and M.C. Teich, "Statistical Properties Of Counting Distributions For Intensity Modulated Sources," J. Opt. Soc. Am. 69, 539-543 (1979).

(3) F. Naderi and A.A. Sawchuk, "Estimation Of Images Degraded By Film-Grain Noise," Appl. Opt. 17, 1228-1237 (1978).

(4) F. Naderi and A. A. Sawchuk, "Detection Of Low-Contrast Images In Film-Grain Noise," Appl. Opt. 17, 2883-2891 (1978).

(5) H.H. Arsenault, C. Gendron, and M. Denis, "Transformation Of Film-Grain Noise Into Signal-Independent Additive Gaussian Noise," J. Opt. Soc. Am. 71, 91-94 (1981).

(6) H.H. Arsenault and M. Levesque, "Combined Homomorphic And Local-Statistics Processing For Restoration Of Images Degraded By Signal-Dependent Noise," Appl. Opt. 23, 845-850 (1984).

(7) J.L. Su and M. L. Williams, "Noise in Disk Data-Recording Media," IBM J. Res. Develop. 18, 570-575 (1974).

(8) G.K. Froehlich, J.F. Walkup, and R.B. Asher, "Optimal Estimation In Signal-Dependent Noise," J. Opt. Soc. Am. 68, 1665-1672 (1978).

(9) G.K. Froehlich, J.F. Walkup, and T.F. Krile, "Estimation in Signal-Dependent Film-Grain Noise," Appl. Opt. 20, 3619-3626 (1981).

(10) R. Kasturi, Adaptive Image Restoration in Signal-Dependent Noise (Institute for Electronic Science, Texas Tech University, Lubbock, Tex., 1982).

(11) M.S. Bartlett, "The Square-Root Transformation In The Analysis Of Variance," J.R. Stat. Soc. Suppl. 3, 68-78 (1936).

(12) J.H. Curtiss, "On Transformations Used In The Analysis Of Variance," Ann. Math. Stat. 14; 107-122 (1943).

(13) F.J. Anscombe, "The Transformation Of Poisson, Binomial, And Negative-Binomial Data," Biometrika 35; 246-254 (1948).

(14) M.F. Freeman and J.W. Tukey, "Transformations Related To The Angular And Square Root," Ann. Math. Stat. 21. 607-611 (1950).

(15) A.A. Sveshnikov, Problems in Probability Theory, Mathematical Statistics, and Theory of Random Functions (Dover, New York, 1968), pp. 136-141.

(16) M.G. Natrella, Experimental Statistics (U.S. Government Printing Office, Washington, D.C., 1963), pp. 20-1 - 20-12.

(17) M.G. Kendall and A. Stuart, The Advanced Theory of Statistics (Hafner, New York, 1966).

(18) P.R. Prucnal, "Receiver Performance Evaluation Using Photocounting Cumulants With Application To Atmospheric Turbulence," Appl. Opt. 19, 3611-3616 (1980).

(19) H.H. Arsenault and M. Denis, "Integral Expression For Transforming Signal-Dependent Noise Into Signal-Independent Noise," Opt. Lett. 6, 210-212 (1981).

(20) P.R. Prucnal and B.E.A. Saleh, "Transformation Of Image-Signal-Dependent Noise Into Image-Signal-Independent Noise," Opt. Lett. 6, 316-318 (1981).

(21) P.R. Prucnal and B.E.A. Saleh, "Evaluation Of Fiber-Optic Error Rates Using A Normalizing Transform," J. Opt. Soc. Am. 72, 1171-1178 (1982).

(22) P.R. Prucnal and M.C. Teich, "Multiplication Noise In The Human Visual System At Threshold: 2.Probit Estimation Of Parameters," Biol. Cyber. 43, 87-96 (1982).

(23) P.R. Prucnal and M.C. Teich, "An Increment Threshold Law For Stimuli Of Arbitrary Statistics," J. Math Psych. 21, 168-177 (1980).

(24) cf. Eq. (17) of Ref. 20 with parameter s=0.

(25) E.g., E. Parzen, Modern Probability Theory and Its Applications (Wiley, New York, 1960).

(26) M. Abramowitz and I.E. Stegun, Handbook of Mathematical Functions (U.S. Government Printing Office, Washington, D.C., 1964), p. 1027.

(27) H. Bateman, Table of Integral Transforms, v. 1 (McGraw-Hill, New York, 1954), pp. 148-149.

PREVIOUS PAGE IS BLANK

II. PHYSICAL AND PHOTOCHEMICAL PROPERTIES OF ELECTRONIC MATERIALS

A. MASKLESS PROJECTION OF ETCHING OF GaAs USING EXCIMER LASER PHOTOCHEMISTRY

(P. Brewer, R.M. Osgood)
(JSEP work unit 4, 1985 - 1988)
(Principal Investigator: R. Osgood (212)280-4462)

In our previous report, gas-phase photochemistry with excimer lasers had shown to be a useful method for the dry etching of elemental and compound semiconductors.[1] The technique can be rapid and anisotropic with little or no surface damage. Since the approach is based on volumetric production of reactive species with concomitant gas-phase diffusion to the surface, previous results have been based on the use of contact or proximity masking for pattern transfer.[2]

In this report, we describe projection dry-etching of GaAs with an ArF excimer laser and HBr precursor gas.[2] Using a gas-phase, photochemically initiated mechanism which is enhanced by surface illumination from the laser, local confined etching is achieved. This approach is in contrast to previously reported laser projection etching of thin films, in which the etching is caused by direct substrate (thermal or electronic) excitation followed by ablation.[3] In addition to Ref. 3, projection etching has been alluded to in talks by Horike at Toshiba and by various IBM researchers. For delicate materials, such as compound semiconductors, ablative etching tends to create surface defects by changing surface composition through nonstoichiometric evaporation. Here we will concentrate on describing some of the physical and chemical considerations for pattern transfer by excimer laser projection dry-etching of GaAs.

One prerequisite for producing high-resolution microstructures when using a gas-phase is that the photochemically initiated process is to use a precursor gas with no spontaneous or dark etch rate. HBr has been shown to have no spontaneous or dark etch rate with GaAs in the temperature range

0°-100°C.[2] Our etching mechanism in the HBr/GaAs system is based on the photodissociation of HBr at 193 nm to produce reactive bromine atoms. Bromine atoms have been shown to have twice the etch rate with GaAs as compared with molecular bromine.[4]

The experimental set-up for the present experiments used a repetitively-pulsed (1-100 Hz) ArF excimer laser at 193 nm with 10%, pulse-to-pulse, power variation. The laser output could be imaged using a 1:1 single-lens system (N.A. = 0.33) or a Schwarzschild reflector (N.A. = 1.25, x 36) directly onto the GaAs (100) substrate housed in a stainless steel, 4-window cell. The cell is diffusion pumped and gases flow through the cell at 0.3 - 1.0 Torr/sec., thus insuring that only nascent dissociation products are in the cell. The GaAs substrates are fixed to a nickle-plated, copper holder which was resistively heated to 60°C. The samples were cleaned by a standard chemical washing procedure and dried with nitrogen before each experiment. Etch depths and etching rates were measured by means of a mechanical stylus, and etching morphology was studied by scanning electron microscopy (SEM).

We have investigated the effect of using several buffer gases on process spatial resolution and on etch rate in order to understand the physical mechanisms involved in these two etch characteristics. From a pattern-transfer point-of-view, the main goal in adding buffer gas is to limit the lateral diffusion of gas-phase reactants. Fig. 1B shows an example of high-resolution microstructures produced by this process under the following experimental conditions: (HBr:500 mTorr, H_2:10 Torr, and GaAs (100) heated to 60°C. These microstructures have resolution comparable to the laser-beam projected image. Two classes of buffer gases were added for linewidth confinement: nonreactive (physical quencher i.e., Argon) and reactive (chemical quencher i.e., ethylene). The effect of the addition of buffer gas on the linewidth, as shown in Fig. 2, is to enhance the resolution of the image until its optical limit is reached. The confinement by the buffer gases appears to stem from reduction of the mean free path of the reactants by physical collisions or chemical reactions. If one plots, for example, a simple linewidth curve based on the form $w_o + 2\lambda$, where w_o is

EFFECT OF BUFFER GAS ON PROJECTION LINE WIDTH RESOLUTION

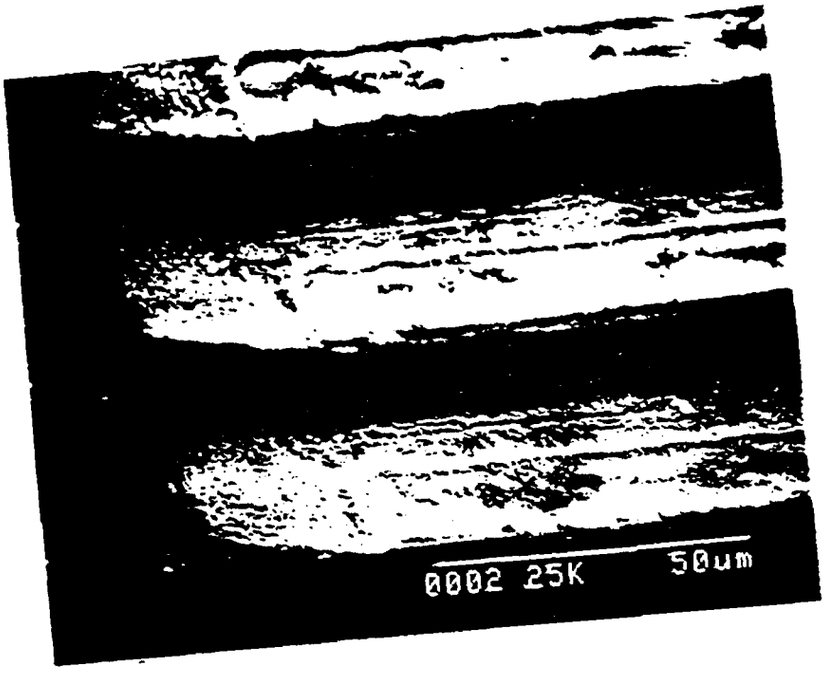

HBr (0.5 Torr)
Width: 21 μm

A

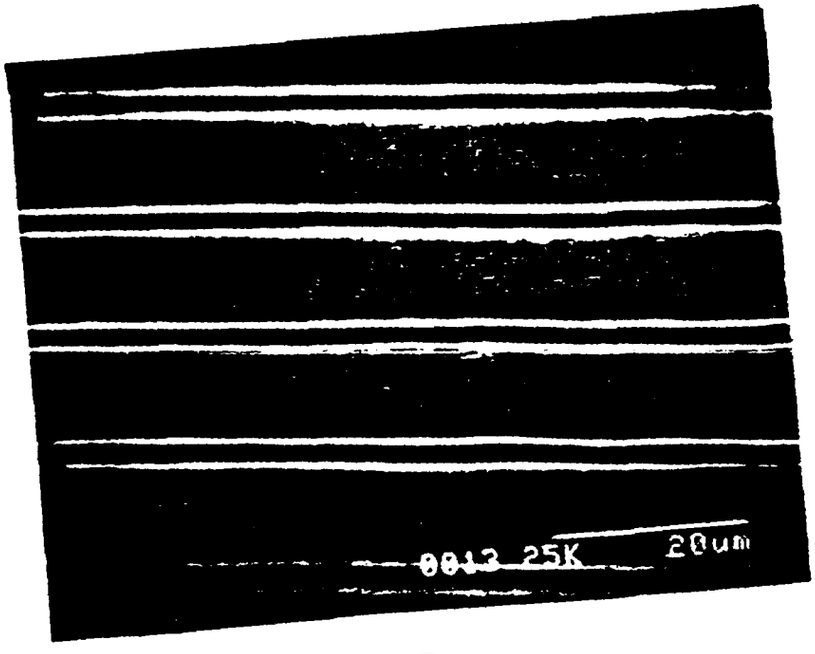

HBr (0.5 Torr)
H_2 (10 Torr)
Width: 4 μm

B

Figure 1: Comparison of resolution of etched features in GaAs with (b) and without (a) the addition of buffer gas.

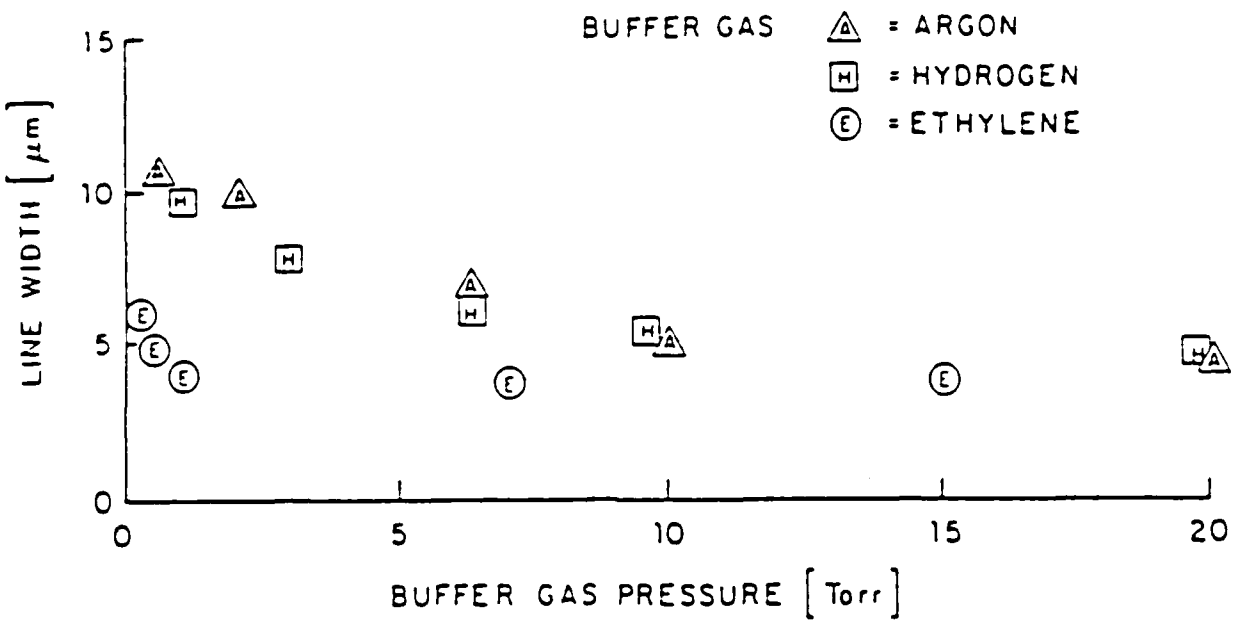

Figure 2: Measurement of the linewidth of projected etched lines as a function of three different gases at 20 mJ/cm^2.

is the optically determined laser-beam image size on the sample, and λ is the gas-phase mean free path (based on kinetic data) for a given precursor/buffer gas pressure combination, one obtains curves of approximately the same functional form; however, the experimental data have consistently smaller linewidths by ~ 5 times.

The GaAs etch rate, shown in Fig. 3 for the case of Ar buffer gas, also obeys nearly a 1/p dependence with increasing buffer gas pressure, p. This form is consistent with the limiting of the laser-produced reactive volume by a factor proportional to a mean free path above the surface determined by the precursor/buffer gas pressure.

We believe that the physical basis for Fig. 2 and Fig. 3 is directly tied to the dynamics of the pulsed-photochemistry which the excimer laser initiates in combination with high-order, gas-surface reaction kinetics. However, in the following discussion, we will first discuss several other phenomena which might, at first, be thought to explain the observed data.

Some general laser-surface interactions which are known to occur during laser initiated etching are pulsed-laser heating,[6] photo-induced carrier generation,[7] and ablative adlayer removel.[8] These processes involving laser-substrate interactions, however, cannot contribute to the overall line-width resolution or etch-rate dependence on buffer-gas pressure. For example, in our experiments, the region of sample under illumination reaches a local maximum surface temperature of $<150^{\circ}$ (lower temperatures are more typical), which subsides to one half of its value after 20 nsec.[2] This temperature rise might at first be thought to enhance significantly the local etch rate; however, the spatial resolution of the process is not in accord with a surface phenomenon. In particular, the expected lateral spatial spread in all of these laser-surface interactions (i.e., heating, electron-hole formation, ablation) are also either confined to below 1 um or take on the laser image size and should not be dependent on buffer gas pressure. Thus, although surface driven laser-initiated etching reactions are known to occur,[1,2,7] they would not lead to the line-width resolution seen in our experiments.

Insofar as the gas-phase photochemistry is concerned, etching by excited-state bromine atoms might, in principle, exhibit behavior dependent

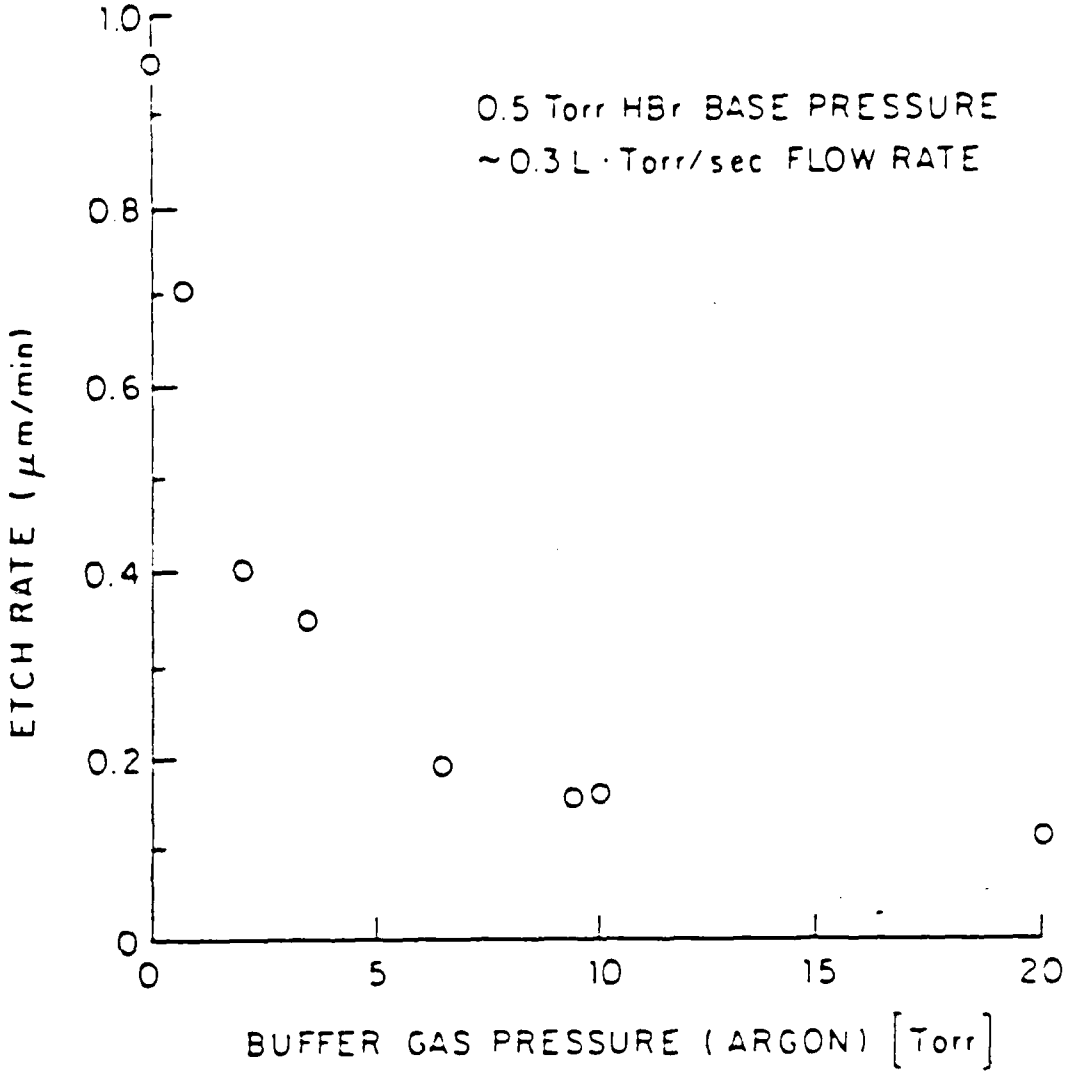

Figure 3: Measurement of feature etch rate as a function of argon buffer gas pressure.

on the type and pressure of the buffer gas added. Note that the translational temperature of the photogenerated bromine atoms is insignificant. However, for the case of electronic deexcitation of bromine atoms, it is known that H_2 and Ar have drastically different cross sections[9] for quenching Br ; as a result, one would expect that the effect of adding argon or H_2 gas would be quite different. In fact, however, the line-width dependence with pressure of the nonreactive buffer gases Ar and H_2 is the same. As a result, electronically excited Br is not responsible for the behavior shown in Figs. 2 and 3.

One mechanism which does fit the observed line-width and etch-rate dependence on buffer gas pressure is a dynamic effect caused by high order, gas-surface reaction kinetics, in conjunction with the pulsed-photochemistry produced by the excimer laser. In particular, we have previously shown that the products of the reactions between GaAs and bromine atoms are primarily $GaBr_3$ and $AsBr_3$.[2,4] Thus an overall reaction scheme can be written:

$$X + 3Br \longrightarrow XBr_3$$

Where X is a surface atom Ga or As. Assuming the following possible step-wise bromination reactions with the surface,

$$X + Br \longrightarrow XBr$$
$$XBr + Br \longrightarrow XBr_2$$
$$XBr_2 + Br \longrightarrow XBr_3$$
$$XBr_3 \ (\underline{surface}) \longrightarrow XBr_3 \ (gas)$$

a third order kinetic reaction can be written for the etch rate:

$$R \longrightarrow K[X][Br]^3 \qquad (1)$$

Note that where K is an overall rate constant for the process, the reaction is nonlinear in radical atom flux, J, which means that surface regions which encounter a high atom flux are etched much faster than the low-concentration regions. For the above scheme, $R \sim J^3$ at low levels of bromine atom flux.

Although the detailed mathematical model is complex for the geometries used in our experiment, it is straightforward to show that the surface atom impingement has a fast high intensity transient component followed by a slow, low-intensity decay.[11] Because of the nonlinearity in the reaction rate alluded to above, this pulsed behavior causes the surface reaction rate to be concentrated immediately following the laser pulse. The duration of the initial high intensity pulse of Br atoms hitting the surface is approximately of duration t_o, where

$$t_o \sim \lambda/v$$

where λ is the atom mean free path and v is the near-thermal velocity of the surface atoms.

In other words, initially the laser beam photodissociates HBr molecules, forming imaged vertical slabs of bromine radicals reaching down to the surface. In a very short time, the bromine radicals within one mean free path move ballistically[10] to the surface with the probability of reaching the surface determined from their position above the surface. The radical flux will be highest in the vicinity of the intersection of the imaged slab and the surface. This nondiffusional flux will give the maximum radical concentration on the surface for all times and, as a result, the radical population close to the surface will then be depleted due to surface reactions and spreading of the gas phase slabs. The combined effects of the rapidly decreasing radical flux with time and the nonlinear reaction kinetics on the surface cause only the earlier portion of the integrated flux to be recorded.

Both the experimental line-width and etch-rate dependencies on buffer-gas pressure can be explained by the above model. The lateral spread of the radical flux on the surface is limited to that due to the atom motion, turning to nearly one mean free path. For the case where the mean free path is larger than the optically-defined feature size, the feature resolution will be blurred by an amount $\sim 1/p^n$ where p is the buffer gas pressure. The exponent n is a coefficient which is appropriate for the order of the reaction being examined. This general behavior is seen in Fig. 1 and 2.

The inverse relationship between the etch rate and buffer gas pressure is a result of the fact that the buffer gas limits the height of the early peaked contribution of the radicals above the surface. By integrating the surface flux with time, it can be shown that the etch rate $R \sim 1/p^n$, again in general agreement with observed data.

In conclusion, we have demonstrated for the first time projection dry-etching of GaAs using an ArF excimer laser and the HBr precursor gas. Line-width resolution down to the optical limit (4 μm) was achieved through the addition of the buffer gases (H_2, Ar, and C_2H_4). The line-resolution and the etch-rate dependencies as a function of buffer gas pressure reveal that the mechanism is related to nonlinear gas-surface reaction kinetics, together with the pulsed-photochemistry produced by the excimer laser. Currently we are investigating further the gas dynamics and surface chemistry involved in this technologically important etching process.

The authors would like to thank Lee Chen of IBM for assistance in apparatus design. This research was also supported by the Air Force of Scientific Research/DARPA under Grant F-49620-84-K-0022 and Army Research Office under Contract DAAG29-85-K-0210.

(1) T.J. Chuang, J. Vac. Sci, Techn. 21, 798 (1982); R.M. Osgood, Jr., Ann. Rev. Phys. Chem. 34, 77 (1983); P.D. Brewer, G.M. Reksten, and R.M. Osgood, Jr., Solid State Techn. 28, 273 (1985).

(2) P.D. Brewer, D. McClure, and R.M. Osgood, Jr., Appl. Phys. Lett., to be published; T. Aridado, H. Okano, M. Sekine, and Y. Horiike in Laser-Controlled Chemical Processing of Surfaces, Mat. Res. Soc. Symp. proc. eds., A.W. Johnson, D.J. Erlich, H. Schlossberg, 29, 167 (1984).

(3) R. Srinivasan, V. Mayne-Banton, Appl. Phys. Lett. 41, 576 (1982).

(4) D. Ibbotson, D. Flamm, and V. Donnelly, J. Appl. Phys. 54, 5974 (1983).

(5) J.O. Hirschfelder, C.F. Curtiss, and B.B. Bird, Molecular Theory of Gases and Liquids (John Wiley and Sons, New York, 1954).

(6) J.F. Ready, J. Appl. Phys. 36, 462 (1965).

(7) F.A. Houle, J. Chem. Phys. 79, 4237 (1983).

(8) G. Koren, F. Ho, and J.J. Ritski, Appl. Phys. Lett. 46, 1006 (1985).

(9) R.J. Donovan and D. Husain, Trans. Faraday Soc. 62, 2987 (1966).

(10) Note that another gas-phase process which might be thought to contribute to spatial localization in gas-phase recombination of Br and H or Br. This process takes many collisions and cannot contribute to our results.

(11) J. Chen, unpublished calculations.

B. CHEMICAL PHYSICS OF INTERFACE REACTIONS

(P. Brewer, C. Yu, H.H. Gilgen, R.M. Osgood)
(JSEP work unit 4, 1985 - 1988)
(Principal Investigator: R. Osgood (212)280-4462)

This work unit is concerned with examination of the basic physics of material removal (etching) reactions at interfaces. The research not only supports the photon-assisted drying eching work of Part A above, but it is also valuable in its own right for understanding and observing new physical phenomena occuring at interfaces, one of the most critical areas of modern electron device and IC technology. At Columbia we have made very important advances in increasing our basic research capability in the area of interface diagnostics and instrumentation. In particular, we have almost completed constructing a time-of-flight apparatus for observing photon-induced surface reactions and we have set up a UHV surface analysis system for observing changes in surface stoichiometry and structure. In addition, we have increased our research on understanding of the physics for light-guided reactions on semiconductor surfaces.

1. Time of Flight System for Analysis of the Fundamental Chemistry of Laser Induced Reactions -- We have recently begun construction of a high-vacuum to UHV time-of-flight measurement system with time resolution of 10 nsec. The system also has an auxiliary unit that can carry out high pressure (1 μ-Torr to 100 Torr) etching processes. A schematic is shown is Fig. 1. The purpose of this system is to determine the GaAs/HBr etching mechanism, the energy distribution functions of the etch product desorbing from the surface adlayer in the GaAs/HBr system, and to determine the cause of crystallographic etching in this system.

Time-resolved, laser-induced, surface mass spectroscopy requires high time resolution and a good signal-to-noise ratio. We have purchased an Extra Nuclear C-50 quadrupole mass spectrometer with 10-nsec response time. The

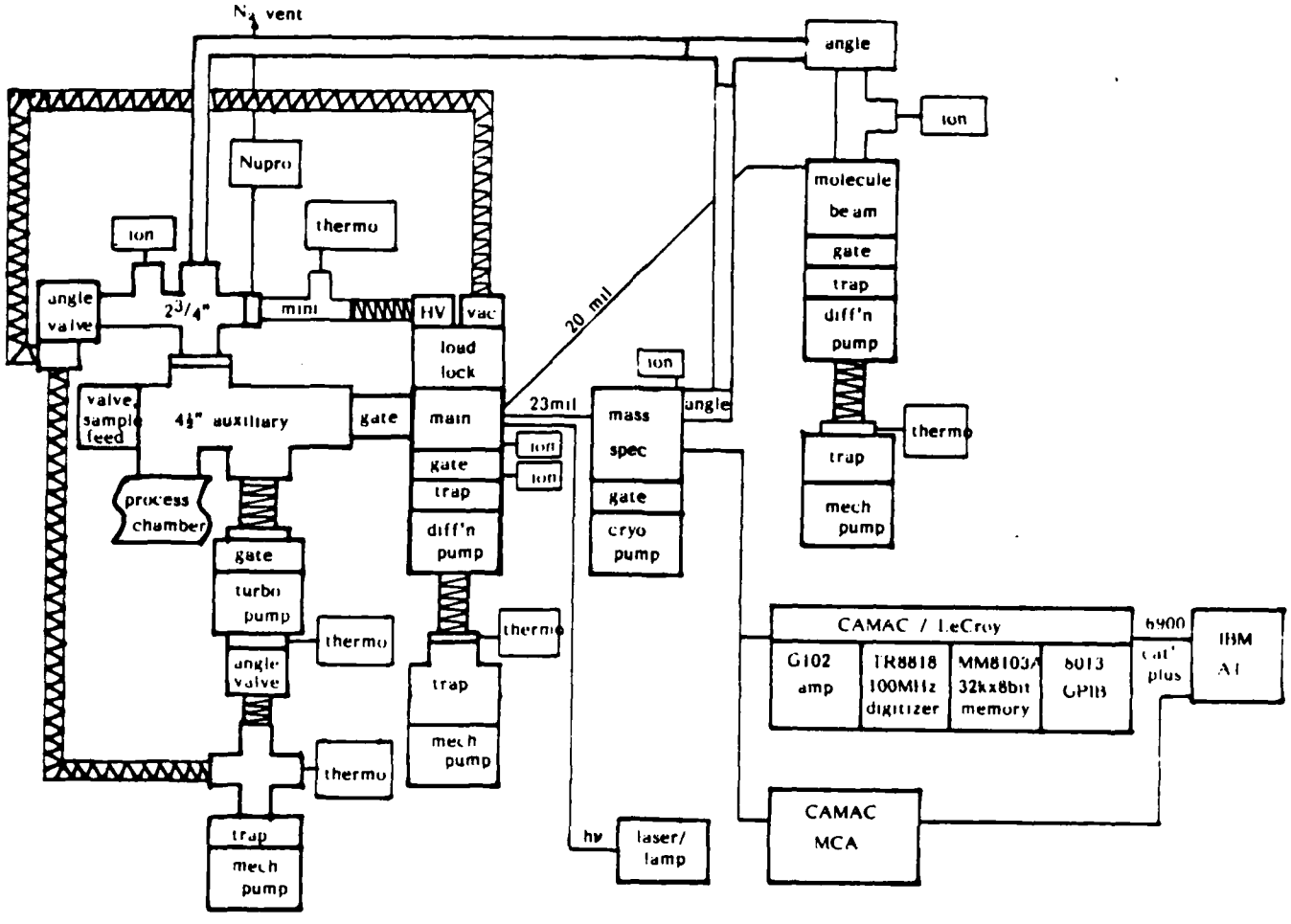

Figure 1: Schematic of time-of-flight measuring system.

time-resolved mass signal is then digitized with a LeCroy built CAMAC system, averaged and recorded on an IBM/AT. The LeCroy TR8818/MM8103A transient digitizer can handle signals up to 100 MHz and has 32K x 8 bit buffer memory. Digitized signal averaging and recording is done in the IBM/AT computer. We have also purchased a discriminator, LeCroy 821, and multichannel, Scalar 352A 100 MHZ, as a multichannel analyzer for the desorbed species emission and mass spectrum. The emission detection can together give a positive species identification. So far, the computer - CAMAC interface has been tested and the CAMAC is ready to receive signal from the C-50 mass spectrometer.

The vacuum system (Fig. 1) consists of the main chamber, mass spectrometer chamber, molecular beam chamber and auxiliary chamber. The main chamber is where the laser-surface interaction takes place. The mass spectrometer chamber is backed by a cryopump and the mass spectrometer ionizer head is cooled and further pumped by an apertured liquid nitrogen shroud to decrease the noise. The pulsed molecular beam source doses the sample surface with high density and monoenergetic parent gases, and radicals can be generated right at the surface when synchronized with a photo-dissociating laser pulse. The beam machine is designed to produce a beam waist of 5 mm at the sample surface. The Newport Research electromagnetic valve driver can produce a nozzle-emission duration as short as 100-μsec pulse. The auxiliary pumping system (i) roughs all systems from atmosphere to 5 mtorr, (ii) roughs the mass spectrometer and cryopump to below 10^{-6} torr, (iii) acts as a high vacuum back-up to all systems in the event of emergency and cold trap pumping, (iv) serves to allow low vacuum to UHV pumping for the fabrication process chamber which is an entirely LF flanged constructed cell for etching and deposition with the presence of ambient gas, and (v) provides main-chamber-sample load-lock vacuum and high vacuum pumping. So far, the main chamber, mass spectrometer chamber, and the molecular chamber are being assembled in our lab.

In the next month time period, all vacuum system are expected to be leak checked; the fabrication process chamber is then expected to be completed. All electronics including the CAMAC crate and computer are expected to be lab mounted. After pump down is achieved, the molecular beam will be calibrated

for mean speed and velocity profile. During this time, the CAMAC/PC wave form processor will be run with a simulation input signal.

In two months time, radicals are expected to be generated at the sample surface and the C-50 is expected to analyze simple, vacuum-ablation, surface-desorption products for calibration.

2. Surface Analysis System -- As part of a recent DoD equipment grant, we have recently purchased and setup a surface analysis system for use by members of the Radiation Laboratory and Microelectronics Sciences Laboratories. The system, made by Leybold Heraeus, was received in September, 1985. Within a few weeks it had already been used to analyze the surface chemistry observed in ultraviolet laser-induced oxidation of GaAs. A very important partner in setting up this research apparatus was the IBM Corporation which, through the auspices of Dr. Daniel Grischowsky, a former Radiation Laboratory student, contributed a Post-Doctoral Fellowship for the person involved in the research on the apparatus.

The UHV machine, which is the first surface analysis system for solid-state research, is equipped for ESCA, Auger, and ISS analysis. In addition, it comes with a load lock system for easy sample insertion, and is equipped with a partial leed analyzer system.

This surface analysis system was first used to characterize the gallium arsenide surface oxidized by ultraviolet light in deionized water. In Fig. 2, X-ray photoelectronspectroscopy (XPS) reveals the change of chemical bonding on the gallium arsenide surface after etching. The decrease of the kinetic energy of the $2P_{3/2}$ and 3d peaks (about 3 eV for arsenic and 1 eV for gallium) indicate the formation of Ga_2O_3 and As_2O_3 during the oxidation process. The drastic decrease of arsenic peak intensity also shows the effective removal of arsenic oxide by water.

Auger electron spectra (AES), shown in Fig. 3, were used to monitor the evolution of surface composition as the etched gallium arsenide surface was sputtered with argon ions. The oxide concentration is about 40% on the surface (normalized to the relative sensitivity) and decreases as a function of depth (sputtering time). On the other hand, arsenic concentration is less than 10% on the surface and increases as probing goes deeper into the

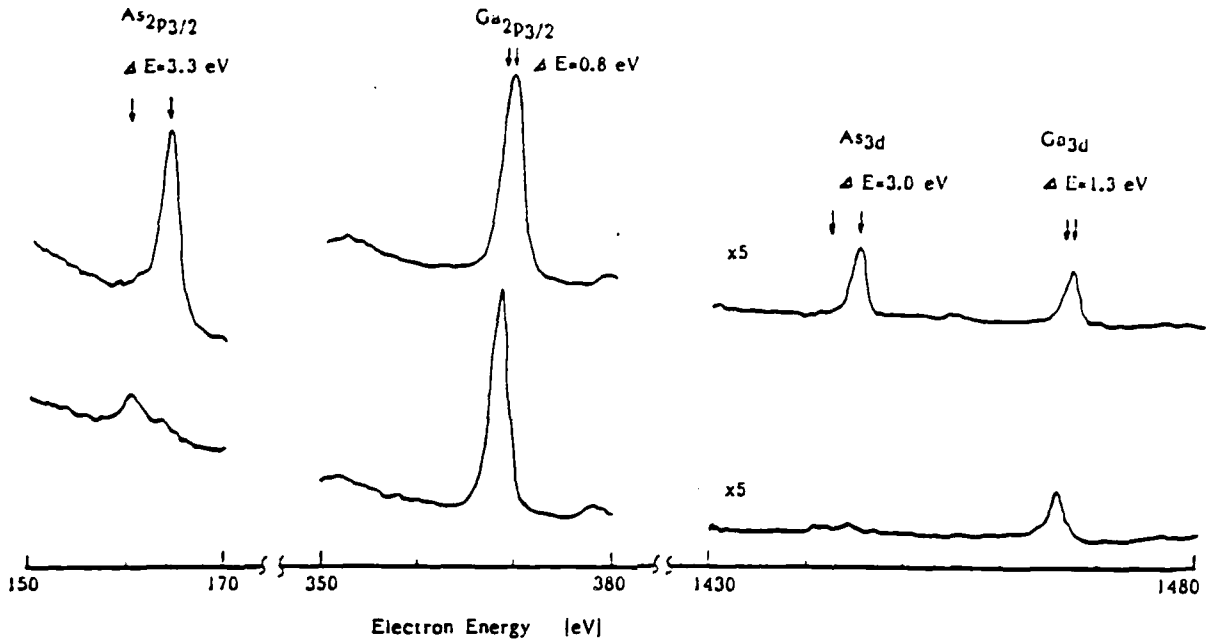

Figure 2: Photoelectron spectra of virgin (upper) and etched (lower) gallium arsenide surfaces. The aluminum K- α-line was used as the exciation source.

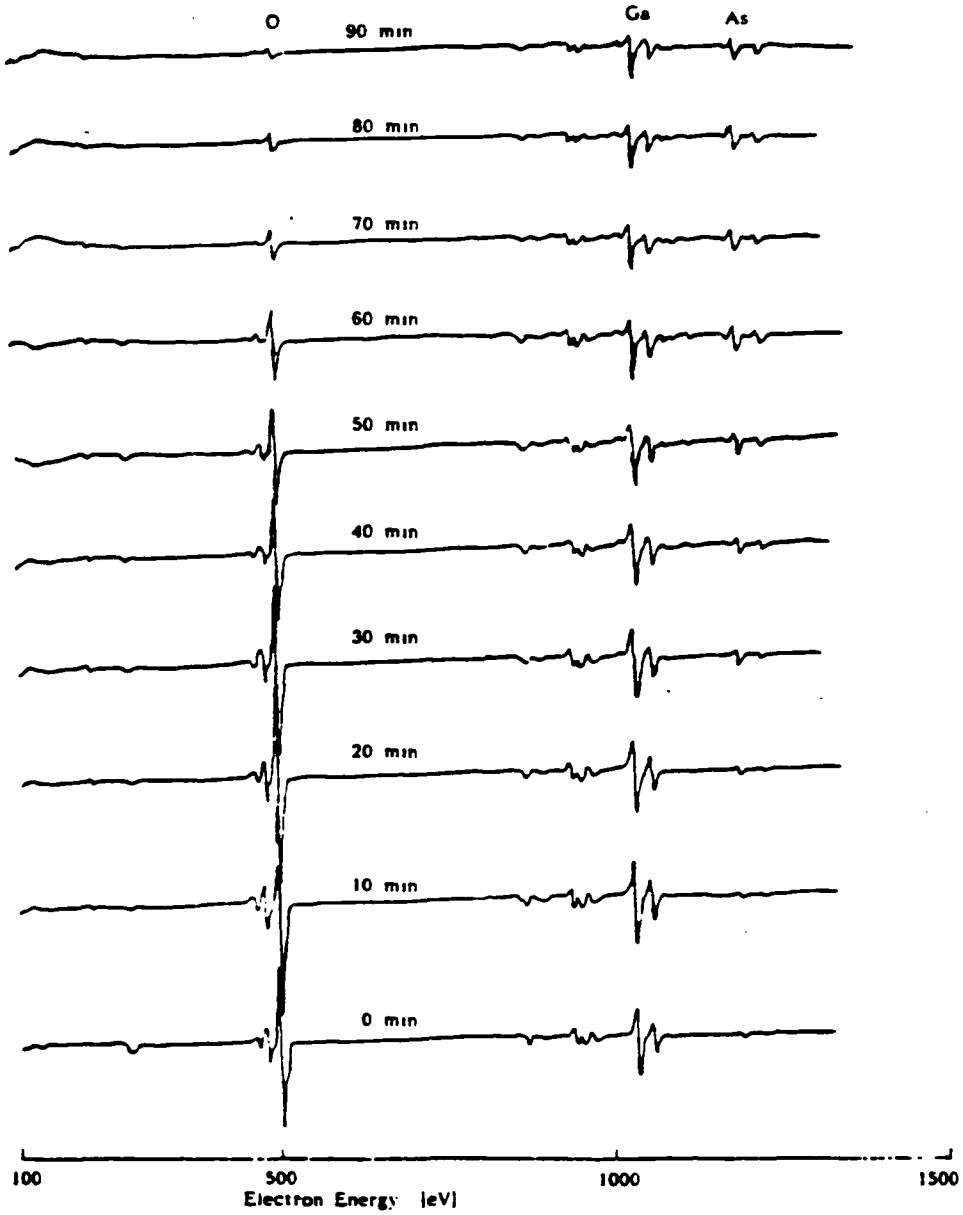

Figure 3: Evolution of the Auger electron spectra of etched gallium arsenide surface when sputtered with 3KV argon ion of 1.5 $\mu A/cm^2$ at 10 min. intervals.

surface. The GaAs stoichiometry is finally restored at the depth of c.a. 500 Å.

Incorporation of this surface analysis system with a laser-surface etching system currently under construction has been conceived. Once realized, surface characterization and/or diagnosis can be made right after the surface is prepared and transfered to the analysis chamber without breaking the vacuum.

Work is also being done on analyzing ion-beam-assisted oxidation of silicon - a project directed by Professor Fossum.

3. Optical Mechanism of UV Light-Induced Aqueous Etching of Semiconductors — The etching process of various types of semiconductors, including Gallium Arsenide, Silicon, and Indium Phosphide, has been studied and characterized in previously reported work. In particular, both visible and ultraviolet light have been used with a variety of dilute etching solutions (typically nitric acid and water) to etch the semiconductors. The energy of the incident photons are absorbed by the surface and can access various energy levels in the solution to foster an oxidation-reduction reaction necessary for etching. Due to various novel optical properties of UV interaction with a semiconductor, via-holes and slits with vertical walls have been fabricated in GaAs. Visible light, however, contains other chemical interactions causing more difficulties in fabricating such structures. In this report we explain the fundamental reasons for achieving such UV anisotropic features.

Figure 4 shows typical profiles of via holes and slits etched through a GaAs wafer. The slits were etched by scanning the wafer perpendicular to the axis of the laser. In all experiments, the laser beam was focused such that the beam waist was on the front of the semiconductor wafer. The entrance of the etched structures is well defined and the surrounding area is undisturbed. Another distinct characteristic of these etchings is their smooth and vertical walls. The etch width, typically 2-3 μm, remains constant even after the depth becomes larger than the confocal parameter. The via holes (and slits) under consideration, however, do not follow one's intuition. Since these vias are created using a Gaussian beam, one would

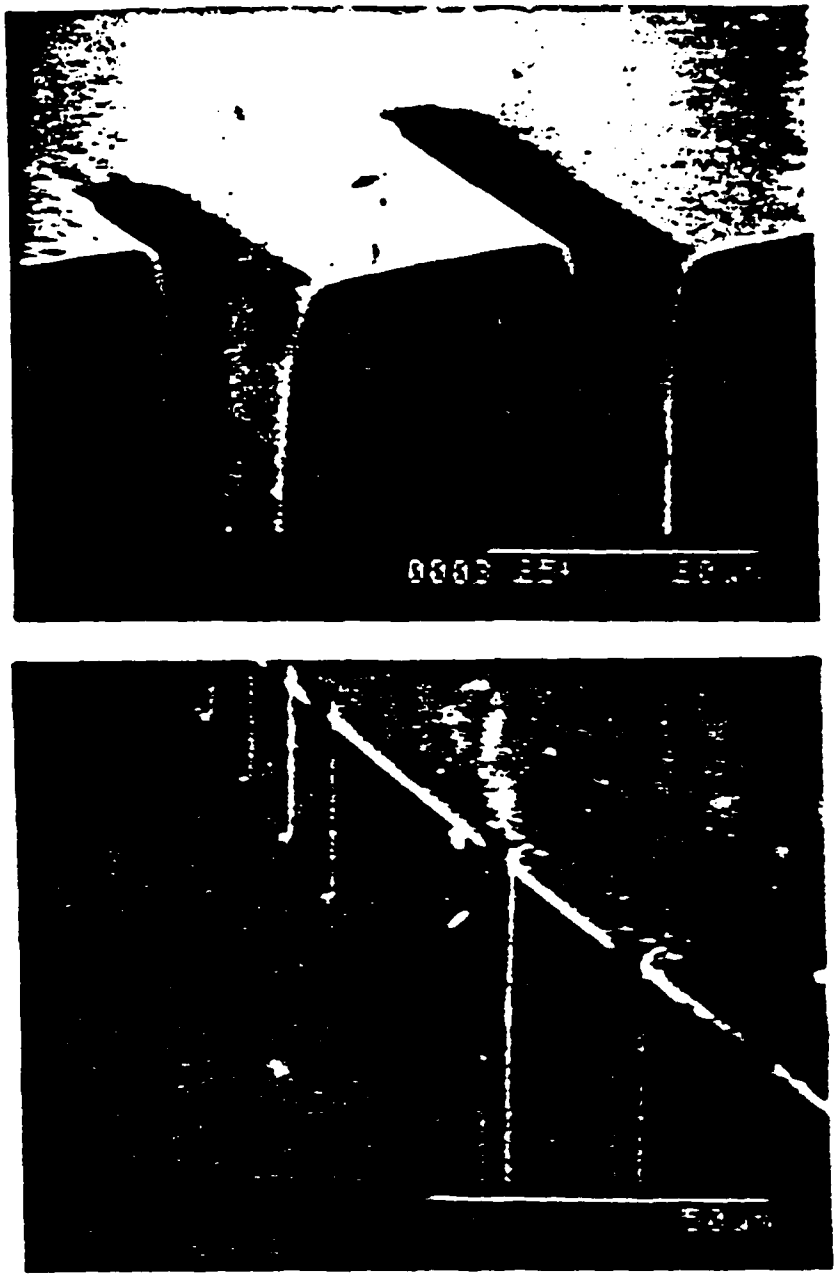

Figure 4: Electron Micrograph of Laser-Etched Microstructures.

think their profiles should also look Gaussian. Absent from the vias shown are the Gaussian wings. Vertical walls and a gradual widening of the hole cannot be predicted by a simple Gaussian shape only. The formation of this anisotropic feature of vertical walls can be modeled and calculated based on a ray optics rather than a wave approach. This reasoning is valid since diffraction effects are not dominant for the depths and wavelengths under consideration here. Also note that the entrance to the via is smooth and not a sharp transition. This would be more representative of a "soft" aperature which tends to inhibit diffraction effects inside the structures.

As each ray of the laser beam strikes the surface, it etches away part of the feature. We assume that the etch rate is linearly dependent on laser intensity absorbed by the surface. The model includes three very important angle-dependent terms: reflectivity (absorption), incident power flux, and etching directionality. As the beam hits the surface, some power is reflected and the rest is absorbed. As the via evolves in profile, the local reflection, and therefore the absorbed power in the surface as well, changes due to incident angle. The correct reflectivity is obtained from a modified version of the Fresnel equations, considering that GaAs, as with many semiconductors in the ultraviolet, looks like a lossy, metal-like material. The surface angle is given by

$$\theta\ (z,r,t) = \tan\ (dz/(t)/dr(t)) \qquad (1)$$

where Z (t) and r(t) are, respectively, the time dependent vertical and radial coordinates of the etched relief. The two components of the local interface velocity of removal (etch rate) are given by:

$$(dz/dt) \propto \exp\ (-r^2)\ (1 - R(\theta)\cos\ (\theta)\cos\ (\theta) \qquad (2)$$

$$(dr/dt) \propto \exp\ (-r^2)(1 - R(\theta))\cos\ (\theta)\sin\ (\theta) \qquad (3)$$

where exp $[-r^2]$ represents the incident Gaussian beam and $[1-R(\theta)]$ is the local absorption. The cos θ term in each equation represents the change in incident power deposited on the surface due to the surface tilt. The last two equations represent the directionality of etching with surface tilt. The

etching is always perpendicular to the plane of the surface. Note that all three angularly dependent terms decrease with wall steepening, while the deviation from the Gaussian shape (Z and r motion of etching) favors the steeper angle.

The above model will not produce via-holes with vertical walls, clipped wings, and gradual widening. As the via develops into a waveguide, light begins to be trapped inside and undergoes internal reflections even in a shallow hole. Due to the Fresnel equations, there is still enough power reflected off of one portion of the feature to again strikes a different portion of the surface. This first internal reflection, or second strike, will contribute to the etching process of the features. The third strike will, however, be much less important since most of the incident power is already absorbed.

An analysis of experimental results is that during the very initial stages of formation of a via hole with a Gaussian beam, the hole follows the intensity distribution and looks almost Gaussian. Further, as seen in the sequence of the electron micrographs of Fig. 5, the initial etch profile should be independent of power as long as the assumption of linearly dependent power etching is valid.

Results of the initial formation of the via from the mathematical model are shown in Fig. 6. In the beginning stages, the hole looks Gaussian since the angularly dependent terms are inconsequential to radial etching. As the hole develops, angularly dependent terms and the second strike become important to cause the hole to deviate from the Gaussian shape. The initial laser strike only as compared to the inclusion of the second strike is depicted in Fig. 7. It is the second strike which really tends to make the walls vertical and which widens up the hole. The power profile of just the second strike is shown in Fig. 8. This shows a certain lensing action by the hole, increasing the power on the bottom of the hole and thereby widening it. A developed via produced by the model is shown in Fig. 9. All the model figures shown display an overall appearance that is in agreement with an actual via. Eventually, portions of the side walls becomes sloped to such a glancing angle that the laser light from the first strike is completely reflected. Also, when the hole is deep enough, the second strike from the

bottom doesn't effect the shallower parts of the wall. Wall erosion, therefore, eventually stops. The incident beam is then optically guided through the hole, while vertical etching continues at the bottom.

A limitation of the model is that the observed diameter of the hole varies with laser power, narrowing with low power and widening up with higher power. This would tend to indicate some weakly nonlinear etching of the hole with incident power. In all cases, however, the overall profile of the shape of the hole is well described by the existing model.

This research was also supported by the Air Force of Scientific Research/DARPA under Grant F-49620-84-K-0022 and Army Research Office under Contract DAAG29-85-K-0210.

LASER-CONTROLLED AQUEOUS ETCHING OF GaAs

INITIAL ETCH PROFILES FOR DIFFERENT LASER INTENSITIES

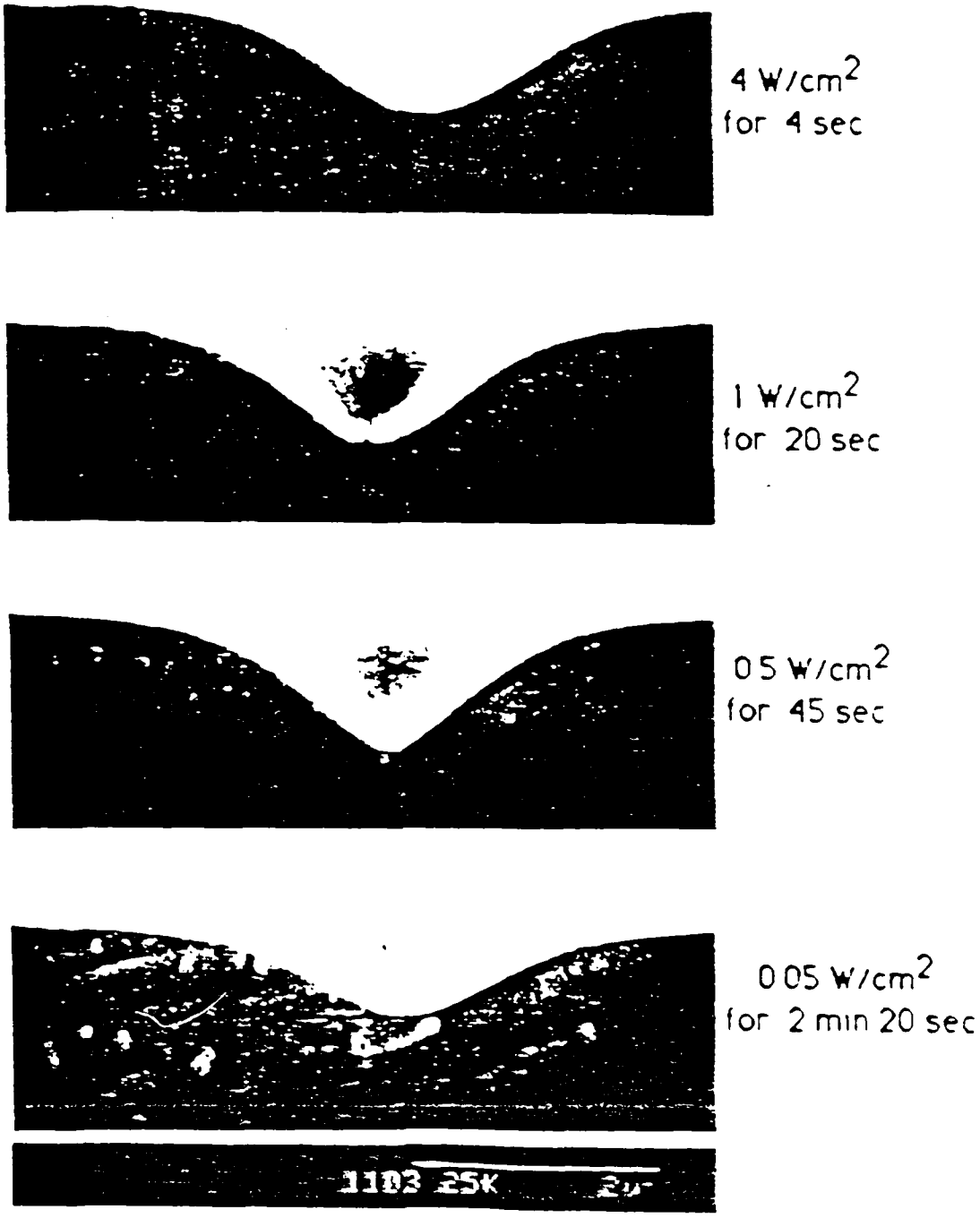

Figure 5: Initial Profiles of Laser-Etched Vias.

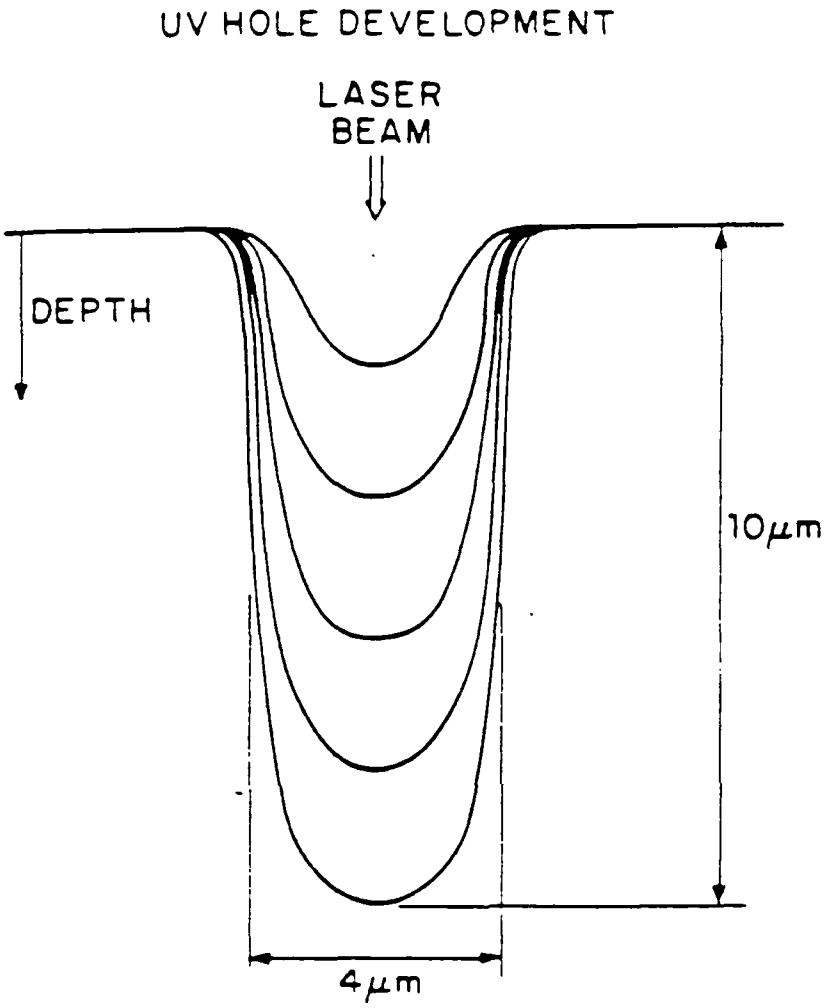

Figure 6: Calculated Profile of Laser-Etched Via.

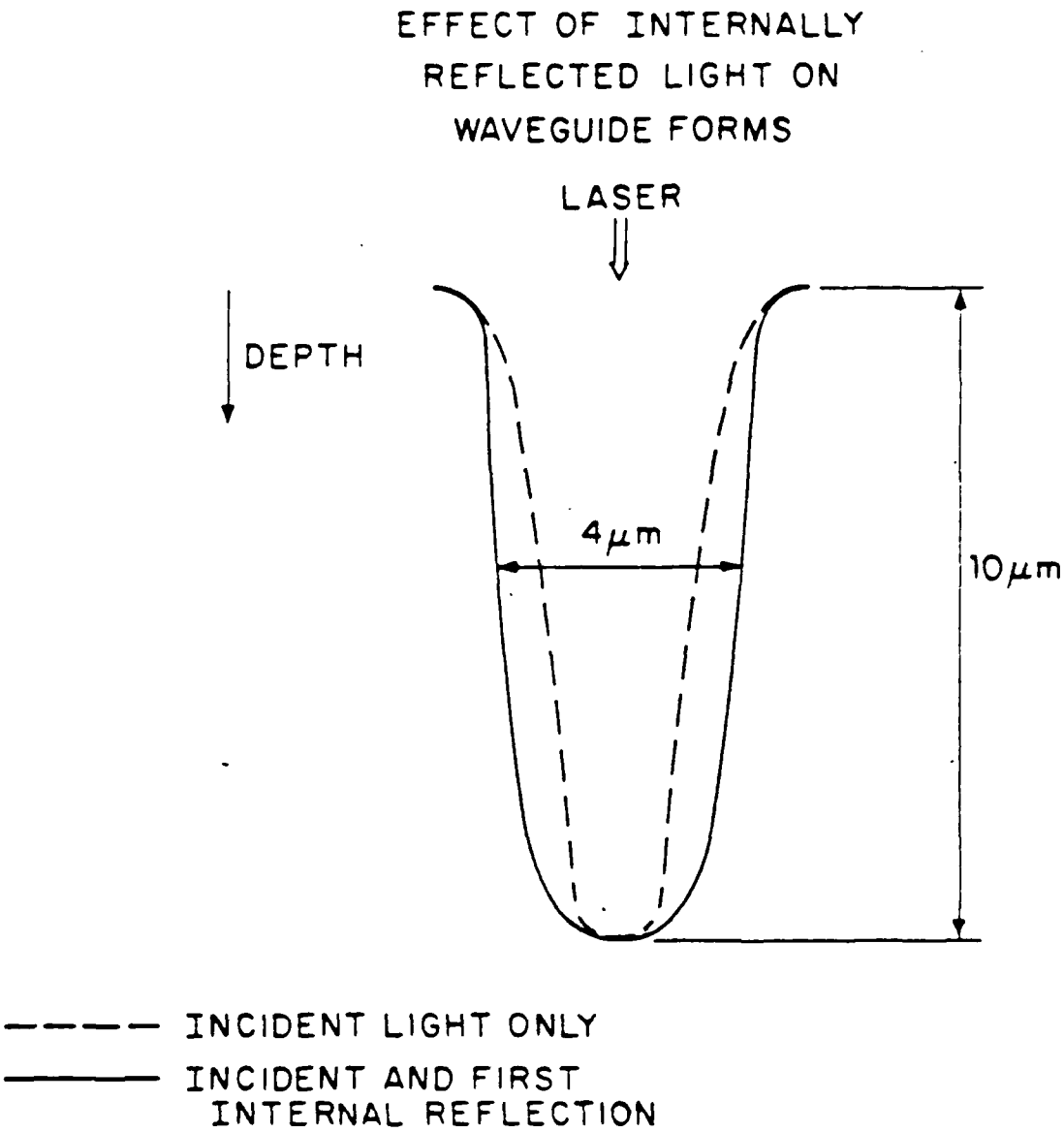

Figure 7: Effect of Internally Reflected Light on Laser-Etched Vias.

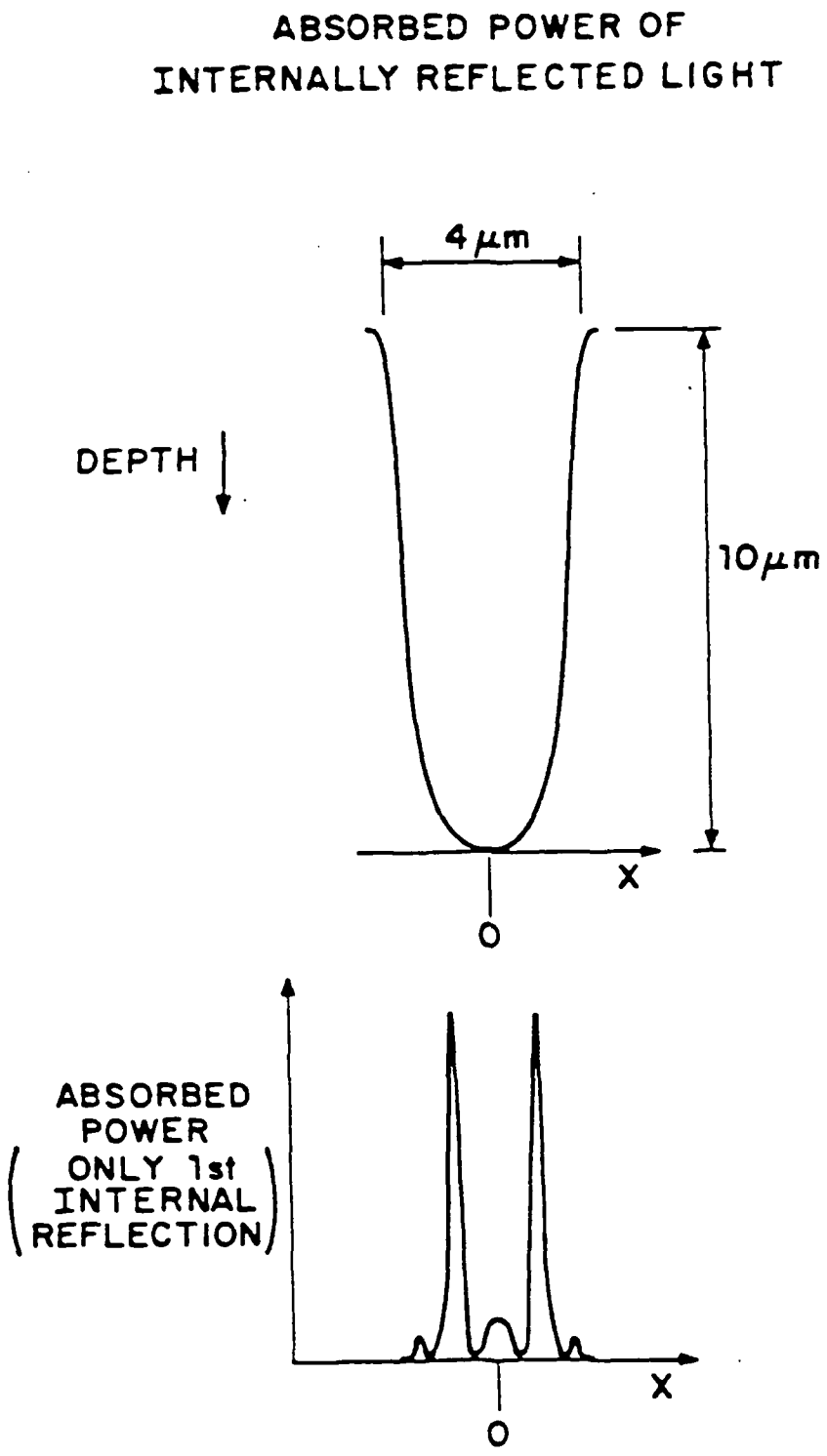

Figure 8: Absorbed Power for Internally Reflected Light (calculated).

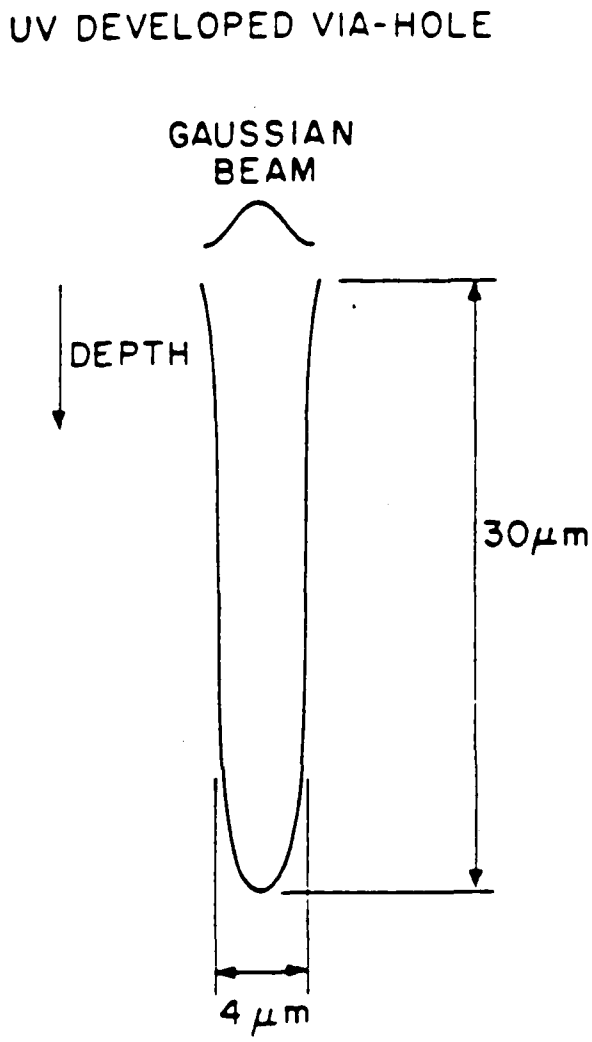

Figure 9: Calculated Profile of Deeply Etched Via.

C. ELECTRONIC STATES AT SILICIDE-SILICON INTERFACES

(E. Yang, H.L. Evans, X. Wu, P.S. Ho)
(JSEP work unit 3, 1985 - 1988)
(Principal Investigator: E. Yang (212) 280-3120)

Ever since Bardeen proposed the surface state model[1] as the basis of Fermi level pinning at metal-semiconductor interfaces, the existence and nature of interface states have become the central issues for understanding Schottky barrier formation. Many early studies have focused on systems with weak metal/silicon interaction where the existence of interface states in the bandgap has often been attributed to metal penetration into the semiconductor.[2] In the past several years, the development of microanalytical techniques has advanced significantly our understanding of the microscopic nature of the interface. It has been found that the interaction at the metal/semiconductor interface is generally not weak and reactions frequently occur, resulting in atomistic changes of the layer, e.g. compound formation, defect generation and interatomic mixing.[3-6] These phenomena modify the stoichiometry, atomic environment and microstructure of the interface. Thus it is important not only to measure interface states, but also to understand how they are affected by interfacial reactions.

Among the metal-semiconductor interfaces, the silicide-silicon interface is characterized by a strong chemical reactivity between the transition metal and silicon atoms. In the past 3-4 years, the chemical and structural characteristics of this interface have been extensively investigated.[3] It is known that silicide formation dominates the interfacial chemistry and the interface is structurally abrupt but contains defects such as atomic steps and misfit dislocations. The Schottky barrier was found to be a true interface property and its nature can be classified to be extrinsic or intrinsic, depending on the extent of the reaction.[7] Particularly interesting is the $NiSi_2$-Si(111) interface, where a difference of 0.14 eV in barrier height has been reported for the twin epitaxial (A and B type) interfaces.[8] A later study found, however, that these two interfaces have

similar barrier height although both exceed the mixed type by about 0.14 eV.[9] It was suggested that the barrier height is determined primarily by the degree of perfection of the interface instead of the specific type of epitaxy.

In spite of the progress, the central issue regarding the nature of the interface states at the silicide-silicon interface remains unresolved. The difficulty lies in the fact that the analytical techniques used so far are primarily surface electron sepectroscopies which do not have the required sensitivity and energy resolution (<0.1eV) to detect the presence of interface states of an amount (about 10^{13} states/cm^2) sufficient to pin the Fermi level (E_f). This is illustrated by the Auger study of the Pd_2Si-Si interface[10] where interface valence states of Si were observed and their position appears to be below E_f. However, these states cannot be accurately measured to assess their role in determining the electrical properties of the interface.

To measure the interface states, electrical techniques designed specifically for metal-semiconductor contact are required. For this purpose, we have developed a capacitance spectroscopy technique[11] and have used it to study a number of silicide-silicon interfaces. Measurement of device capacitance is a major, nondestructive electrical technique for obtaining information on impurity concentrations and trap levels in semiconductor devices. When a trap level charges and discharges under the influence of an applied small-signal voltage, there is a contribution to the device capacitance. Various modifications of this basic principle have arisen (deep level transient spectroscopy, capacitance voltage profiling, photocapacitance, etc.) in order to isolate the effects of traps in different regions of the semiconductor or at different energy levels. One such modification as implemented by Nicollian and Geotzberger[12] is routinely used to characterize the oxide-semiconductor interface in metal-oxide-semiconductor (MOS) structures. Basically this technique involves sweeping the Fermi level past the interface state energy level so that the trap state changes occupancy and contributes to the capacitance and conductance of the structure. When one attempts to apply the same theory and procedure to metal-semiconductor (MS) contacts. however, results are much harder to

obtain.

The major difficulty in applying the MOS technique to the MS structure is that the majority-carrier Fermi level must be swept through the band gap in order to obtain information about interface levels in the band gap. This means that the MS structure must be in the forward-biased regime.[13] In the MOS structure the large energy barriers presented by the oxide inhibit current flow from the silicon to the gate. There is essentially no current flow and aside from the conductance due to the interface states, there is negligible real component of the admittance. In the forward-biased Schottky diode, on the other hand, there is a hugh conductance due to the thermionic emission of carriers from the semiconductor to the metal. This hugh real component, Gp, overwhelms the imaginary capacitive component, ωCp, making measurements extremely difficult. Indeed, for low-frequency measurements, values of Gp are commonly 10^2-10^4 times as large as ωCp. Usual methods of separating the two components by simply tuning the phase of a phase sensitive detector without the device in place, do not give the required accuracy for full deconvolution. Another method, developed by Barret and Vapaille,[14] using a bridge to null the real component and then measuring the imaginary component, is extremely tedious and requires much time and adjustment for each data point. The technique described below is much simpler to apply and requires relatively little modification of already existing reverse bias measuring apparatus.

In Fig. 1 is shown the apparatus for implementing accurate phase forward bias capacitance measurement. The diode is represented by the small-signal conductance Gp in parallel with the small-signal capacitance Cp. Gp has contributions from both the interface states and the forward-biased current while Cp is composed mainly of interface state capacitance. To set the phase and ensure that it is set correctly, a parallel test resistor of reasonably large conductance is placed in the circuit. If the phase is incorrectly set and a test resistor is placed between A and B in parallel with Cp, the measured value of Cp will change. However, if the phase is perfectly set, no pure conductance between A and B will influence the measurement of Cp. To correctly set the phase, measurements of Cp are made at a given bias and small-signal level with and without the test resistor. The phase is tuned

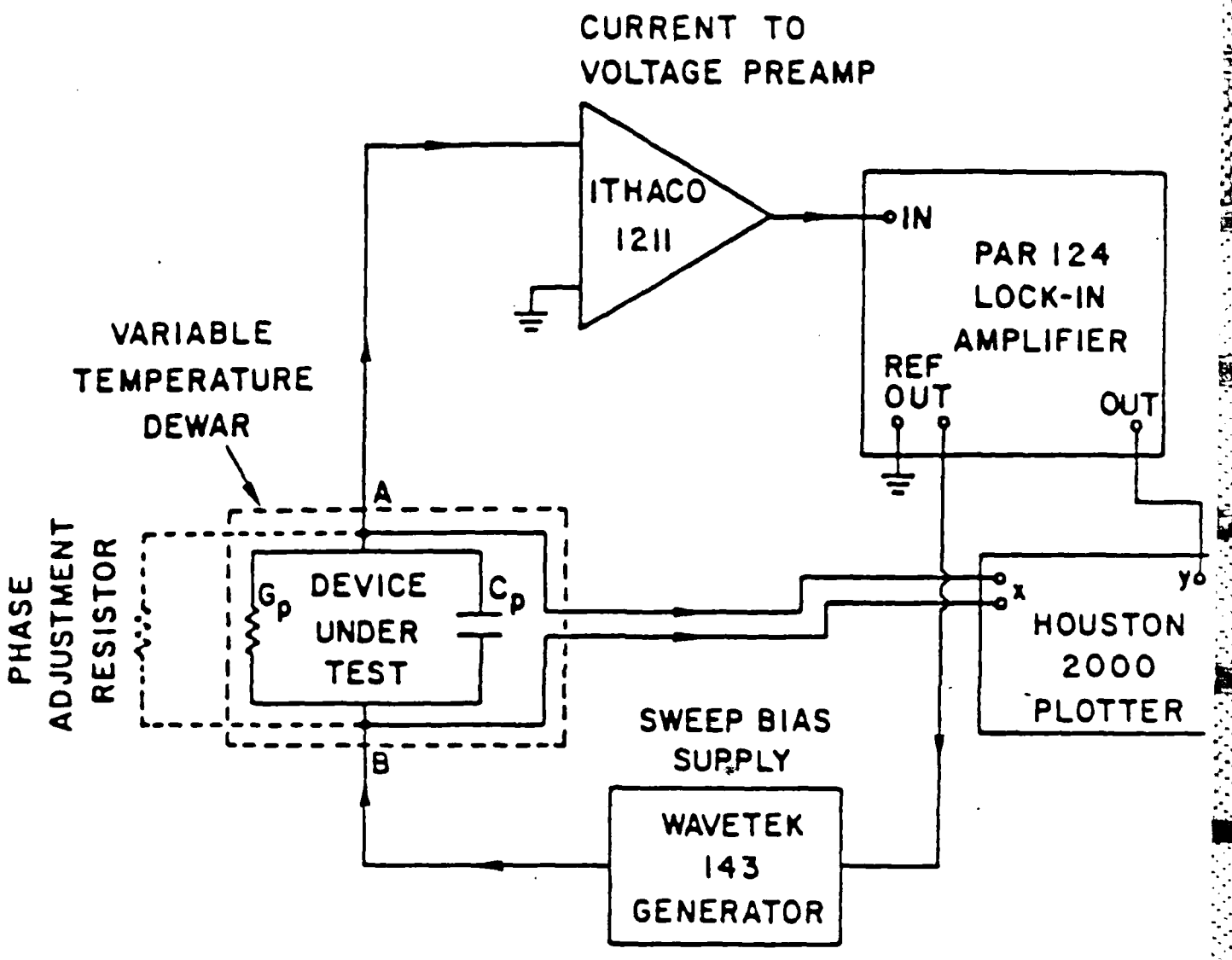

Figure 1: Accurate Phase Capacitance Spectroscopy

until both measurements are equal.

In our experiment, n-type (111) silicon samples were chemically or UHV cleaned before metal evaporation, and an aluminum back contact was provided. The UHV cleaning was carried out by several heating steps and a flash to 1100°C for a few seconds. The barrier height was meaured using I-V (in-situ) and photoresponse techniques. The interface state measurement was made outside the vacuum system by carrying out capacitance versus voltage scans as a function of temperature and frequency (from 20 Hz to 3 kHz).

The results obtained for a chemically cleaned Pd_2Si/Si diode at 100 Hz are shown in Fig. 2. The validity of this new technique is demonstrated in the figure. The variation of both conductance (Gp) and capacitance (ωCp) with voltage as determined using the accurate phase procedure is shown. The difference between the two components is clear even though the real component is more than three order of magnitude larger than the imaginary component. (Note the sensitivity of the capacitance curve is 4000 times that of the conductance curve). If the phase is incorrectly determined, the results are shown in Fig. 3. Here, computer simulation of phase errors as small as 0.1° shows how the identity of the capacitance component is lost in the huge conductance. Depending on the magnitude of the phase error, the incorrect capacitance curve has a shape between that of the conductance and the true capacitance curve. (Again, the sensitivity of the capacitance curve is 4000 times that of the conductance curves.) Thus, the phase tuning must be done extremely carefully. However, once the setting is determined at a given frequency, voltage and temperature scans can be made without any readjustment. This is in contrast to the Barret method where adjustments have to be made for each new value of voltage or temperature.

The data resulting from the accurate phase capacitance spectroscopy (APCS) measurement require certain adjustment before it can be strictly interpreted. This is due to a nonlinear effect in the lock-in amplifier when the signal level is too high. As can be seen in Fig. 2, at the higher values of dc bias, the capacitance curve rises and is not symmetrical with the low voltage regime. This nonlinearity arises because of the need to use sensitivity ranges to measure the capacitance which are far below those required to handle the real current component caused by the increasing

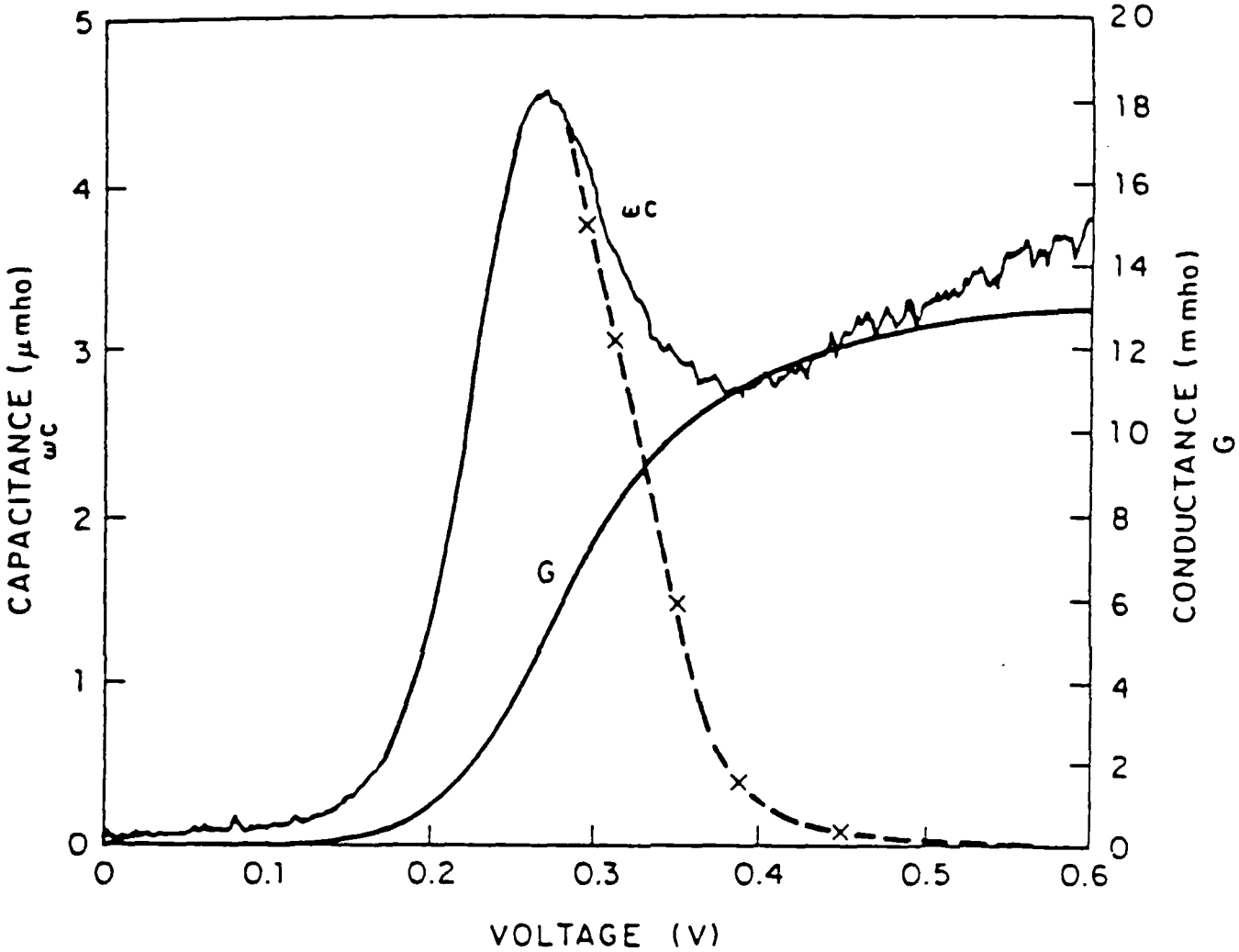

Figure 2: Conductance (G) and capacitance (ωC) for Pd-nSi diode at 104 Hz. Capacitance scale is 4000 times as sensitive as the conductance scale.

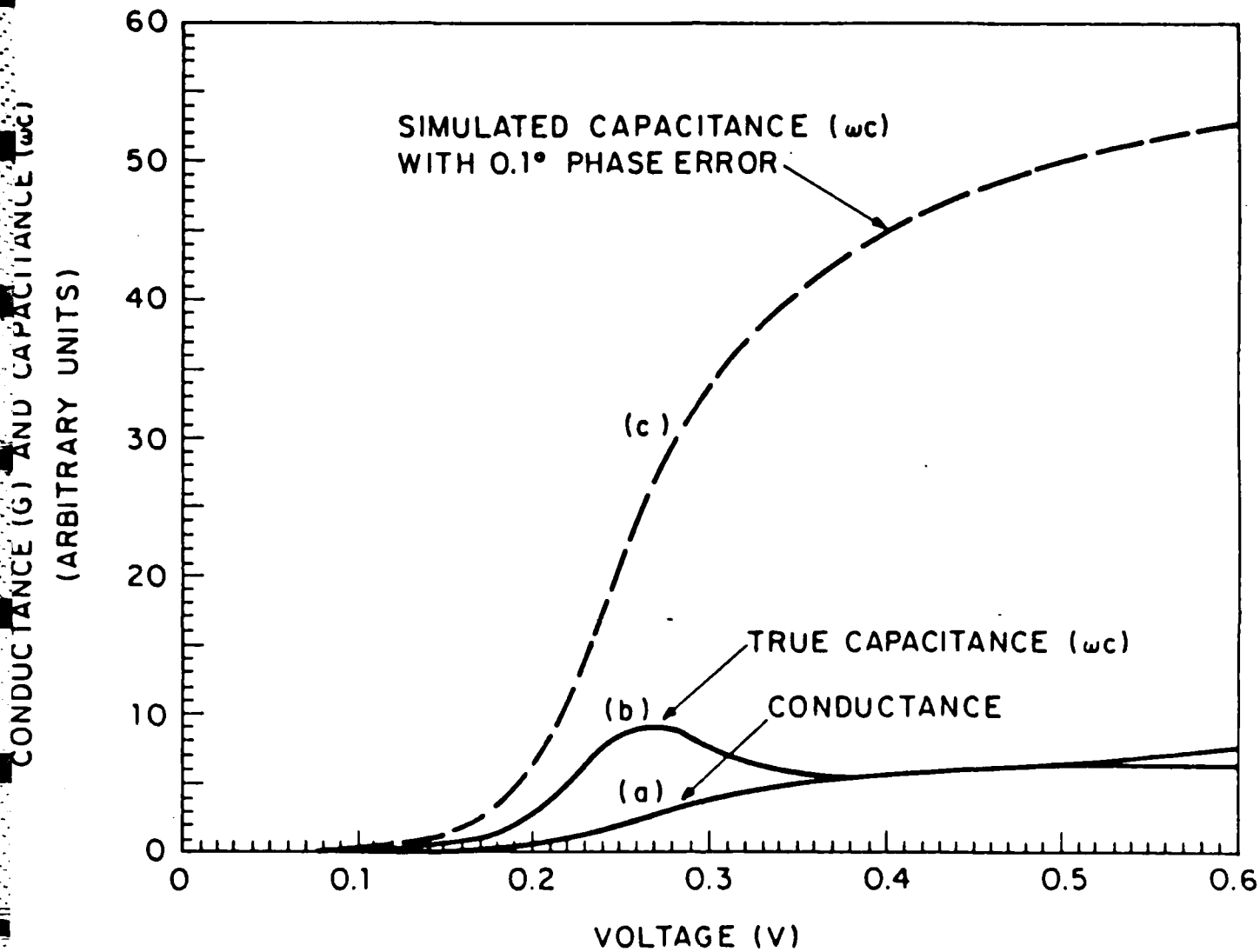

Figure 3: f = 104 HZ: a) conductance, b) accurately measured capacitance (ωC), c) simulated capacitance (ωC) with 0.1° phase error. The capacitance scales are 4000 times more sensitive than the conductance scale.

conductance. If the diode is removed and replaced by a variable resistor, it is found that the capacitance measured is as shown if Fig. 4. As the variable resistor is decreased beyond a certain value, the measured capacitance deviates from zero. By carefully inspecting Fig. 2 and 4, it is noted that the conductance needed to cause the deviation from zero in Fig. 4 is the same as the device conductance at which the capacitance curve in Fig. 2 begins to rise. Thus a set of curves similar to Fig. 4 made for different sensitivity readings of the lock-in can be used to calibrate the APCS measurement. Such a calibration is shown by the dashed line in Fig. 2. It is important to note that the test resistor used for phase determination should not be small enough to cause the lock-in to enter its nonlinear regime when placed in parallel with the device conductance.

The capacitance curve at room temperature shows a distinct peak at 0.27 U for the as deposited interface. The data obtained at other frequencies and temperatures indicate that a single time-constant model involving charge exchange only with the majority carrier band is inadequate to describe the diode behavior. Nor can the density of states be calculated exactly since the quasi-Fermi level is not flat at high bias. While studies are in progress to evaluate the density and distribution of the interface states from the temperature and frequency data, we can estimate the number of charge states from the peak capacitance at low frequency. For the Pd_2Si/Si interface, the data at 100Hz correspond to a total density of states of about 10^{13} per cm^2.[13]

The effect of silicide formation on the interface states can be observed from their annealing behavior shown in Fig. 5. The annealing condition, 250°C for 30 min., was chosen to convert the as-deposited interface into a well-reacted Pd_2Si/Si interface. After annealing, the total density of states decreases by a factor of about three while its distribution is significantly sharpened. In addition, the spectral peak shifts down by 30 mV, which corresponds to the change observed in the barrier height.

The behavior of the states observed for an UHV interface before and after annealing (Fig. 6) is similar to the chemically cleaned interface. Comparable reduction in the total density (4x) and down shift of peak position (45 mV) were observed and the latter correlates to the change from

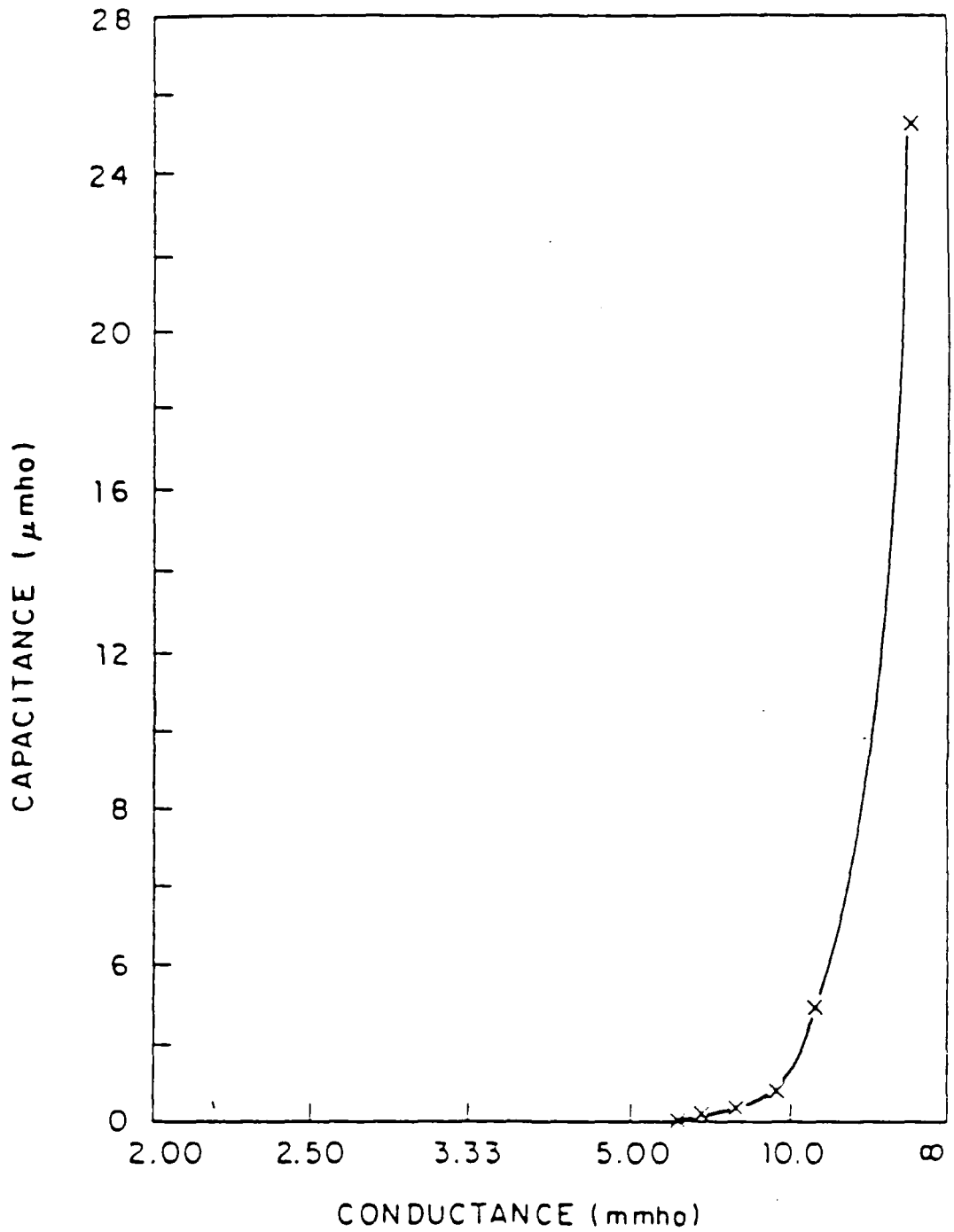

Figure 4: Capacitance measured using a variable resistor as the test device.

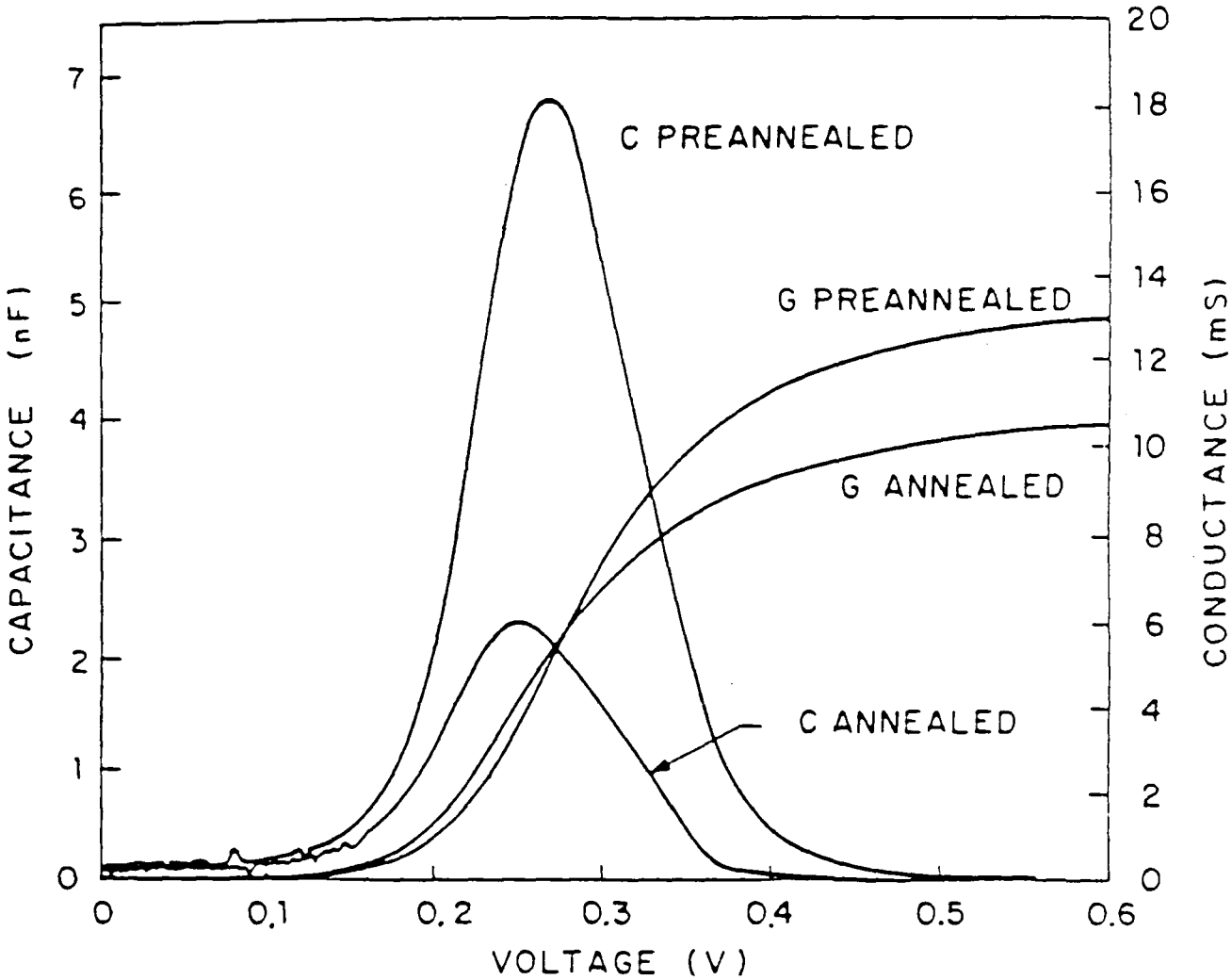

Figure 5: Conductance G and Capacitance C spectra observed from a chemically cleaned Pd_2Si/nSi Schottky contact before and after annealing at 250°C as a function of frequency and forward-bias voltage. Note the different scales for G and C.

0.78 to 0.73 eV in the barrier height. The observed behavior demonstrates the true interface nature of these states. For the as-deposited case, the interface contains extrinsic interface defects, e.g. oxide and contaminants, which give a high density and broad distribution of these states. As the reaction proceeds to establish a more perfect interface, the density of interface states is reduced significantly. Our results show that silicide formation changes two differeent initial interfaces (chemically cleaned or UHV prepared) to one with essentially the same characteristic states.

More striking correlation of the structural perfection and interface states was observed at the epitaxial Ni silicide interfaces. The capacitance spectra of type A and type B diodes as shown in Fig. 7 indicate that the density of states (DOS) is about the same for the epitaxial diodes. The peak position in forward bias voltage is almost identical in spite of the different crystal orientations. On the other hand, the striking contrast between epitaxial and nonepitaxial interfaces is shown in Fig. 7. The fabrication procedures for these two Schottky barriers were the same except that the annealing temperature for type B' was around 250°C. High resolution TEM showed that the type B' has nonepitaxial growth and the resulting barrier height was 0.65 eV. The type B diode has a barrier height of 0.78 eV and the density of states is 1/6 that of the type B' diode. This is a clear evidence that the number of interface states is higher for nonepitaxial interface than for epitaxial interface. This is the first direct measurement known to us that correlates the interface states with the epitaxial and nonepitaxial structures.

As for the influence of surface contamination, we have investigated the effects of oxygen and carbon on the nickel silicide/silicon system. The experimental data indicate that carbon lowers the peak position in forward voltage but the density of states remains essentially the same. The lower peak position correlates to a lower barrier height as obtained from both I-V and phototresponse measurements. A high dosage of carbon, however, changed the capacitance spectra rather drastically so that we were not able to interpret the data. As for the effect of oxygen, an exposure of 20 L has little influence, but a dosage of $5x10^{9}$L (corresponding to about a monolayer coverage of oxygen) moved the capacitance peak and significantly modified the

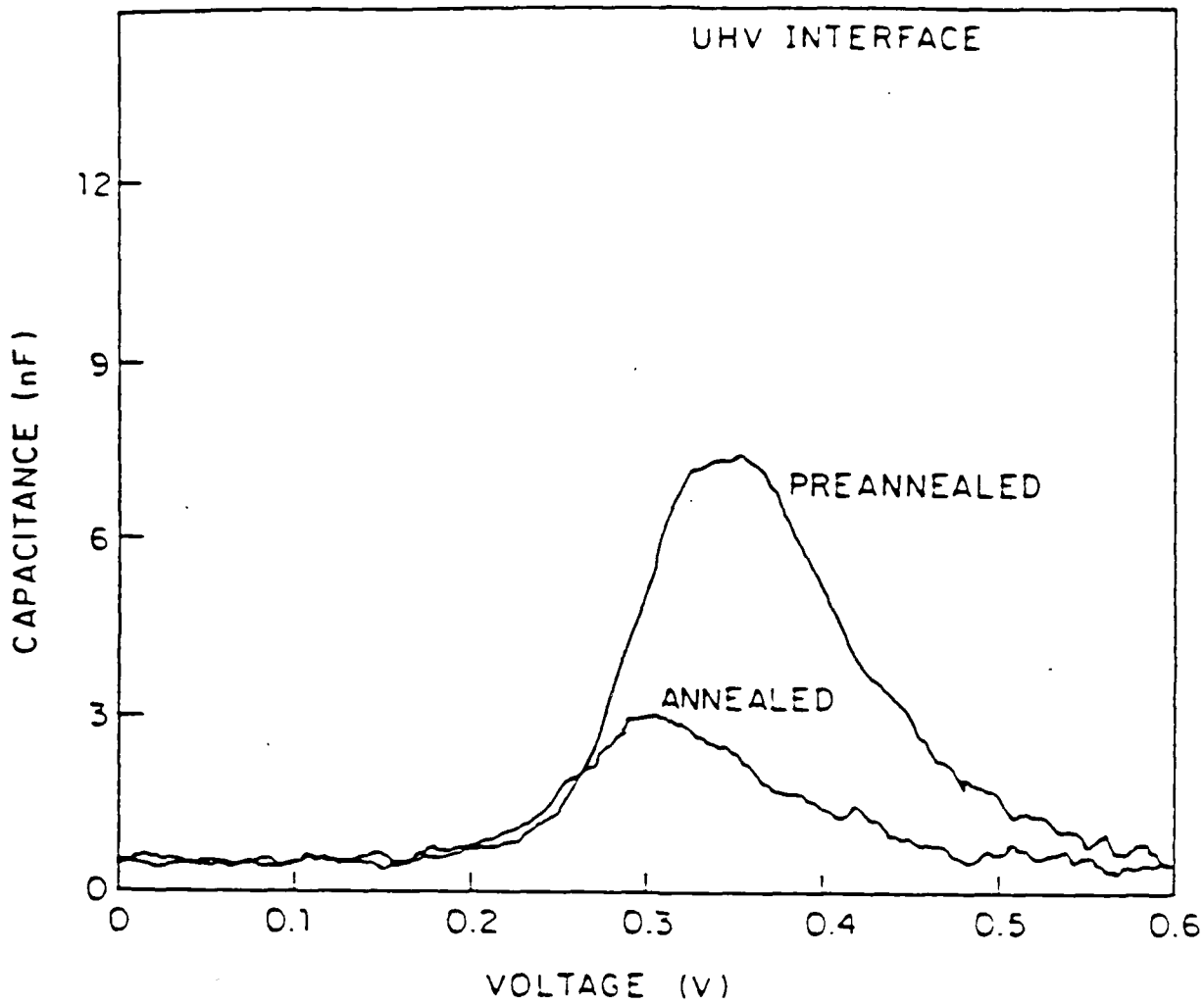

Figure 6: Observed changes of the capacitance spectra for a UHV cleaned Pd/Si interface.

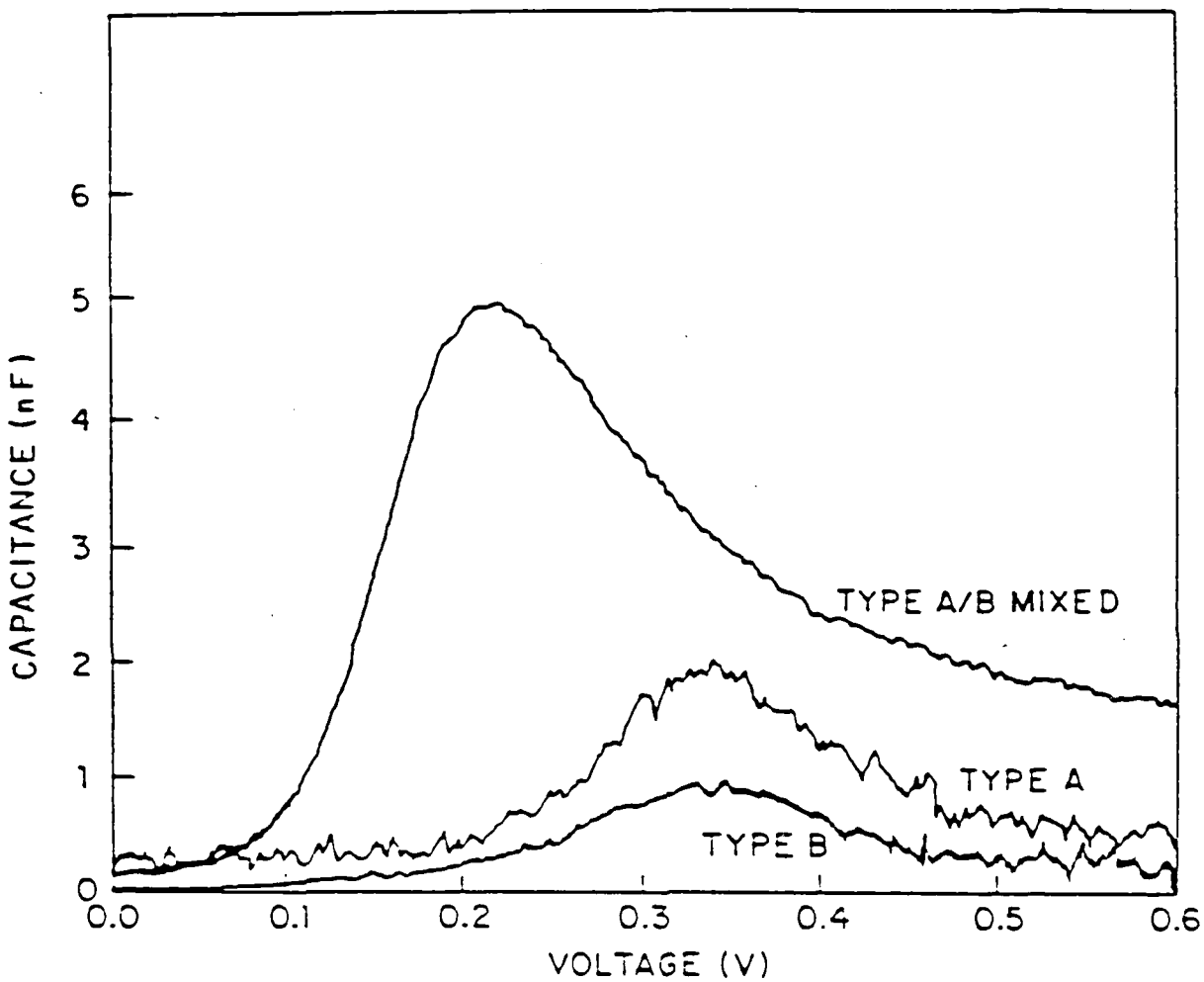

Figure 7: Capacitance spectra observed for different epitaxial $NiSi_2$-Si(111) interfaces, including A and B single types and a mixed type.

DOS.

We have studied a number of silicide-Si interfaces and found interface states with distribution and chacteristics close to those reported here. In general, similar effects of annealing on the distribution and density of the states were observed and the direction and amount of the shift correlate with the change in the barrier height. This seems to be the general trend of the effect of silicide formation on the electrical characteristics of the interface.

In summary, we have observed states existing in the Si bandgap at the silicide-Si interface. Upon annealing, their density and distribution change to reflect a more perfect interface as a result of silicide formation. For the interfaces studied, the shift in the peak position correlates well to the change in the barrier height, indicating that the same group of states is detected. This suggests that these states are associated with the same kind of bonding defects of the silicon atoms at, or very close to, the interface. Furthermore, the observation on the Ni silicides shows that their character is influenced strongly by the degree of perfection of the interface. The nature of such defects remains to be clarified. Although structural defects specific to the interface have been observed by high-resolution TEM for several silicide-silicon systems, including the $Pd_2Si/Si(111)$ interface,[5] it is not clear whether such defects can account fo the observed states. Recently Si dangling bonds of interfacial vacancies have been proposed to account for Fermi level pinning in silicide-silicon interfaces.[6] It would be very interesting to check whether our results which reveal the empty instead of the occupied states are consistent with this particular model.

This research was also supported by NSF under Grant No. NSF ECS 82-17677 and performed in collaboration with IBM. P.S. Ho is presently at the IBM Watson Research Center.

(1) J. Bardeen, Phys. Rev. 71, 717 (1947).

(2) See reviews by M.L. Cohen, Kad. Electron Phys. 51, 1 (1980).

(3) P.S. Ho and G.W. Rubloff, Thin Solid Films 80, 433 (1982); G.W. Rubloff, Surface Science 132, 268 (1983).

(4) W.E. Spicer, I. Lindau, P. Skeath, C.4 Su and P. Chye, Phys. Rev. Lett. 44, 420 (1980).

(5) R.H. Williams, J. Vac. Sci, Technol. 18, 929 (1981).

(6) L. J. Brillson, C.F. Brucker, N.G. Stoffel, A.D. Katnani and G. Margaritondo, Phys. Rev. Lett. 46, 838 (1981).

(7) P.S. Ho, J. Vac. Sci. Technol. A1 745 (1983).

(8) R.T. Tung, Phys. Rev. Lett. 52, 461 (1984).

(9) M. Liehr, P.E. Schmid, F.K. LeGoues and P.S. Ho, Phys. Rev. Lett. (1985) to be published.

(10) P.E. Schmid, P.S. Ho, H. Foll and G.W. Rubloff, J. Vac. Sci. Technol. 18, 937 (1981).

(11) H.L. Evans, E.S. Yang and P.S. Ho, Appl. Phys. Lett. 46, 486 (1985).

(12) E.H. Nicollian and A. Goetzberger, Bell Syst. Technol. J 46, 1055 (1967).

(13) P. Muret and A. Deneuville, J. Appl. Phys. 53, 6289 (1982).

(14) C. Barret and A. Vapaille, Solid State Electron. 18, 25 (1975).

(15) H. Foll, P.S. Ho and K.N. Tu, Philos. Mag. A45, 31 (1982); J.M. Gibson, J.C. Bean, J.M. Poate and R.T. Tung, Thin Solid Films 93, 91 (1982).

(16) O. F. Sankey, R.E. Allen and J. D. Dow, Solid State Comm. 49, 1 (1984).

PREVIOUS PAGE IS BLANK

D. TUNNELING IN A METAL-SEMICONDUCTOR-SEMICONDUCTOR THIN FILM STRUCTURE

(E.S. Yang, Q. Hua D. Yang, G. Yang)
(JSEP work unit 2, 1985 - 1988)
(Principal Investigator: E. Yang (212)280-3120)

In the past two decades, efforts have been made to explore the potential of the tunnel diode[1] because of its ultra-fast switching speed. By and large, these efforts have not been successful owing to the difficulties in controlling the junction and in finding a fabication technique to form integrated devices. For these reasons, the study of tunneling structures has been rather limited. Yet, the trend toward smaller and faster devices indicates that the research of tunneling will soon find its way back to "respectability". We report here a tunneling junction that is easily produced at room terperature. The junction characteristics are controllable, and it does not appear to be difficult to make in integrated form. The basic idea is to modify a metal-semiconductor contact by introducing a thin near-intrinsic semiconductor layer between the metal and the bulk semiconductor.The result is a tunneling junction for majority carriers under forward bias. The reverse saturation current is small but not negligible, and the breakdown voltage is quite high. It is shown that a good ohmic contact can be converted into a tunneling rectifier with this technique. Potential applications include MESFETs, tunnel transistors, detectors and integrated circuits. We present here a physical model and obtain some useful device parameters for an Al-aSi-nSi diode. Experimental data are presented to demonstrate the basic features of majority carrier tunneling.

The physical structure and energy band diagram for the thin-film sandwich are shown in Fig. 1a and 1b. We use an intrinsic amorphous silicon film as the tunneling barrier between the metal and the bulk semiconductor. The effective band gap of the a-Si is assumed to be 1.4 eV.[5,6] Experimentally, the a-Si layer is deposited by electron-beam evaporation, and it has a thickness of less than 40A. Such a film may very well be a fine-grain poly-silicon, but it is not possible to clearly distinguish its

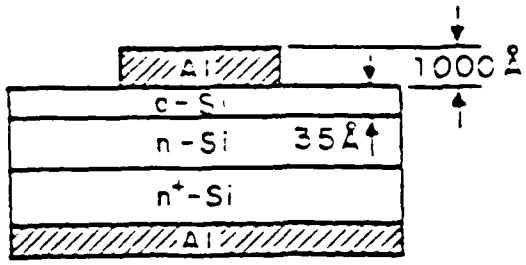

(a)

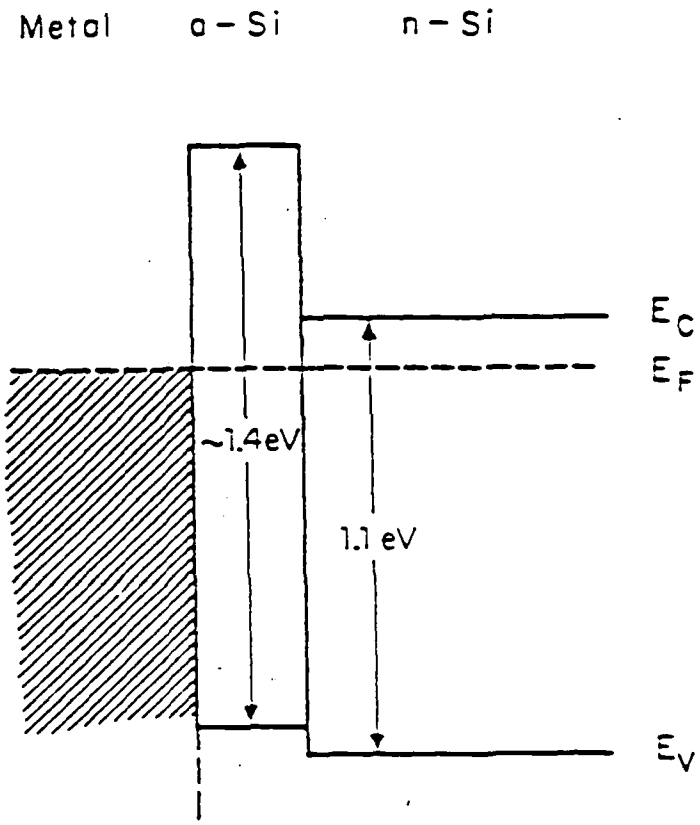

(b)

Figure 1a and 1b: A thin-film M-aSi-nSi tunneling structure (a) with energy band diagrams at thermal equilibrium (b), forward biased (c), and reverse biased (d). The flat band condition at zero bias will be clarified by capacitance data. The band gap of aSi is taken from the literature.

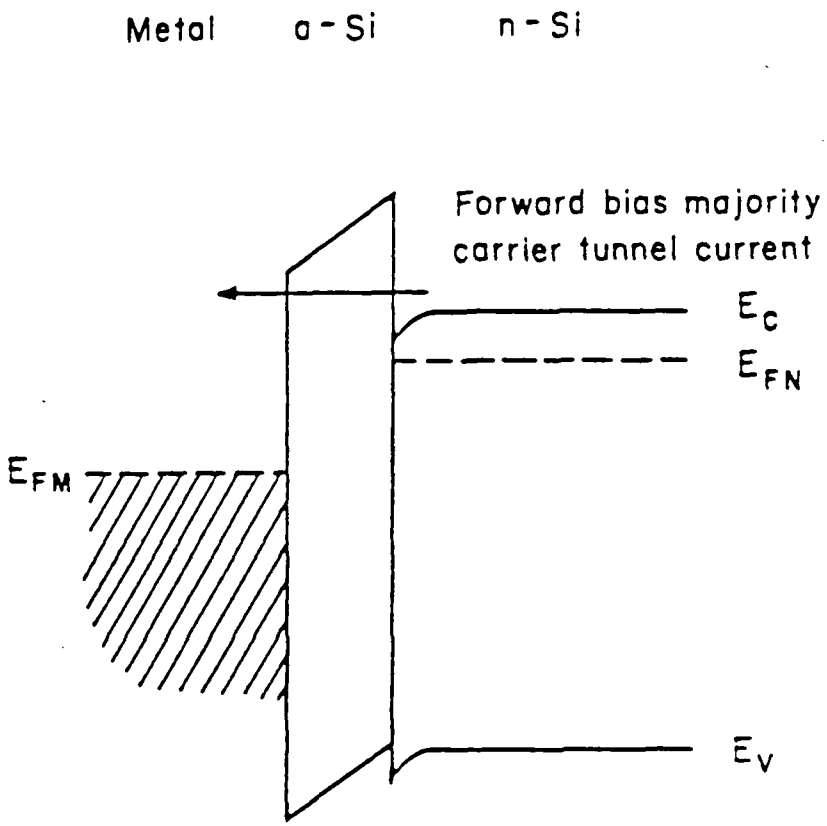

Figure 1c: A thin-film M-aSi-nSi tunneling structure (a) with energy band diagrams at thermal equilibrium (b), forward biased (c), and reverse biased (d). The flat band condition at zero bias will be clarified by capacitance data. The band gap of aSi is taken from the literature.

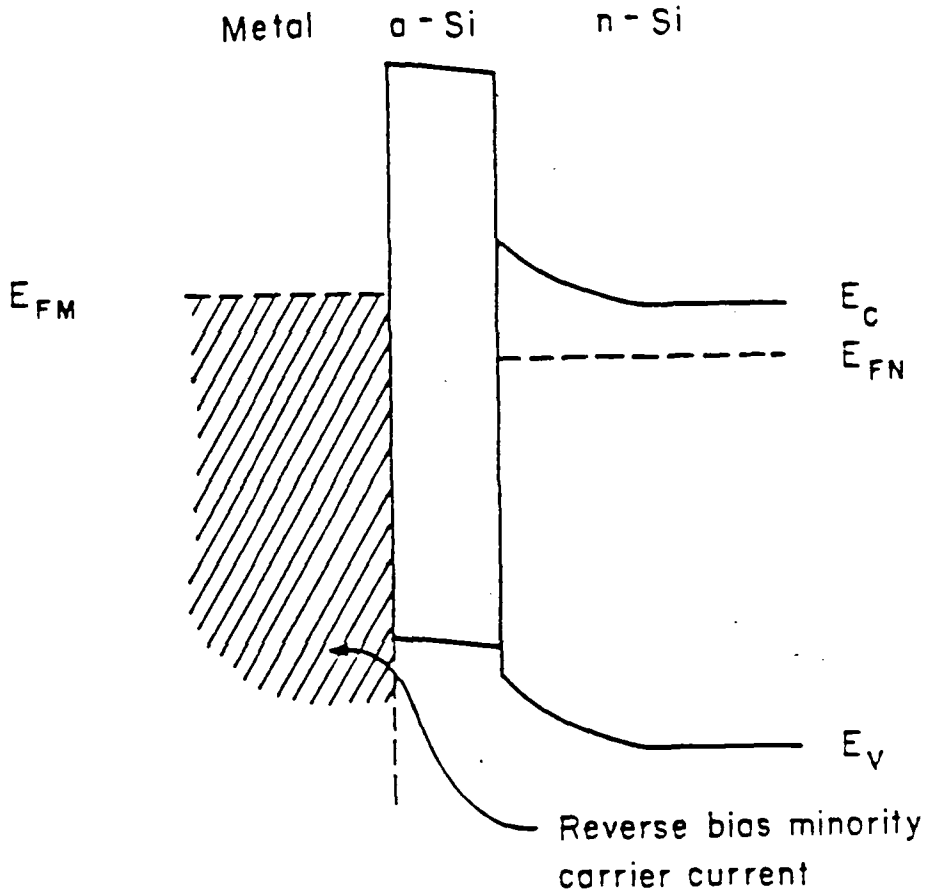

Figure 1d: A thin-film M-aSi-nSi tunneling structure (a) with energy band diagrams at thermal equilibrium (b), forward biased (c), and reverse biased (d). The flat band condition at zero bias will be clarified by capacitance data. The band gap of aSi is taken from the literature.

structural properties. In the diagram shown, the bulk silicon is described by the flat-band condition. This is obviously an idealized situation, but it turns out to be a reasonable assumption which agrees with the capacitance data to be presented later.

As a positive voltage is applied to the metal side, its Fermi level moves downward to produce a band diagram depicted in Fig. 1c. The intrinsic nature of the interface layer is important here; its high resistivity keeps most of the applied voltage across the a-Si film. The voltage drop across the bulk semiconduction is small because an accumulated layer is formed. Since the bias voltage produced a positive slope in the energy band diagram in the a-Si layer, the resulting interfacial electric field gives rise to a downward band bending in the n-type substrate. The conduction band edge of the a-Si film is clearly above that of the bulk so that the transport of majority carriers would have to be by means fo tunneling. Electrons in the conduction band of the substrate may tunnel through the a-Si barrier to reach the metal side. The accumulation of electrons in the substrate next to the aSi-Si interface provides ample supply of carriers for tunneling and, at the metal side of a-Si, there are a large number of available empty states in the metal. Therefore, the current can be described approximately by the MIM tunneling theory derived by Stratton[2] or Simons[3]. In the low bias region, the current density is given by[2]

$$I = I_o \frac{\pi c_{10} kT}{\sin(\pi c_{10} kT)} e^{-b_{12} V^2} e^{c_{10} V/2} \qquad (1)$$

where

$$I_o = \frac{120 \times 1.1 \times 10^{-2}}{(c_{10}\ k)^2} e^{-b_{10}} \qquad (2)$$

$$X = b_{10}/2c_{10} \qquad (3)$$

In the foregoing equations, m is the electronic mass, q is the electronic charge, k is Boltzmann constant, T is temperature in Kelvin, and the

constants b_{10}, b_{12}, and c_{10} are coefficients from power series expansions, and X represents the barrier height. Equation (1) describes the current-voltage characteristics of the diode under forward bias.

With a reverse bias voltage, the energy band diagram is shown in Fig. 1d. Here, an upward band bending appears in the bulk silicon in order to satisfy Gauss's law at the aSi-nSi interface. When the biasing voltage is small, the electrons in the metal cannot tunnel through because their energy position corresponds to the forbidden gap in the bulk silicon. As the reverse bias is increased, the band bending in the bulk increases to form a thick depletion layer. Under this condition, electrons in the metal must tunnel through both the amorphous layer and the depletion layer - an unlikely possibility with proper design. Consequently, there is essentially no electron tunneling current in the reverse-bias direction. In the valence band, however, there is no barrier for holes to reach the metal from the substrate. The minority carrier current is limited only by diffusion as holes move from right to left. As a result, a significant reverse saturation current exists in the device. The only way to reduce this reverse current is to increase the doping of the substrate as well as its minority carrier diffusion length. Increase of the impurity concentration will, however, decrease the breakdown voltage.

The fabrication details of the tunnel rectifier have been given in a separate paper.[4] Here, we show the current-voltage characteristics at different temperatuers for a typical diode in Fig. 2. The saturation current Jo can be obtained by extrapolating the current to the ordinate as shown in Fig. 2. The slope of the dotted line is $c_{10}/2$. Making use of Eq. (1) at a given voltage, one may calculate b_{12}. Substituting values of Jo and c_{10} yields the barrier height. At room temperature, the barrier height was found to be .67eV. This value is larger than the half band gap which is not too far from the assumption of an intrinsic amorphous silicon layer. The thickness of the a-Si layer was deduced to be 36Å which is the same as the measurement from the thickness monitor in the evaporator. The temperature dependence of the barrier height is shown in Fig. 3 where the dots correspond to the data points and the solid line is the theoretical values given by

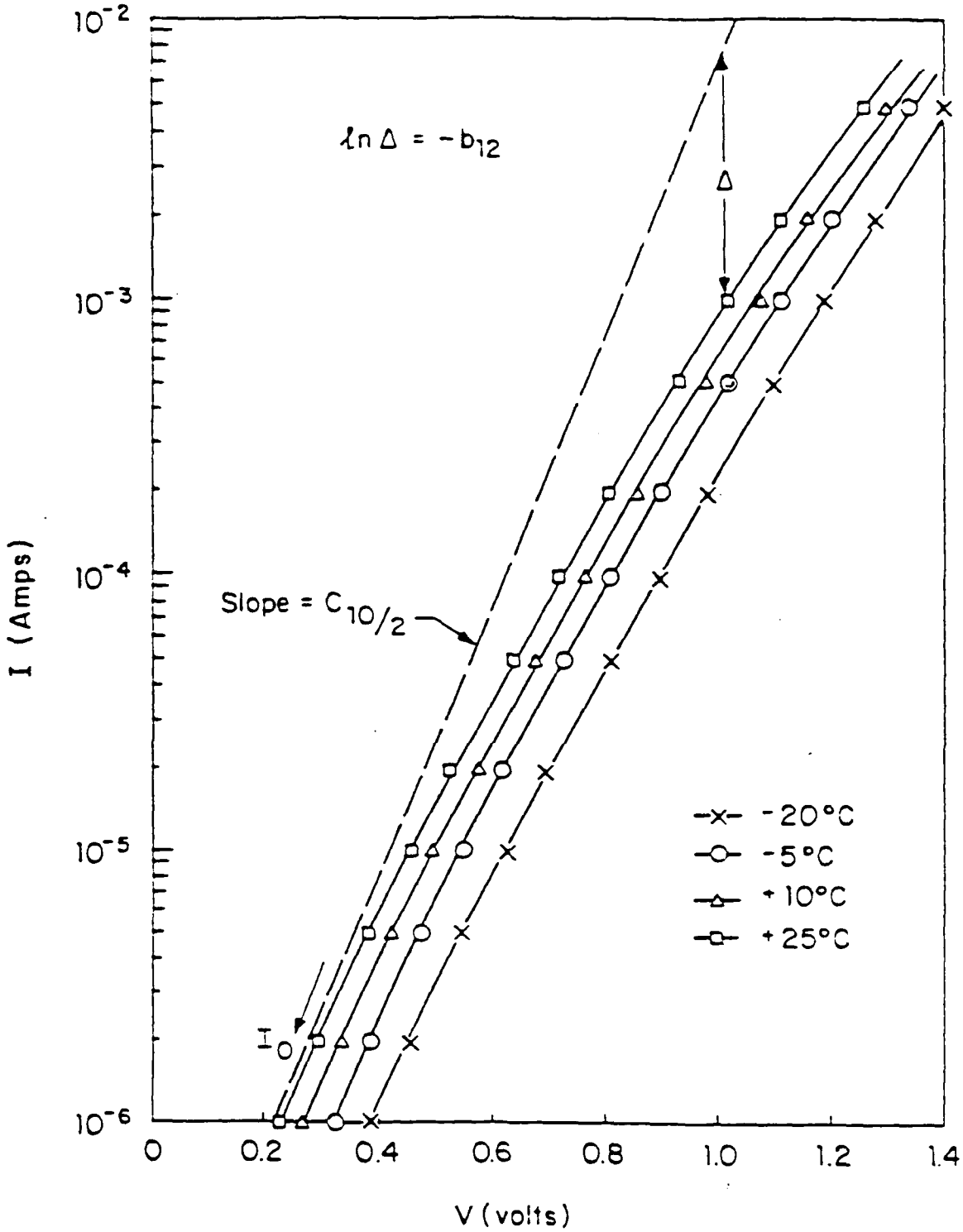

Figure 2: Forward biased current-voltage characteristics with temperature as a variable. Matching of these curves with Stratton's theory yields the transport parameters, in particular, the barrier height of tunneling.

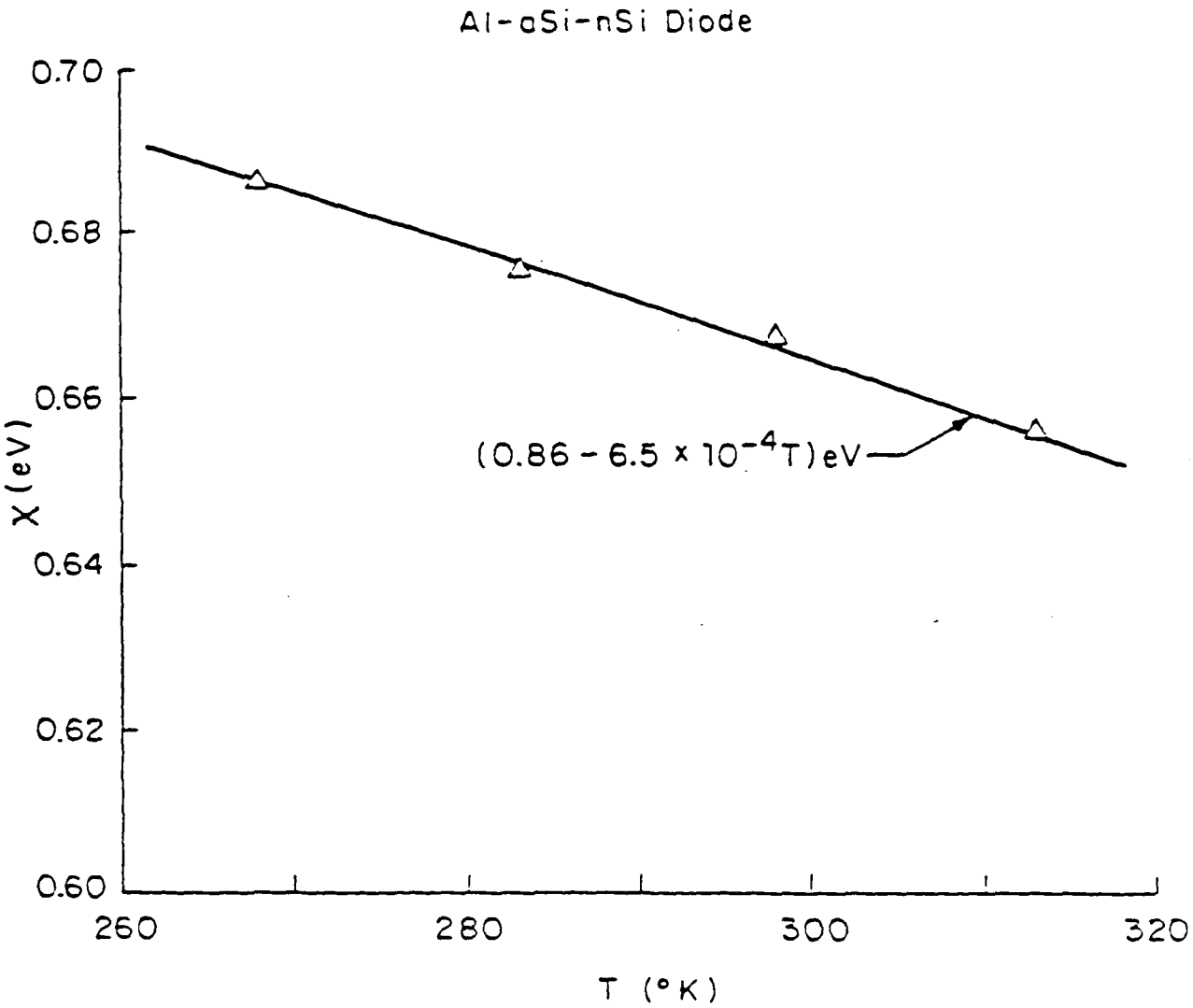

Figure 3: Temperature dependence of the tunneling barrier height as calculated from data shown in Fig. 2.

$$E - 0.86 - 6.5 \times 10^{-4} T \qquad (4)$$

It is noted that the barrier height has a temperature coefficient about twice of the silicon forbidden gap.

In Fig. 4, we show the capacitance-voltage characteristic of the diode in reverse bias. Extrapolation of the straight line yields a built-in voltage very close to zero. After testing a number of diodes, it was found that the built-in voltage varied from -15mV to +15mV, indicating that the zero bias condition is very close to the flat-band condition.

The forward I-V characteristics, i.e. the majority carrier current, is insensitive to light. However, the reverse saturation current increases with light intensity similar to an intimate Schottky barrier or p-n junction. This shows that the reverse current is constituted by diffusion limited minority carriers. All these experimental data indicate that the energy band diagram of Fig. 1 is a reasonable representation of the tunnel structure.

It has been demonstrated that a thin amorphous silicon layer can be used as a tunneling barrier between a metal and a silicon substrate. The energy band diagram of the device under different biasing conditions is presented to clarify the carrier transport mechanisms. Within a limited temperature range, the forward current-voltage characteristics follow Stratton's theory of tunneling in an MIM structure. The reverse current is caused by minority-carrier diffusion which is not limited by the interfacial layer. As a result, one can adjust the ratio of the two currents at will. One possible application is in photovoltaic devices where the open-circuit voltage increases when the majority carrier current is reduced; these devices, however, need a high quality interface that is not satisfied by the present fabrication method.

This work was also supported by NSF under Grant No. NSF ECS 82-17677.

(1) L. Esaki, Phys. Rev. 109, 603 (1958).

(2) R. Stratton, J. Phys. Chem. Solids 23, 1177 (1962).

AD-A163 402 RESEARCH INVESTIGATION DIRECTED TOWARD EXTENDING THE USEFUL RANGE OF THE ELECTROMAGNETIC SPECTRUM(U) COLUMBIA RADIATION LAB NEW YORK G W FLYNN ET AL. 2/4

UNCLASSIFIED 31 DEC 85 DAAG29-85-K-0049 F/G 20/6 NL

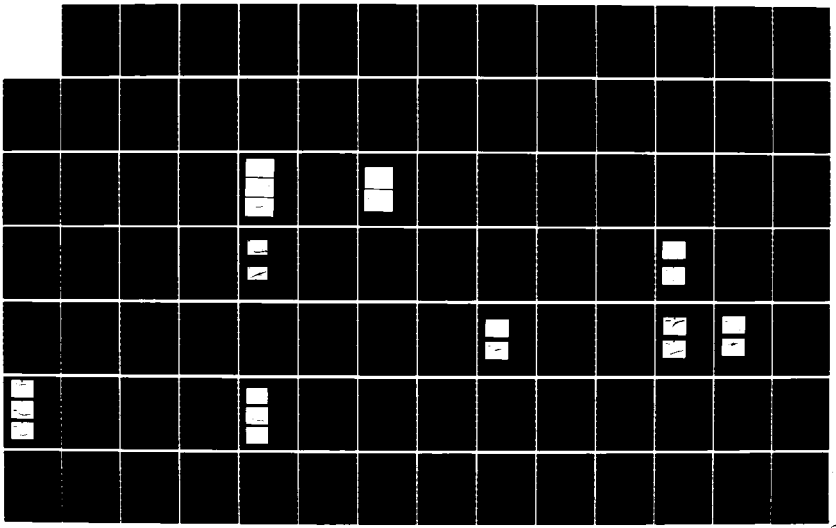

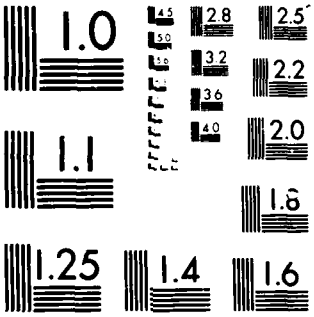

MICROCOPY RESOLUTION TEST CHART

NATIONAL BUREAU OF STANDARDS 1963-A

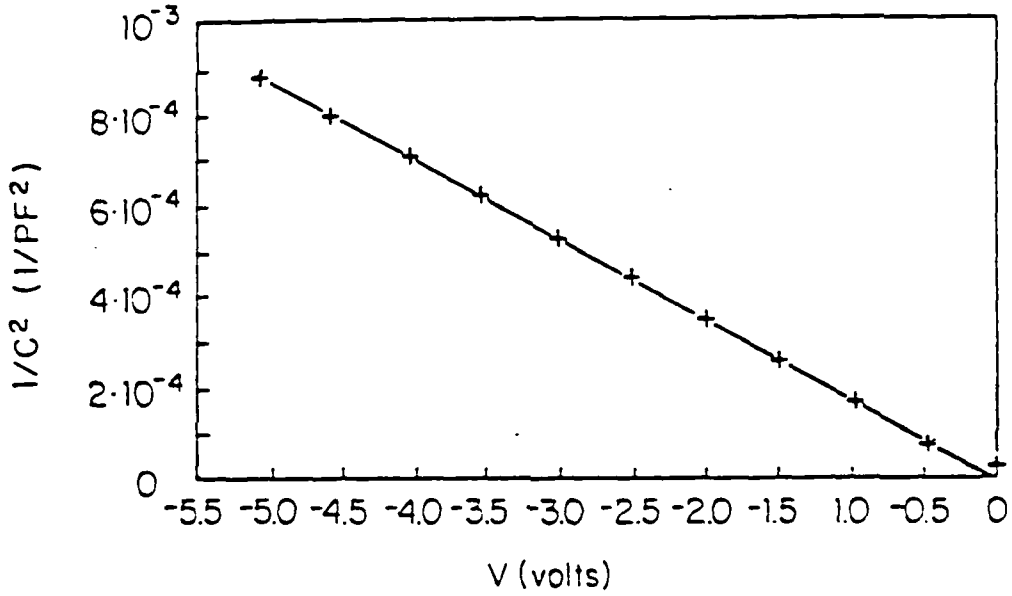

Figure 4: Reverse biased capacitance-voltage characteristics showing essentially zero built-in potential. This result supports the flat band assumtion used in Fig. 1b. It should be pointed out that direct contact between aluminum and 10 Ω -cm nSi without annealing has a built-in potential greater than 100 mV.

$$E - 0.86 - 6.5 \times 10^{-4} T \qquad (4)$$

It is noted that the barrier height has a temperature coefficient about twice of the silicon forbidden gap.

In Fig. 4, we show the capacitance-voltage characteristic of the diode in reverse bias. Extrapolation of the straight line yields a built-in voltage very close to zero. After testing a number of diodes, it was found that the built-in voltage varied from -15mV to +15mV, indicating that the zero bias condition is very close to the flat-band condition.

The forward I-V characteristics, i.e. the majority carrier current, is insensitive to light. However, the reverse saturation current increases with light intensity similar to an intimate Schottky barrier or p-n junction. This shows that the reverse current is constituted by diffusion limited minority carriers. All these experimental data indicate that the energy band diagram of Fig. 1 is a reasonable representation of the tunnel structure.

It has been demonstrated that a thin amorphous silicon layer can be used as a tunneling barrier between a metal and a silicon substrate. The energy band diagram of the device under different biasing conditions is presented to clarify the carrier transport mechanisms. Within a limited temperature range, the forward current-voltage characteristics follow Stratton's theory of tunneling in an MIM structure. The reverse current is caused by minority-carrier diffusion which is not limited by the interfacial layer. As a result, one can adjust the ratio of the two currents at will. One possible application is in photovoltaic devices where the open-circuit voltage increases when the majority carrier current is reduced; these devices, however, need a high quality interface that is not satisfied by the present fabrication method.

This work was also supported by NSF under Grant No. NSF ECS 82-17677.

(1) L. Esaki, Phys. Rev. 109, 603 (1958).

(2) R. Stratton, J. Phys. Chem. Solids 23, 1177 (1962).

(3) J.G. Simmons, J. Appl. Phys. 34, 1793 (1963).

(4) E.S. Yang, Q.H. Hua, D.K. Yang, KG.S. Yang and P.S. Ho, Appl. Phys. Lett. 44, 1144 (1984).

(5) C.R. Wronski, B. Abeles, G.D. Cody, T. Tiedje, Appl. Phys. Lett. 37, 96 (1980).

(6) R.J. Nemanich, Semiconductor and Semimetals 21, Part C, 375 (1984).

PREVIOUS PAGE IS BLANK

E. A STUDY OF THE PHOTOVOLTAIC EFECT OF A SEMICONDUCTION GRAIN BOUNDARY BY A SCANNING LASER BEAM

(J.S. Song and E.S.Yang)
(JSEP work unit 2, 1985 - 1988)
(Principal Investigator: E.S. Yang (212)280-3120)

Grain boundaries have been known to be the dominant factor governing the electrical transport processes in polycrystalline semiconductior.[1-4] Along the grain boundaries, a large density of distributed interface states is found resulting from dislocations or impurity segregations.[5,6] The charge of interface states produces a potential barrier which impedes majority carrier current flow, thus reducing the mobility and increasing the resistivity. These states also behave as very effective recombination centers lowering the overall minority carrier lifetime and diffusion length.[4,7,8] Among the methods used to measure the grain-boundary parameters[9-13] the application of a laser beam has many advantages. Sample preparation is simple, and the carrier generation and profile are well characterized. Also, a highly focused laser beam allows us to examine an individual grain boundary in a sample containing multiple grains.

In this work we will present a model for the photovoltaic effect of the grain boundary caused by a scanning laser beam, which can be used to measure the diffusion length within the grain and the recombination velocity at the grain boundary.

Let us consider a p-type silicon bicrystal sample with a grain boundary across the whole width. The holes trapped in the interface states of the grain boundary give rise to a potential barrier which impedes the carrier transport. The grain-boundary potential barrier may be represented by the back-to-back Schottky diodes as shown in Fig. 1(a). When excess carriers are produced in one side of the grain boundary by a laser beam [Fig. 1(b)], the potential barrier on that side of the grain boundary is reduced, giving rise to the photovoltaic effect (Fig. 2).

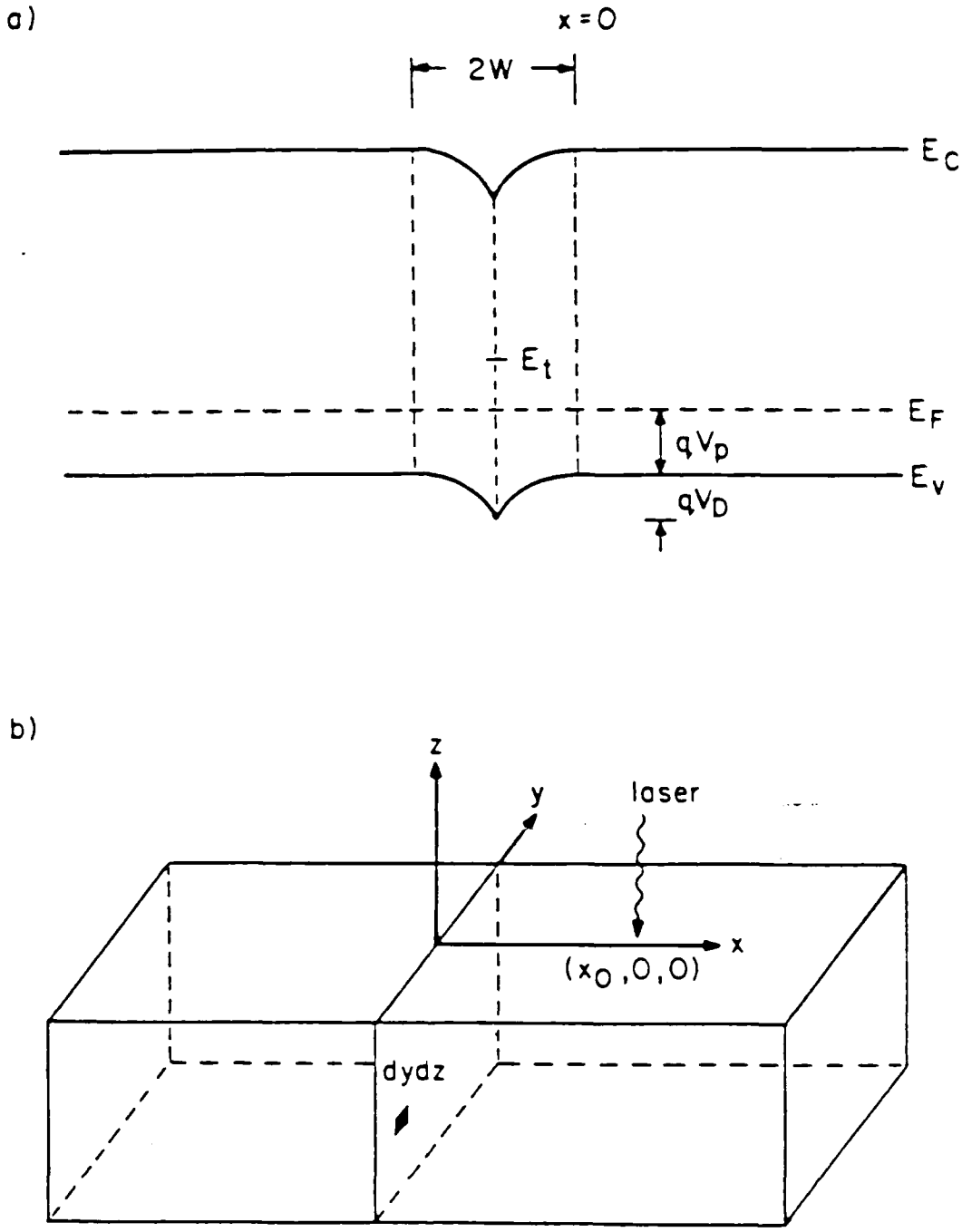

Figure 1(a) and 1(b): Electron energy diagram near the grain boundary in the dark. (b) The geometry of the sample under illumination. The grain boundary and the depletion layers are regarded as a single plane. The shaded area represents a small section of the grain boundary where V'_D is calculated.

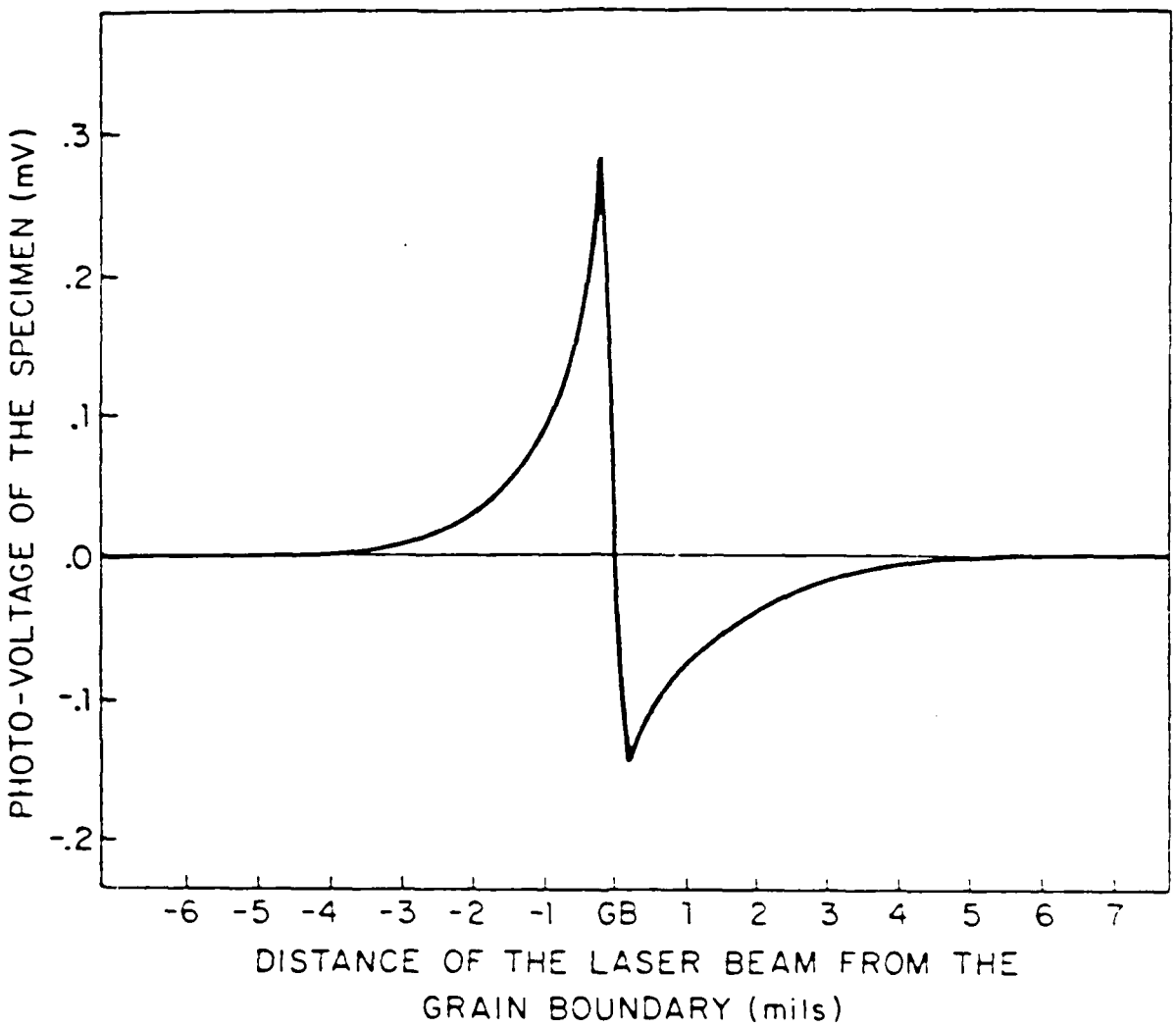

Figure 2: Photovoltaic effect of a grain boundary by a scanning laser beam. V_{oc} is the open-circuit voltage of the sample under illumination and x is the position of the laser beam.

Assuming a point source of excess carriers generated at $(X_o,0,0)$, we may solve the following minority carrier continuity equation to obtain the steady-state excess minority carrier concentration:

$$\partial \Delta n(x,y,z)/\partial t = D_n \nabla^2[\Delta n(x,y,z)] - \Delta n(x,y,z)/\tau_n + (1-R)\eta G\delta(x-x_n)\delta y\delta z. \quad (1)$$

D_n is the minority carrier diffusion constant, τ_n is the minority carrier lifetime, η is the internal quantum efficiency, R is the reflectivity of the surface, and G is the incident photon rate. This equation may be solved by regarding the grain boundary and the depletion layers as a single plane with a recombination velocity s. The boundary conditions for this problem are deduced from the following assumptions:

(1) The recombination at the free surface is assumed to be negligible:

$$D_n\left(\frac{\partial \Delta n(x,y,z)}{\partial z}\right)_{z=0} = 0 \quad (2)$$

(2) The excess minority carriers at the depletion layer edge on both sides of the grain boundary are the same because the width of the depletion layers is much narrower than the diffusion length, therefore

$$\Delta n(0^-,y,z) = \Delta n(0^+,y,z) \quad (3)$$

(3) When the minority carriers cross over the grain boundary, it can be assumed that the recombination takes place only at the grain-boundary interface. The recombination in the depletion layer is negligible because the depletion layer is much narrower than the diffusion length. Therefore, the flux of the minority carriers should be conserved except for the recombination at the interface:

$$D_n\left(\frac{\partial \Delta n(x,y,z)}{\partial x}\right)_{x=0^+} = [s\Delta n(x,y,z)]_{x=0^-} - D_n\left(\frac{\partial \Delta n(x,y,z)}{\partial x}\right)_{x=0^-} \quad (4)$$

Solving the continuity equation with these boundary conditions, the excess carriers reaching the grain boundary can be obtained by the method developed by van Roosebroeck.[14]

$$\Delta n(0, y, z) = [(1 - R)\eta G/2\pi L_n D_n]\Big(e^{-r}/r) - (sL_n/2D_n)\int_0^\infty [\exp(-(sL_n/2D_n)\xi - r_\xi)/r_\xi]d\xi\Big), \tag{5}$$

$$r = [(x - x_0)^2 + y^2 + z^2]^{1/2}/L_n,$$

$$r_\xi = [(x + x_0 - \xi)^2 + y^2 + z^2]^{1/2}/L_n.$$

These excess carriers change the probability of occupancy of interface states at the grain boundary and thus the potential barrier of the grain boundary. The probability of occupancy of an interface state at equilibrium follows the Fermi-Dirac function.

$$f_t(E_t) = 1/[e^{(E_t - E_F)/kT} + 1]. \tag{6}$$

E_t is the trap energy level and E_F is the Fermi energy level. However, this equation cannot be used if the sample is illuminated because it is no longer under thermal equilibrium. The probability of occupancy of a trap under nonequilibrium conditions was derived by Shockley and Read.[15]

$$f_t(E_t) = (n - n_i e^{(E_t - E_i)/kT}) \times (n + p + 2n_i \cosh[(E_t - E_i)/kT])^{-1}, \tag{7}$$

where

$$n = (n_0 - \Delta n)\exp[V_D/V_T],$$

$$p = (p_0 - \Delta n)\exp[-V_D/V_T]$$

assuming $\Delta p \simeq \Delta n$.

n and p are carrier concentrations at the grain boundary under illumination, n_o and p_o are carrier concentrations in the grains with no illumination, Δn is the excess electron concentration at the edge of the depletion layer of the grain boundary, n_i is the intrinsic carrier concentration, V'_D is the built-in potential of the grain boundary under illumination, and E_i is the intrinsic Fermi elergy level. Assuming a discrete trap energy level with density N_t, the number of trapped holes at the grain boundary is given by

$$Q^{tr} = qN_t(1-f_t) \tag{8}$$

This should be balanced by the charge in the depletion region.

$$Q^{sep} = \sqrt{8q\epsilon}\left[V'_D(p_0 - n_0) - V_T(p_0 + \Delta n)(e^{-V'_D/V_T} - 1) - V_T(n_0 - \Delta n)(e^{V'_D/V_T} - 1)\right]^{1/2}, \tag{9}$$

which was derived by solving Poisson's equation including free carriers following Brew's Method.[16]

From Eqs. (5), (7), (8) and (9), the built-in potential barrier of the grain boundary under illumination can be calculated if we know N_t and E_t. This modification of grain-boundary potential barrier under illumination alters the conductance across the grain boundary. Therefore, from the thermionic emission model for the current-voltage relatinoship across a grain boundary,[17]

$$I = \alpha A^* T^2 (e^{V/V_T} - 1) \times \int_A \exp\{-[V_p - V'_D(0, y, z)]/V_T\} dA. \tag{10}$$

V is the applied voltage across the grain boundary, V_t is kT/q, α is the attenuation factor,[18] A^* is the Richardson constant, T is temperature, V_p is the difference between the conduction band and the Fermi energy level,

$V'_D(0,y,z)$ is the modified grain-boundary potential at (0,y,z) on the grain-boundary plane under illumination, and A is the area of the grain boundary.

The minority carrier recombination current of the grain boundary is

$$I_n = \int_A qs\Delta n(0,y,z)dA. \tag{11}$$

Under the open circuit condition, an equal number of holes is needed to accomplish recombination, so that the electron and hole currents exactly cancel out, and thus the net current to the grain boundary is zero. The hole current is supplied by the thermionic emission current.

$$\begin{aligned} I_p &= aA^*T^2(e^{V_{oc}/V_T} - 1) \\ &\quad \times \int_A \exp\{-[V_p + V'_b(0,y,z)]/V_T\}dA \\ &= aA^*T^2(V_{oc}/V_T) \\ &\quad \times \exp\{-[V_p + V'_b(0,y,z)]/V_T\}dA \\ \text{for } V_{oc} &< V_T. \end{aligned} \tag{12}$$

V_{oc} is the open-circuit voltage across the grain boundary under illumination which can be obtained from setting $I_n = I_p$ provided that we know the diffusion length and the recombination velocity at the grain boundary. Conversely, we can find out the diffusion length and the recombination velocity by matching hte calculated V_{oc} vs x_o curve to the experimental curve (Fig. 3).

The sample was cut from a p-type Wacker polycrystalline silicon wafer so that there would be only one grain boundary in the sample and the grain boundary would lie on the yz plane of the sample. This was confirmed later by the response of the sample to the laser beam. The size of the sample was 0.254 cm X 1 cm X 0.043cm. The doping density of the Wacker polycrystalline silicon wafer was obtained by C-V measurement and was 6.5 X $10^{14}/cm^3$. The

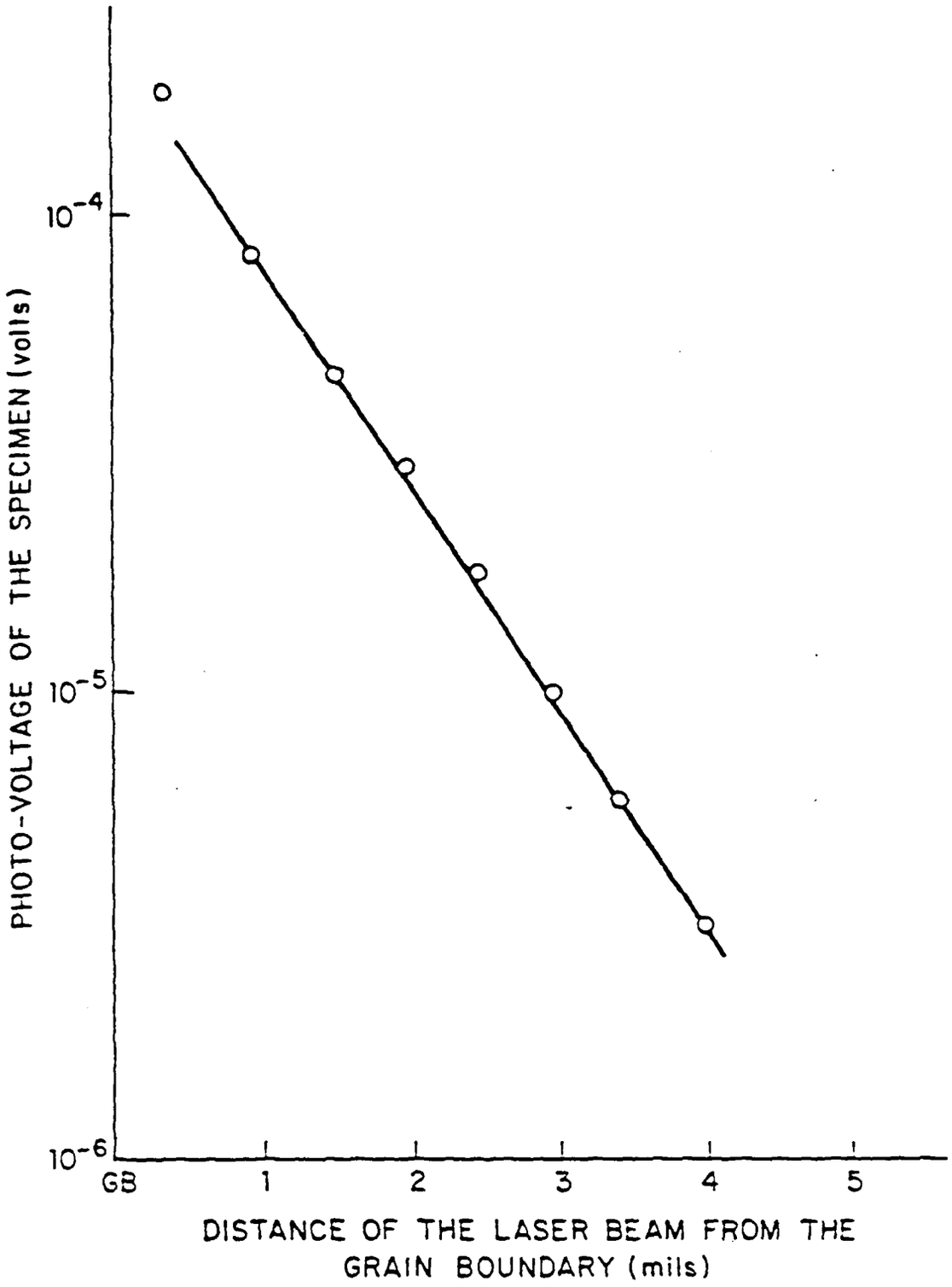

Figure 3: Analysis of experimental data to obtain the recombination velocity at the grain boundary and the diffusion length. The solid line is the V_{oc} calculated with s = 1430 cm/s and L_n = 22.7 μm. The dots represent the experimental data.

sample ws mechanically polished with 1-μm diamond powder to get rid of mechanical damage on the surface and to reduce the chemical polishing time. After the mechanical polishing, the sample was chemically treated in CP-4 for 30 s. After polishing gold ohmic contact was deposited on both ends of the specimen with background pressure of 2×10^{-6} Torr.

The sample was mounted in the cold head of a cryogenic system which was on a movable X-Y stage. The laser was focussed on the sample through the window of the cold head. The sample was moved perpendicular to the grain boundary by the micrometer of the X-Y stage and the open-circuit voltage across the samlpe and the position of the laser spot were recorded on a X-Y recorder.

The experiment was performed at a temperature range between 265 and 325 ^{o}K. The typical experimental curve is shown in Fig. 2. The laser spot was moved from the left to the right. The diameter of the laser spot 10 μm. As the temperature wasincreased, the photovoltaic signal was reduced due to reduction of diffusionlength and lowering of dV/dI at the grain boundary. Matching the experimental data and the calculated curves, we obtained the diffusion length and the recombination velocity at the grain boundary as tabulated in Table I.

By using the basic mobility and recombination equations, we find the diffusion length is inversely proportional to temperature.

$$
\begin{aligned}
L_n &= \sqrt{D_n \tau_n} \\
&= \sqrt{(kT/q)\mu_n/(C_n v_{th} N_t)} \\
&\propto \sqrt{T^{-3/2}/T^{1/2}} \\
&\propto T^{-1}.
\end{aligned}
\qquad (13)
$$

Fig. 4 shows a good match between the measured diffusion lengths and the theoretical dependence of diffusion length on the temperature.

To obtain the interface state density and the energy level, the dark sample resistivity, using the interface state density and the energy level as

TABLE I: The diffusion length and the recomgination velocity obtained at various temperatures

Temp. (K)	L_n (μm)	s (cm/s)
295.2	22.7	1430
300.3	22.5	1550
305.3	21.8	1630
310.1	21.4	1700
315.3	21.0	1750
320.1	20.9	1820
325.3	30.6	2010

variables, was compared with the experimental data. The best match was realized when the interface state density was 1.31 X $10^{11}/cm^2$ and the energy level was 0.45 eV from the valence band (Fig. 5).

A model for the photovoltage change with a scanning laser spot has been developed. Detail modeling of the photo-voltage change near the grain boundary provides a method to measure the minority carrier diffusion length and the recombination velocity at the grain bouondary. Our study indicates that the photovoltaic effect across a grain boundary is observable and its behavior follows that of a Schottky barrier. Although in the present case the grain boundary is seen as two Schottky barriers connected back-to-back, the induced photovoltage conforms to the open-circuit voltage calculation of a solar cell. The measured recombination velocity (~ 2000 cm/sec) and diffusion length (20 μm) appear to be within the expected values for cast polycrystalline silicon wafers. The limited temperature data show that the model describes the photovoltaic effect well.

This work was also supported by NSF under Grant No. NSF-ECS 82-17677, and IBM.

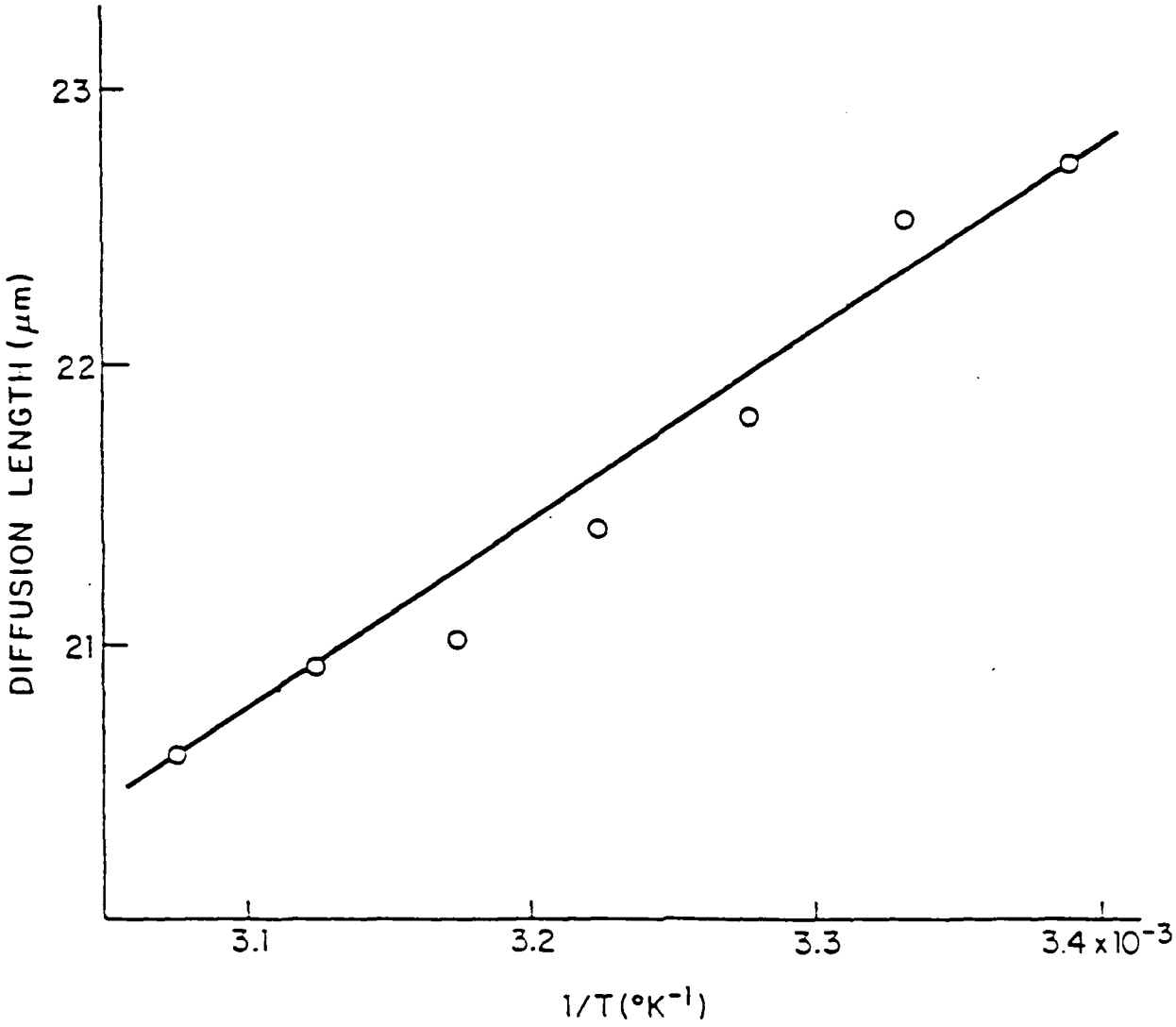

Figure 4: Plot of L_n vs 1/T shows the diffusion length is inversely proportional to the temperature. The solid line goes to (0,0), the origin of the graph.

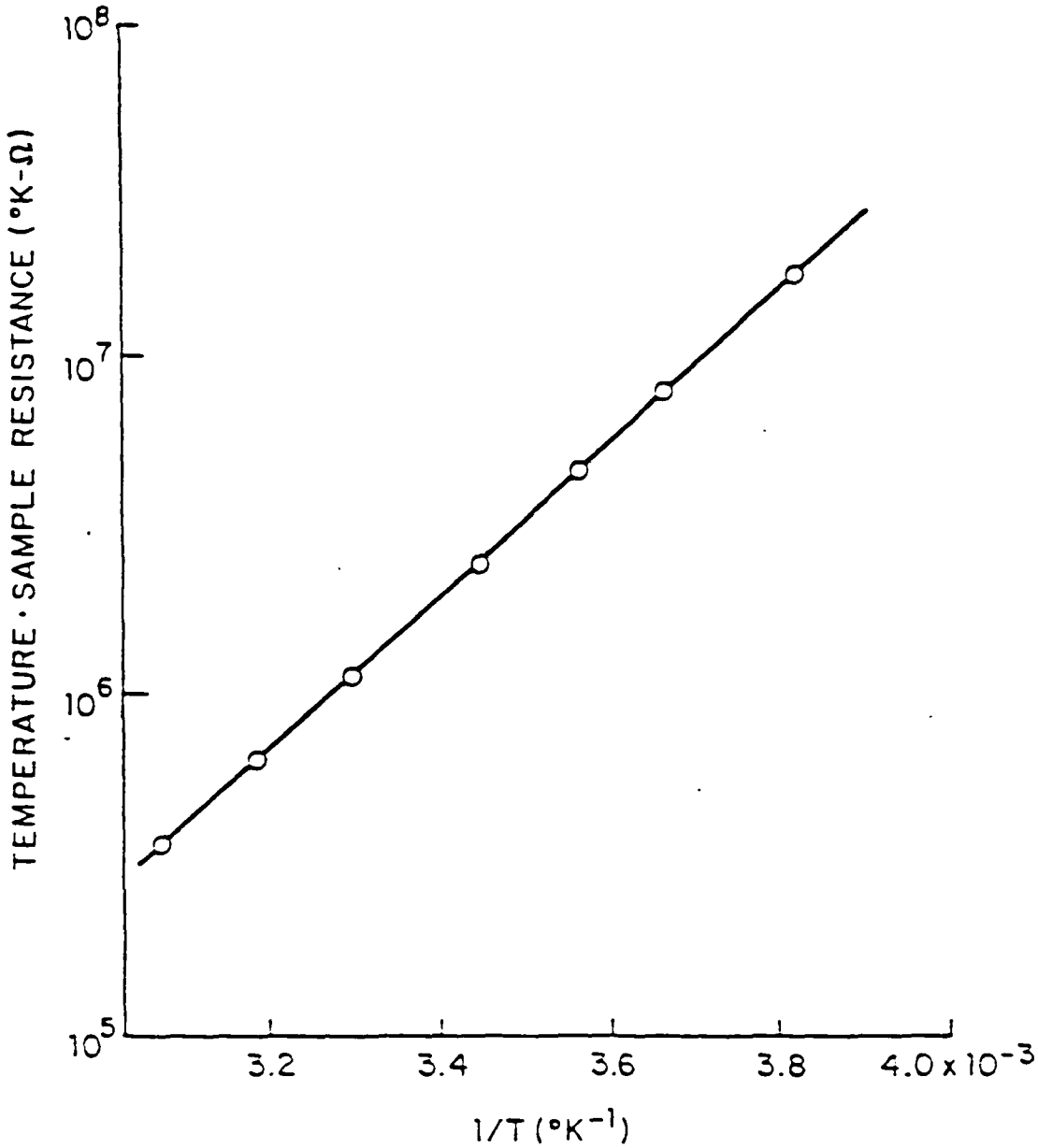

Figure 5: Temperature dependence of the sample resistance.

(1) W.E. Taylor, N.H. Odel, and H.Y. Fan, Phys. Rev. 88, 867 (1952).

(2) H.F. Matare, H. Kedesdy, A MacDonald, and A. Petersen, Phys. Rev. 98 1179 (1955).

(3) R.K.Mueller, J. Appl. Phys. 32 640 (1961).

(4) P. Rai-Choudhuri, and P.L. Hower, J. Electrochem. Soc. 120, 1761 (1973).

(5) W.T. Read, Philos. Mag. 45, 775 (1954).

(6) H.J. Queisser, K. Hubner and W. Shockley, Phys. Rev. 123, 1245 (1961).

(7) T.I. Kamins, J. Appl. Phys. 42, 4357 (1971).

(8) J.Y.W. Seto, J. Electrochem. Soc. 122, 701 (1975).

(9) Chenming Hu and Clifford Drowley, Solid State Electro. 21, 965 (1978).

(10) J. Martinez, A. Criado, and J. Piqueras, J. Appl. Phys. 52, 1301 (1981).

(11) C.H. Seager, J. Appl. Phys. 52, 3960 (1981).

(12) Jiri Mareck, J. Appl. Phys. 53, 1454 (1982).

(13) P. Panayotatos, E.S. Yang and W. Hwang, Solid State Electron. 25, 417 (1982).

(14) W. van Roosebroeck, J. Appl. Phys. 26, 380 (1955).

(15) W. Shockley and W.T. Read, Phys. Rev. 87, 835 (1952).

(16) J.R. Brews, Physics of the MOS Transistor in Silicon Integrated Circuits, ed., D. Kahng, Academic, New York, 1981, p. 7.

(17) R.L. Petritz, Phys. Rev. 104, 1508 (1956).

(18) C.M. Wu and E.S. Yang, Appl. Phys. Lett. 40, 49 (1982).

F. DEVICE FABRICATION FACILITY

(E. Fossum)
(JSEP work unit 4, 1985 - 1988)
(Principal Investigator, E. Fossum (212)280-3107)

A facility for fabricating electronic devices has been under development at Columbia for the past two years. At the present time, it is possible to routinely fabricate metal-oxide-semiconductor (MOS) type devices, including field-effect transistors (MOSFETs), with excellent operating characteristics. Nearing completion is the renovation of a 200 keV ion implanter donated by IBM, East Fishkill, and a low-pressure chemical vapor deposition (LPCVD) system. On order, through NSF ERC funding, is a sub-micron mask aligner, a custom sputter/E-beam deposition system, and a rapid thermal annealer. With the addition of this equipment, the fabrication of GaAs devices at Columbia should become possible in 1986.

G. ANALOG CHARGE-COUPLED COMPUTING

(E. Fossum)
(JSEP work unit 4, 1985 - 1988)
(Principal Investigator, E. Fossum (212)280-3107)

A new type of analog computer, the charge-coupled computer, is under investigation. The research is underway for both silicon and gallium arsenide (GaAs). The silicon charge-coupled computer is a surface-channel MOS technology. Two different charge-coupled computers were designed and recently fabricated in the Columbia Microelectronics Sciences Laboratories. One computer is designed for magnitude comparison operations such as analog-to-digital conversion, and the second is designed for recursive filtering. Both are fully programmable by varying external clocking waveform timing. Testing of these devices is awaiting the completion of a CCD test station currently under construction.

Charge-coupled computing in GaAs is also under investigation. A

buried-channel MESFET-like technology is being explored. Structures for analog computation have been modelled and a fabrication process is being designed. Preliminary device layout is underway.

H. ROOM TEMPERATURE OXIDATION OF SILICON

(E. Fossum)
(JSEP work unit 4, 1985 - 1988)
(Principal Investigator, E. Fossum (212)280-3107)

A low energy (60 eV) ion beam has been used to oxidize the surface of a silicon wafer. A mixture of argon and oxygen was used to grow an ultra-thin (42 angstroms) layer of SiOx at room temperature. A working MOSFET was fabricated using this process. The damage caused by the bombardment was found to be fairly minimal, resulting in decreased channel mobility and some flat-band voltage shift. These effects were removed by post-metallization annealing at 400°C. Further investigation to understand the effect of ion beam energy, gas composition, and dose on oxide thickness and quality is underway.

I. OPTICAL FIBER INTERCONNECT PHOTODETECTOR

(E. Fossum)
(JSEP work unit 4, 1985 - 1988)
(Principal Investigator, E. Fossum (212)280-3107)

A photodetector has been fabricated in a cavity formed by anisotropic laser-assisted etching. The photodetector is a silicon p-n junction diode formed by diffusion with appropriate metallization for electrical testing. The photodetector is a component of a optical fiber receiver structure being investigated in collaboration with Professor Prucnal and Professor Osgood, and which will be useful in optical-fiber-based interconnections between electronic chips.

III. GENERATION AND DYNAMIC PROPERTIES OF METASTABLE SPECIES FOR QUANTUM ELECTRONICS AND LASER MICROPROCESSING

A. UV LASER ENHANCED CHEMISTRY IN PLASMA ETCHING OF GaAs

(J. Chu, R. Osgood and G. Flynn)
(JSEP work unit 5, 1985 - 1988)
(Principal Investigators: R. Osgood (212)280-4462
G. Flynn (212)280-4162

1. Introduction — There are important advantages to using ultraviolet laser radiation to control or modify the chemical species in the plasma discharge environment of a semiconductor processing reactor.[1,2] This approach allows one to control separately the production of the desired gas-phase chemical species and the ion bombardment in the plasma chamber. The selectivity is essentially achieved via the separate control of the ion flux and energies by the plasma breakdown voltages and of the reactive neutral species by the enhanced laser driven photochemical process. This fabrication concept is appropriate to the dry etching of soft III-IV semiconductor materials such as GaAs where it is desirable to achieve maximum etch rate and important to minimize surface damage with minimal ion bombardment effect. Nevertheless, the most attractive features in materials processing arise from the influence of ion bombardment in plasma or ion-assisted etching where the nature of the directional bombardment or physical impact of the ions on the surface is necessary in order to achieve fine anisotropic etching features.

Recently the use of visible and UV lasers in conjunction with plasma etching reactors has been investigated in our laboratory.[2,3,4] Thus far only surface mechanisms and localized effects have been studied in the laser-enhanced etching of semiconductor materials in a plasma chamber. In particular, it was observed that laser illumination of the Si surface in a CF_4/O_2 plasma locally enhances the etch rates via photogenerated minority carriers at low laser power densities and a largely thermal effect at high

laser power densities. In this study, we are interested in investigating the effect of altering or modifying only the plasma chemistry via UV laser radiation in a plasma etcher. Typically, the 193nm output of an excimer laser is directed over a GaAs sample in a pulsed discharge of HBr. Laser enhanced etch rates and ion bombardment modification of surfaces are examined.

2. Experimental — A schematic diagram of the laser controlled plasma etching system composed of a pulsed plasma discharge reactor in conjunction with a repetitively-pulsed (1-100 Hz) excimer laser is shown in Fig. 1. Typically the 193nm output of the excimer laser is not focussed and is directed through a 2mm slit before it is allowed to pass over the GaAs substrate which is housed in a stainless-steel reactor chamber. The beam aperture ensures that the UV laser irradiates only into the plasma discharge region and does not illuminate either the semiconductor surface or the discharge electrodes. The reactor chamber is diffusion pumped and a typical flow rate of 25 sccm is maintained for an HBr pressure of 5 torr. No measurable spontaneous etching rate was observed for the HBr parent gas in the present temperature range studied (20 - 100^{0}C). When necessary the spectral emission of the plasma discharge can be examined and resolved via a 3/4-meter monocromator and PMT detection scheme.

The timing component of the plasma discharge relative to the excimer laser trigger is controlled by a pulse discharge generator which is capable of producing discharge pulses having variable time durations with time delays in the nanosecond range. Thus far, discharge voltages applied to the pulse plasma etcher could be varied from 0 - 1.5 kvolts producing plasma current from 0 - 35mA (as measured across a 50 ohms resistor in the plasma circuit). Typically, the plasma reactor was triggered synchronous to the excimer laser at a breakdown voltage of 650 volts for a 200 μsec duration at a frequency of 30 Hz. The plasma etcher was usually operated at near threshold breakdown voltages to avoid high energy ion bombardment damage to the surface. The average plasma power applied to the plasma etcher was about 30 - 50 mW which was much (10 - 20 times) lower than the average laser power.

The GaAs substrates were fixed to a stainless steel holder which could

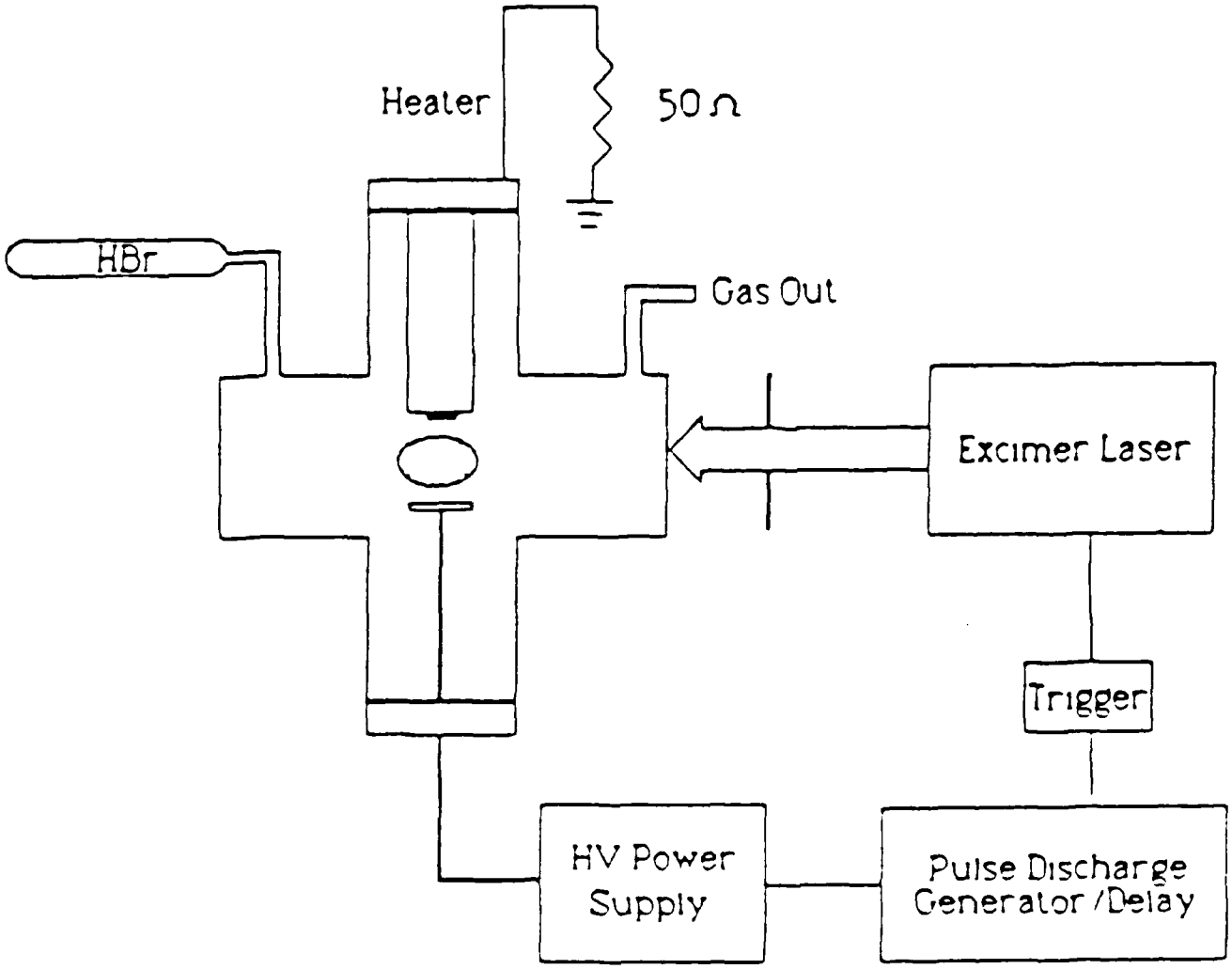
Heater
50 Ω
HBr
Gas Out
Excimer Laser
Trigger
HV Power Supply
Pulse Discharge Generator /Delay

Figure 1

be resistively heated from 23° to $100^{\circ}C$ and in addition, electrically biased relative to the anode electrode of the plasma reactor. The particular type of GaAs substrate studied and etched was of n-type doping with a (100) crystal orientation. The GaAs substrates were commercially polished and had etch pit densities $< 900/cm^2$. In each experiment, the samples were cleaned by a standard chemical washing procedure[5] and dried with nitrogen before processing. In order to study and measure the basic parameters involved in the etching process, masking of the GaAs substrates was achieved using a positive photoresist patterned with a standard mask aligner. After a lift-off procedure following a chrominum evaporation, the final GaAs samples were produced with a chrominum patterned line mask (with linewidths of about 25 microns). Etch depths and etching rates were measured by means of a mechanical stylus, and the etching morphology was studied by scanning electron microscopy (SEM).

3. Results and Discussion -- In this study, we are interested in the effects and changes in the etching characteristics of GaAs due to 193nm laser irradiation into a pulsed HBr plasma reactor. Particular emphasis and importance is given to examining the modification of etching features and profiles due to the combined effects of ion bombardment and laser generated chemical species. Basically in a HBr plasma chamber, spectroscopic studies show that various radicals and ions such as H, Br, Br+, and HBr+ are generated in the plasma discharge via the electron impact dissociation and ionization processes (see Fig. 2). In the etching process, reactive Br atoms are adsorbed on the GaAs surface and subsequent surface reactions lead to the formation of (fully) brominated metal salts such as $GaBr_3$ and $AsBr_3$ which are nonvolatile liquid products at room temperature. This brominated liquid-product layer will limit the etching process and load the surface with impurities. It has been shown previously that the etching of GaAs increases exponentially with temperature and that the predominant mechanism is the thermal desorption of nonvolatile etching products[6,7,8] which leads to open reactive surface sites. In our HBr plasma etching experiments, the variation of the etch rate as a function of the substrate temperature is shown in Fig. 3 which does exhibit a strong temperature effect. In the low temperature

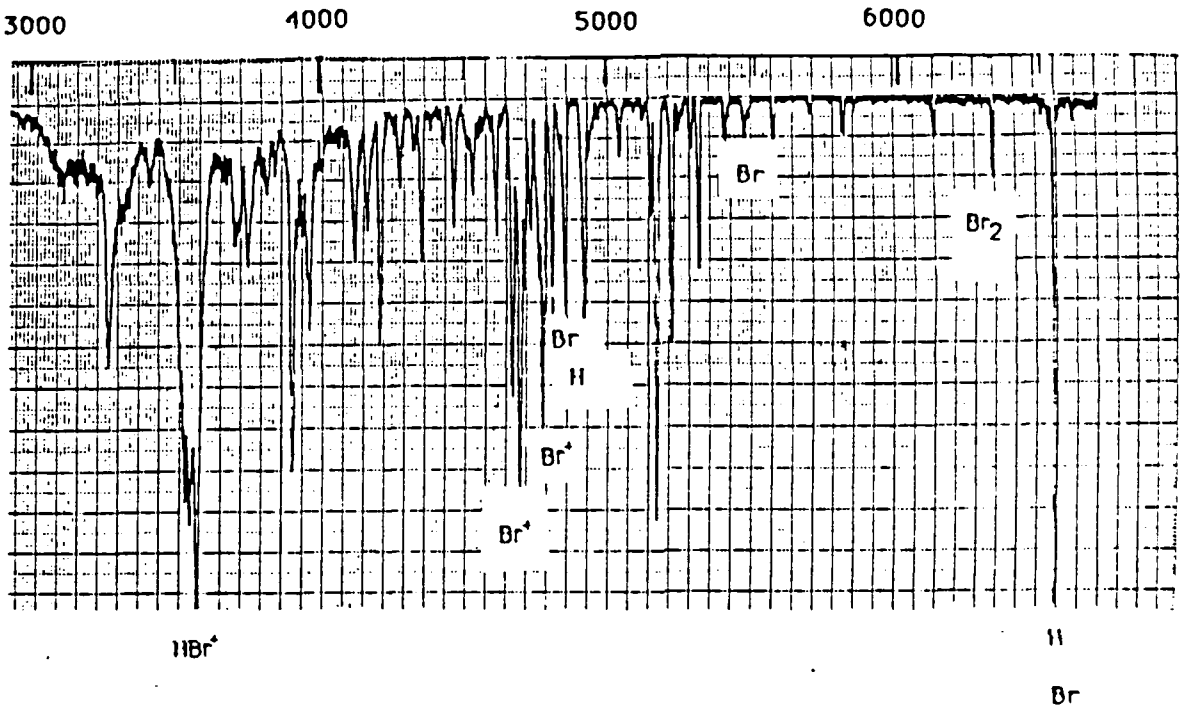

HBR PLASMA EMISSION

Figure 2

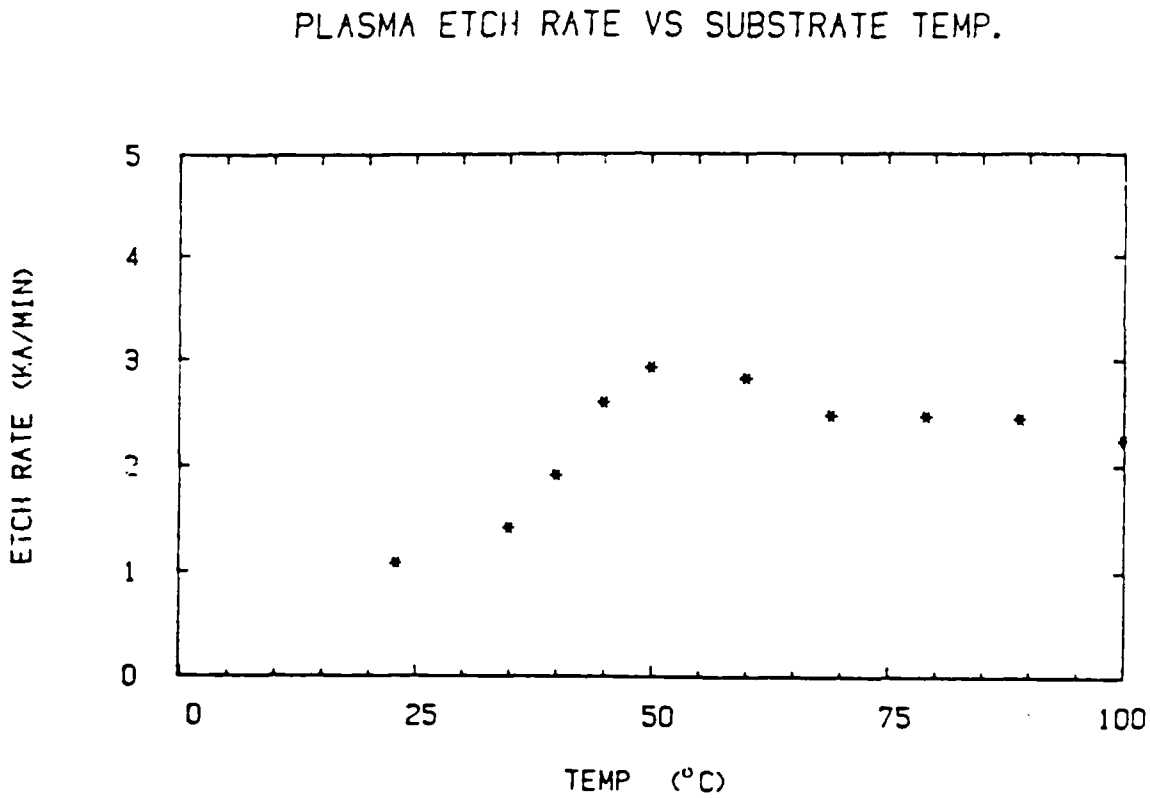
PLASMA ETCH RATE VS SUBSTRATE TEMP.
ETCH RATE (KA/MIN)
5
4
3
2
1
0
0
25
50
75
100
TEMP (°C)

Figure 3

region, 20° - $40^{\circ}C$, the etching processes and rates are hindered by the liquid formation of etching products on the surface. The surface morphology is in general smooth with random droplet macrostructures formed from the masking of the surface by the gallium bromide salts. As the substrate temperature is increased above $50^{\circ}C$, the etch rate increases by 100% over the rate observed at lower temperatures and no macroscopic liquid products are seen on the surface after the plasma processing. In this temperature range, the surface morphology is improved over that at room temperataure with the surface quality being smooth and flat. At the higher substrate temperatures, the etching rate appears to become almost constant and has associated with it a large uncertainty due to the limited accuracy in the present measurements of fine linewidths which are deep. During the plasma etching experiments, the 417 nm Ga fluorescence was detected in the plasma emission indicating the presence of gallium etched products.

In order to further our investigation of dry etching of GaAs, we studied the effect of directing the 193 nm laser output into the HBr plasma etcher. The primary photochemical processes of HBr at 193 nm are the production of H atoms with both ground-state Br and spin-orbit excited-state Br atoms.[9]

$$HBr \longrightarrow H + Br\ (^2P_{3/2})\quad 85\%$$

$$HBr \longrightarrow H + Br\ (^2P_{1/2})\quad 15\%$$

Following laser irradiation, spectroscopic measurements show a greatly increased population or production of reactive Br radical species in the reactor chamber due to the UV laser direct photolysis of HBr into H and Br atoms. This laser increased Br radical concentration does cause the etching process to go at a much faster rate than with an unirradiated discharge. This enhancement is ullustrated in Fig. 4, which shows and compares the etch rate with and without laser irradiation at fixed plasma etching conditions as a function of substrate temperature. Note that the laser enhancement is most pronounced at higher substrate temperatures. This trend essentially reflects the fact that ion bombardment in our plasma reactor does not remove the entire surface (product) adlayer during the etching process. The laser

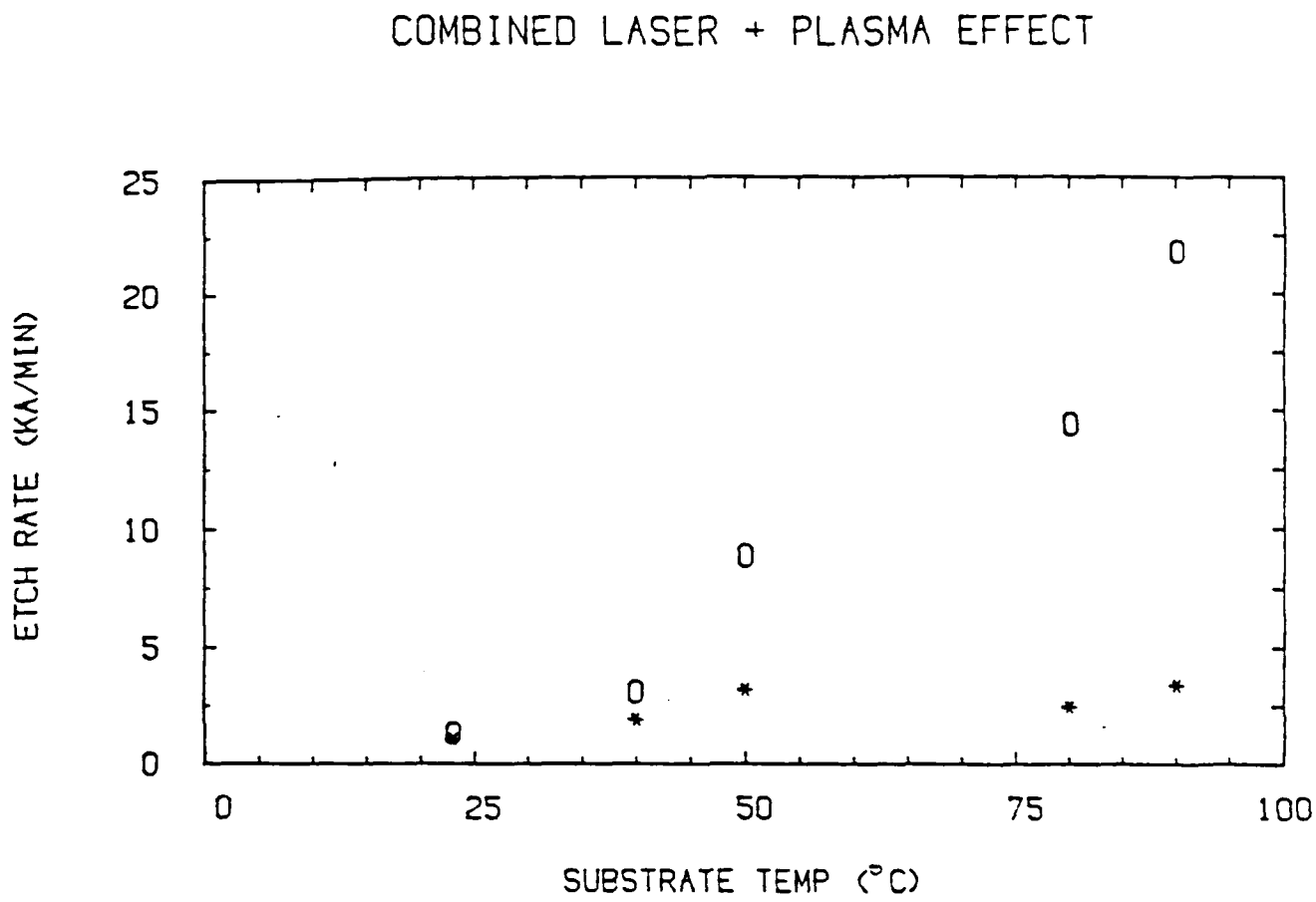
COMBINED LASER + PLASMA EFFECT
ETCH RATE (KA/MIN)
25
20
15
10
5
0
0
25
50
75
100
SUBSTRATE TEMP (°C)

Figure 4

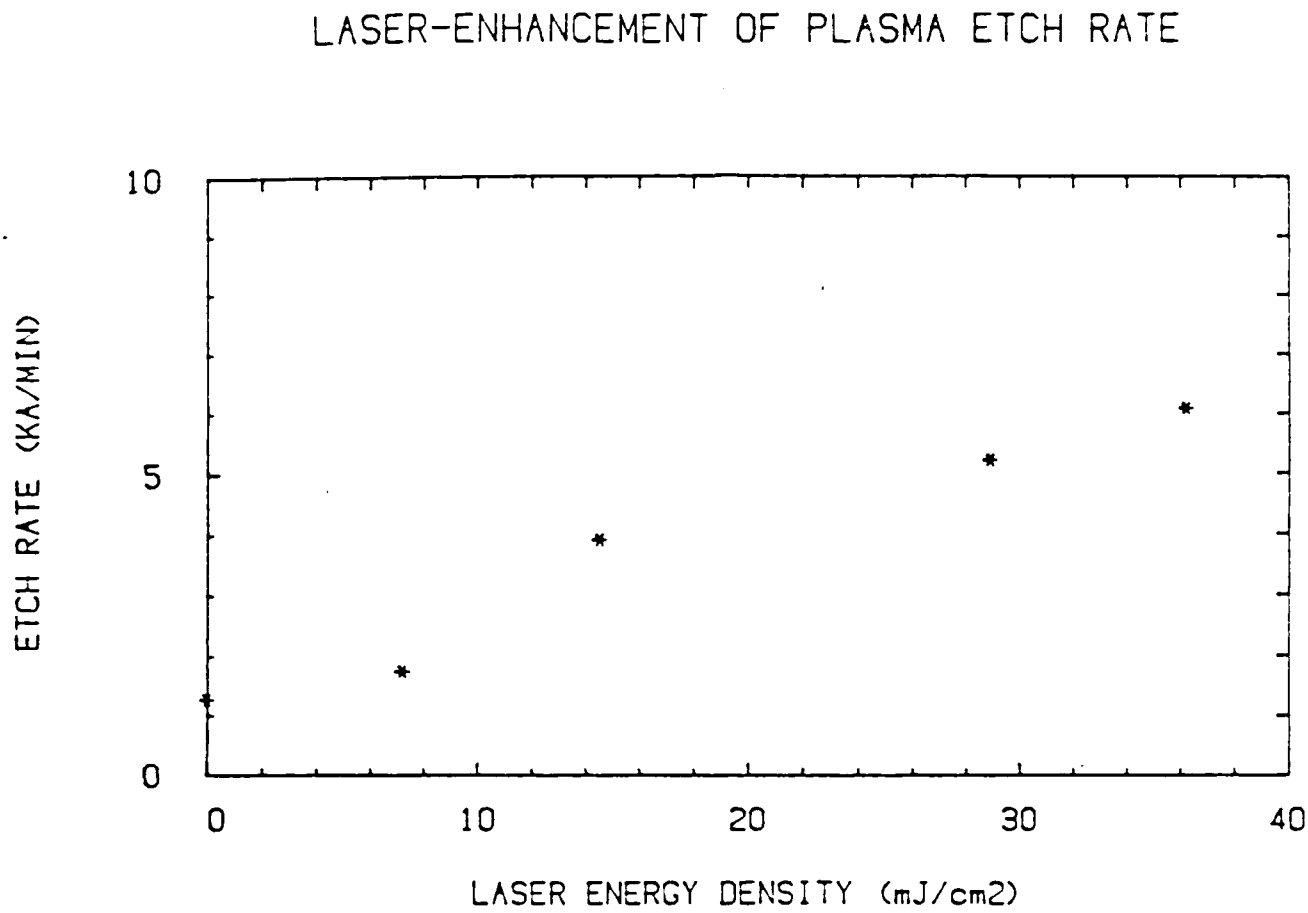
LASER-ENHANCEMENT OF PLASMA ETCH RATE
ETCH RATE (KA/MIN)
10
5
0
0
10
20
30
40
LASER ENERGY DENSITY (mJ/cm2)

Figure 5

enhancement of the plasma etching rate for GaAs (100) at fixed plasma conditions (at 50°C) as a function of laser power density is shown in Fig. 5. The etching rate appears to exhibit a linear dependence which is indicative of the fact that the UV laser driven photo-production of Br atoms dominates the etching process, and enhances the plasma etch rate by greater than a factor of 5. In addition to having effects on the etching process, we have also observed the laser effect of a lowering of the plasma breakdown voltage due to the laser irradiation into the plasma region. Fig. 6 shows the laser (power) effect on the maximum delay time for the plasma breakdown to occur after laser irradiation as a function of the applied voltage to the plasma reactor.

One (undesirable) aspect of isolating and invoking Br atom etching reactions in the dry etching of GaAs is that selective crystallographic etching is known to occur.[5,10] The cause of this highly anistropic etching is the chemical reactivity of gas-phase Br atoms with specific crystal planes of the GaAs substrate. By using crystallographic masking techniques, the availability of certain crystal planes is limited. Ir this study, masking of the GaAs (100) samples was performed normal to the (110) cleavage planes using straight line grid-patterns approximately 25 microns wide. As anticipated, for the 90° masking orientation, crystal facets are seen to develop at 45° to the original (100) direction in the case of just laser etching (as shown in Fig. 7a). These facets are identified as the (111) planes which are schematically shown in Fig. 8 to indicate the available crystal planes due to the masking orientation. In contrast, plasma processing as well as the combined laser plus plasma etching does show different etching featuers and profiles relative to crystallographic effects (see Figs. 7b and 7c, respectively). Furthermore, by continued etching of this mask orientation, the (111) planes self terminate to form v-groove microstructures for just laser etching as shown in Fig. 9a. As desired, the case for laser plus plasma etching (see Fig. 9b) does show modified etching features compared to crystallographic etching, demonstrating the combined effect of ion bombardment and laser enhanced chemistry in a plasma etcher.

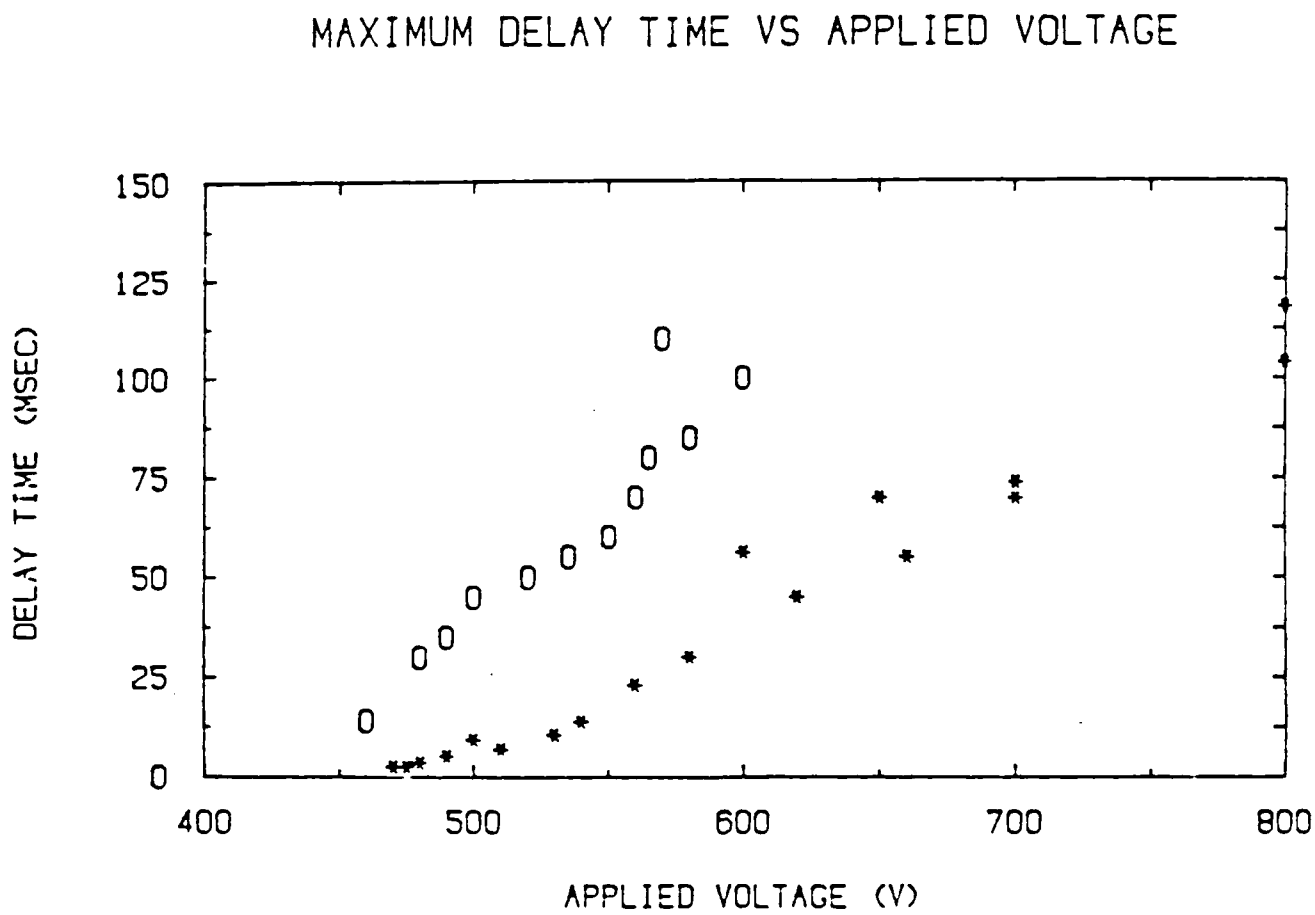
MAXIMUM DELAY TIME VS APPLIED VOLTAGE
DELAY TIME (MSEC)
150
125
100
75
50
25
0
400
500
600
700
800
APPLIED VOLTAGE (V)

Figure 6

INCIPIENT ETCH PROFILES

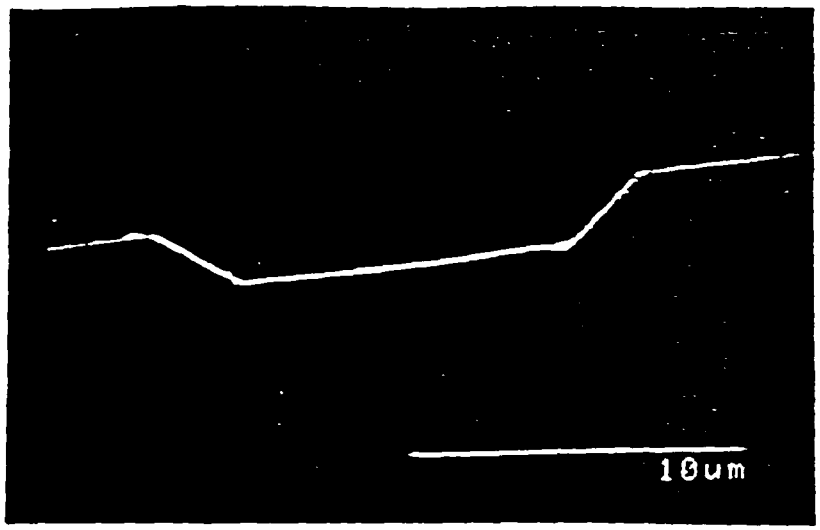

LASER ALONE

A

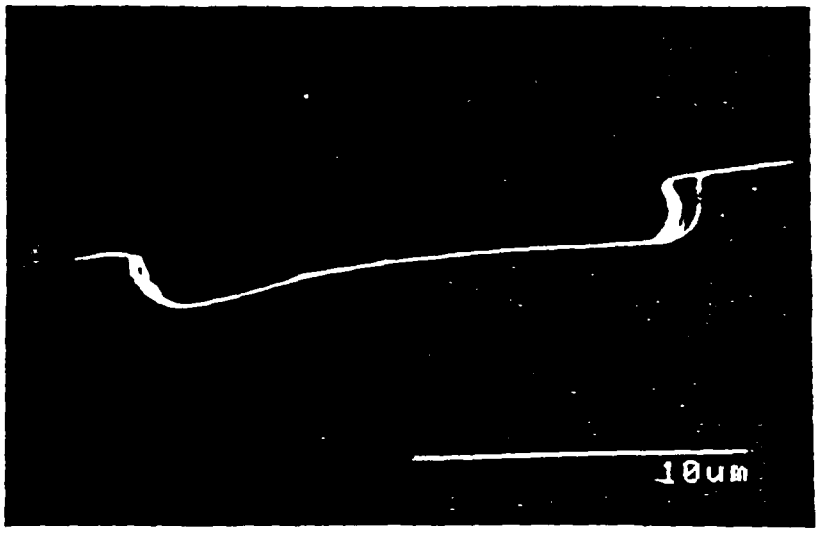

PLASMA ALONE

B

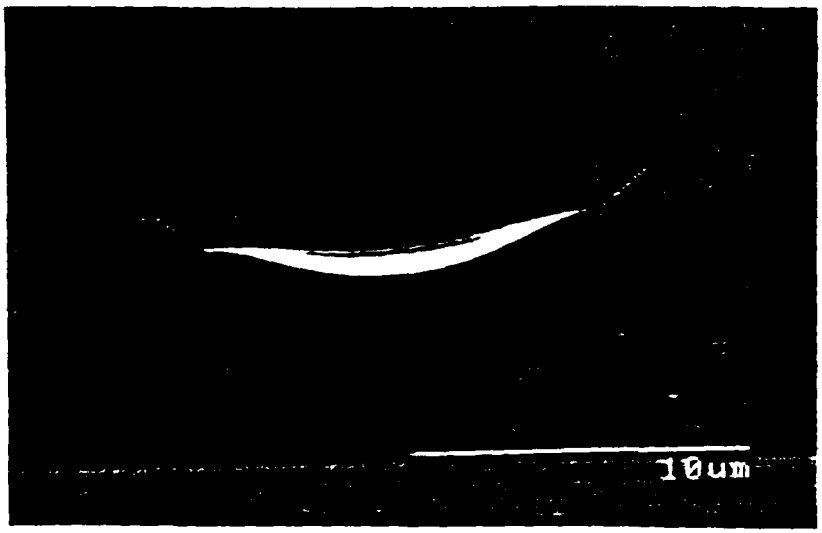

LASER PLUS PLASMA

C

Figure 7 (a), (b), (c)

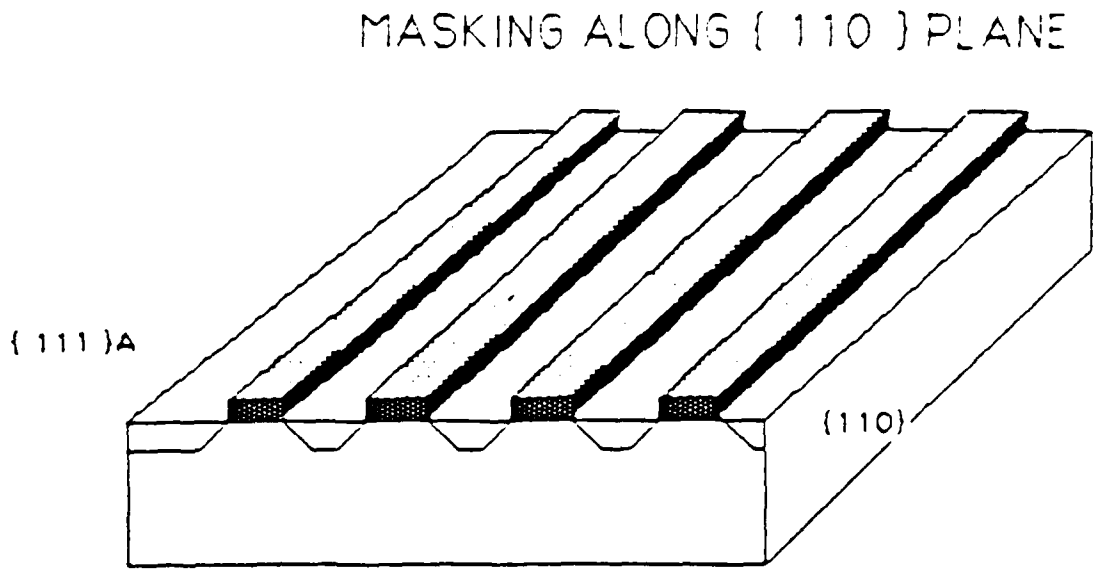
MASKING ALONG { 110 } PLANE
{ 111 }A
{110}

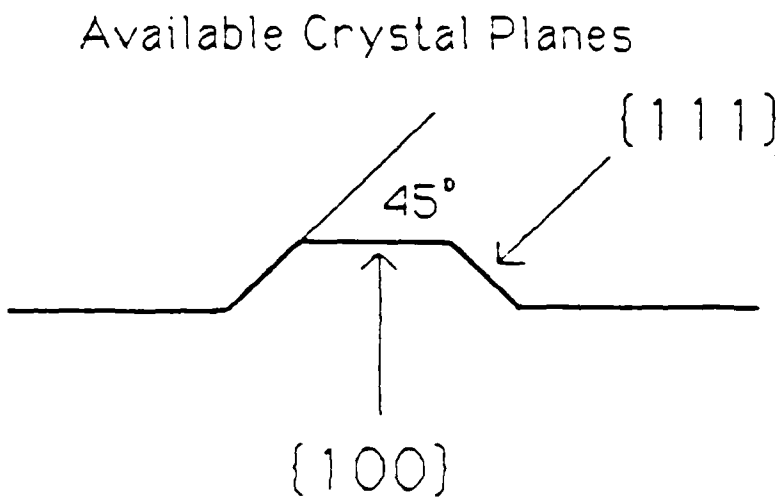
Available Crystal Planes
{111}
45°
{100}

Figure 8

FULLY DEVELOPED PROFILES

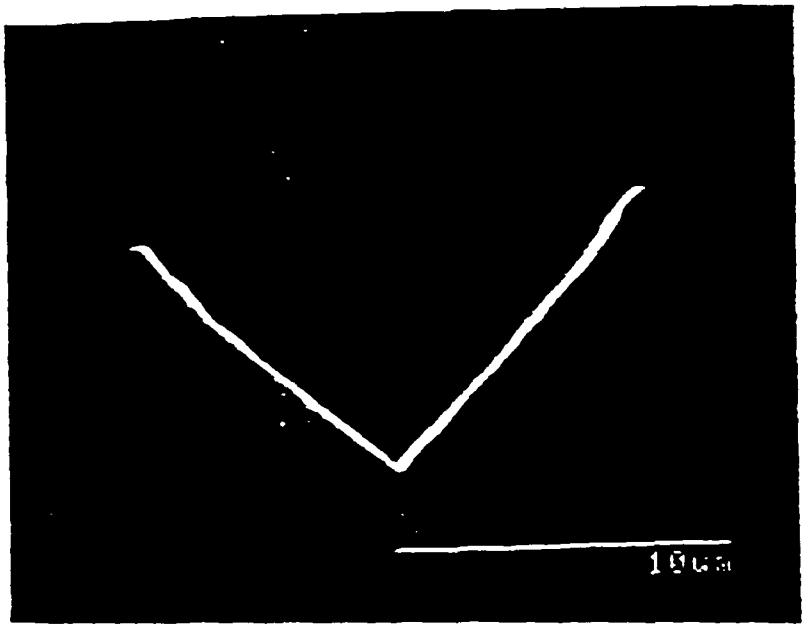

LASER ALONE

A

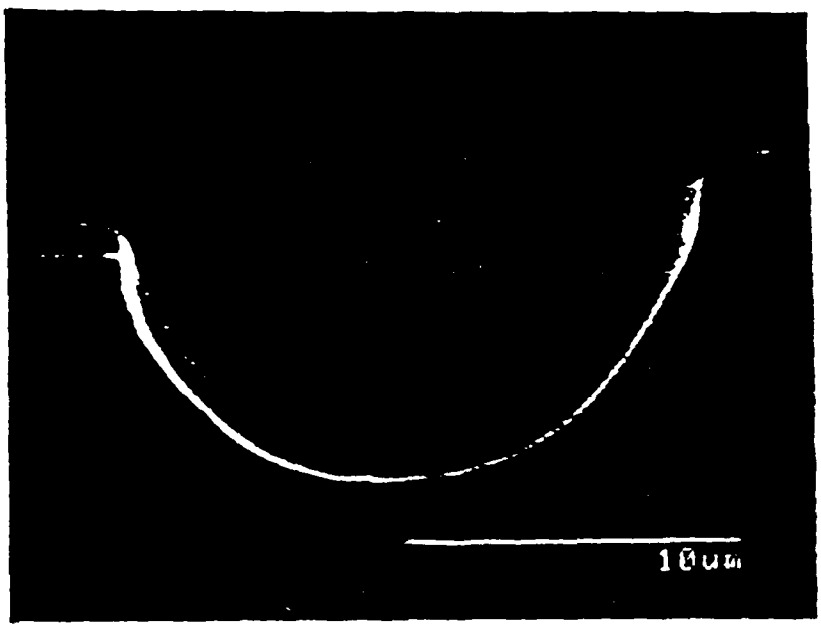

LASER PLUS PLASMA

B

Figure 9 (a) and (b)

This research was also supported by the National Science Foundation under Grant CHE-80-23747 and the Department of Energy under contract DE-AC-02-78ER04940.

(1) N. Tsukada, S. Semura, H. Saito, S. Sugata, K. Asakawa, Y. Mita, J. Appl. Phys. 55, 3417 (1984).

(2) W. Holber, G. Reksten, R.M. Osgood, Jr., Appl. Phys. Lett., 46, 201 (1985).

(3) G. Reksten, W. Holber, R.M. Osgood, Jr., Laser Chemical Processing of Semiconductor Devices Mat. Res. Soc. Ext. Abs., F. Howle, T. Deutsch, R.M. Osgood, Jr., eds., (1984) p. 115.

(4) W. Holber, G. Reksten, R.M. Osgood, Jr., Appl. Phys. Lett., to be published.

(5) S. Ghandi, VLSI Fabrication Principles, New York, John Wiley and Sons, 1983.

(6) D. Ehrlich, R.M. Osgood, Jr. and T. Deutsch, Appl. Phys. Lett. 36, 698 (1980).

(7) T. Deutsch in Laser Diagnostics and Photochemical Processing for Semiconductor Devices, R.M. Osgood,Jr., S.R.J. Brueck and D.H. Schlossberg, eds., New York, North-Holland, 1985, p. 225.

(8) P. Brewer, S. Halle and R.M. Osgood, Jr., Appl. Phys. Lett. 45, 475 (1984).

(9) H. Okabe, Photochemistry of Small Molecules New York, Wiley Interscience, 1980.

(10) D. Ibbotson, D. Flamm and V. Downelly, J. Appl. Phys. 54 (10), 5974 (1983).

B. TRANSLATIONAL ENERGY CHARACTERISTICS OF RADICALS AND IONS IN A CAPILLARITRON SUPERSONIC NOZZLE DISCHARGE

(T.H. Allik, B.B. Brady, G.W. Flynn, G.B. Spector)
(JSEP work unit 5, 1985 - 1988)
(Principal Investigator: G.W. Flynn (212)280-4162)

1. Introduction -- The formation and chemistry of ions and radicals are important in varied applications. For example, in the field of microelectronics, ions and radicals of many species play a role in the etching and implantation of semiconductor surfaces. Ions and radicals, which often have poorly characterized spectra are also important in many gas phase reactions. Since both ions and radicals are usually created with large amounts of excess energy, many different quantum states may be populated. This large variety of states gives rise to congested spectra and also allows for a myriad of competing channels in the reactions of these substances. If ions and radicals could be created in just a few of their lowest energy states, it would simplify the spectroscopy significantly, allow for the preparation of specific states and make possible the subsequent study of state-to-state reaction rates.

A supersonic beam or jet is one device which can be used to simplify the spectra of complex species such as ions and radicals. As an excitation source, many investigators[1-4] have used a laser to create radicals in or near the throat of a nozzle allowing them to cool in the expansion; others[5] have used an electron gun further downstream to create ions from a cold neutral beam. In both cases the internal energies of these species are subsequently studied using laser-induced-fluorescence (LIF).[6,7] An alternative method of creating cold metastable species is by a discharge. Recently, electronic emission from rotationally cold OH radicals created in a corona discharge has been observed.[8] Since the rotation-to-translation energy transfer rates are fast in most species,[9] hot fragments formed in discharges at the nozzle throat can cool to the temperature of the buffer gas.

One possible means of producing cold ions in a beam is via charge transfer collisions. Since charge transfer cross sections are relatively large ($10-10^2 Å^2$)[10] and the pressure is appreciable along the beam axis (10^{-6} torr), efficient charge transfer reactions can occur. Parent and daughter ions born early in the supersonic expansion have the potential to be vibrationally and rotationally hot. As these ions flow from the nozzle throat, they can suffer charge transfer collisions. Symmetric resonant charge transfer of the type

$$A^+(\text{hot}) + A(\text{cold}) \longrightarrow A(\text{hot}) + A^+(\text{cold})$$

will cool the ion distribution provided the concentration of A(cold) >> A^+(hot). Asymmetric charge transfer of the type:

$$A^+(\text{hot}) + B(\text{cold}) \longrightarrow A(\text{hot}) + B^+(\text{cold})$$

will produce a nascent distribution of B^+. In the present work we have used a capillaritron-discharge-source[11-14] supersonic nozzle molecular beam apparatus to characterize the energy distributions of the ion and radical species in a beam. Radicals have been conveniently produced with this device and their velocity distribution is characterized by a very low temperature. We also find evidence for charge transfer processes which produce relatively low energy cold ion distributions.

A mixture of CH_4 and CO_2 was used to produce OH radical whose translational energy was determined by conventional time-of-flight techniques. The radicals were detected with an electron bombardment ionizer-quadrupole mass spectrometer assembly. The translational energy distribution of the OH radical was characterized by a temperature(T_s) of 7K. Ions were also created in the discharge with Ar or CF_4, but the translational energy distribution was characterized by a temperature greater than 10^4 K. Ion energies were measured electrostatically.

2. Conclusions -- (1) A molecular beam source, the capillaritron, has been employed to create translationally cold radical species; (2) With ion currents of up to 3 milliamps the neutral parent molecules in the capillaritron show nearly the same velocity distribution as in an unperturbed molecular beam source; (3) Ion beams can be generated in the capillaritron with an average translational energy of approximately 25 eV and a 2-5 eV

energy width.

This work is described more fully in The Journal of Physical Chemistry 88, 3204 (1984)

This research was also supported by the National Science Foundation under Grant CHE-80-23747 and the Department of Energy under contract DE-AC-02-78ER04940.

(1) T. A. Miller, B. R. Zegarski, T. J. Sears, and V. E. Bondybey, J. Phys. Chem. 84, 3154 (1980).

(2) A. Carrington and R. Tuckett, Chem. Phys. Letts. 74, 19 (1980).

(3) B. M. de Koven, D. H. Levy, H. H. Harris, B. R. Zegarski, and T. A. Miller, J. Chem. Phys. 74, 5659 (1981).

(4) D. L. Monts, T. G. Dietz, M. A. Duncan, and R. E. Smalley, Chem. Phys. 45, 133 (1980).

(5) M. I. Lester, B. R. Zegarski, and T. A. Miller, J. Phys. Chem. 87, 5228 (1983).

(6) M. Heaven, L. DiMauro, and T. A. Miller, Chem Phys. Letts. 95, 347 (1983).

(7) D. E. Powers, J. B. Hopkins, and R. E. Smalley, J. Phys. Chem. 85, 2711 (1981).

(8) A. T. Droege and P. C. Engelking, Chem. Phys. Letts. 96, 316 (1983).

(9) W. H. Flygare, Acc. Chem. Res. 1, 121 (1968).

(10) W. D. Davis and T. A. Vanderslice, Phys. Rev. 131, 219 (1963)

(11) J. F. Mahoney, J. Perel, and A. T. Forrester, Appl. Phys. Letts. 38, 320 (1981).

(12) J. Perel, J. F. Mahoney, B. E. Kalensher, and A. T. Forrester, "Investigation of the Capillaritron Ion Source For Electric Propulsion," AIAAA-81-0747, AIAA 15th International Electric Propulsion Conference, Las Vegas, NV (21-23 April 1981).

(13) J. Perel and F. Mahoney, "Analysis of the Operation of the FACS," ASMS, 30th Annual Conference, Honolulu, HW (6-11 June 1982).

(14) D. M. Goebel, J. Perel, J. F. Mahoney, and A. T. Forrester, J. Appl. Phys. 53, 2904 (1982).

C. DIODE LASER PROBING OF VIBRATIONAL PRODUCT STATE DISTRIBUTIONS IN METAL-MOLECULE COLLISIONS: $HG(6^3P_1)-CO_2(mn^{\ell}p)$

(B.B. Brady, G. B. Spector, L. Chia and G.W. Flynn)
(JSEP work unit 5, 1985 - 1988)
(Principal Investigator: G.W. Flynn (212)280-4162)

1. Introduction — The quenching of the electronically excited states of mercury atoms has been the subject of many studies.[1-12] A large number of atoms, diatomic and small polyatomic molecules have been used to quench the excited singlet, $Hg(6^1P_1)$, triplet, $Hg(6^3P_1)$, and metastable, $Hg(6^3P_0)$, states of mercury. The rate of depletion of Hg states was detected by either flashlamp absorption or laser-induced fluorescence(LIF), and the quenching cross section to the ground state or lower excited states was determined. In only a few cases, involving diatomic quenchers, have investigators looked at the states populated in the collider gas by the quenching process.[1,2,3,7] Polyatomic molecules, which have more than one vibrational degree of freedom, each with a different frequency, can yield more information about the quenching process and provide a better test of the theories which have been used to describe this phenomenon.[13,14] In order to take advantage of this increased information, however, a technique for probing various modes of a polyatomic quencher must be available. Such a technique has been recently developed[15,16] and used to study high energy collision events and photofragmentation processes.

The interaction of metals with molecules is also interesting because of its importance in catalysis. Small clusters of metal atoms have been investigated because they may be useful as models for catalysis at surfaces.[17,18] The properties of small metal clusters, however, vary greatly and in a seemingly random manner with size.[19-21] The interaction of individual metal atoms with molecules is thus important and the investigation of such interactions is a logical first step toward understanding the catalytic activity of small metal clusters.

In this paper we have studied the internal excitation of CO_2 caused by

collisions with $Hg(6^3P_1)$. CO_2 was chosen because transitions involving a one-quantum change in its ν_3 mode have almost the largest absorption coefficient in the infrared(IR) spectral region. This fact, combined with the large number of such transitions (including hot bands) whose frequencies have been determined to a high degree of accuracy, makes CO_2 a particularly convenient quenching molecule to study using IR absorption techniques.[15]

Past experiments have shown that the rate of quenching of $Hg(6^3P_1)$ by CO_2 is extremely fast, taking place in approximately 4 gas kinetic collisions.[5,10-12]

$$Hg(6^3P_1) + CO_2 \longrightarrow Hg(6^1S_0) + CO_2 \qquad (1)$$

$$Hg(6^3P_1) + CO_2 \longrightarrow Hg(6^3P_0) + CO_2 \qquad (2)$$

In addition, most of the quenching is to the ground state with channel 2 above contributing less than 0.1% to the total quenching cross section.[4,11] Fig. 1 shows an energy level diagram for the Hg/CO_2 system. One other channel which has been studied and found to proceed with a quantum yield of less than 1% is the decomposition of CO_2 to CO.[6]

$$Hg(6^3P_1) + CO_2 \longrightarrow HgO + CO \qquad (3)$$

This reaction has been found to have a CO quantum yield which increases as the square of the light intensity, and the mechanism has been postulated to involve a metastable CO_2 (perhaps a low-lying triplet state produced by process 1) undergoing collision with a second excited mercury atom.

$$Hg(6^3P_1) + CO_2 \longrightarrow HgO + CO \qquad (4)$$

An important innovation which makes possible the probing of polyatomic molecule internal states produced by quenching collisions, is the development of the diode laser probe technique.[15,16] The diode, which is a cw laser device having excellent amplitude stability, can be tuned with high

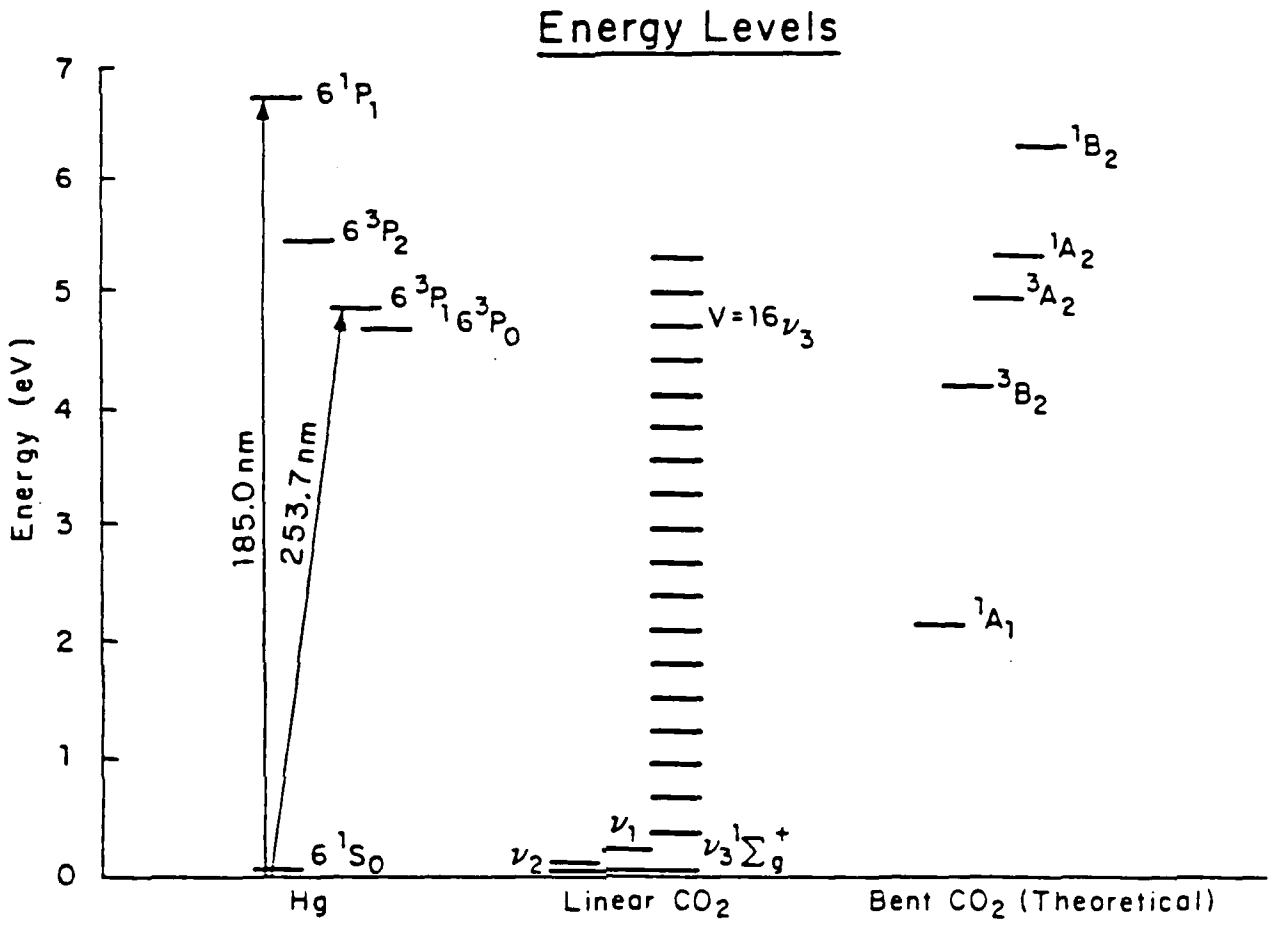
Energy Levels
Energy (eV)
7
6
5
4
3
2
1
0
$6\,^1P_1$
$6\,^3P_2$
$6\,^3P_1$ $6\,^3P_0$
$6\,^1S_0$
185.0 nm
253.7 nm
$V=16\nu_3$
ν_1
ν_2
$\nu_3\,^1\Sigma_g^+$
$^1B_2$
$^1A_2$
$^3A_2$
$^3B_2$
$^1A_1$
Hg
Linear CO_2
Bent CO_2 (Theoretical)

Figure 1

resolution (.001 cm^{-1}) throughout the IR spectral range. Because of the anharmonicities present in CO_2 (and in most other small molecules), this is sufficient resolution to separate individual vibration-rotation lines of the type

$$CO_2(mn^{\ell}p,J) + hc\bar{\nu} \longrightarrow CO_2(mn^{\ell}p+1,J+1) \qquad \text{(R branch)} \quad (5a)$$

$$CO_2(mn^{\ell}p,J') + hc\bar{\nu}' \longrightarrow CO_2(mn^{\ell}p+1,J'+1) \qquad \text{(R branch)} \quad (5b)$$

$$\bar{\nu} - \bar{\nu}' \gg .001 \ cm^{-1}$$

or to separate transitions with different m,n,ℓ, and p quantum numbers. In (5a,b) above, m, n, and p are the number of vibrational quanta, respectively, in the symmetric stretch mode ν_1, the bending mode ν_2, and the asymmetric stretching mode ν_3. The J quantum number describes the rotational level and ℓ is the vibrational angular momentum. Since such transitions "ride" the very strong ν_3 absorption coefficient and have essentially the same effective oscillator strength as the $00^00 \rightarrow 00^01$ transition, even the infrared inactive ν_1 symmetric stretch mode (10^00) and the bending ν_2 fundamental (01^10), whose emission at 15 μm is difficult to detect, can be easily observed and probed. Hence all three normal vibrational modes of CO_2 can be specifically studied and the excitation produced in each by collisions can be measured. Absolute values of population changes can also be determined by direct calibration of the absorptions using cold unexcited gas. The diode laser is relatively intense for an IR source (~1 mW) and has low divergence which allows long path lengths to be used thus providing excellent sensitivity. Finally, because the diode laser continuously monitors the transition of interest, the time response is limited only by the bandwidth of the IR detection system.

A final advantage of studying CO_2 is that the asymmetric stretching vibration is metastable with respect to the bending/symmetric stretching vibrations. Approximately 30,000 collisions are required to exchange energy

between these modes. Thus the asymmetric stretch and bending modes can be studied essentially independently and the importance of each in quenching can be assessed. The competition between these modes is particularly interesting since one is low frequency (667 cm^{-1}) and one is high frequency (2349 cm^{-1}). Theoretical calculations[13,14] indicate that low and high frequency modes should be affected very differently by quenching.

2. Experimental Section -- The present apparatus is shown in Fig. 2. A Lambda Physik EMG 101 excimer laser, operating at 308 nm, 20 Hz, was used to pump an FL2002 dye laser. The output of the C-500 dye at 508 nm(10-15 mJ) was passed through a KPB crystal (Cleveland Optical Crystals) to obtain the second harmonic(254 nm, <.1 mJ). The doubled output of the dye was then tuned to coincide with the Hg absorption line at 253.7 nm. The excitation beam was passed through the sample cell colinearly with the diode laser probe beam. In the sample cell CO_2 gas was mixed with Hg vapor. The diode laser light was detected after passing through the cell by a SBRC InSb IR detector and matched amplifier. The IR detector output was digitized with a Biomation transient recorder(8100) and averaged with a Nicolet 1170 signal averager. The overall response time of the detection system was 1.0 μsec. The Laser Analytics diode laser was tuned to one of several CO_2 ro-vibrational transitions near 2311 cm^{-1} and the transient absorption monitored. The cell pathlength was 43 cm. The CO_2 lines probed included

00^01 ----> 00^02 P(15), 2311.923 cm^{-1}

02^20 ----> 02^21 P(15), 2311.762 cm^{-1}

10^00 ----> 10^01 P(18), 2311.593 cm^{-1}

3. Results -- A typical trace depicting the change in population of the 00^01 level due to Hg quenching is shown in Fig.3. The rise, which cooresponds to an increase in population of 00^01, can be observed in the lower panel (b). Similar traces were also taken monitoring 02^20. The rate

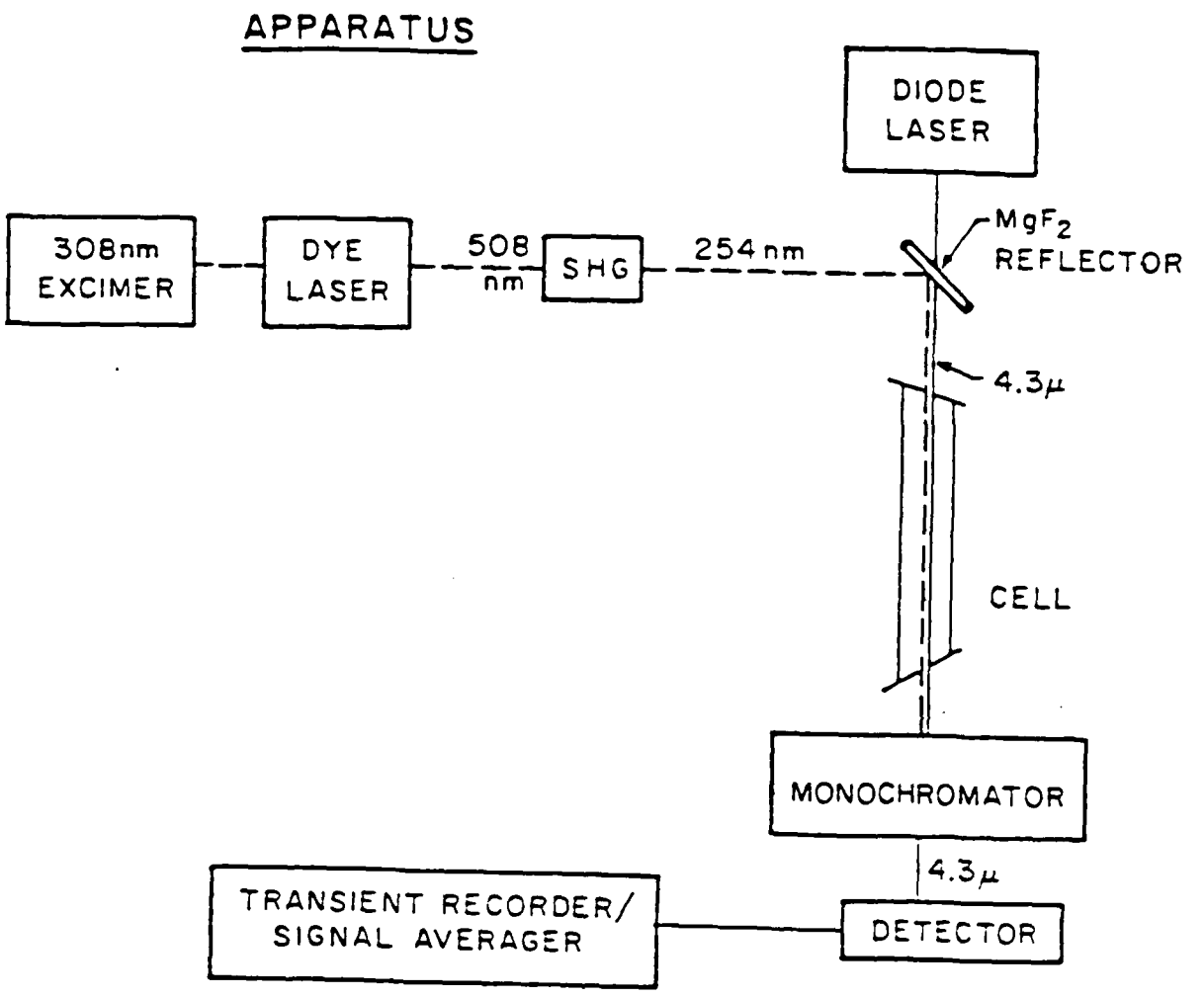
APPARATUS
DIODE LASER
308nm EXCIMER
DYE LASER
508 nm
SHG
254 nm
MgF_2 REFLECTOR
4.3μ
CELL
MONOCHROMATOR
4.3μ
TRANSIENT RECORDER/ SIGNAL AVERAGER
DETECTOR

Figure 2

of rise can be obtained from a non-linear least squares fit to an exponential function. The rates obtained at various CO_2 pressures for both ν_3 and $2\nu_2$ (Hg pressure remaining constant) are plotted in Fig. 4. A linear least-squares fit of the data points gives a slope which corresponds to a rate of 3.75×10^{12} cc/molec-sec or 120 $msec^{-1}$ $torr^{-1}$(80 gas kinetic collisions). Both the ν_3 and $2\nu_2$ rise time data fall on the same least squares line within experimental error.

By measuring the maximum amplitude of the absorption increase, a value for the number of vibrationally excited CO_2 molecules produced per excited Hg atom can be determined. The number of quanta in the ν_3 mode per laser shot was calculated from the intensity of the diode laser at the detector before the dye laser fires,(I(4.3 μm)) the change in diode laser intensity after the dye laser fires (ΔI(4.3 μm)), the volume of the diode laser irradiation zone, and the absorption coefficient for the CO_2 line probed.[15] The number of excited Hg atoms is measured from the difference in the intensity of the dye laser after it passes through the cell with and without mercury present, (ΔI(254nm)). The number of photons absorbed is equal to the number of excited Hg atoms (N_{Hg}).

4. Conclusions — (1) Although the quenching of $Hg(6^3P_1)$ by CO_2 takes place in 4 gas kinetic collisions, 80 collisions are required for the mercury electronic energy to show up in the low lying vibrational levels of CO_2. This suggests the existence of a metastable state of CO_2 which is produced by the quenching process; (2) Both the ν_2 bending mode and the ν_3 antisymmetric stretching mode of CO_2 are filled at the same 80 gas kinetic collision rate during the quenching process, suggesting that both modes are filled from a common origin; (3) For each electronically excited mercury atom quenched by a CO_2 molecule, 22 ± 6 quanta of bending excitation and 1.3 ± 0.3 quanta of antisymmetric stretch excitation are produced in CO_2, suggesting that statistical considerations based on the density of vibrational states play at least some role in the partitioning of energy among the vibrational modes; (4) The conversion of mercury electronic energy into CO_2 vibrational energy is unexpectedly efficient. If radiative loss due to spontaneous emission from Hg is properly accounted for, in excess of 80% of the mercury

$$Hg^* + CO_2(00°0) \longrightarrow CO_2(00°1) + Hg$$

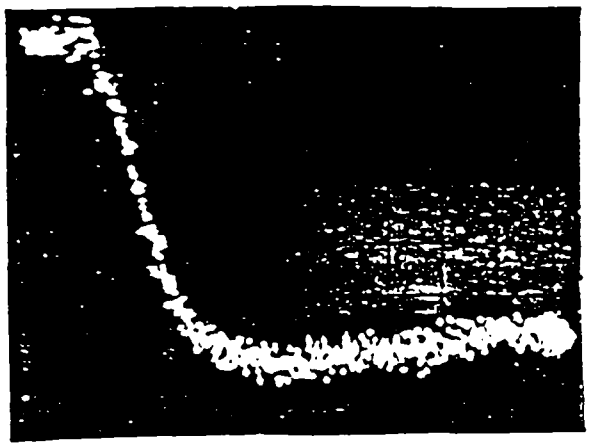

$00°1 \longrightarrow 00°2$ P(15)

P_{CO_2} = 1.0 torr

Time base = 51.2 μs

1024 shots

Laser Fires

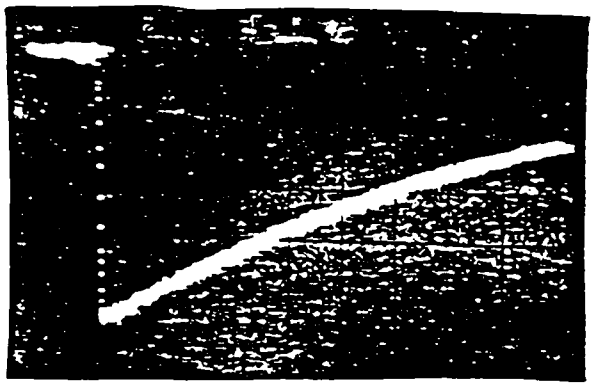

$00°1 \longrightarrow 00°2$ P(15)

P_{CO_2} = 9.86 torr

Time base = 409.6 μs

1024 shots

Figure 3

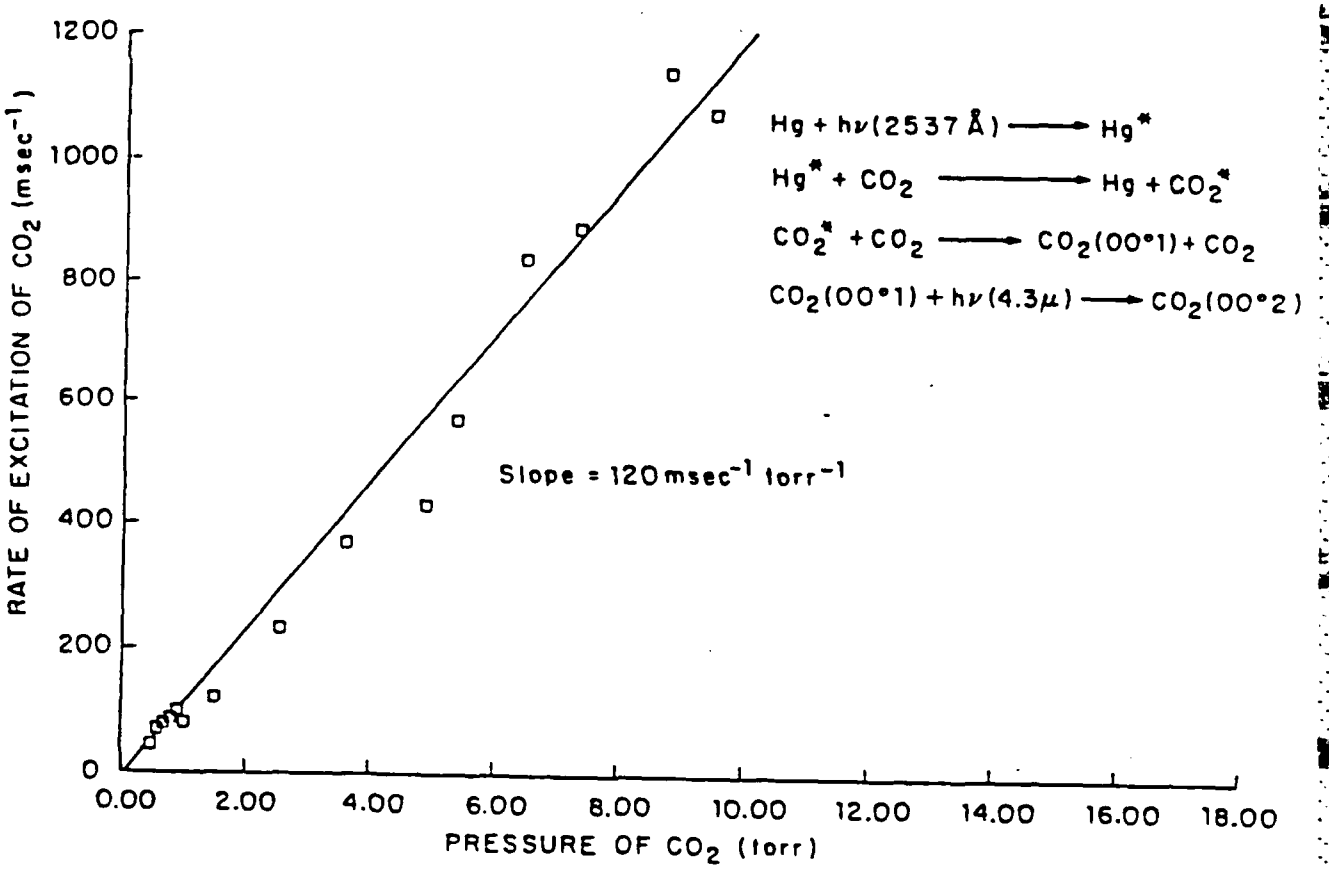
1200
1000
800
600
400
200
0
RATE OF EXCITATION OF CO_2 ($msec^{-1}$)
0.00
2.00
4.00
6.00
8.00
10.00
12.00
14.00
16.00
18.00
PRESSURE OF CO_2 (torr)
$Hg + h\nu(2537\,Å) \longrightarrow Hg^*$
$Hg^* + CO_2 \longrightarrow Hg + CO_2^*$
$CO_2^* + CO_2 \longrightarrow CO_2(00^01) + CO_2$
$CO_2(00^01) + h\nu(4.3\mu) \longrightarrow CO_2(00^02)$
Slope = 120 $msec^{-1}$ $torr^{-1}$

Figure 4

electronic energy is converted to CO_2 vibrational energy; (5) Using energy conservation arguments, the CO_2 metastable state produced by Hg quenching has an energy of 32,000 $\pm$ 8000 cm^{-1}; (6) Based on the above observations, the metastable state of CO_2 produced in the Hg quenching process is tentatively identified as a CO_2 triplet. Production of triplet CO_2 allows spin to be conserved during the quenching of Hg. This postulate also agrees well with earlier photochemical data in which triplet CO_2 has been suggested as an intermediate in the two photon production of CO from Hg, CO_2, and light. Definitive confirmation of the nature of the metastable CO_2 level awaits spectroscopic detection of this interesting species.

This research was also supported by the National Science Foundation under Grant CHE-80-23747 and the Department of Energy under contract DE-AC-02-78ER04940.

(1) G. Karl, P. Kruus and J. Polanyi, J. Chem. Phys. 46,224, (1967).

(2) G. Karl, P. Kruus, J. Polanyi and W. Smith, J. Chem. Phys. 46, 244, (1967).

(3) Y. Fushiki and S. Tsuchiya, Chem. Phys. Lett. 22, 47, (1973).

(4) H. Horiguchi and S. Tsuchiya, Bull. Chem. Soc. Japan 44, 3221, (1971).

(5) A. Vikis, G. Torrie and D. LeRoy, Can. J. Chem. 50, 176, (1972).

(6) O. Strausz and H. Gunning, Can. J. Chem. 39, 2244, (1961).

(7) G. Karl and J. Polanyi, J. Chem Phys. 38, 271, (1963).

(8) H. Okabe, Photochemistry of Small Molecules, New York, J. Wiley and Sons, 1978.

(9) J. Calvert and J. Pitts, Jr., Photochemistry, New York, J. Wiley and Sons, 1966.

(10) R. Cvetanovic, Prog. React. Kinet., 2, 39, (1964).

(11) A. Callear and J. McGurk, J. Chem Soc. Faraday Trans 2, 69, 97, (1973).

(12) J. Deech, J. Pitre and L. Krause, Can. J. Phys., 49, 1976, (1971).

(13) R. Levine and R. Bernstein, Chem. Phys. Lett., 15, 1, (1972).

(14) M. Gonzalez, G. Karl and P. Watson, J. Chem. Phys. 57, 4054, (1972).

(15) J. Chu, C. Wood and G. Flynn, J. Chem. Phys., 81, 5533, (1984).

(16) J. Chu, C. Wood, G. Flynn and R. Weston, Jr., J. Chem. Phys., 80, 1703, (1984).

(17) L.S. Brown and S.L. Bernasek, J. Chem. Phys. 82, 2110, (1985).

(18) S.L. Bernasek and S.R. Leone, Chem. Phys. Lett., 84, 401, (1981).

(19) R.E. Smalley, Laser Chemistry, 2, 167 (1983).

(20) A. Kaldor, E. Rohlfing, and D.M. Cox, Laser Chemistry, 2, 185, (1983).

(21) E. Parks, K. Liu, S. Richtsmeier, L. Pobo and S. Riley, J. Chem. Phys. 82, 5470, (1985).

D. DYNAMICS OF HIGH ENERGY COLLISION PROCESSES

(J.A. O'Neill, Ji Ye Cai, and G.W. Flynn)
(JSEP work unit 5, 1985 - 1988)
(Principal Investigator: G.W. Flynn (212)280-4162)

1. Introduction — Studies of the transfer of energy between translational and internal degrees of freedom yield detailed information about the mechanism of vibrational excitation processes involving small molecules. Such information is of importance in the characterization and control of chemically energetic systems as well as in the development of improved models of collisional energy transfer.

Recent investigations of translational to vibrational/rotational (T-V/R) energy transfer involve the vibrational excitation of small molecules upon collisions with translationally "hot" hydrogen atoms produced in the excimer laser photolysis of various hydrogen containing species.[1-6] Through dissociation of the proper diatomic or triatomic hydride, both mass and energy dependent information can be obtained about these collisional processes. Recently, a new technique has been developed in our laboratory which investigates T-V energy exchange using a tunable infrared diode laser absorption probe.[7,8] The narrow bandwidth (0.001 cm^{-1}) of the diode laser easily allows for the resolution of individual ro-vibrational levels within the molecule. Also, through the proper choice of infrared transition, any vibrational state can be studied. The applicability of this method to all vibrational levels of CO_2 is achieved by taking advantage of the strong ν_3 absorption coefficient and realizing that the population in any ro-vibrational state can be studied by tuning the laser to a transition of the type:

$$CO_2(mn^{\ell}p,J) + h\nu(4.3\mu m) \longrightarrow CO_2(mn^{\ell}p+1,J \pm 1). \qquad (1)$$

Here, the letters m, n and p designate the number of ν_1 (symmetric stretching) vibration, ν_2 (bending) vibration and ν_3 (antisymmetric

stretching) vibration, and J denotes the number of rotational quanta. Moreover, absolute population changes in each state can be determined by calibrating the observed absorption changes using the ambient population of excited states in room temperature CO_2 as a standard.

The process investigated in the present study involves the vibrational excitation of CO_2 by fast deuterium atoms produced upon photolysis of D_2S at 193 nm. This process can be represented by the following mechanism:

$$D_2S + h\nu\ (193\ \text{nm}) \longrightarrow D^*\ (E_{CM} = 2.16\ \text{eV}) + DS \qquad (2)$$

$$D^* + CO_2(00^00) \longrightarrow D + CO_2(mn^{\ell}p) \qquad (3)$$

Generally, in the presence of a large excess of ground state CO_2 molecules, as is the case in our experiments, highly vibrationally excited states of CO_2 rapidly decompose to the fundamental vibrational levels by a succession of vibration-to-vibration equilibration processes of the type:[10]

$$CO_2(mn^{\ell}p) + (m+n+p-1)CO_2(00^00) \longrightarrow mCO_2(10^00) + nCO_2(01^10) + pCO_2(00^01) \qquad (4)$$

As a result of these collisional processes, the steady state population distribution in the ν_2 bend and the ν_3 asymmetric stretch can be determined in CO_2 by probing the $01^10 \longrightarrow 01^11$ and the $00^01 \longrightarrow 00^02$ transitions respectively. The motivation for the present work stems from an attempt to determine the mass dependence of impulsive collisions in T $\longrightarrow$ V/R energy exchange mechanisms through comparison with previous studies involving H_2S/CO_2 mixtures. The details of these studies have been described in a forthcoming paper,[9] and only the important results will be summarized here.

2. Results

(a) Determination of vibrational Population changes -- Excimer laser photolysis of D_2S in mixtures with CO_2 yields dynamic absorption

signals for the 01^10 --> 01^11 P(29) and 00^01 --> 00^02 P(15) transitions. Typical signals for these transitions are indicated in Fig. 1.

Absorption signals for the 00^01 ---> 00^02 P(15) transition were obtained for pressures ranging from 0.1 torr to 2.0 torr for several mole fractions of D_2S/CO_2. Typically, these signals exhibit an initial fast change in absorption which is limited by the response time of the detector (1.5 μsec) at pressures as low as 0.1 torr. Low pressure studies were performed with D_2S/CO_2 mixtures which demonstrate that this preliminary rise in the observed signal is not due to direct excitation of the 00^01 level itself, but rather is due to the rapid filling of 00^01 through such resonant collisional processes as:

$$CO_2(01^11) + CO_2(00^00) \longrightarrow CO_2(01^10) + CO_2(00^01) \qquad (5).$$

The 00^01 signals also exhibit a second slow absorption change which rises at a rate of approximately 200 $msec^{-1}$ $torr^{-1}$. Van Veen and co-workers have shown that upon photodissociation of H_2S at 193 nm, approximately 10% of the HS fragments are produced with vibrational excitation in levels greater than v=0.[10] Assuming that roughly the same behavior holds upon dissociation of D_2S at this wavelength, the slowly rising component of the signal can be tentatively assigned to the V-V energy transfer between DS and CO_2.

At 0.5 torr for a mixture of $1D_2S/4CO_2$, collisions of fast D^* atoms with CO_2 produce $(6.0\pm1.5) \times 10^{-2}$ CO_2 molecules with one quantum of ν_3 excitation for each D^* initially produced. Under typical conditions with a UV laser energy of 5 mJ, a cell pathlength of 43 cm, and a pressure of 0.5 torr, this corresponds to approximately a sixty-fold increase in ν_3 population over ambient room temperature conditions. Under the same conditions, a mixture of $1H_2S/4CO_2$ yields $(11.6\pm2.9) \times 10^{-2}$ $CO_2(\nu_3)$ for each H^* initially produced.

Transient absorption signals were obtained while monitoring the 01^10 ---> 01^11 P(29) transition of CO_2 upon collisional excitation by translationally hot D^* atoms. A cell pathlength of 6 cm was selected to prevent attenuation of the diode laser beam by the significant ambient CO_2 population in 01^10 at room temperature ($N_{01^10} = 0.081\ N_{00^00}$) prior to the UV

T-V Excitation of CO_2 by D^*

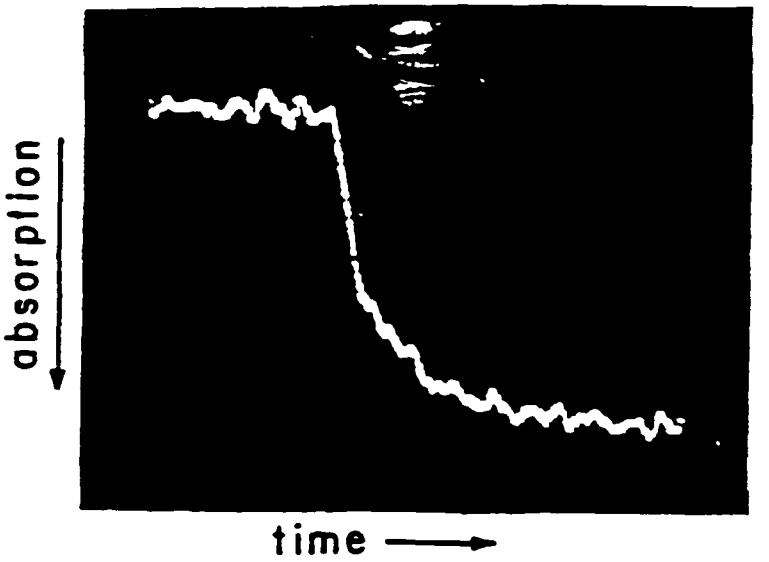

$00^01 \longrightarrow 00^02$ P(15)
P_{TOTAL} = 1.0 torr
Number of Shots = 5
40 μsec full scale
L = 43 cm
(D_2S/CO_2 = 1/4)
(λ = 193 nm)

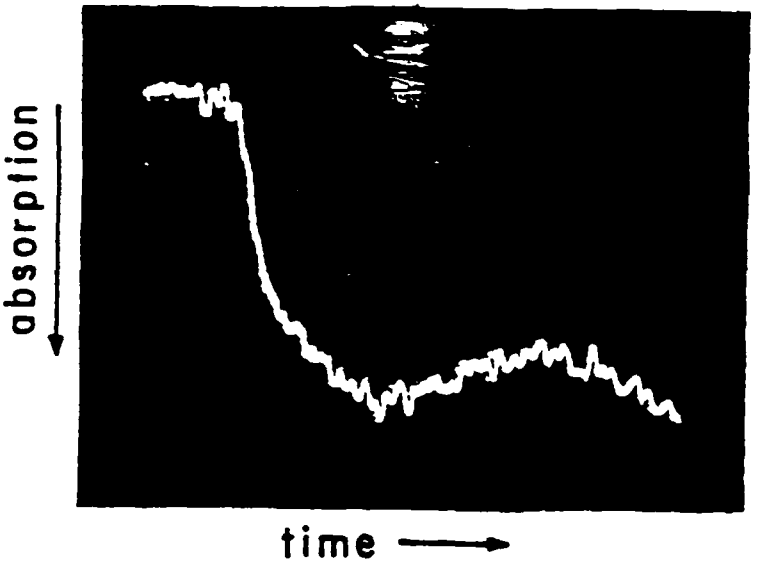

$01^10 \longrightarrow 01^11$ P(29)
P_{TOTAL} = 0.5 torr
Number of Shots = 100
40 μsec full scale
L = 6 cm

Figure 1

photolysis pulse.[8] These signals demonstrate an initial prompt change in absorption with a rate that is detector limited, and a second rise which is somewhat slower (see Fig. 1). The preliminary fast rise is due to the direct production of CO_2 states containing one quantum of ν_2 excitation such as 01^10 and 01^11. For a mixture of $1D_2S/4CO_2$ with a typical excimer energy of 5 mJ/pulse at 0.5 torr, this initial component of the signal corresponds to the formation of $(4.8\pm1.2) \times 10^{-1}$ CO_2 molecules with one quantum of ν_2 excitation for each D^* initially produced. This represents approximately a 9.8% increase in ν_2 population over room temperature conditions. Under the same experimental conditions, a mixture of $1H_2S/4CO_2$ at 0.5 torr was observed to give $(8.3\pm9.5) \times 10^{-1}$ for each H^* atom formed. The ratios of ν_2 quanta to ν_3 quanta produced by hot atom/CO_2 collisions are D_2S/CO_2:$N(\nu_2)/N(\nu_3) = 8$; H_2S/CO_2:$N(\nu_2)/N(\nu_3) = 3.5$.

(b) Analysis of cooling rate of D atoms — In order to describe the collisional deactivation of translationally energetic D^* produced in the excimer laser photolysis of D_2S, a simple kinetic model can be used.[8] After the initial production of D^* at 193 nm, the hot atom can be cooled through collisions producing vibrationally excited CO_2 molecules in T ⟶ V/R processes such as:

$$(k_i^{TV}): D^* + CO_2 \longrightarrow D + CO_2\ (\nu_i) \qquad (6)$$

or in such thermalization processes as:

$$(k_{1i}^{TH}): D^* + CO_2 \longrightarrow D + CO_2(mn^{\ell}p) \qquad (7)$$

$$(k_{2i}^{TH}): D^* + D_2S \longrightarrow D + D_2S \qquad (8)$$

where k_{1i}^{Th} and k_{2i}^{Th} are the rates of cooling of D^* below the threshold level necessary to produce excitation in vibrational mode i. Using a straightforward kinetic analysis,[8] the ratio of initially produced hot deuterium atoms $[D^*]_0$ to vibrationally excited CO_2 molecules $[CO_2]$ arising

from collisions is found to be

$$[D^*]_0/[CO_2(\nu_3)] = k_{13}^{Th}/k_3^{TV} + (k_{23}^{Th}/k_3^{Th})([D_2S]/[CO_2]) \qquad (9)$$

Fig. 2 illustrates the results of a study of the behavior of absorption intensity measurements of $[D^*]_0/[CO_2(\nu_3)]$ as a function of varying ratios of $[D_2S]/[CO_2]$. A least squares analysis of this data yields a slope of 47.3 ± 12.3 and an itercept of 4.9 ± 2.5. As suggested by equation (9) in the kinetic model presented above, these results imply that the rate of colling of D^* below the level required to produce vibrational excitation in ν_3 is about 10 times greater for D^* -D_2S collisions than for D^* -CO_2 collisions, $(47.3/4.9 = k_{23}^{Th}/k_{13}^{Th})$ while the rate of thermalization of hot deuterium by D_2S is 47 times greater than the rate of ν_3 excitation $(k_{23}^{Th}/k_3^{TV} = 47.3)$.

Equation (9) above can be rewritten in the following manner:

$$k_3^{TV}[CO_2] = \gamma_3[CO_2(\nu_3)]/[D^*]_0 \qquad (10)$$

where i.e. $\gamma_3 = k_{13}^{Th}[CO_2] + k_{23}^{Th}[D_2S]$. In order to determine the rate of direct excitation of vibrational quanta in the ν_3 antisymmetric stretching mode, fluorescence experiments were performed to measure γ_3, the total rate of cooling of hot deuterium atoms. A mixture of 3% D_2S in CO_2 was chosen to minimize any effects on the observed fluorescence rates due to the transfer of vibrational energy between CO_2 and D_2S and to slow the cooling rate as much as possible. The observed fluorescence signals display a single exponential rise with a rate corresponding to the total cooling rate, γ_3, for D atoms.[8]

Fig. 3 shows the results of a study of the IR fluorescence risetime as a function of pressure. A least squares analysis of this data yields a rate of $\gamma_3/P = (1.75 \pm 0.23) \times 10^4$ msec^{-1} torr^{-1} in the range of 0.04-0.2 torr. At higher pressures, the fluorescence risetime could not be measured due to the response time of the detector system (Au:Ge, 77K, 0.1 μsec). Combining this information with the absorption intensity measurement of $[CO_2(\nu_3)]/[D^*]_0 = (1.34 \pm 0.34) \times 10^{-1}$ for a 3% mixture of D_2S in CO_2 at 0.5 torr gives a value of $k_3^{TV} = (2.4 \pm 0.9) \times 10^3$ msec^{-1} torr^{-1} for the direct production of $CO_2(\nu_3)$

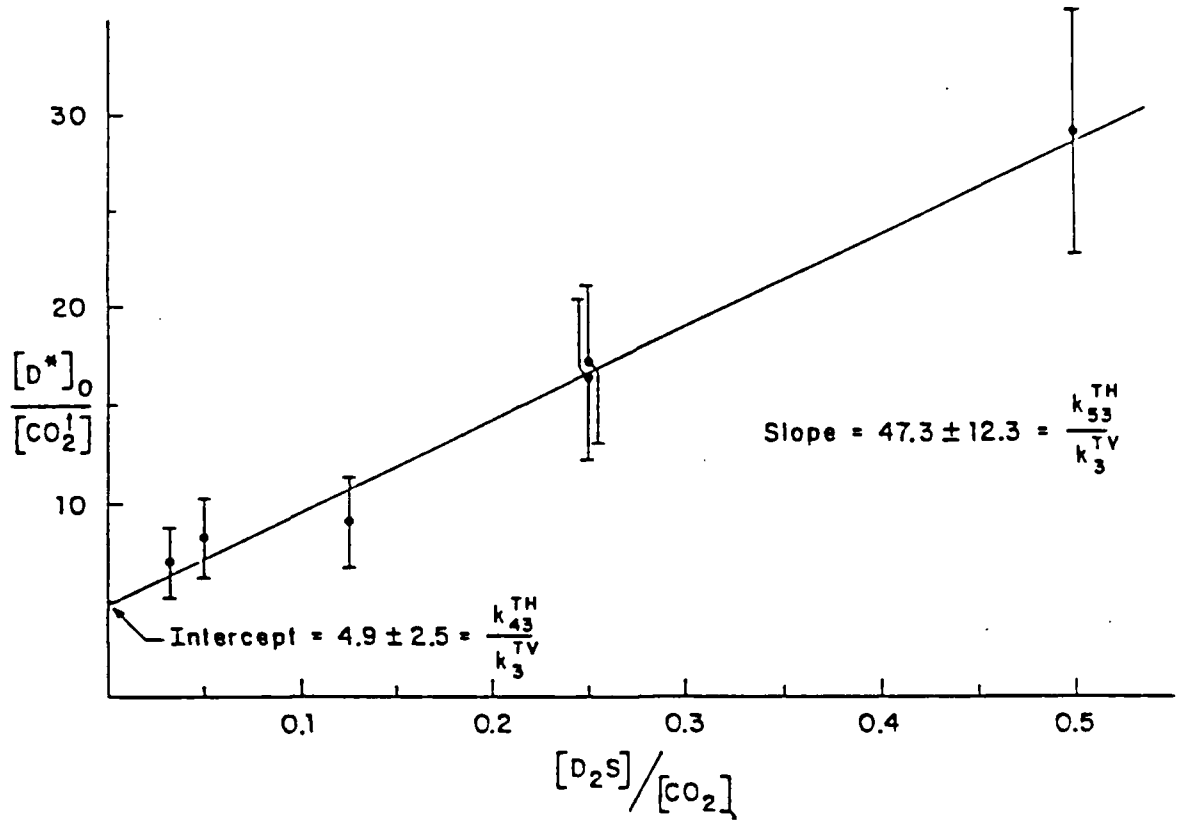
30
20
10
$\frac{[D^*]_0}{[CO_2^\dagger]}$
Slope = 47.3 ± 12.3 = $\frac{k_{53}^{TH}}{k_3^{TV}}$
Intercept = 4.9 ± 2.5 = $\frac{k_{43}^{TH}}{k_3^{TV}}$
0.1
0.2
0.3
0.4
0.5
$[D_2S]/[CO_2]$

Figure 2

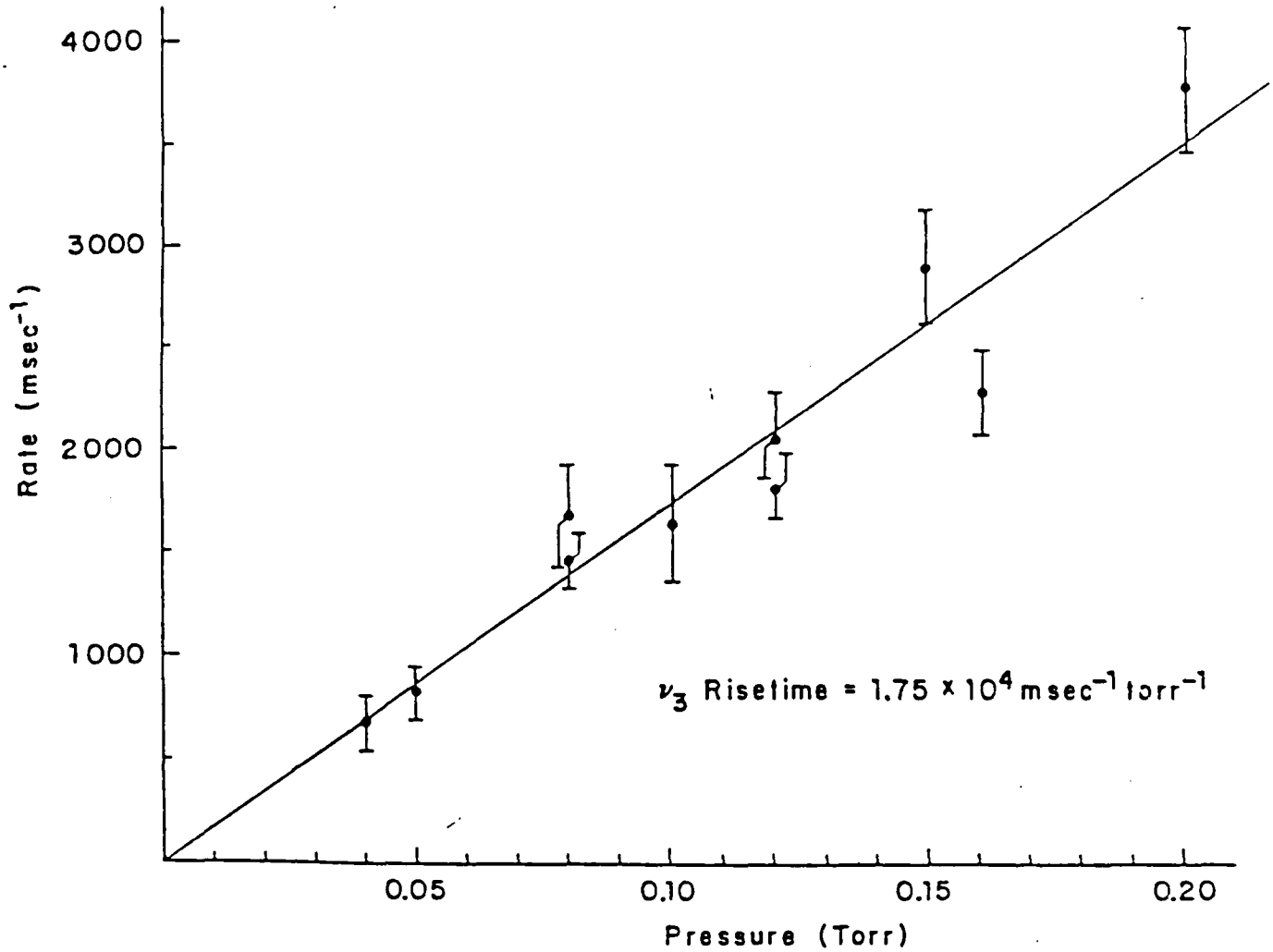

Figure 3: Plot of rate vs. pressure for the risetime of CO_2 4.3 μm fluorescence following 193 nm photolysis of D_2S in a 1/30 mixture of D_2S and CO_2. Least squares analysis yields a slope of $(1.75 \pm 0.23) \times 10^4$ msec^{-1} torr^{-1}.

quanta.

4. Discussion — With the assumption that the first collision of an initially generated D^* atom with CO_2 produces the vibrational excitation observed in these experiments, the present results can be used to determine a cross-section for the excitation of ν_3 vibrational quanta. Data for mixtures ranging from 1/2 to 20/1, D_2S/CO_2, give values of the cross-section for ν_3 excitation which vary from 0.56 to 0.92 A^2. This value is the same within experimental error as the corresponding value in the H^*/CO_2 system ($\pi\sigma^2=0.8\pm0.4A^2$) determined in the present study using a 1/8, H_2S/CO_2 mixture. Again, this value compares favorably with the cross section for ν_3 excitation by H^*, $\pi\sigma^2=0.4\pm0.2A^2$, obtained using data from a 3% H_2S/CO_2 mixture and reported earlier.[8]

5. Conclusions

a. A high resolution diode laser absorption probe has been used to examine the vibrational excitation of CO_2 molecules by collisions with fast deuterium atoms produced in the excimer laser photolysis of D_2S at 193 nm. Information concerning the mass dependence of impulsive collisions in T-->V/R excitation processes was obtained by comparison of the present results with previous observations made in the H/CO_2 system.

b. The probability for excitation of a ν_3 quantum in any CO_2 vibrational state by D^* is about 1-2% per gas kinetic collision which is similar to that found in previous studies for the hot H/CO_2 system.

c. The probability for excitation of a ν_2 quantum by D^* is about 8-9 times more efficient than that for ν_3 excitation. This compares with a 4-5 times greater propensity for the production of ν_2 over ν_3 quanta in the H/CO_2 system.

d. The cooling of hot deuterium atoms below the threshold for excitation of a CO_2 ν_3 quantum requires approximately 2 gas kinetic collisions with D_2S or 15 collisions with CO_2.

e. As in the case of H^*/CO_2 collisions, direct excitation of the fundamental ν_3 antisymmetric stretching level 00^01 by hot D atoms has been found to be small.

f. Comparision of experimental results for H^* and D^* excitation of CO_2 shows that a simple classical picture emphasizing only the relative masses of the collision partners cannot be used to predict the observed data.

g. The increased probability for excitation of the bending mode ν_2 over the antisymmetric stretch mode ν_3 by D^* versus H^* is qualitatively that expected from a simple argument based on the Fourier component of the force acting during H^* or D^*/CO_2 collisions, but quantitative agreement with such a simple picture is lacking.

This research was also supported by the National Science Foundation under Grant CHE-80-23747 and the Department of Energy under contract DE-AC-02-78ER04940.

(1) C.R. Quick, Jr., R.E. Weston, Jr., and G.W. Flynn, Chem. Phys. Lett. 83, 15 (1981).

(2) F. Magnotta, D.J. Nesbitt, and S.R. Leone, Chem. Phys. Lett. 83, 21 (1981).

(3) C.F. Wood, G.W. Flynn, and R.E. Weston, Jr., J. Chem. Phys. 77, 4776 (1982).

(4) C.A. Wight and S.R. Leone, J. Chem. Phys. 78, 4875 (1983).

(5) J.O. Chu, G.W. Flynn, and R.E. Weston, Jr., J. Chem. Phys. 78, 2990 (1983).

(6) C.A. Wight and S.R. Leone, J. Chem. Phys. 78, 4823 (1983).

(7) J.O. Chu, C.F. Wood, G.W. Flynn, and R.E. Weston, Jr., J. Chem. Phys. 80, 1703 (1984).

(8) J.O. Chu, C.F. Wood, G.W. Flynn, and R.E. Weston, Jr., J. Chem. Phys. 81, 5533 (1984).

(9) J.A. O'Neill, J.Y. Cai, G.W. Flynn and R.E. Weston, Jr., J. Chem. Phys. 84, 0000 (1986).

(10) G.N.A. Van Veen, K.A. Mohamed, T. Baller, and A.E. DeVries, Chem. Phys. 74, 261 (1983).

E. MARKING VIBRATIONAL STATES BY THEIR KINETIC BEHAVIOR

(J.A. O'Neill, Chen Xi Wang, Ji Ye Cai, and G.W. Flynn)
(JSEP work unit 5, 1985 - 1988)
(Principal Investigator: G.W. Flynn (212)280-4162)

1. Introduction — Recently, a high speed, high resolution diode laser probe technique has been developed which allows for the time resolved, state specific investigation of molecules involved in various types of dynamic events.[1] This method has been successfully applied to the study of vibrationally excited CO_2 molecules which have been produced by photodissociation,[2] by collisions with fast moving atoms,[3,4] and by electronic to vibrational (E-V) energy transfer processes.[5] A key prerequisite for these types of experiments is the accurate identification of specific vibration-rotation spectral lines in the absorption spectrum of the CO_2 molecule. Transitions which originate from the lowest level of the antisymmetric stretch mode (00^01) can be readily identified by using a CO_2 laser operating at 9.6 or 10.6 microns to excite this level while simultaneously observing the 00^01-00^02 transition with the diode laser:

$$CO_2(10^00/02^00) + h\ (10.6/9.6\mu) \longrightarrow CO_2(00^01) \quad \text{(laser pump)} \quad (1)$$

$$CO_2(00^01) + h\ (4.3\mu) \longrightarrow CO_2(00^02) \quad \text{(Diode probe)} \quad (2)$$

Because the CO_2 laser produces a large increase in the population of the 00^01 level, it effectively tags or marks transitions which originate there, making them easy to identify. Due to rapid collisional coupling of the type:

$$CO_2(01^10) + CO_2(00^01) \longrightarrow CO_2(01^11) + CO_2(00^00) \quad (3)$$

$$2CO_2(00^01) \longrightarrow CO_2(00^02) + CO_2(00^00) \quad (4)$$

levels such as 01^11 and 00^02 are also marked, but to a lesser degree. The present work was motivated by the desire to develop a simple marker for

identifying bending levels in CO_2 based on their collisional pumping by CH_3F which can be easily and conveniently excited by a CO_2 laser.

Fortunately, vibrational energy transfer processes have been studied extensively in both CH_3F[6-9] and CO_2[10-13] by themselves, which facilitates the unravelling of the intermolecule energy transfer processes. As will be seen from the present study, both the bending and antisymmetric stretch modes of CO_2 are marked by collisional energy transfer and laser pumping in CH_3F/CO_2 mixtures, though at different times. Thus, CH_3F actually serves as a very general tag for both kinds of CO_2 modes.

2. Experimental -- The output from a Q-switch CO_2 laser (1 mJ/Pulse, 0.5 μsec pulse width, 200 pulses/sec) is made co-linear with the light from a continuous wave, continuously tunable diode laser (typical power 1 mW) operating in the 4.3μm region, through the use of a germanium beamsplitter. Diode laser radiation is monitored with an InSb (77 K) detector/amplifier system having a response time of 1 μsec. A MgF_2 blocking filter is used to separate the CO_2 and diode laser radiation after traversing the sample cell (30 cm long, 1 inch diameter, pyrex with NaCl window). A half meter monochromator is used to select a single mode of the diode laser, and a transient recorder, triggered by a pulse derived from the Q-switch laser, is used to monitor the time dependent changes in sample absorption which follow pumping by the CO_2 laser. A signal averager was used to add successive traces from the transient recorder to improve signal/noise ratios. The CO_2 laser was operated on both the 9.6 and 10.6μ branches.

3. Results -- The CH_3F molecule can be pumped for the most part only by the CO_2 laser's P(20) 9.6μ line which moves population from the vibrationless ground state to the v=1 level of the ν_3 mode (see Fig. 1 for a relevant vibrational energy level diagram). On the other hand, $^{12}CO_2$ is pumped by all CO_2 laser lines which move CO_2 molecules from the 10^00 or 02^00 level to 00^01. $^{13}CO_2$ however, is not significantly excited by our Q-switch laser which operates on natural $^{12}CO_2$. Three different types of experiments were used to unravel the energy transfer processes in CH_3F/CO_2 mixtures. In

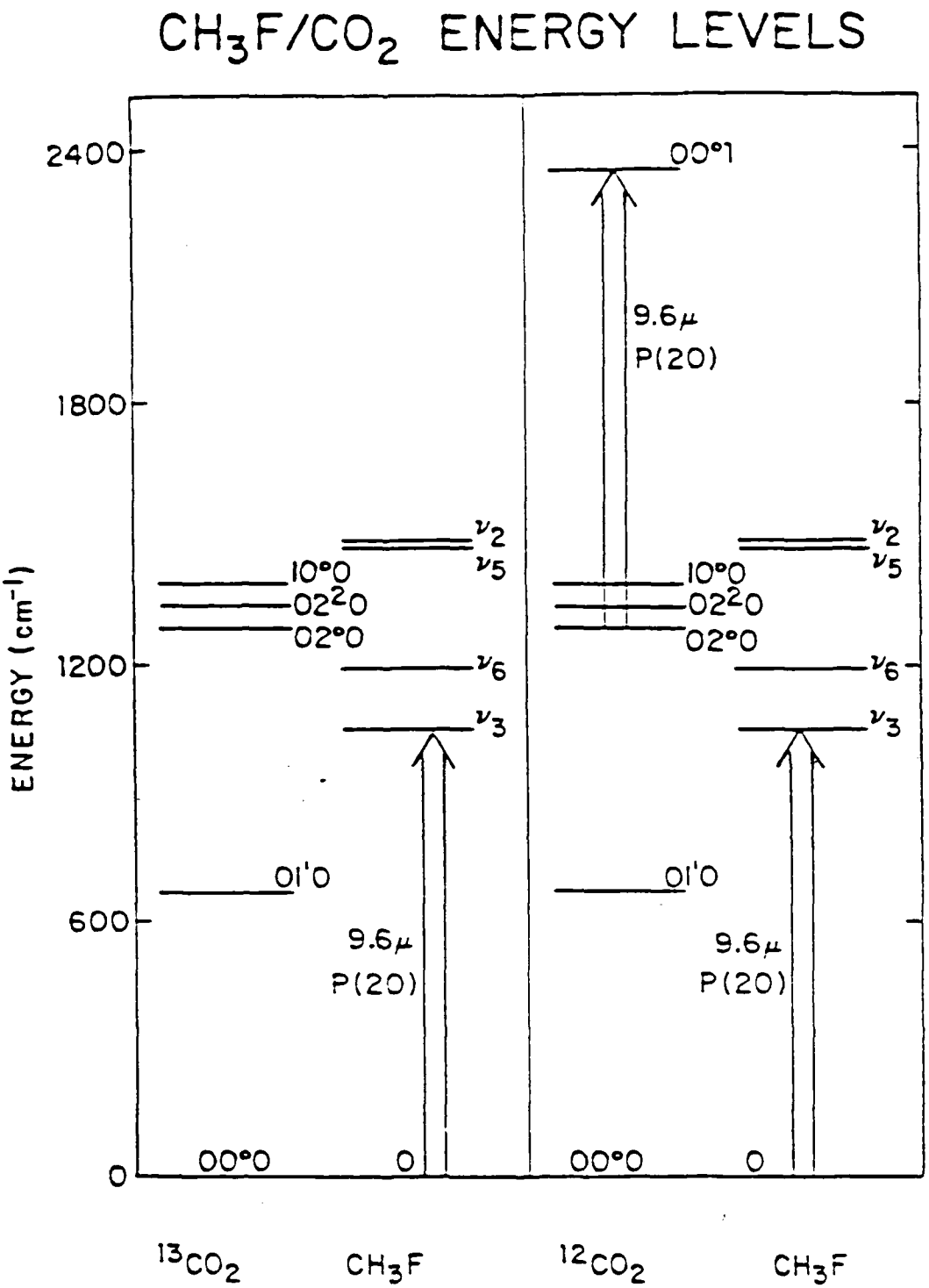
CH3F/CO2 ENERGY LEVELS
ENERGY (cm-1)
2400
1800
1200
600
0
00°1
9.6μ
P(20)
ν2
ν5
10°0
02²0
02°0
ν6
ν3
01'0
00°0
0
13CO2
CH3F
12CO2
CH3F

Figure 1:

the first, mixtures of $^{13}CO_2$ and CH_3F were irradiated with the P(20), 9.6μ line of the CO_2 laser which excited only CH_3F. These experiments establish the overall energy transfer rate between $^{13}CO_2$ and CH_3F involving largely the bending modes of CO_2 and ν_3, ν_6, and (ν_2, ν_5) levels of CH_3F (see Fig. 1). This rate of intermolecule vibration-vibration (V-V) energy transfer turns out to be the slowest rate of interest in the present experiments. In the second experiment mixtures of $^{12}CO_2/CH_3F$ were irradiated by CO_2 laser lines other than P(20) (termed here P[other]). Since CH_3F is not excited by the Q-switch laser in these experiments, these studies serve largely to probe the relaxation pathways for the 00^01 level of CO_2 due to collisions with CH_3F. CH_3F turns out to be a rather efficient relaxer of the CO_2 00^01 level. In the third experiment, relaxation processes were investigated in $^{12}CO_2/CH_3F$ samples which were irradiated by the P(20), 9.6μ CO_2 laser line which pumps both $^{12}CO_2$ and CH_3F in these mixtures. These studies are sensitive to all the energy transfer processes which exchange vibrational excitation between the two molecules. The results obtained in these three different kinds of experiments are described below.

(a) $^{13}CO_2/CH_3F$ <u>Mixtures Irradiated by the P(20), 9.6μ Transition</u> -- The diode laser was set to probe either the R(31) or the R(28) 02^20 ---> 02^21 transition, both of which gave identical results because rotational equilibration is quickly completed at the pressures used in these experiments. Typical absorption changes for the diode laser probe are shown in Fig. 2a and 2b following Q-switch laser excitation. Initially, absorption increases following CO_2 laser pumping (Fig. 2a). In Fig. 3, the rate of growth of this absorption is plotted versus total pressure in a 1:1 $^{13}CO_2/CH_3F$ mixture demonstrating a pressure dependent rate of 3.3 $msec^{-1}$ $torr^{-1}$. Fig. 2b shows absorption changes on a longer time scale returning to equilibrium with two different characteristic rates. The slower of these is just the rate of thermal conductivity out of the diode laser beam and its amplitude can be reduced nearly to zero by the addition of Ar which also slows the rate. The faster of the observed "decay" rates corresponds to overall vibrational-translation/rotation (V-T/R) energy transfer which is of relatively little interest in the present study. The growth rate of the

$1CH_3F/1^{13}CO_2$ Pump: 9.6 μm P(20)

Probe: 02^20 —— 02^21 R(31) $^{13}CO_2$

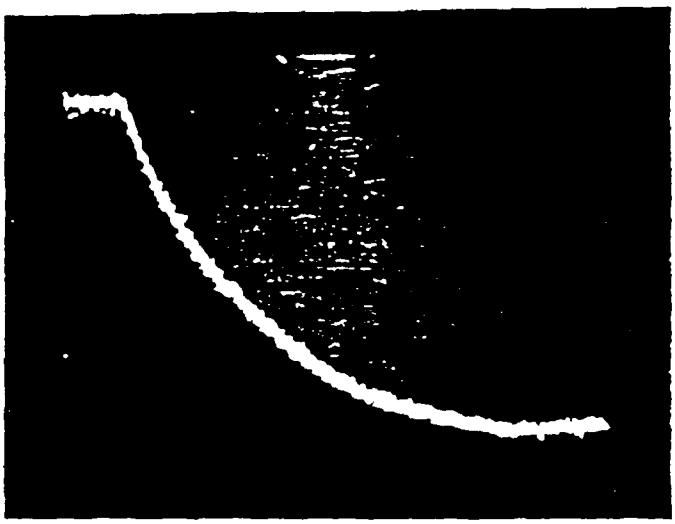

P_{TOTAL} = 2.0 torr

200 μsec Full Scale

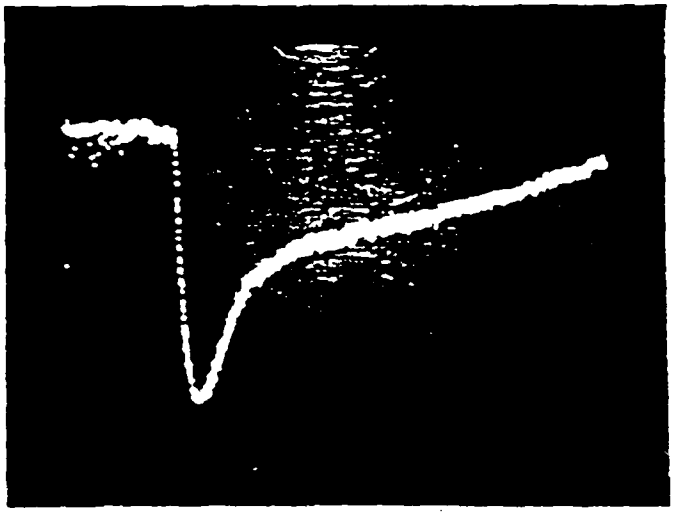

P_{TOTAL} = 2.0 torr

4000 μsec Full Scale

Figure 2:

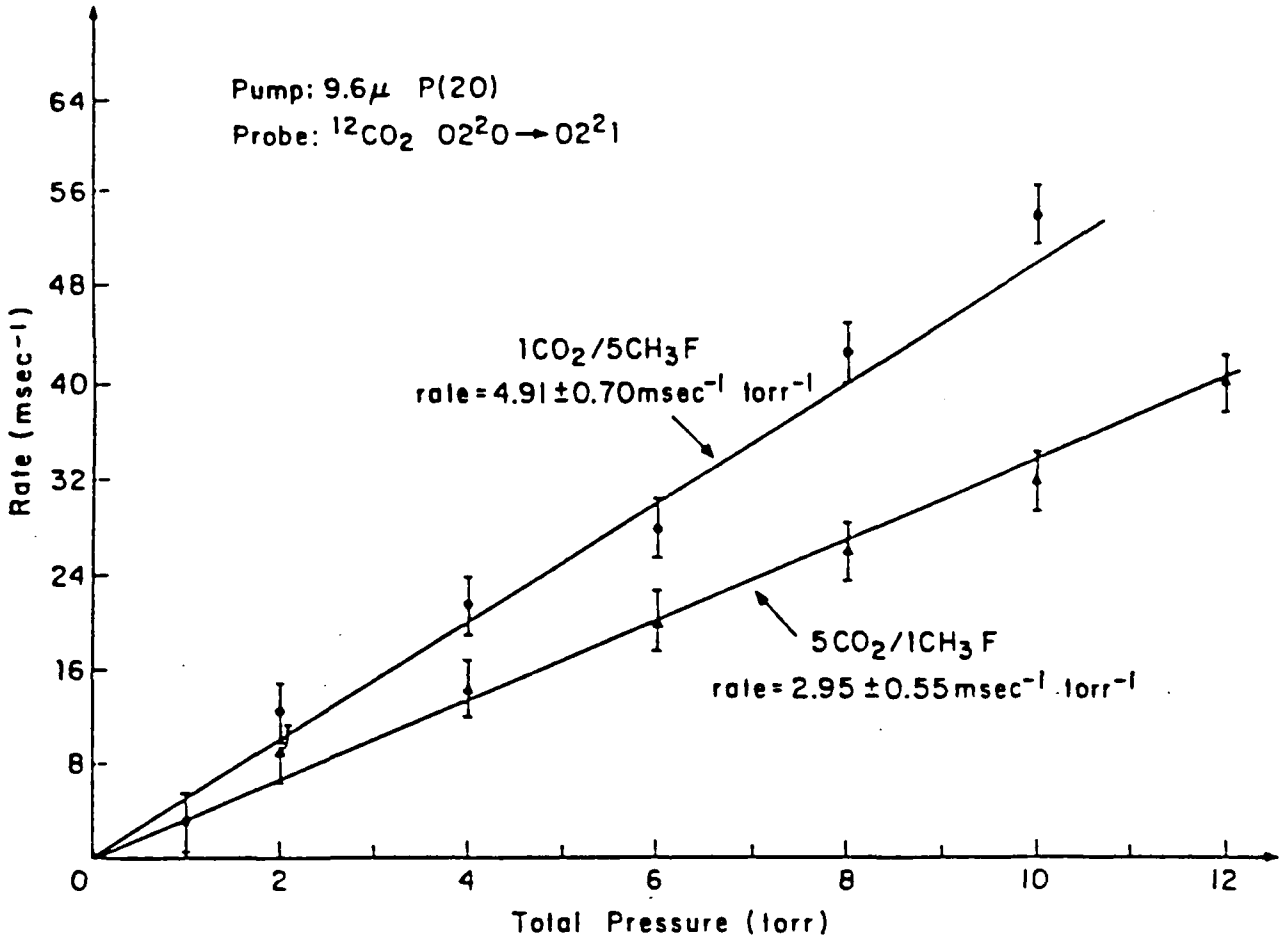
Pump: 9.6μ P(20)
Probe: $^{12}CO_2$ $02^20 \rightarrow 02^21$
$1CO_2/5CH_3F$
rate = 4.91 ± 0.70 msec^{-1} torr^{-1}
$5CO_2/1CH_3F$
rate = 2.95 ± 0.55 msec^{-1} torr^{-1}
Rate (msec^{-1})
Total Pressure (torr)
0
2
4
6
8
10
12
8
16
24
32
40
48
56
64

Figure 3

absorption change corresponding to the process shown in Fig. 2a was also measured in 1:5 (CO_2:CH_3F) mixtures and the rate was found to be 5.5 $msec^{-1}$ $torr^{-1}$.

(b) $^{12}CO_2/CH_3F$ Mixtures Pumped By Laser Lines Other Than P(20)9.6μ -- Initial experiments were performed with the diode laser set to probe the P(47), 00^01--00^02 transition which is sensitive to population changes in only the 00^01 level because 00^02 has a negligible population under our experimental conditions. Fig. 4 shows absorption changes in both pure $^{12}CO_2$ and 1:1 $^{12}CO_2/CH_3F$ mixtures following Q-switch CO_2 laser pumping. Absorption increases initially since the pulse laser places molecules in the 00^01 level. In pure CO_2 the absorption returns to its ambient level at a rate of 0.33 $msec^{-1}$ $torr^{-1}$ in good agreement with the overall relaxation rate of the 00^01 level measured by the standard infrared fluorescence methods nearly 20 years ago.[10,11] The decay rate of the excess population in 00^01 is much faster in the presence of CH_3F, with an overall relaxation rate of 22 $msec^{-1}$ $torr^{-1}$ measured in a 1:1 mixture. This is, of course, not surprising since the fact that CH_3F absorbs 9.6μ CO_2 laser radiation means that the process $CO_2(00^01)$ + $CH_3F(0)$ ---> $CO_2(02^00)$ + $CH_3F(\nu_3)$ must be nearly resonant.

(c) $^{12}CO_2/CH_3F$ Mixtures Pumped By the 9.6μ P(20) CO_2 Laser Line -- In a second set of experiments on $^{12}CO_2/CH_3F$ mixtures, the diode laser was set to probe the P(46), 02^20--02^21 transition of CO_2 while the Q-switch laser was set to the 9.6μ, P(20) line which excites both 00^01 of CO_2 and ν_3 of CH_3F. Absorption changes observed in this set of experiments are both complicated and a sensitive function of $^{12}CO_2/CH_3F$ mixture composition. The qualitative behavior of these signals is as follows (see Fig. 5). Initially absorption decreases as the CO_2 laser pumps molecules out of the 02^00 level since 02^20 is rapidly coupled to this state by collisions.[14,15] Following this essentially detector-limited decrease in absorption, the population of the CO_2 overtone bending levels is increased by two processes. The first is the relaxation of 00^01 by $CH_3F(0)$ which is expected to return population to the 02^00 state as noted above. The second is energy transfer from the CH_3F ν_3 level which is also pumped by the P(20), 9.6μ Q-switch laser line.

$CH_3F/^{12}CO$ Pump: 9.6μ P(20)

Probe: 00°1 ⟶ 00°2 P(47) $^{12}CO_2$

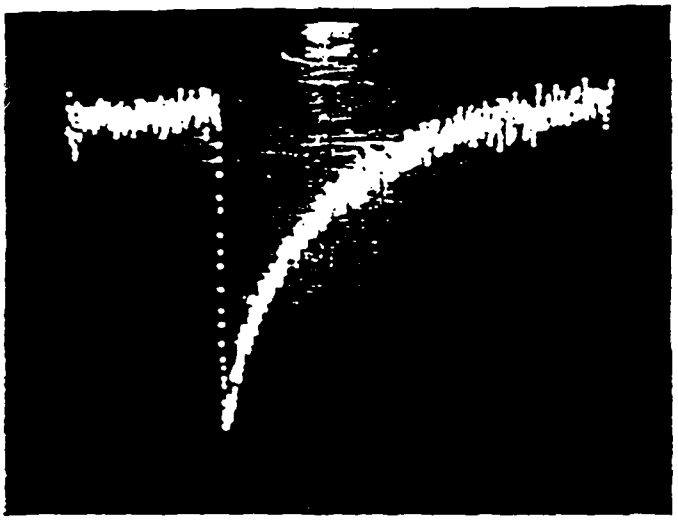

$10CH_3F/1^{12}CO_2$

P_{TOTAL} = 0.5 torr

200μsec Full Scale

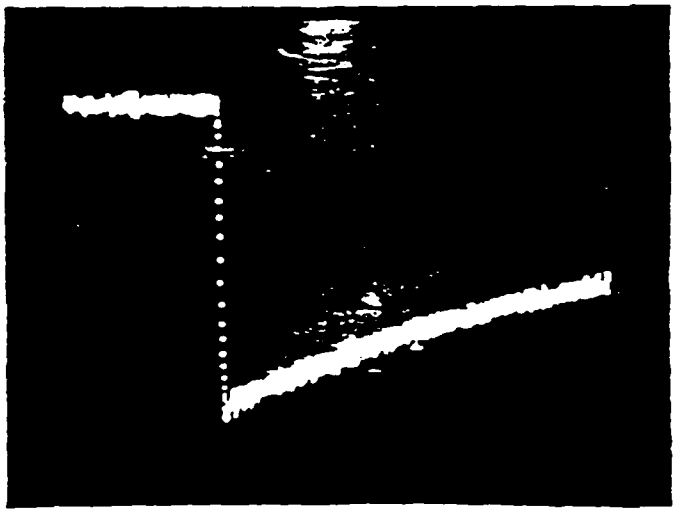

Pure CO_2

P_{TOTAL} = 0.5 torr

200μsec Full Scale

Figure 4

$CH_3F/^{12}CO_2$ Pump: 9.6μ P(20)

Probe: $02^20 \longrightarrow 02^21$ P(46) $^{12}CO_2$

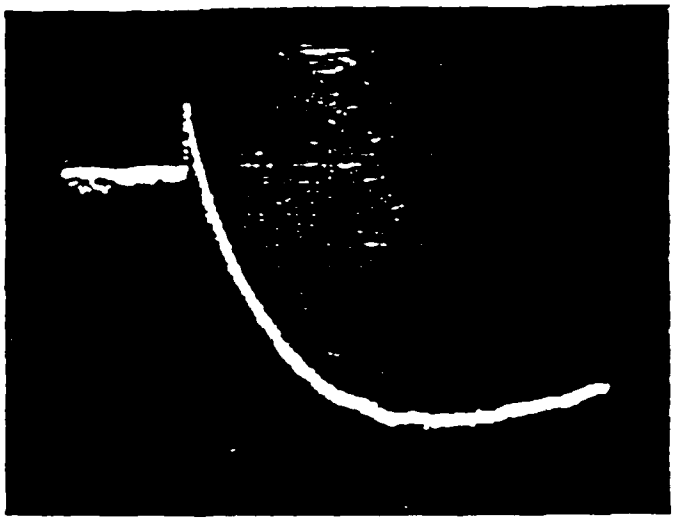

$1CH_3F/1\,^{12}CO_2$

$P_{TOTAL} = 2.0$ torr

1000μsec Full Scale

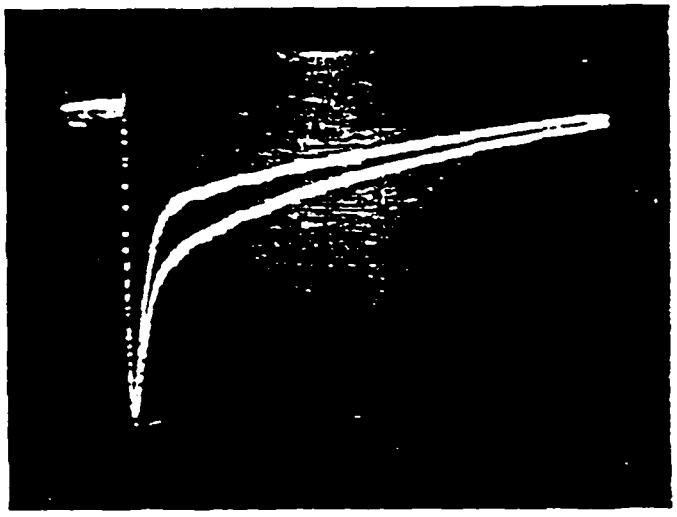

Upper Trace:

5 torr CH_3F
5 torr CO_2
30 torr Ar

Lower Trace:

5 torr CH_3F
5 torr CO_2

4000μsec Full Scale

Figure 5

Although pumping of 02^00 by relaxation of 00^01 is rapid by comparison to pumping by energy transfer from CH_3F ν_3, the amplitude of this first process is small compared to that of the second in 1:1 mixtures of the two gases. In 5:1 CO_2/CH_3F mixtures where the amplitudes of these two pumping mechanisms become comparable, their rates also becme comparable due to the decrease in the partial pressure of CH_3F, and the rates are difficult to separate in the experimental data. While we have been able to clearly identify the presence of an energy transfer rate corresponding to transfer from vibrationally excited CH_3F to CO_2(3.3 $msec^{-1}$ $torr^{-1}$ in a 1:1 mixture), the presence of pumping by relaxation of 00^01 of CO_2 (22 $msec^{-1}$ $torr^{-1}$ in a 1:1 mixture) could only be detected qualitatively by the poor fit of exponential decay curves to the early part of the absorption curves. In mixtures of $^{12}CO_2/CH_3F$ pumped by 9.6μ CO_2 absorption due to relaxation of 00^01 by $CH_3F(0)$ can be clearly observed since pumping from vibrationally excited CH_3F is very small under these conditions (see Fig. 6).

Further work on the CH_3F/CO_2 system is presently underway in our laboratory in order to measure the rates of vibrational energy flow between[12,13] CO_2 and CH_3F at various mole ratios. The results of these experiments, when interpreted in the light of a suitable kinetic model, should elucidate the overall mechanism of energy transfer between CO_2 and CH_3F. Also, experiments are in progress which investigate the efficiency of CH_3F in "pumping" higher bending mode vibrations in CO_2 such as the 03^30 second overtone vibration.

This research was also supported by the National Science Foundation under Grant CHE-80-23747 and the Department of Energy under contract DE-AC-02-78ER04940.

(1) J.O. Chu, C.F. Wood, G.W. Flynn and R.E. Weston, Jr., J. Chem. Phys. 80, 1703 (1984).

(2) C.F. Wood, J.A. O'Neill, and G.W. Flynn, Chem. Phys. Lett. 109, 317 (1984).

(3) J.O. Chu, C.F. Wood, G.W. Flynn and R.E. Weston, Jr., J. Chem. Phys. 81, 5533 (1984).

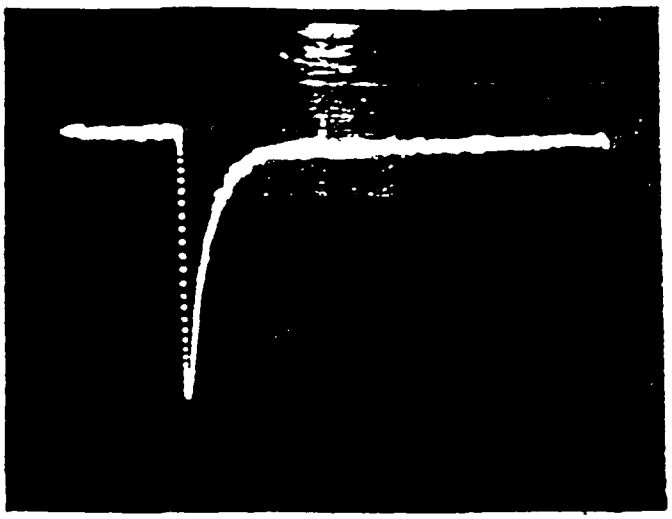

$1CH_3F/1^{12}CO_2$

Pump: 9.6μ P(20)

Probe: $00^01 \rightarrow 00^02$ P(47)

P_{TOTAL} = 10 torr

100μsec Full Scale

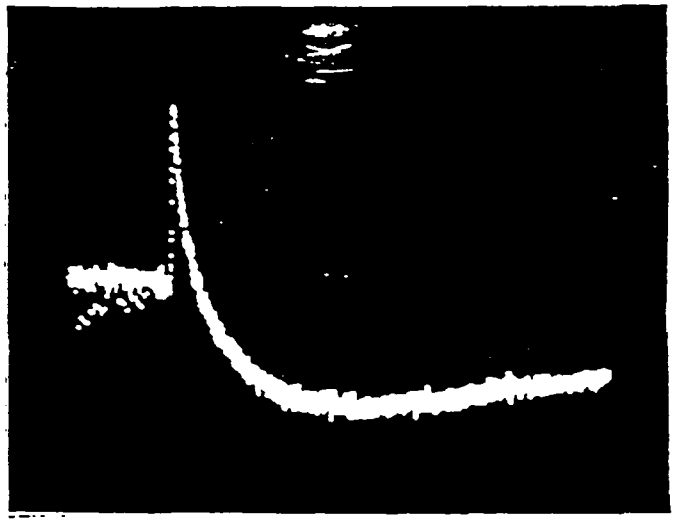

$1CH_3F/1^{12}CO_2$

Pump: 9.6μ P(J$\neq$20)

Probe: $02^20 \rightarrow 02^21$ P(46)

P_{TOTAL} = 10 torr

100μsec Full Scale

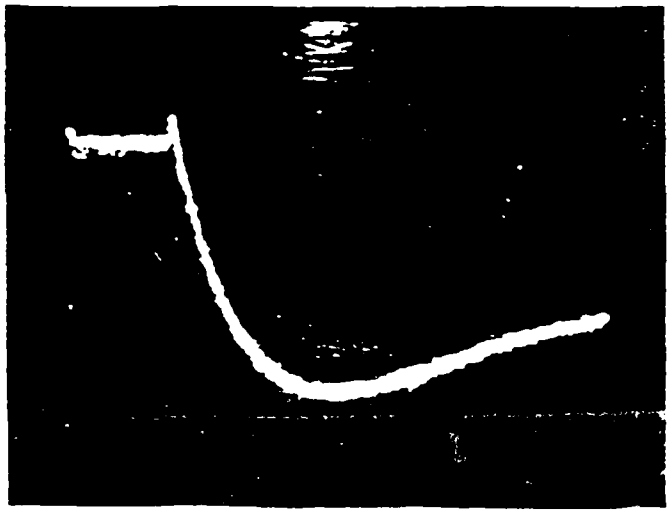

$1CH_3F/1^{12}CO_2$

Pump: 9.6μ P(20)

Probe: $02^20 \rightarrow 02^21$ P(46)

P_{TOTAL} = 10 torr

100μsec Full Scale

Figure 6

(4) J.A. O'Neill, J.Y. CAi, G.W. Flynn and R.E. Weston, Jr., 'Diode Laser Probes of CO_2 Vibrational Excitation Produced by Collisions wth Hot Deuterium Atoms from the 193 nm. Excimer Laser Photolysis of D_2S," manuscript in preparation.

(5) B.B. Brady, G.B. Spector, L. Chia and G.W. Flynn, work in progress.

(6) E. Weitz, G.W. Flynn and A.M. Ronn, J. Chem. Phys. 56, 6060 (1972).

(7) E. Weitz and G.W. Flynn, J. Chem. Phys. 58, 2781 (1973).

(8) V.A. Apkarian and E. Weitz, J. Chem. Phys. 71, 4349 (1979).

(9) R.S. Sheorey and G.W. Flynn, J. Chem. Phys. 72, 1175 (1980).

(10) L.O. Hocker, M.A. Kovacs, C.K. Rhodes, G.W. Flynn, and A. Javan, Phys. Rev. Lett. 17, 1233 (1966).

(11) C.B. Moore, R.E. Wood, B.L. Hu, and J.T. Yardley, J. Chem. Phys. 46, 4222 (1967).

(12) I. Burak, Y. Noter, A. Szoke, IEEE J. Quant. Electr. QE-9, 541 (1973).

(13) J.T. Yardley and C.B. Moore, J. Chem. Phys. 46, 4491 (1967).

(14) R.K. Huddleston and E. Weitz, Chem. Phys. Lett. 83, 174 (1981).

(15) C. Dang, J. Reid and B.K. Garside, Appl. Phys. B 31, 163 (1983).

F. PROBING HIGH ENERGY OVERTONE STATES OF MOLECULES WITH DIODE LASERS

(J.A. O'Neill, Ji Ye Cai, G.W. Flynn)
(JSEP work unit 5, 1985 - 1988)
(Principal Investigator: G. Flynn (212)280-4162)

1. Introduction — The excitation of vibrational states of molecules by fast moving "hot" atoms offers an opportunity to study the dynamics of fundamental collision processes in various small molecules. In the case of CO_2, diode laser absorption experiments have provided a wealth of information about the vibrational excitation which occurs during the inelastic collisional scattering of this molecule with H^* and D^* atoms having translational energies in the range of 2 eV.[1] These earlier studies have shown that bending excitation of CO_2 is considerably more probable than excitation of antisymmetric stretching motion. The present experimental investigation examines for the first time the CO_2 vibrational levels 03^30 and 01^11 produced by collisions with hot D atoms having a translational energy of 2 eV. Schematically, these experiments can be represented by the following equations:

$$D_2S + h\nu\ (193nm) \longrightarrow DS + D^* \qquad \text{(Hot atom production)} \qquad (1)$$

$$D^* + CO_2(00^00) \longrightarrow CO_2(03^30) + D \qquad \text{(Collisional excitation)} \qquad (2)$$

$$D^* + CO_2(00^00) \longrightarrow CO_2(01^11) + D \qquad \text{(Collisional excitation)} \qquad (3)$$

$$CO_2(mn^\ell p) + h\nu\ (4.3u) \longrightarrow CO_2(mn^\ell p{+}1) \qquad \text{(Diode laser probing)} \qquad (4)$$

Because information already exists concerning the efficiency of excitation of the CO_2 states 01^10 and 02^20 by hot hydrogen atoms,[1] the new data obtained in the present study provides a measure of the collisional excitation probability for successively higher states within a given vibrational mode (the 01^10, 02^20 and 03^30 bending mode levels in CO_2). Such data can be used to test for the presence of gap laws and the importance of changes in the number of vibrational quanta in determining the efficiency of collisional

excitations. Ultimately, the relaxation behavior of high vibrational levels is intimately connected to the rate of unimolecular and bimolecular chemical reactions, and data obtained concerning these relaxation processes can be expected to serve as a test of potential surfaces employed in scattering calculations.

2. Results — The details of our excimer laser photolysis/diode laser probe double resonance apparatus have been described in detail[1] and only the important results will be summarized here.

Upon excimer laser photolysis of D_2S in mixtures with CO_2, transient absorption changes were observed while monitoring the $01^10 \rightarrow 01^11$ P(29) transition. A typical signal for this transition is depicted in Fig. 1. In order to prevent attenuation of the diode laser beam by the significant CO_2 population in 01^10 at room temperature (N_{010}=0.081xN_{000}) prior to the UV photolysis pulse, a sample cell length of 6 cm was chosen, and signals were obtained for pressures ranging from 0.2 to 2.0 torr. These curves depict an initial increase in the absorption of the diode laser which is detector limited, and a second change which is somewhat slower. The preliminary fast component of these signals corresponds to the direct production of CO_2 states which contain one quantum of ν_2 vibration such as 01^10 and 01^11. Previous work on this system has demonstrated that in a $1D_2S/4CO_2$ mixture with an excimer laser energy of 5 mJ/pulse at 0.5 torr, this initial change in absorption corresponds to the production of ($4.8 \pm 1.2 \times 10^{-1}$ CO_2 molecules with one quantum of ν_2 excitation for each D atom which is initially produced.

The slower increase in the 01^10 absorption signals has a measured rte which agrees well with that attributed to the ladder climbing process in the bending mode:[2]

$$CO_2(02^20) + CO_2(00^00) \rightarrow 2CO_2(01^10) \qquad (5)$$

This portion of the signal has an amplitude which is approximately 50% of the fast rise intensity, and it corresponds to the direct formation of one or more of the $02^20, 02^00, 10^00$ states, which are tightly coupled by collisions,

T-V Excitation of CO_2 by D^*

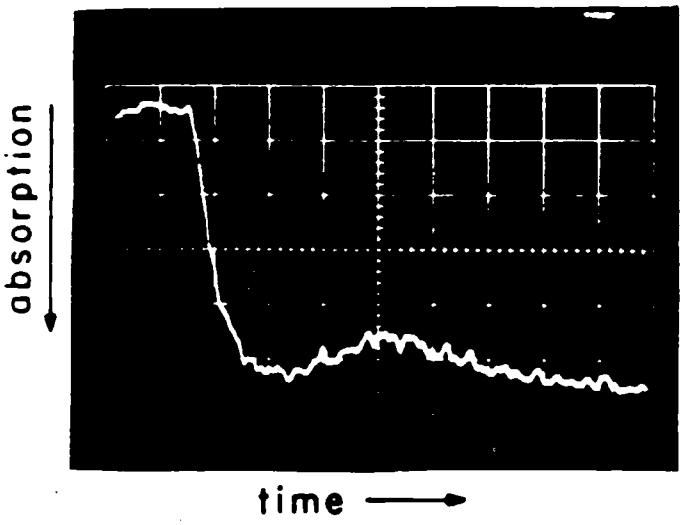

$01^10 \longrightarrow 01^11$ P(29)
P_{TOTAL} = 0.5 torr
Number of Shots = 100
40 μsec full scale
L = 6 cm

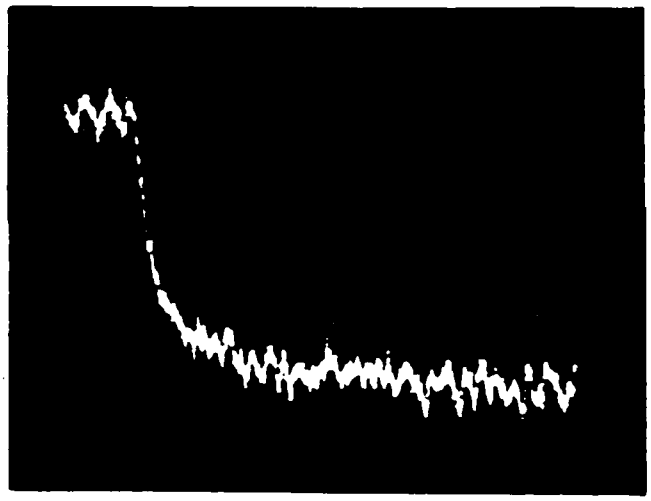

$01^11 \longrightarrow 01^12$ R(19)
P_{TOTAL} = 0.1 torr
Laser Shots = 150
D_2S/CO_2 = 1/4
40 μsec full scale

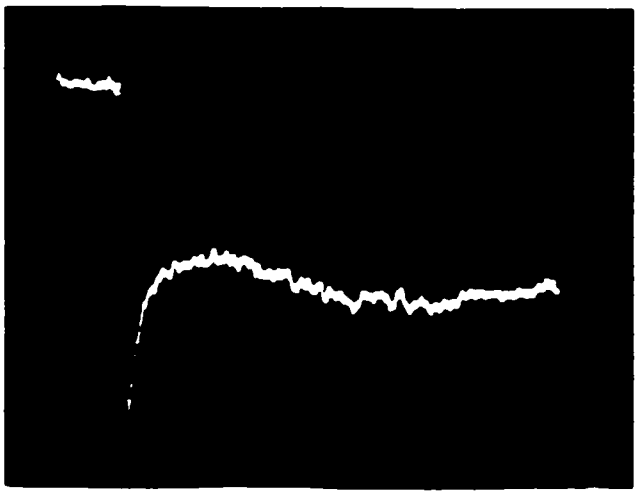

$03^30 \longrightarrow 03^31$ R(18)
P_{TOTAL} = 0.75 torr
Laser Shots = 50
D_2S/CO_2 = 1/4
100 μsec full scale

Figure 1

followed by the relaxation of these states to the 01^10 level via eqn. 5. From this it is possible to conclude that the number of molecule produced in the ν_2 overtone/ ν_1 fundamental levels during the D/CO_2 collisional interaction is about 1/2 of that formed in the lower lying bending fundamental.

In order to determne the contribution of the 01^11 combination state to the measured 01^10 --> 01^11 absorption intensity, signals were obtained for the 01^11 ---> 01^12 R(6), R(16), R(19), P(25) transitions. A representative absorption curve for this transition is shown in Fig. 1. These signals were obtained for a $1D_2S/4CO_2$ mixture in a 207 cm sample cell for pressures ranging from 0.05 to 2.0 torr. The absorption curves demonstrate an initial prompt change which is detector limited even at a pressure of 0.05 torr. This initial increase in absorption corresponds to the direct population of the 01^11 level during the D/CO_2 interaction. At a total pressure of 0.5 torr and an excimer laser pulse energy of 4 mJ/pulse, the intensity of the preliminary 01^11 absorption change corresponds to the production of 2.5 x 10^{-3} CO_2 molecules with bend-stretch excitation for each D atom initially formed. This number of excited molecules is very small in comparison with the number which was counted in the 01^10 vibrational level. Thus, the contribution of the combination state 01^11 to the 01^10 ---> 01^11 signal is negligible. By analogy, the contribution of he upper state is expected to be small for all of the other bending manifold transitions of the type $0n^{\ell}0$ ---> $0n^{\ell}1$. Fig. 2 presents the results of a pressure dependent study of the number of vibrationally excited CO_2 molecules produced in the 01^10 and 01^11 states normalized for the initial number of hot D atoms created by the UV photolysis pulse.

Transient absorption signals were also obtained for the 03^30 ---> 03^31 P(23), P(34), R(10) transitions in CO_2 upon collisional excitation by translatonally energetic deuterium atoms. A typical signal for this transition is indicated in Fig. 1. Measurements were made of the population produced in this level by collisions with hot D atoms for a mixture of $1D_2S/CO_2$ at pressures of 0.125 to 2.0 torr in a 207 cm sample cell. The absorption curves obtained in this manner typically demonstrate an initial fast increase in absorption, followed by a two component relaxation process.

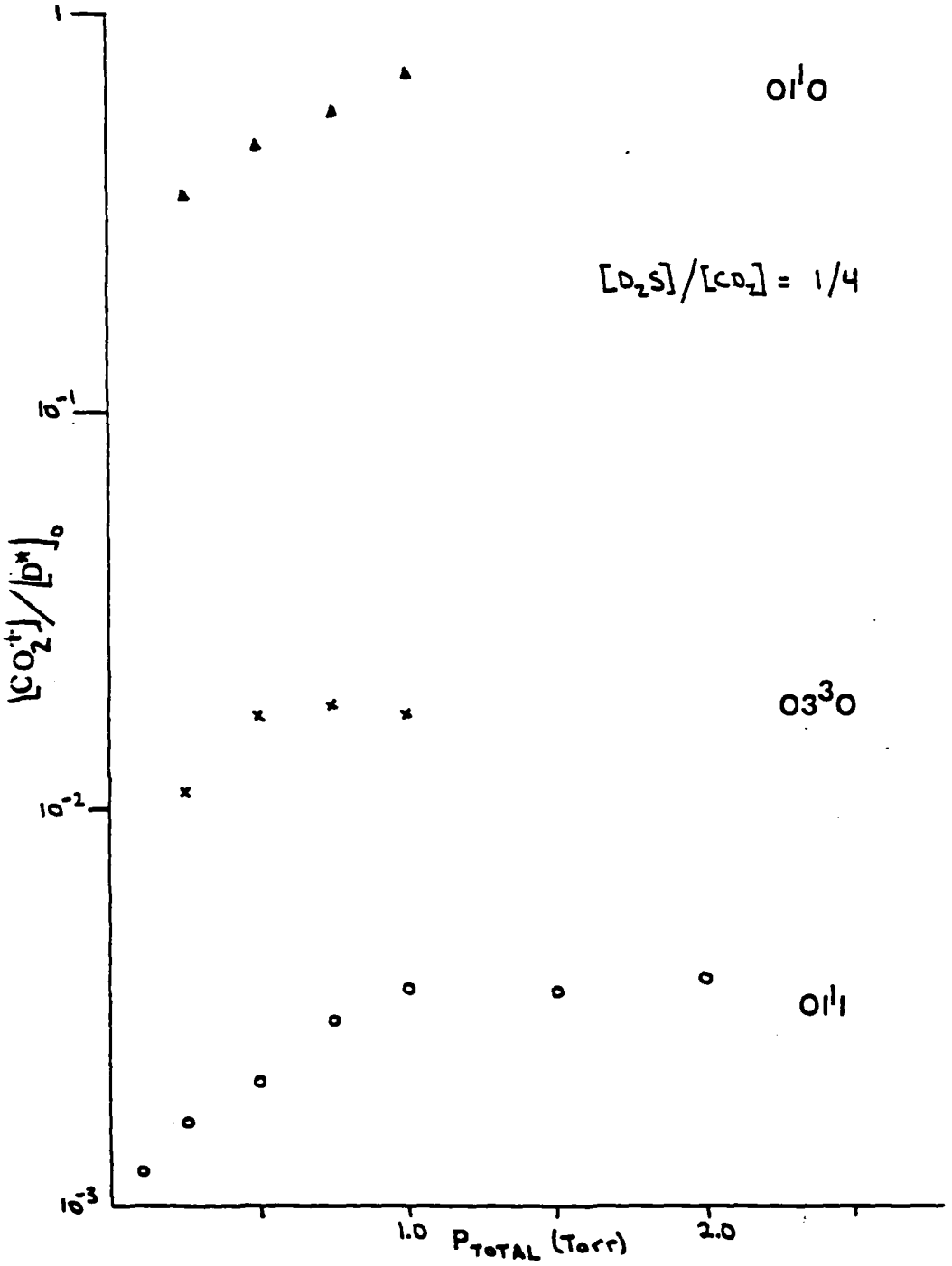

Figure 2:

The prompt increase was observed to be detector limited at all pressures studied, and it is attributed to the direct formation of CO_2 molecules in the second ν_2 bending overtone 03^30. At 0.75 torr in the usual 1/4 mixture with an excimer laser energy of 4 mJ/pulse, the amplitude of this initial absorption change corresponds to the formation of 1.0×10^{-2} CO_2 molecules in the 03^30 vibrational level for every D atom produced in the excimer photolysis process. The results of a pressure dependent study of this nascent population obtained from studying the $03^30 \longrightarrow 03^31$ transition is presented in Fig. 2 for comparison with the 01^10 and 01^11 results.

The first component of the relaxation process observed in the $03^30 \longrightarrow 03^31$ absorption signal has a rate which agrees with that determined for the ladder climbing process among the CO_2 bending states process (5). The fact that this ladder climbing process corresponds to a toal decrease in the number of molecules in the 03^30 vibrational level suggests that this state is not being filled appreciably by the higher energy 04^40 level. In addition, this observation clearly demonstrates that the vibrational temperature of the 03^30 level excedes that of the lower bends $01^10,02^20$ even though the number of vibrational quanta produced in 03^30 is substantially less than that in the lower levels. Experiments are presently underway in our laboratory to identify and probe the 04^40 level directly during the D/CO_2 collisional interaction.[3]

This research was also supported by the National Science Foundation under Grant CHE-80-23747 and the Department of Energy under contract DE-AC-02-78ER04940.

(1) J.O Chu, C.F. Wood, G.W. Flynn, and R.E. Weston, Jr., J. Chem. Phys. 81, 5533 (1984).

(2) V.A. Apkarian and E. Weitz, J. Chem. Phys. 71, 4349 (1979).

(3) J.A. O'Neill, T.G. Kreutz, and G.W. Flynn, work-in-progress.

G. DIODE LASER PROBING OF HIGH ENERGY MOLECULAR STATES USING A DISCHARGE REFERENCE CELL FOR LEVELS IN THE ELECTRON VOLT RANGE

(T. Kreutz, J. O'Neill and G. Flynn)
(JSEP work unit 5, 1985 - 1988)
(Principal Investigator: G. Flynn (212)280-4162)

Recently, our ability to locate and probe extremely weak absorption lines associated with high vibrational levels of CO_2 has been greatly improved by the addition of a CO_2 discharge reference cell to our diode spectrometer. In a typical experiment, we study the relaxation dynamics of vibrationally excited CO_2 using time domain absorption spectroscopy with a tunable diode laser. The population in a given CO_2 vibrational level (n,m,p) is probed by tuning the laser to the strong transition (n,m,p) -> (n,m,p+1) in the 4.3 μ region and monitoring the intensity transmitted through the gas folloiwng an initiation/excitation pulse from a second laser. A significant difficulty arises when the vibrational level to be probed is only sparsely populated at room temperature, in which case the spectral line is extremely weak and its exact line position is uncertain. The probe laser must then be tuned 'dynamically' onto linecenter, i.e. the laser frequency is varied systematically through the appropriate spectral region until an absorption signal appears. Unfortunately, this procedure is extremely time consuming and is often impossible in experiments which require extensive signal averaging. Worse still, the relatively congested spectrum of vibrationally excited CO_2 severely complicates this procedure, effectively limiting the absorption probe technique to levels which are well populated at room temperature.

We have circumvented this difficulty by using a CO_2 discharge tube to significantly enhance the steady state populations in these high vibrational levels. Used as a frequency reference cell, the discharge tube enables us to locate absorption lines associated with highly vibrationally excited levels of CO_2, and to frequency lock the diode laser onto these lines. In the

discharge cell a high voltage DC discharge is applied to a low pressure mixture of CO_2, N_2, and He, providing steady state, non-Boltzman populations of highly vibrationally excited CO_2. While the CO_2 rotational temperature remains relatively low, the effective vibrational mode temperatures are greatly increased (e.g. 2250 K for the asymmetric stretching mode, ν_3). In Fig. 1, we compare typical absorption spectra for the CO_2 discharge reference cell with the high voltage discharge turned on and off. Note the dramatic increase in the number of available absorption lines when the discharge is used. Accurate assignments of the additional lines are made possible by high resolution spectroscopy of discharge-excited CO_2 which has been recently completed in the 4.3 μ region with a high resolution FTIR spectrometer. Spectral constants for most of the CO_2 isotopes have been reported for levels as high as 5 bending quanta (ν_2) and 13 asymmetric stretching quanta (ν_3). The combination of the discharge reference cell and calculated spectral line position and intensities enables us to unambiguously assign and probe thousands of lines heretofore unavailable.

In practice, a small portion of the diode laser light is split off from the main experimental cell, passed through the discharge tube, and detected with an infrared detector. The absorption signal can be sent to a lockin-detector whose derivative signal is fed back into the diode laser current controller for frequency stabilization. This configuration 'locks' the laser frequency onto the peak of a single absorption line throughout the duration of an experiment.

The discharge reference cell is a particularly important development for an ongoing series of research projects which examine high energy molecular states. These experiments seek to clarify aspects of molecular reaction dynamics by mapping out the vibrational energy distribution in CO_2 as it evolves from the reaction transition state. For example, extensive excitation in the bending mode has been observed in CO_2 generated in the UV photolysis of pyruvic acid, a finding that is consistent with the evolution of the linear CO_2 molecule from the bent configuration (sp^2 hybridization) present in the carboxylic acid. Our ability to probe high vibrational levels in the CO_2 bending manifold enables us to determine which levels are directly excited as the molecule is being formed. This technique is being applied to

both gas phase and surface reactions in which the nature of the transition state has been characterized in spectroscopic or theoretical studies, with the hope of establishing correlations between the transition state and energy disposal in the product molecules. This research will eventually enable us to measure the nascent rotational/vibrational energy distribution and infer details of the chemical dynamics of much more complex reactions.

This research was also supported by the National Science Foundation under Grant CHE-80-23747 and the Department of Energy under contract DE-AC-02-78ER04940.

Figure 1

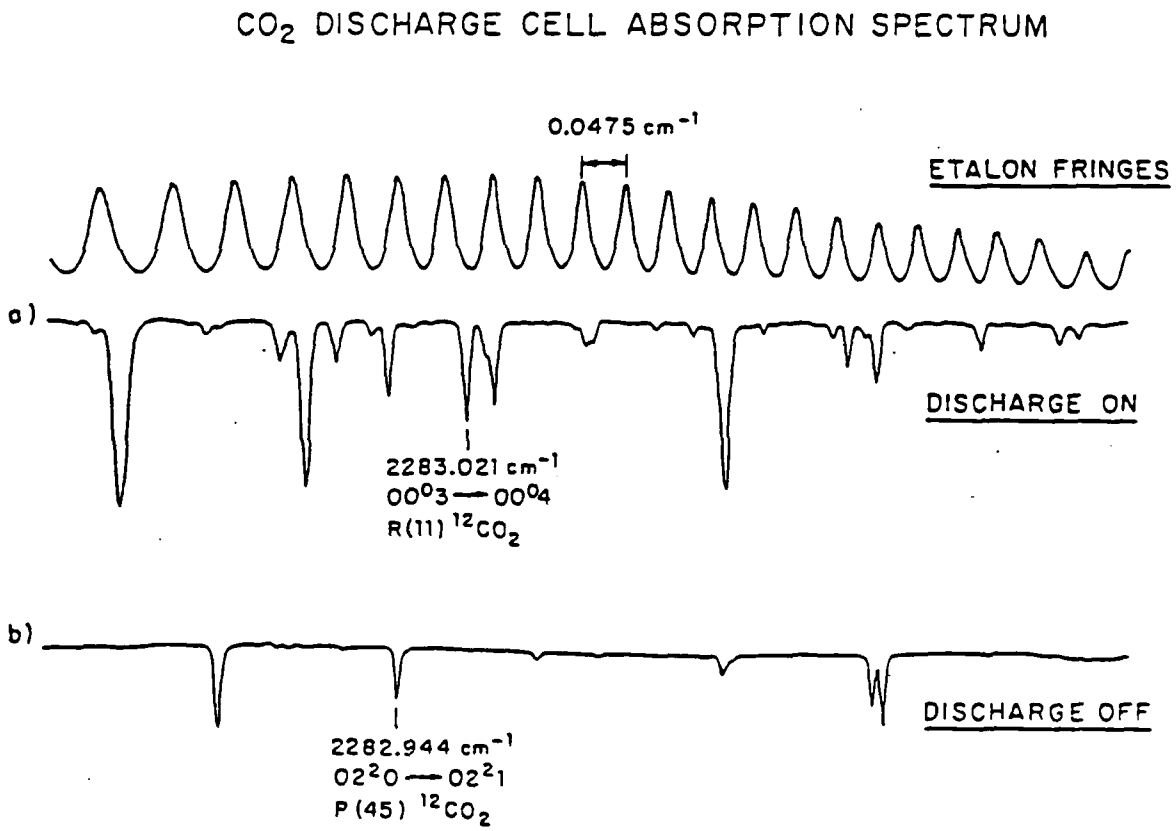
CO_2 DISCHARGE CELL ABSORPTION SPECTRUM
0.0475 cm^{-1}
ETALON FRINGES
a)
DISCHARGE ON
2283.021 cm^{-1}
$00^03 \rightarrow 00^04$
R(11) $^{12}CO_2$
b)
DISCHARGE OFF
2282.944 cm^{-1}
$02^20 \rightarrow 02^21$
P(45) $^{12}CO_2$

H. BOLOMETRIC EVIDENCE FOR CLUSTER FORMATION IN SUPERSONIC MOLECULAR BEAMS OF CO_2 AND C_4F_8

(G.B. Spector, B.B. Brady and G.W. Flynn)
(JSEP work unit 7, 1982 - 1985)
(Principal Investigator: G. Flynn (212)280-4162)

1. Introduction -- Cluster formation in molecular beams or free jet expansions of various species has been a subject of interest for a number of years. Molecular beams can be used to study such van der Waals' molecules, which form with condensation during supersonic expansion. Both the optimum conditions for forming clusters in beams and the optimum conditions for avoiding them are reasonably well known.[1-4] A description and analysis of the spectra of many of these van der Waals' molecules has been given in detail[5,6] and the bond strengths,[7,8] structure,[9,10] synthetic conditions[11] and energy transfer rates[12] of many clusters have been obtained using supersonic expansion techniques. Experiments have also been performed to investigate the importance of clusters in chemical reactions[13-15] and their interactions with surfaces.[16]

Quantitative methods for the determination of the distribution of van der Waals' molecules in supersonic expansions are still being developed.[17] Mass spectrometry provides only limited information concerning the cluster content of a beam or jet, as electron-bombardment ionization can easily dissociate the weak van der Waals' bond in many clusters. Thus, absolute percentages of clusters cannot be determined in this way. In the past few years, the technique of vibrational predissociation, where a laser predissociates clusters in the near collisionless or collisionless region of a beam, has been used with both mass spectrometers[18,19] and liquid helium cooled bolometers[20-23] as detectors. The predissociation leads to an attenuation of the molecular beam signal; this "negative" signal can be related to the cluster percentage in a beam.

In the present experiments we have used a bolometer to detect clusters

in molecular beams of CO_2 and C_4F_8. The bolometer measures total energy flux, which is composed of translational, internal and adsorption energies. Adsorption energy is simply the energy released to the bolometer when a particle condenses on its surface. The translational energy is determined simultaneously with the total energy flux by using a mass spectrometer for time-of-flight (TOF) measurements. Thus, the sum of internal and adsorption energies can be determined by difference. An upper limit for the internal energy can be obtained using the isenthalpic expansion equation for a free jet. In previous experiments,[24-26] the adsorption energy was approximated by the negative heat of vaporization of the particle under investigation, which, was found to be experimentally valid for Ar.[26] In the present experiments, the adsorption energy is investigated and used as a measure of the cluster content of a beam.

In molecular beams of CO_2, there is considerable cluster formation. Mass spectrometric studies have indicated the presence of extremely large clusters in expansions of neat and seeded beams of this molecule.[2] The internal energy of monomeric CO_2 is quite small in comparison to its adsorption energy; thus, it is an ideal molecule for studying adsorption energy in an experiment sensitive to the sum of internal plus adsorption energy. C_4F_8, by contrast, has considerable internal energy per molecule and also forms clusters readily. The adsorption energy trends determined for CO_2 can be used to estimate limits on the internal and adsorption energies of C_4F_8 and hence its degree of clustering.

2. Experimental -- A liquid He cooled bolometer measures energy flux, W ($W \sim n\langle v\rangle E_{tot}$), an ion gauge flux meter measures beam flux, F ($F \sim n\langle v\rangle$) and a mass spectrometer measures average velocity, $\langle v\rangle$, using time-of-flight (TOF) techniques. E_{tot} is the total energy of a particle striking the bolometer. From the TOF studies, velocity distributions are obtained; thus, the internal energy can be determined by difference. A low power, cw CO_2 laser, crossed at 90° with the molecular beam, is used both for irradiation inside a transparent capillary nozzle for excitation experiments and for vibrational predissociation experiments in the collisionless or

near-collisionless region downstream from the nozzle exit, similar to the experiments of Scoles, et al.[20-23] Stagnation pressures varied from 0-80 PSI. The source chamber pressure of the highly condensable C_4F_8 and CO_2 never rose above 1×10^{-5} Torr with liquid nitrogen cooling of the chamber.

3. Summary of Results -- (1) Supersonic molecular beams of CO_2 and C_4F_8 have been studied using a bolometer, mass spectrometer and flux meter to determine their energy characteristics; (2) At low backing pressures, the experimentally determined adsorption energy released by a CO_2 molecule upon condensation on a 1.8K bolometer surface was found to be in good agreement with that derived from the heat of vaporization of the molecule at the triple point; (3) At high backing pressures where significant clustering of CO_2 is known to occur, the effective adsorption energy determined experimentally for CO_2 was less than predicted and dropped essentially to zero at the highest stagnation pressures; (4) The effective adsorption energy measured experimentally for beams of C_4F_8 was always well below that predicted from the heat of vaporization for the molecule, suggesting the presence of significant numbers of clusters for C_4F_8 at all experimentally attainable pressures; (5) A simple model has been used to reconcile the observed decrease in effective adsorption energy by taking into account the formation of clusters in the beam; (6) The combination of bolometer, flux meter and mass spectral time-of-flight data, coupled with appropriate energy conservation considerations, has been found to provide a reasonably sensitive test for the presence of clusters in molecular beams.

We would like to thank Professor R.B. Bernstein for a series of fruitful discussions. In addition, we would like to acknowledge Professors B.J. Berne and J.L. Skinner for assistance with the theoretical model and Dr. J.T. Yardley for the loan of a high pressure gauge.

This research was also supported by the National Science Foundation under Grant CHE-80-23747 and the Department of Energy under contract DE-AC-02-78ER04940.

(1) J.B. Anderson, R.P. Andres and J.B. Fenn, Adv. Chem. Phys. 10, 275 (1966).

(2) O.F. Hagena and W. Obert, J. Chem. Phys. 56, 1793 (1972).

(3) D. Golomb, R.E. Good and R.F. Brown, J. Chem. Phys. 52, 1545 (1970).

(4) D. Golomb, R.E. Good, A.B. Bailey, M.R. Busby and R. Dawborn, J. Chem. Phys. 57, 3844 (1972).

(5) D.H. Levy, Ann. Rev. Phys. Chem. 31, 197 (1980).

(6) D.H. Levy, Adv. Chem. Phys. 47, 323 (1981).

(7) M. Hoffbauer, C.F. Giese and W.R. Gentry, J. Phys. Chem. 88, 181 (1984).

(8) M.J. Howard, S. Burdenski, C.F. Giese and W.R. Gentry, J. Chem. Phys. 80, 4137 (1984).

(9) G.D. Stein and J.A. Armstrong, J. Chem. Phys. 58, 1999 (1973).

(10) R.E. Smalley, D.A. Auerbach, P.S.H. Fitch, D.H. Levy and L. Wharton, J. Chem. Phys. 66, 3778 (1977).

(11) R.E. Smalley, D.H. Levy and L. Wharton, J. Chem. Phys. 64, 3266 (1976).

(12) M.P. Casassa, D.S. Bomse and K.C. Janda, J. Chem. Phys. 74, 5044 (1981).

(13) A. Gonzalez-Urena, R.B. Bernstein and G. Phillips, J. Chem. Phys. 62, 1818 (1975).

(14) D.R. Hardin, K.B. Woodall and R. Grice, Mol. Phys. 26, 1057 (1973).

(15) W.S. Struve, T. Kitigawa and D.R. Herschbach, J. Chem. Phys. 54, 2759 (1971).

(16) D. Dreyfuss and H. Wachman, Proceedings of the 12th International Symposium on Gas Dynamics (AIAA, New York, 1980) p. 183

(17) U. Buck and H. Meyer, Phys. Rev. Lett. 52, 109 (1984).

(18) J. Geraedts, S. Setiadi, S. Stolte and J. Reuss, Chem. Phys. Lett. 78, 277 (1981).

(19) J. Geraedts, S. Stolte and J. Reuss, Z. Phys 304A, 170 (1982).

(20) T.E. Gough, R.E. Miller and G. Scoles, J. Chem. Phys. 69, 1588 (1978).

(21) T.E. Gough, R.E. Miller and G. Scoles, J. Phys. Chem. 85, 4041 (1981).

(22) T.E. Gough, R.E. Miller and G. Scoles, Chem. Phys. Lett. 97, 155 (1983).

(23) D. Bassi, A. Boschetti, G. Scoles, M. Scotoni and M. Zen, Chem. Phys. 71, 239 (1982).

(24) D.R. Coulter, F.R. Grabiner, L.M. Casson, G.W. Flynn and R.B. Bernstein, J. Chem. Phys. 73, 281 (1980).

(25) M.I. Lester, D.R. Coulter, L.M. Casson, G.W. Flynn and R.B. Bernstein, J. Phys. Chem. 85, 751 (1981).

(26) M.I. Lester, L.M. Casson, G.B. Spector, G.W. Flynn and R.B. Bernstein, J. Chem. Phys. 80, 1490 (1984).

I. VIBRATIONAL PREDISSOCIATION OF SF_6 CLUSTERS IN A SUPERSONIC MOLECULAR BEAM

(B.B. Brady, G.B. Spector and G.W. Flynn)
(JSEP work unit 7, 1982 - 1985)
(Principal Investigator: G.W. Flynn (212)280-4162)

1. Introduction -- Cluster formation in molecular beams of various species has been a source of interest for a number of years.[1] Spectroscopists, dynamicists and theorists have studied van der Waals molecules using varied techniques. Unfortunately, the detection of clusters in molecular beams is not always a straightforward task. Many weakly bound van der Waals species dissociate in the electron-bombardment ionization region of a mass spectrometer. Thus, the major fraction of the clusters may be detected at the monomer or fragment masses, with no clue as to their original size. Although some signal may be detected at the parent cluster mass, such peaks do not provide an absolute measure of the amount of that particular cluster in the beam. Mass spectrometry, therefore, provides only limited information about the distribution of various clusters in a molecular beam. Similarly, flux detection has been found to be inaccurate in calculating the absolute cluster percentage.[2] Thus, the use of lasers to predissociate clusters has become an alternative method of study. Vibrational predissociation has been observed with visible lasers in the electronically excited states of van der Waals molecules[3-5] and IR lasers have been used to induce predissociation in the ground electronic state.[6,7]

In a previous study, the internal energy (E_{int}) in a molecular beam of SF_6[8-10] was measured. Using a bolometer, mass filter and flux meter, E_{int} at various laser and thermal excitation conditions was obtained. An isenthalpic expansion equation for conservation of enthalpy in a free jet was employed to predict E_{int} from time-of flight data. The predicted values of E_{int} were considerably larger than those measured experimentally at high nozzle temperatures (T_{nz}). The effect of cluster formation on measurements of E_{int} in these thermal experiments was considered, but no clusters were detected

mass spectrometrically. The data presented here, taken under similar experimental conditions, give a clearer idea as to the importance and possible effect of clusters in the previous experiments.

Dimers of SF_6 in a neat molecular beam were predissociated in the collisionless region by a low power, cw CO_2 laser. The dimers were detected by the decrease in energy flux, measured with a bolometer, when the dissociated particles left the beam. A model is developed which allows upper and lower limits on the percent dimer to be determined from the change in energy flux upon laser irradiation.

In conclusion, a sensitive laser technique has shown that dimers are present in neat beams of SF_6 under conditions corresponding to nozzle pressures ranging from 0 to 1,000 torr and nozzle temperatures of 290 to 550K. The percent of dimer found, however, is relatively small and does not appear to significantly affect the results of previous work.

A paper describing this work in detail will appear shortly in the Journal of Physical Chemistry.

This research was also supported by the National Science Foundation under Grant CHE-80-23747 and the Department of Energy under contract DE-AC-02-78ER04940.

(1) D.H. Levy, Annu. Rev. Phys. Chem. 31, 197 (1980) and references cited therein.

(2) W.R. Gentry, Rev. Sci. Instr. 53, 1492 (1982).

(3) C. Parmenter, J. Phys. Chem. 86, 1735 (1982) and references cited therein.

(4) D.V. Brumbaugh, J.E. Kenny and D.H. Levy, J. Chem. Phys. 78, 3415 (1983).

(5) R.E. Smalley, D.H. Levy and L. Wharton, J. Chem. Phys. 64, 3266 (1976).

(6) M. Hoffbauer, C.F. Giese and W.R. Gentry, J. Phys. Chem. 88, 181 (1984).

(7) M.F. Vernon, D.J. Krajnovich, H.S. Kwok, J.M. Lisy, Y.R. Shen and Y.T. Lee, J. Chem. Phys. 77, 47 (1982).

(8) D.R. Coulter, F.R. Grabiner, L.M. Casson, G.W. Flynn and R.B. Bernstein, J. Chem. Phys. 73, 281 (1980).

(9) M.I. Lester, D.R. Coulter, L.M. Casson, G.W. Flynn and R.B. Bernstein, J. Phys. Chem. 85, 751 (1981).

(10) M.I. Lester, L.M. Casson, G.B. Spector, G.W. Flynn and R.B. Bernstein, J. Phys. Chem. 80, 1490 (1984).

IV. PICOSECOND ENERGY TRANSFER AND PHOTOFRAGMENTATION SPECTROSCOPY

A. PHOTOPHYSICS AND PHOTOCHEMISTRY OF DIVALENT CARBON INTERMEDIATES

(E.V. Sitzmann, J. Langan and K.B. Eisenthal)
(JSEP work unit 6, 1985 - 1988)
(Principal Investigator: K.B. Eisenthal (212)280-3175)

Motivated by our observation of a large solvent effect[1] on singlet to triplet $S_1 \rightarrow T_o$ spin relaxation in diphenylcarbene (95 ps in isoctane and 310 ps in CH_3CN) we initiated a study on the effects of solvent intermolecular perturbations on carvbenes having different structures and in a wider range of environments. The carbene-solvent interactions are important not only in affecting intramolecular relaxation in the carbene itself ($S_1 \rightarrow T_o$) but in modifying the chemistry as well. Based on our studies [1-4] of diphenylcarbene (DPC) we proposed that the solvent dependent dynamics resulted from a change in the singlet-triplet energy gap which alters the singlet-triplet spin-orbit interaction. The solvent dependence of the energy gap was a consequence of the different energy stabilization of the polar singlet relative to the less polar triplet. This prediction that the gap was larger in a nonpolar solvent was confirmed for DPC [3,4]. The energy splitting in nonpolar isoctane was 1400 cm^{-1} compared with 950 cm^{-1} for polar acetonitrile.

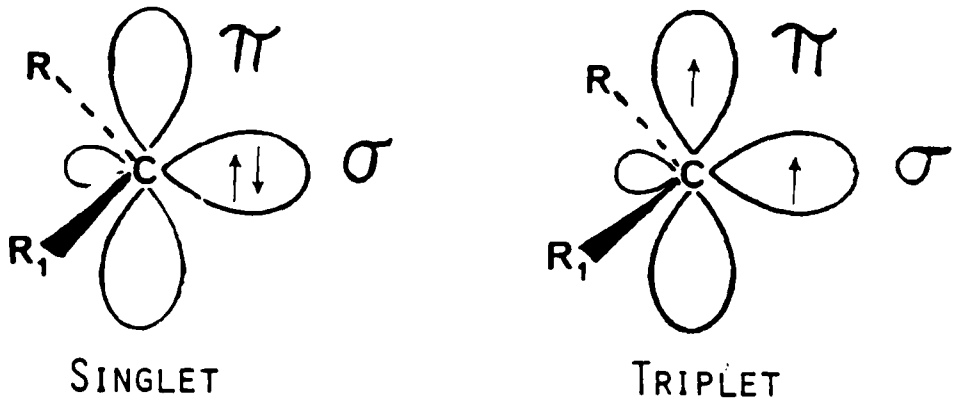

Scheme 1: Electronia configurations of lowest singlet and triplet states of Carbene.

Our study of the rates of intersystem crossing in DPC in solvents of different polarity showed that the rate constant decreased as the energy gap decreased. This is an inverse energy gap law in that intersystem crossing rates usually increase as the gap decreases. The key factor is that DPC has a small energy gap whereas the usual energy gap law applies to large gaps. The consequence of the small gap is that there is a sparse manifold of triplet vibronic states (ground triplet plus vibrations) with which the singlet is coupled. As the energy gap increases, e.g. in the less polar solvents, the triplet vibronic levels become increasingly congested in the vicinity of S_1 due to the contributions of higher frequency vibrations and due to the decrease in the spacing between the triplet vibronic levels. Accordingly, the rate of $S_1 \rightarrow T_o$ intersystem crossing increases.

1. Intramolecular Isotope Effects — To gain insight into $S_1 \rightarrow T_o$ relaxation and to further test the explanation of the variation of k_{ST} with ΔE_{ST} in carbenes we have investigated the effects of deuteration on intersystem crossing [5]. Since deuteration increases the number of final triplet vibronic states in the vicinity of the singlet S_1, it should increase the rate of intersystem crossing according to our explanation of the variation of k_{ST} with ΔE_{ST} due to solvent polarity. This corresponds to an inverse isotope effect which has precedents[6-8] in the $S_1 \rightarrow T_o$ intersystem crossing in some aromatics. Verification of this idea was obtained by comparing the rate of $S_1 \rightarrow T_o$ intersystem crossing of perdeuterated diphenylcarbene (DPC-d_{10}) versus perhydro diphenylcarbene (DPC-h_{10}) in a variety of solvents, Fig. 1. The origin of this effect is the small singlet-triplet splitting in diphenylcarbene which results in an intersystem crossing to a sparse manifold of triplet vibronic states. Deuteration increases the number of final triplet vibronic states in the vicinity of the singlet and in that way increases the intersystem crossing rate. The magnitude of the isotope effect is dependent on the solvent used. This dependence is caused by the variation of the singlet-triplet energy gap with solvent, the isotope effect being largest in the solvent for which diphenylcarbene has the smallest gap. We thus find a description of intersystem crossing in diphenylcarbene as a radiationless transition from S_1

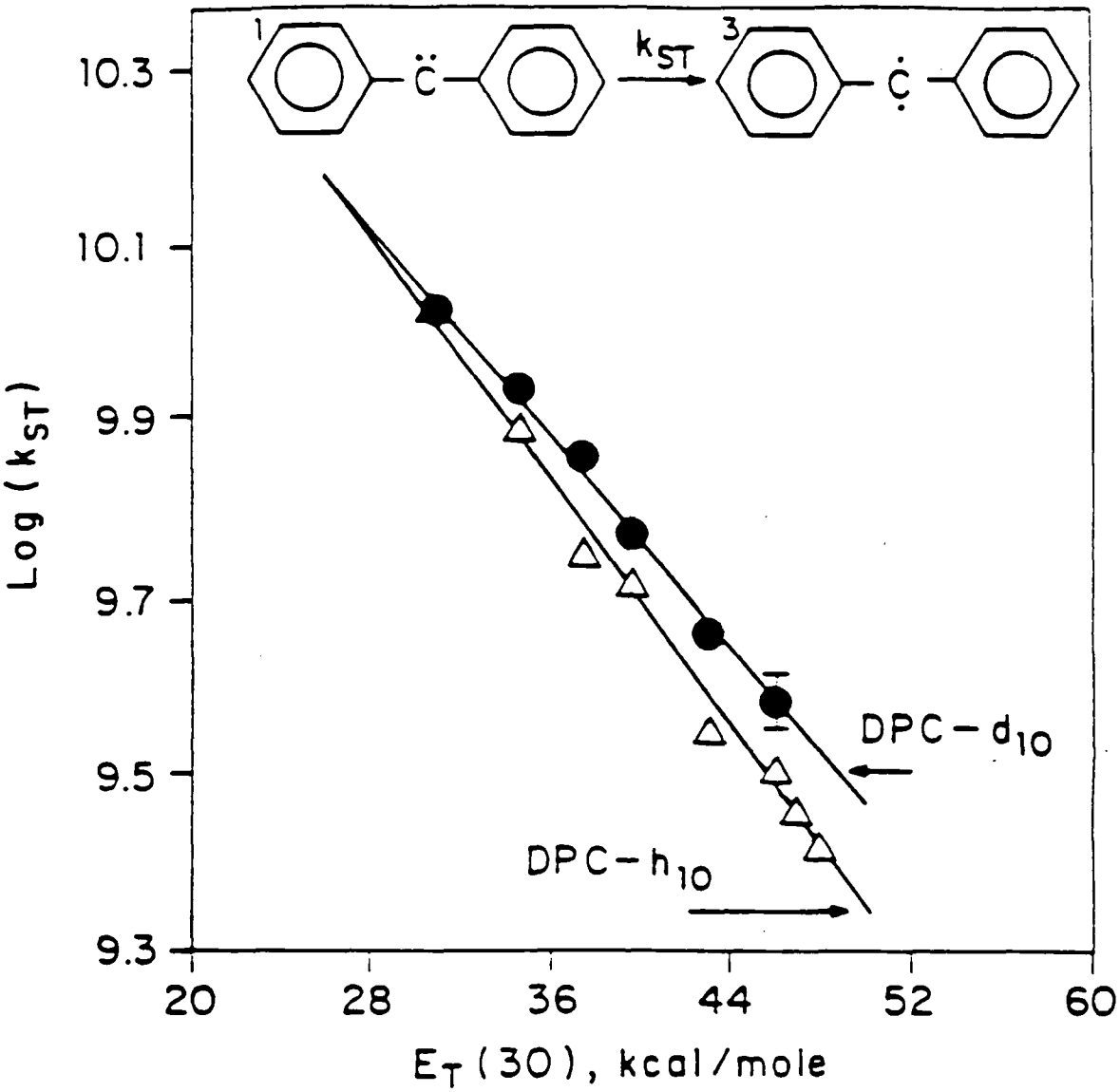

Figure 1. Plot of the logrithum of k_{ST} versus the solvent polarity parameter $E_T(30)$ for diphenylcarbene-h10 (Δ) and diphenylcarbene-d-10 (0).

to a sparse triplet manifold, due to the small energy gap, accounts for both the dependence of intersystem crossing on solvent polarity (an inverse gap effect) as well as the inverse isotope effect in a given solvent.

2. Relation Between Carbene Structure and Energy Relaxation --

(a) Dibenzocycloheptadienylidene -- A key feature in the description of energy relaxation in carbenes is the structure of the carbene and how it influences the $S_1 \rightarrow T_o$ dynamics. In order to examine this question in greater detail, we studied[9,10] another aromatic carbene, bibenzocycloheptadienylidene (DCHD). This molecular intermediate is similar to DPC, differing by an ethylenic bridge which connects the two phenyl rings to the central carbon atom.

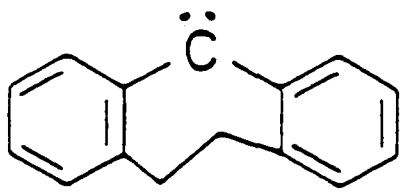

Dibenzocycloheptadienylidene (DCHD)

One effect of the restricting $-CH_2-$ groups in DCHD is to increase the angle between the central carbon and the connected phenyl rings relative to DPC. The results of the laser induced fluorescence experiment for DCHD are shown in Fig. 2. From our measurements of k_{ST} in a variety of solvents we find that DCHD also manifests an exponential dependence of k_{ST} on the solvent polarity parameter $E_T(30)$[11], hence giving the linear relationship shown in Fig. 3. The slopes for DPC and DCHD differ but the same exponential dependence of k_{ST} on $E_T(30)$ is seen.

From our findings in two aryl carbenes, DPC and DCHD, we proposed[9,10] that the $S_1 \rightarrow T_o$ transition was more rapid for DCHD (80 ps) than DPC (310ps)

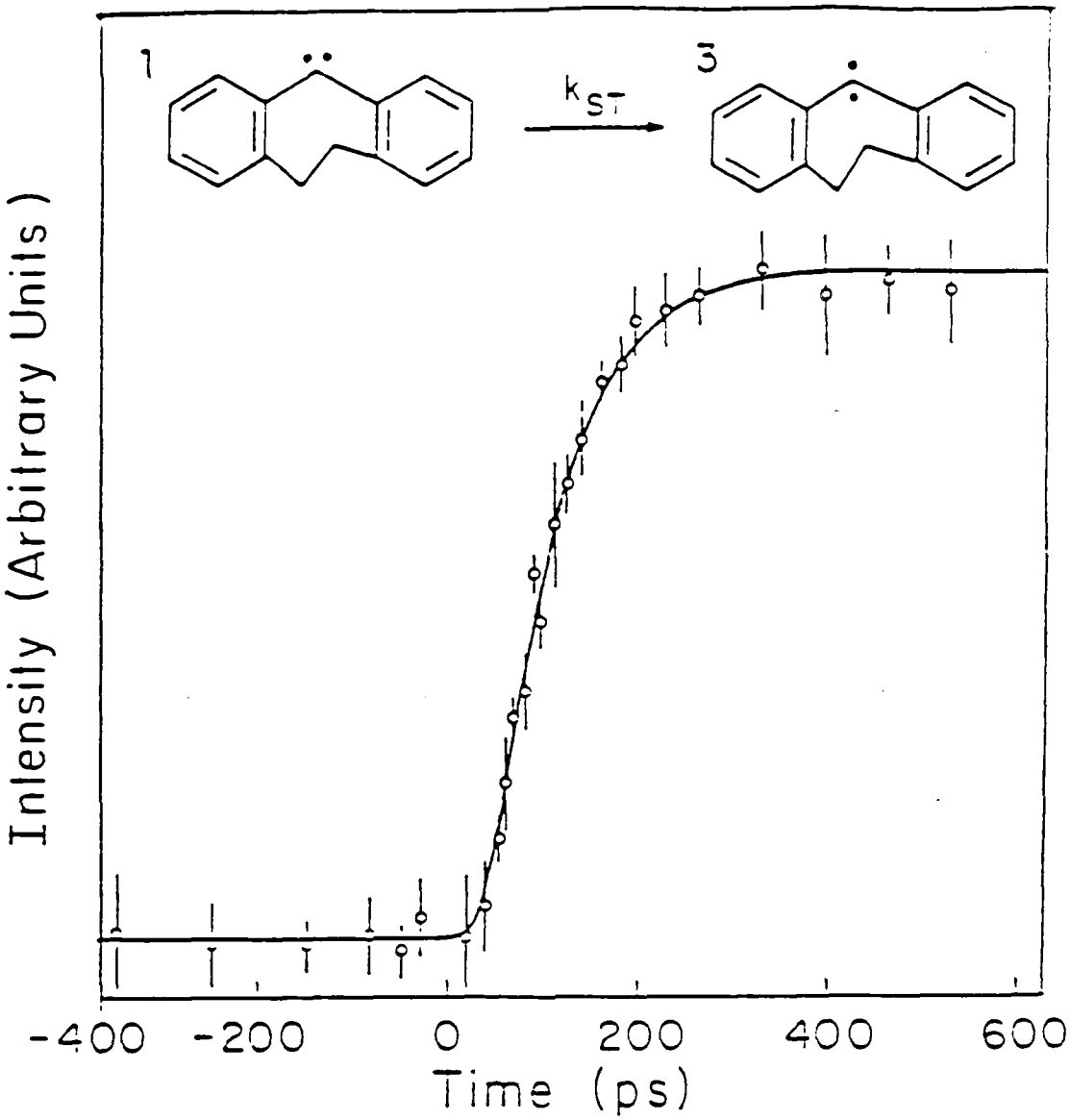

Figure 2. Laser-induced fluorescence of DCHD in tetrahydrofuran at 298 K as a function of time delay between 266 nm excitation and 355 nm probe pulses. The solid curve is a calculated fit.

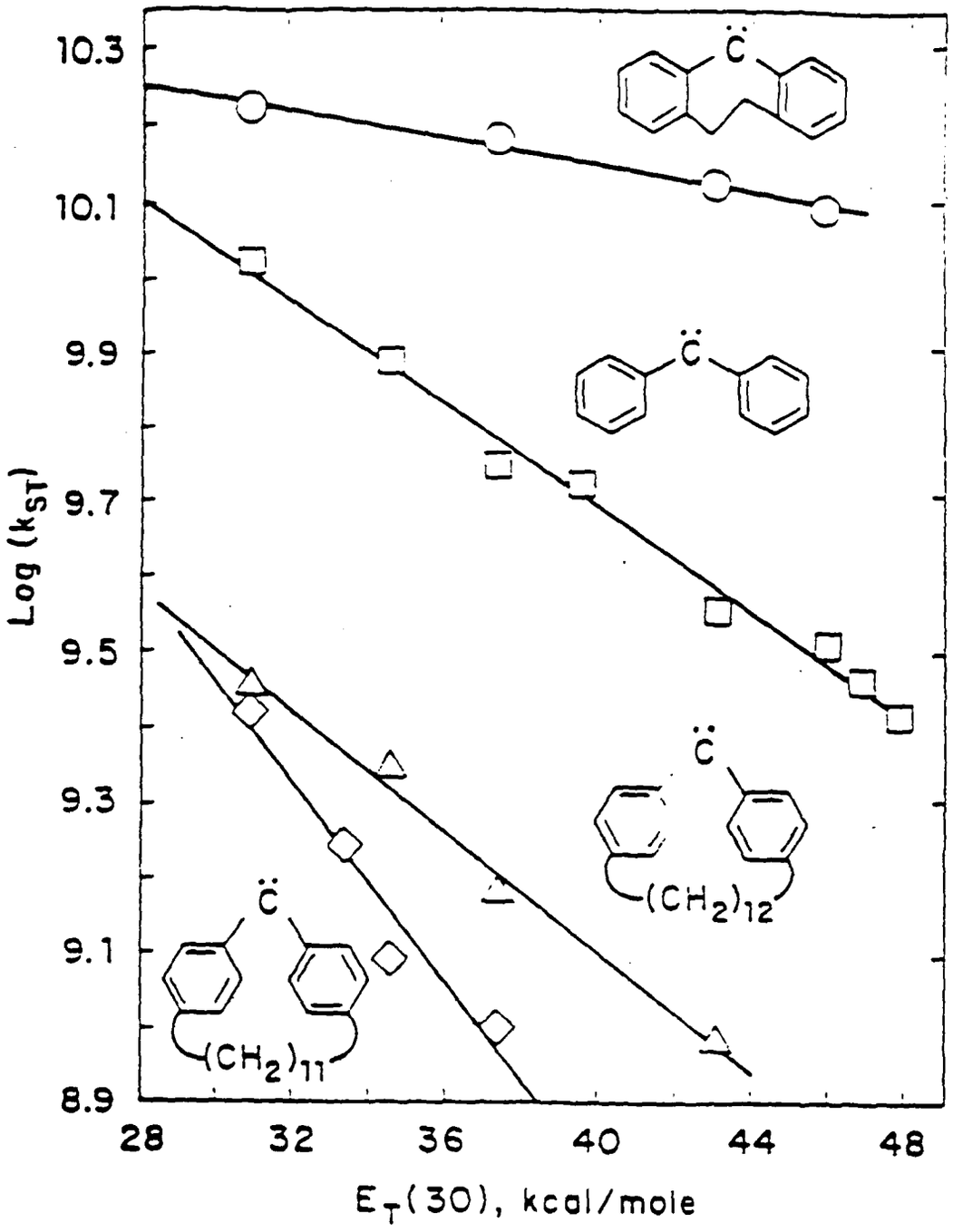

Figure 3. Intersystem crossing rates of dibenzocycloheptiadienylidene (O), diphenylcarbene (□), [1,12]C paracyclophane carbene (Δ) and [1,11]C paracyclophane carbene (◇) as a function of the solvent polarity parameter $E_T(30)$.

due to the larger energy gap in DCHD 1700 cm^{-1} versus 950 cm^{-1} for DPC. This energy gap ordering is a result of the variation of the central angle and phenyl-phenyl twist in the series of aromatic carbenes. This view is supported by theoretical calculations [12,13] that showed that as the central angle in a diaryl carbene decreases, i.e. the carbene becomes more bent, the singlet-triplet gap decreases. Since DPC is more bent than DCHD it has a smaller gap and thus a slower intersystem crossing $S_1 \rightarrow T_o$. This energy gap ordering is responsible for the ordering of the k_{ST} values, due to variation in the carbene structure in this case and due to variation in the solvent polarity for a given carbene for the case discussed earlier.

(b) Paracyalophane Carbenes — For the case of DCHD it was found that an ethylenic moiety linking the two phenyl rings can increase the bond angle of the central methylene carbon atom. However, by employing a slightly different construction for the $-(CH_2)_n-$ bridge one can also decrease the bond angle of the aromatic methylene, as exemplified by the paracyclophane carabenes. The paracyclophane carbenes are highly strained molecular intermediates, and as such, form a unique subclass of chemical intermediates. These diarylcarbenes possess specific steric and electronic structures which

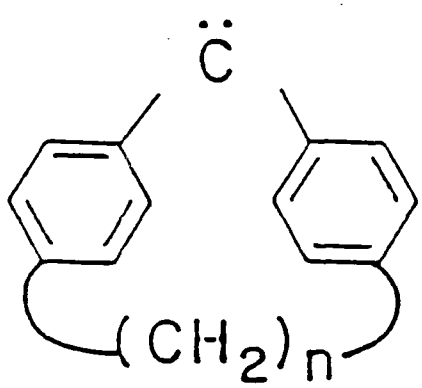

[1,n]C
Paracyclophane Carbene

depend on the length of the para-substituted alkane linkage.[14] For

example, EPR studies have shown[14] that there is a systematic decrease of the bond angle of the central methylene carbon atom (as well as an increase in the degree of phenyl-phenyl twist) in going from DPC to the [1,11]C paracyclophane. Furthermore, in collaboration with Professor Staab and Professor Turro we have determined that the energy splitting for [1,12]C is $\simeq 650\ cm^{-1}$ and for [1,11]C it is $\simeq 330\ cm^{-1}$.[15] The paracyclophane carbenes therefore have a very small singlet-triplet energy gap, which may be related to the fact their geometric sructures require small bond angles.

We have determined the intersystem crossing rate (k_{ST}) in a variety of solvents for the [1,12]C as well as for the [1,11]C paracyclophane carbene.[16] As illustrated by Fig. 3, the intersystem crossing rate in both paracyclophane carbenes exhibit a dramatic solvent polarity effect, being largest for the [1,11]C. It is also found that the paracyclophanes manifest an exponential dependence of k_{ST} on the solvent polarity parameter $E_T(30)$, hence giving the linear relationship shown in Fig. 3. It is pointed out hat the striking polarity dependence is the largest such effect observed for aryl carbenes, and is fully consistent with the fact that these carbenes possess an unusually small ΔE_{ST}.

(c) Dimesitylcarbene (DMC) — For the four aromatic carbenes, ranging from the paracyclophanes ($\Delta E_{ST} \simeq 300\ cm^{-1}$) up to and including DCHD ($\Delta E_{ST} \simeq 1700\ cm^{-1}$), it was found that they have sufficiently small energy gaps such that the rate of $S_1 \rightarrow T_o$ intersystem crossing decreases as the energy gap decreases, due to the solvent polarity effect. On the other hand, we have predicted that for a large singlet-triplet splitting the vibronic level structure in the triplet will be sufficiently dense so that the intersystem crossing rate will be a decreasing function of ΔE_{ST}, i.e., a normal gap dependence, which is typically found for large molecules. This limit where the relaxation dynamics of the intersystem crossing of a carbene follows the normal gap dependence is illustrated in the case of dimesitylcarbene (DMC). DMC is similar to DPC insofar as it is a simple divalent aromatic hydrocarbon which possesses a ground triplet state.[17-19] However, we have determined that its low lying singlet lies $>2450\ cm^{-1}$

AD-A163 402 RESEARCH INVESTIGATION DIRECTED TOWARD EXTENDING THE USEFUL RANGE OF THE ELECTROMAGNETIC SPECTRUM(U) COLUMBIA RADIATION LAB NEW YORK G W FLYNN ET AL. 3/4

UNCLASSIFIED 31 DEC 85 DAAG29-85-K-0049 F/G 20/6 NL

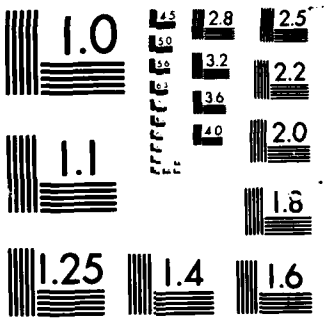

MICROCOPY RESOLUTION TEST CHART
NATIONAL BUREAU OF STANDARDS-1963-A

above the ground triplet.[20] The large singlet-triplet splitting found for DMC is attributed to the large steric repulsion between the mesityl groups bonded to the central methylene carbon which causes a more linear geometry for DMC and hence a larger ΔE_{ST}, compared to DPC. The dependence of k_{ST} on change in ΔE_{ST} for DMC[20] is opposite to the dependence observed for aryl

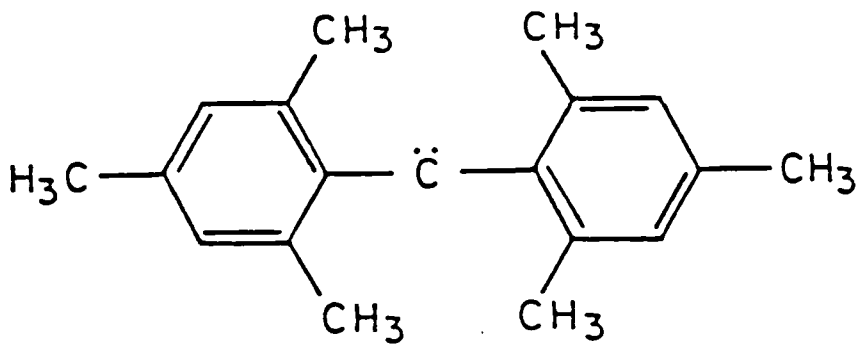

Dimesitylcarbens (DMC)

carbenes possessing smaller energy gaps, Fig. 4. Interestingly, in a nonpolar solvent such as isoctane, one finds that DMC does not fit the energy gap ordering of the intersystem crossing rates as observed for carbenes possessing small energy gaps. For instance, one finds the k_{ST} is larger for DCHD ($k_{ST} = 1.66 \times 10^{10}\ s^{-1}$) than it is for DMC ($k_{ST} = 1.05 \times 10^{10}\ s^{-1}$), even though DMC has the larger energy gap (see Fig. 5). A linear correlation, however, is found between the solvent dependence of the intersystem crossing rate and the energy splitting in all the carbenes that have been characterized. Taking the slope (β) of the line obtained from $\log(k_{ST})$ versus $E_T(30)$ as a measure of the dependence of the intersystem crossing rate on the solvent polarity it is found that the slope increases in value in the order of DMC > DCHD > DPC > [1,12]C > [1,11]C, which is identical to the ordering of the energy gaps for these carbenes (Fig. 6). We thus find that [1,11]C, which has the smallest gap in the group, has the most negative slope. For the carbenes with larger energy gaps (e.g. DCHD and DMC) the dependence on solvent polarity is weaker. Of particular significance is the

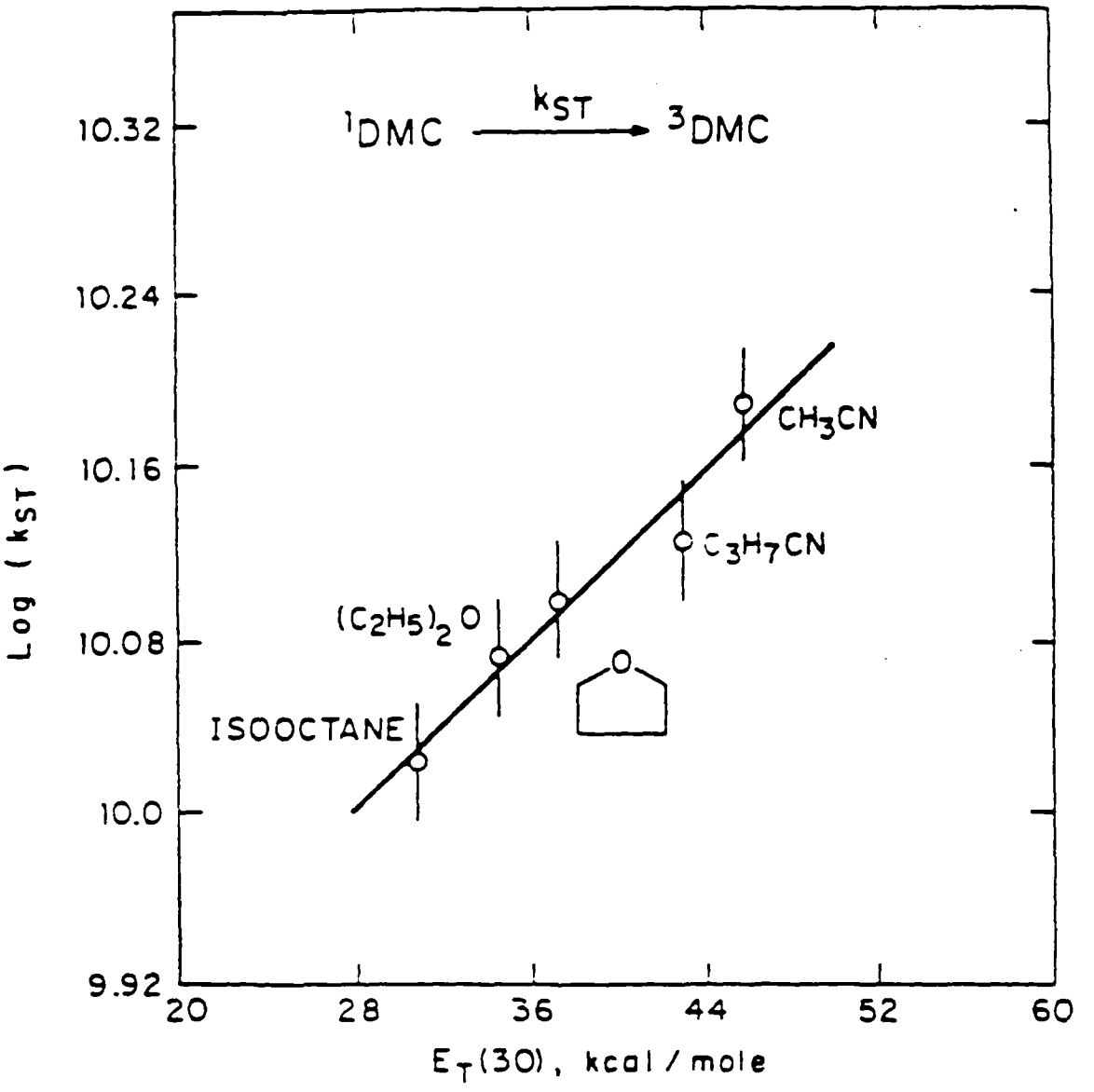

Figure 4. Intersystem crossing rate of dimesitylcarbene as a function of the solvent polarity parameter $E_T(30)$.

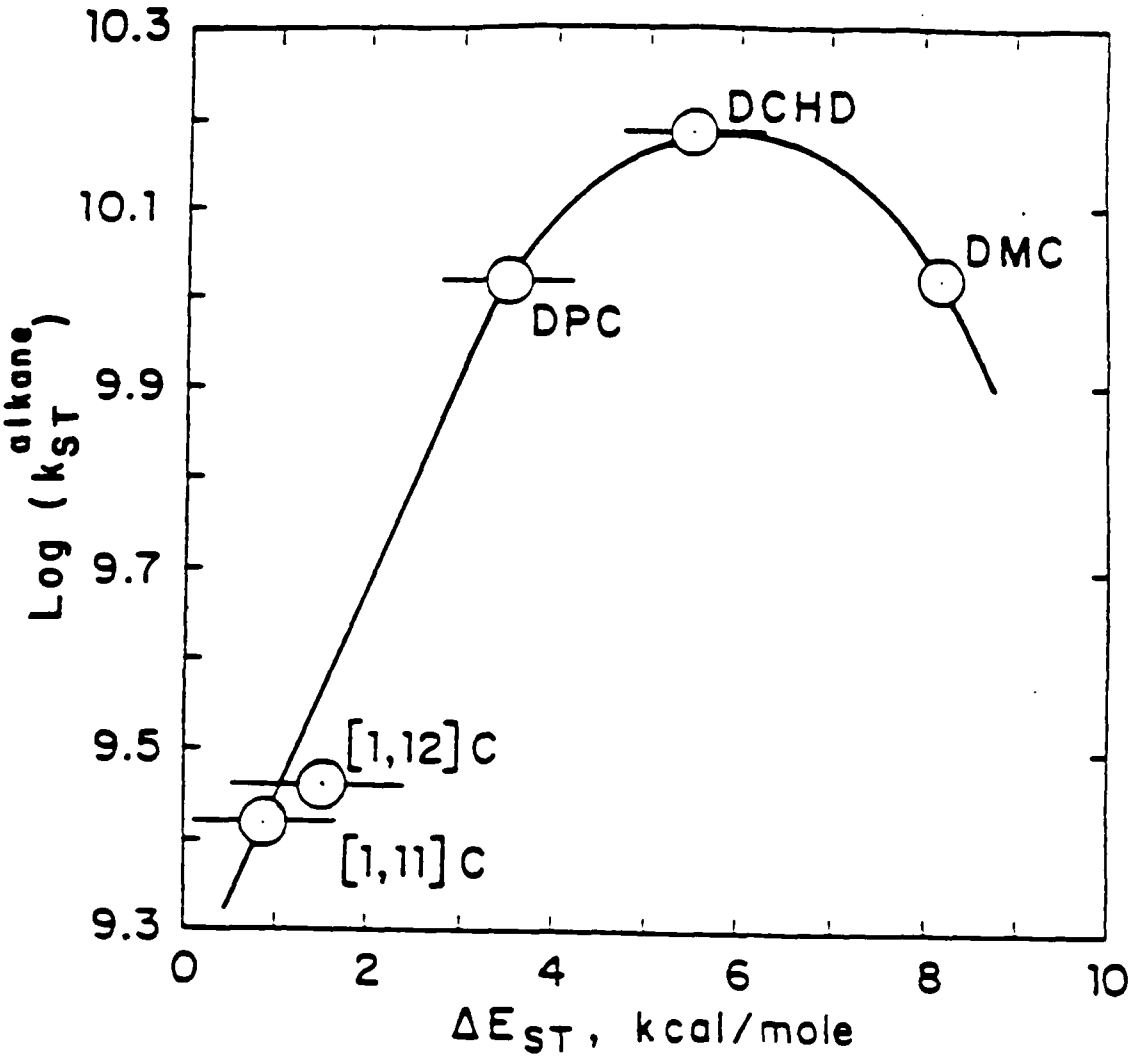

Figure 5. Plot of the logrithum of k_{ST}, obtained in nonpolar alkane solvent, versus ΔE_{ST} for various carbenes.

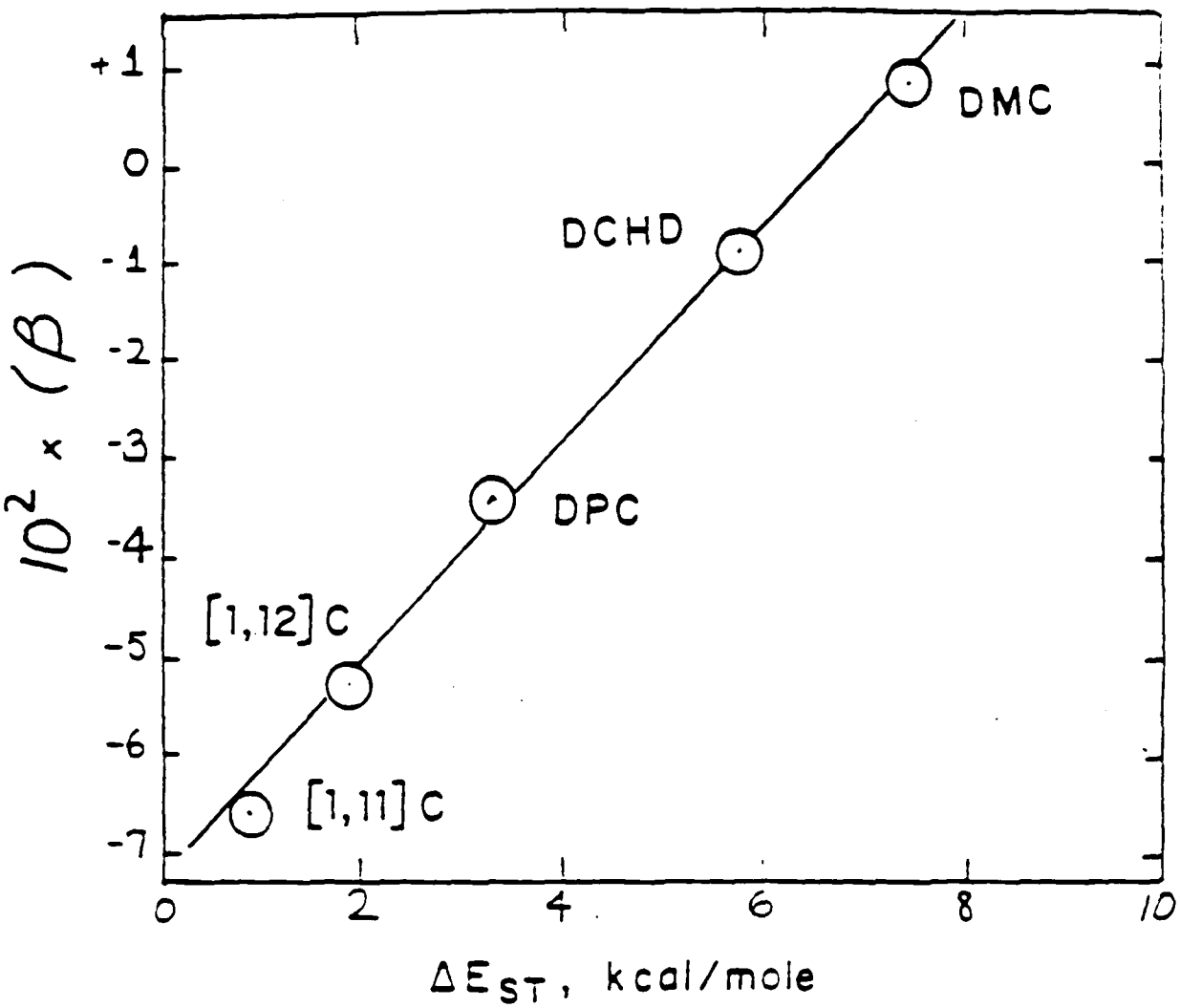

Figure 6. Solvent polarity dependence of k_{ST}, as a function of the singlet-triplet energy splitting for aryl carbenes. β is obtained from linear least squares fit of $\log(k_{ST}) = \alpha + \beta E_T(30)$, see text.

fact that we see a turn over in the solvent polarity dependence in going from DCHD to DMC. Namely, the slope (β) is negative for DCHD but positive for DMC. Such a result is reasonable if the triplet vibronic level structure in the vicinity of the singlet switches from the limit of a sparse manifold to the statistical limit of a dense manifold when the ΔE_{ST} is made large.

In summary, we have found that the singlet to triplet intersystem crossing rate of diaryl carbenes is a sensitive function of the energy splitting separating the singlet and ground triplet states. The solvent environment can also affect the intersystem crossing rate by altering the energy gap through a solvent polarity effect mechanism. A consistent picture of the relaxation dynamics in carbenes has been found by relating the solvent polarity dependence of the intersystem crossing rate to the ΔE_{ST}. The carbenes examined could be grouped into two main categories. Those which possess small ΔE_{ST} (<2000 cm^{-1}) fall into the sparse gap limit, and will exhibit inverse deuterium isotope effects as well as an inverse gap effect on intersystem crossing rates. The second group, as exemplified by DMC, is characterized by having a large ΔE_{ST} (> 2450 cm^{-1}) and/or a dense manifold of states, which results in the rate of intersystem crossing being an inversely varying function of the energy splitting.

3. Effects of Reactants on Modifying Intramolecular Energy Relaxation of Carbenes — A particularly important carbene reaction is the quenching of the singlet state with alcohols to form ethers.[21,22] Although it is a classic carbene reaction, no direct kinetic information was known about it. Using picosecond methods we have[23] been able to provide quantitative kinetic information on this reaction as well as to provide further insight into the intermolecular effects on intersystem crossing of carbenes. By measuring the singlet state lifetime of the carbene in the presence of the alcohols we were able to show that the reactant molecules provide not only a chemical decay channel for the singlet state but also an intramolecular decay channel which is due to a solvent polarity effect. These chemical and physical effects can act in opposite directions leading to novel results such as a significant increase in the singlet state lifetime upon addition of reacting molecules.

Photoexcitation of diphenyldiazomethane in the ultraviolet yields ^{1}DPC upon loss of nitrogen from the excited singlet state of the diazo compound. Once formed, ^{1}DPC can either react with alcohol to form ether or can decay via intersystem crossing into the ground triplet manifold (Scheme 2). The rate of triplet formation (^3k_f) in this case should then be equal to the sum of the rate of singlet-triplet converstion (k_{ST}) and the pseudo-first-order rate of singlet quenching (k_1[ROH]).

$$1/\tau_{^1DPC} = {}^3k_f = k_{ST} + k_1[ROH] \qquad (1).$$

The value of ^3k_f was measured by means of the laser induced fluorescence experiment, and was used to evaluate the effects of alcohol on the singlet state dynamics.

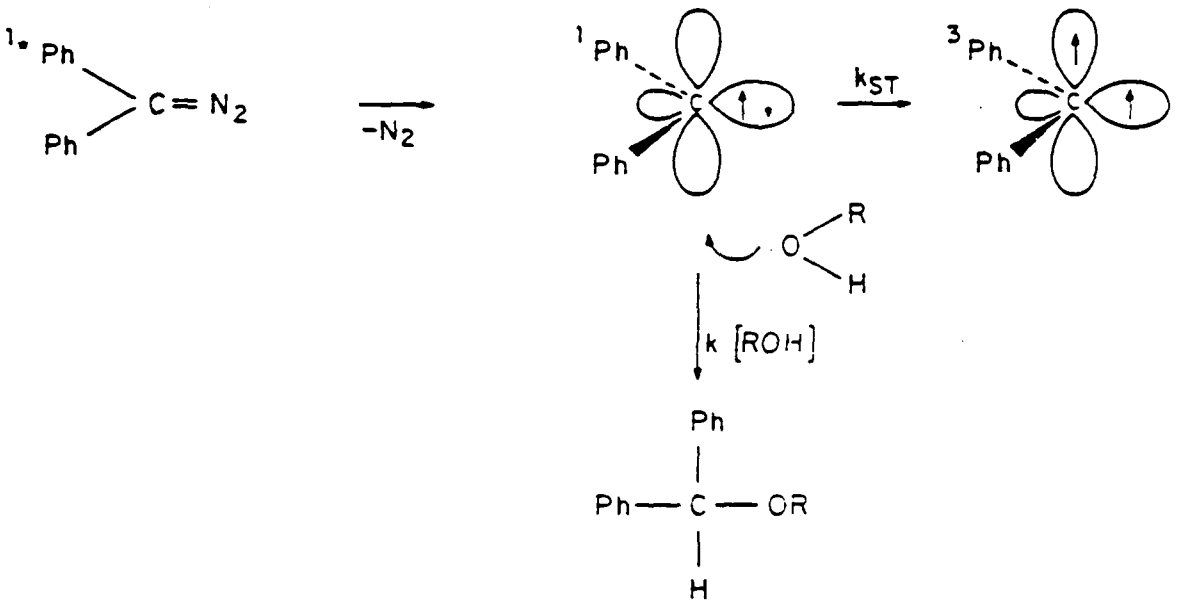

Scheme 2. Alcohol quenching of singlet diphenylcarbene.

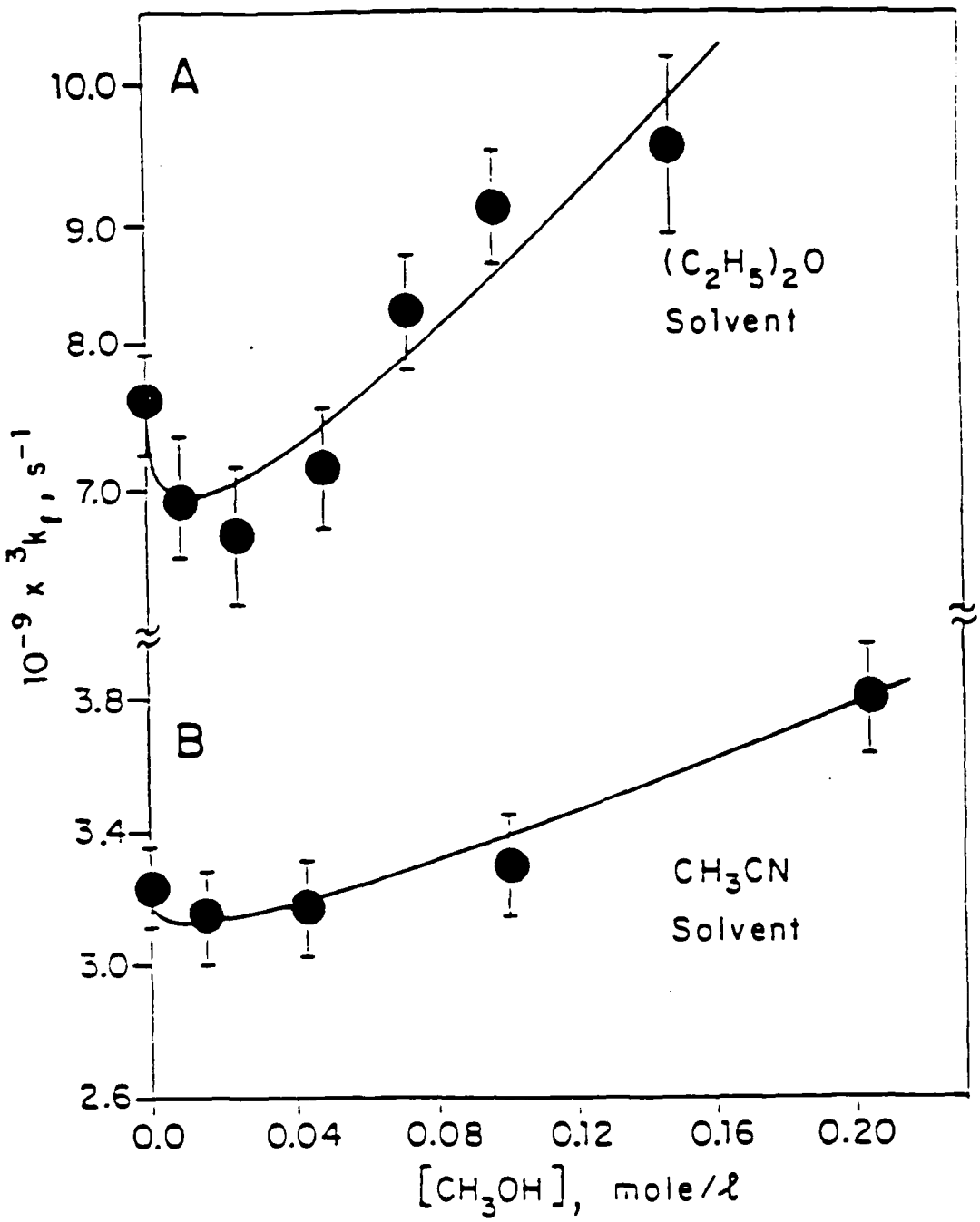

Figure 7. ${}^3k_f$ as a function of methanol concentration, using diethylether (A) and acetonitrile (B) as a solvent. The solid curves are calculated fits.

Using methanol as the quencher it is found that the rate of triplet formation is not a linear function of the alcohol concentration. It is found (Fig. 7) that with increasing concentration of methanol the value of ${}^3k_f$ initially decreases and then, after reaching a minimum, increases linearly. An even more dramatic effect is produced when diethylether is used as a solvent, where a sharp minimum in ${}^3k_f$ is clearly seen as the concentration is increased. These observations can be explained by recognizing the effect of solvent polarity on k_{ST}. A consequence of this dependence for bimolecular reactions of the carbene will be a significant change in the carbene spin equilibration rate may result by the addition of reactant molecules. In other words, k_{ST} may no longer remain a constant, but may change as the concentration of the quencher changes. Hence if solvent polarity is a rapidly varying function of alcohol concentration k_{ST} must then become a function of alcohol concentration as well. Since methanol is much more polar than acetonitrile and diethylether, it is expected that k_{ST} will decrease upon addition of methanol to the solvent, due to the increase in polarity of the mixture. At a low methanol concentration the rate of chemical quenching is small compared to k_{ST} and in this domain polarity effects will dominate the singlet state dynamics resulting in an increase in the singlet state lifetime. At high methanol concentration, the chemical decay channel dominates the singlet state dynamics, dwarfing the effects of alcohol on k_{ST}, and ${}^3k_f$ increases with quencher concentration in a linear fashion.

It is pointed out that if one were to use an alcohol and a solvent which have the same polarities, then no change in k_{ST} is expected on adding alcohol; for this case a simple linear dependence of ${}^3k_f$ is expected. Verification of this idea was obtained (Fig. 8) by choosing 3-pentanol ($E_T(30)$ = 45.7 kcal/mole) as the solvent. It is found that ${}^3k_f$ is a linearly increasing function of the 3-pentanol concentration. The slope of the fitted line yields the rate constant of $k_1 = (2.04 \pm 0.08) \times 10^9\ M^{-1}S^{-1}$. The intercept, which according to equation (1) must equal k_{ST} is found to be equal to $(3.29 \pm 0.04) \times 10^9\ s^{-1}$, the same as the experimentally determined value of k_{ST} in the neat solvent, $(3.23 \pm 0.19) \times 10^9\ s^{-1}$. After correcting for the polarity effects due to the addition of the alcohol quencher one can obtain the intrinsic reactivity of ^{1}DPC with different alcohols in a given

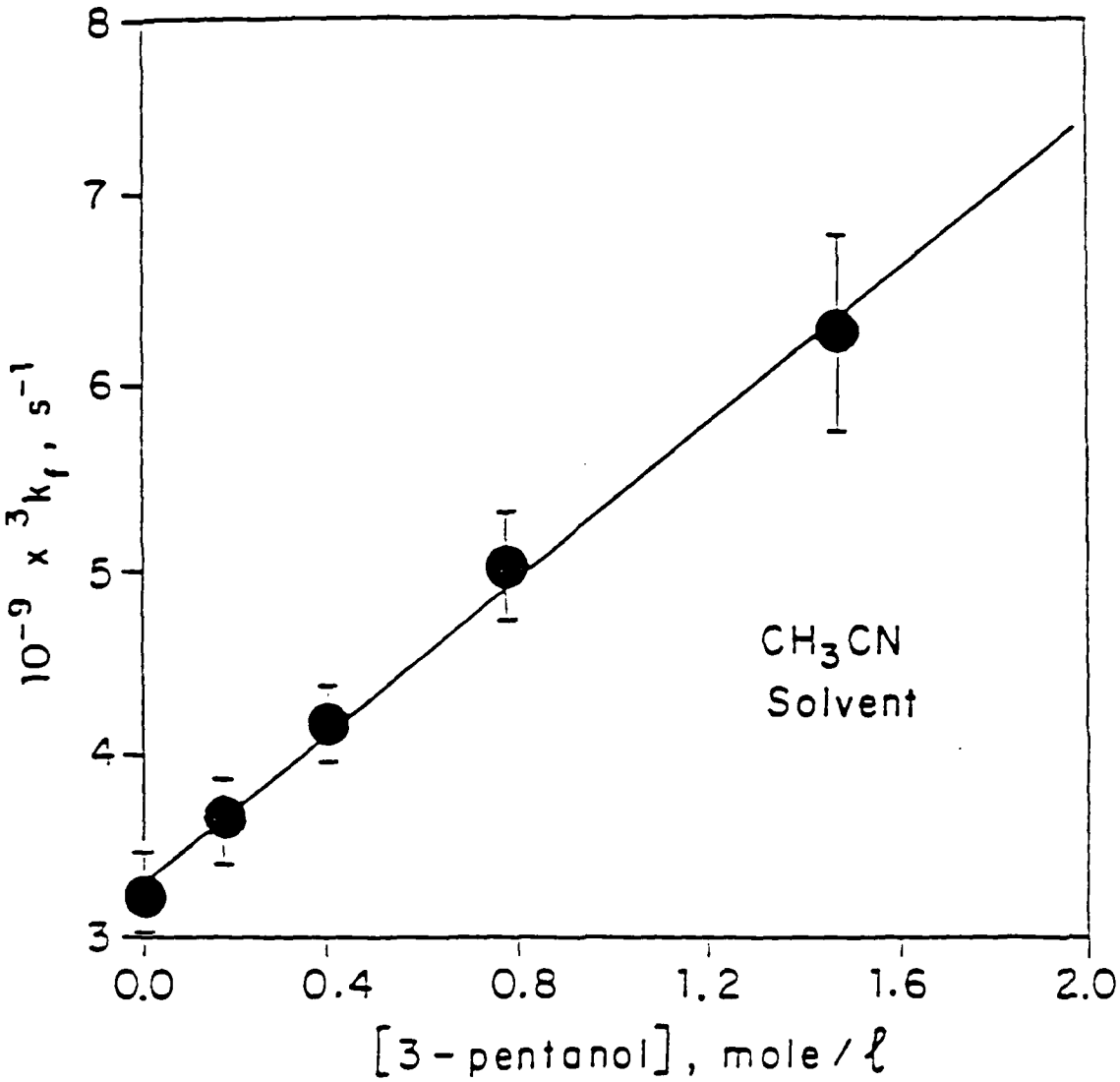

Figure 8: ${}^3k_f$ as a function of 3-pentanol concentration, using acetonitrile as solvent.

solvent. In this way it is found that methanol is 2.5 times more reactive than 3-pentanol with ^{1}DPC, in acetonitrile. This result is consistent with the model which relates reactivity with O-H bond lability of the alcohol.[3,4,24,25]

This work was also supported by the Air Force Office of Scientific Research under Grant AFOSR-84-0013B and the National Science Foundation under Grant NSF-CHE82-11593.

(1) E.V. Sitzmann, J. Langan, and K.B. Eisenthal, J Am. Chem. Soc., 106 (1984) 1868.

(2) K. B. Eisenthal, R.A. Moss and N.J. Turro, Science, 225 (1984) 1439 .

(3) E.V. Sitzmann and K.B. Eisenthal, in Applications of Picosecond Spectroscopy to Chemistry, K. B. Eisenthan, ed., (D. Reidel Publishing, Dordrecht, 1984) 41.

(4) K.B. Eisenthal, N.J. Turro, E.V. Sitzmann, I.R. Gould, G. Hefferon, J. Langan and Y. Cha, Tetrahedron, 41(1985) 1543 .

(5) J.G. Langan, E.V. Sitzmann and K.B. Eisenthal, Chem. Phys. Lett., in press (1985).

(6) A. Amirav, M. Sonnerschein and J. Jortner, Chem. Phys. Lett., 100 (1983) 488..

(7) E.C. Lim and H.R. Bhattacharjee, Chem. Phys. Lett., 9 (1971) 249.

(8) B. Sharf and R. Silbey, Chem. Phys. Lett., 5 (1970) 314.

(9) J.G. Langan, E.V. Sitzmann, and K.B. Eisenthal, Chem. Phys. Lett., 110 (1984) 521.

(10). E.V. Sitzmann, J.G. Langan, Z.Z. Ho and K.B. Eisenthal, in Ultrafast Phenomena IV, D.H. Auston and K.B. Eisenthan, eds., (Springer-Verlag, Berlin, 1984) 330.

(11) C. Reichardt in Molecular Interactions, H. Ratajeck, W.J. Orville-Thomas, eds., (John Wiley, N York, 3, 1982) 241.

(12) J. Metcalfe and E.A. Halevi, J. Chem. Soc., Perkin Trans. II, 534 (1977).

(13) R. Hoffman, G.D. Zeiss and G.W. Van Dine, J. Am. Chem. Soc., 90 (1968) 1485 .

(14) R. Alt, H.A. Staab, H P. Reisenauer and G. Maier, Tetr. Lett., 25 (1984) 633.

(15) K.B. Eisenthal, H.A. Staab and N.J. Turro, unpublished results.

(16) K.B. Eisenthal, H.A. Staab, E.V. Sitzmann, R. Alt and J.G. Langan, manuscript in preparation.

(17) H.E. Zimmerman and D.H. Paskovich, J. Am. Chem. Soc., 86 (1964) 2149.

(18) A.S. Nazran, E.J. Gabe, Y. Lepage, D.J. Northcott, J.M. Park, and D. Griller, J. Am. Chem. Soc., 105 (1983) 2912.

(19) A.S. Nazran, D. Griller, J. Am. Chem. Soc., 106 (1984) 543.

(20) K.B.Eisenthal, D. Griller, E.V. Sitzmann, and J.G. Langan, manuscript in preparation.

(21) W. Kirmse, Carbene Chemistry, 2nd ed., Academic Press, New York, 1971.

(22) G.L. Closs, and B.E. Rabinow, J. Am. Chem. Soc., 98 (1976) 8190.

(23) E.V. Sitzmann, J.G. Langan, and K.B. Eisenthal, Chem. Phys. Lett., 112 (1984) 111.

(24) W. Kirmse, Annalen 666 (1963) 9.

(25) E.V. Sitzmann, Y. Wang and K.B. Eisenthal, J. Phys. Chem. 87 (1983) 2283.

B. TWISTED INTERNAL CHARGE TRANSFER PHENOMENA

(J.M. Hicks, M.T. Vandersall and K.B. Eisenthal)
(JSEP work unit 6, 1985-1988)
(Principal Investigator: K.B. Eisenthal (212)280-3175)

1. Hydrogen Bonding and Polarity Effects on Barrier Crossings in Solution: p-dimethylamino-benzonitrile in n-alcohols - To continue the study of polar solvent effects on the dynamics of excited state charge transfer, the Twisted Internal Charge Transfer (TICT) of p-dimethylamino-benzonitrile (DMABN) was studied in n-alcohol solutions. DMABN undergoes both a structural change (90° twist about the amino-phenyl bond) and an electronic change (charge transfer from the dimethylamino portion to the benzonitrile moiety) in the excited state in polar solvents.[1] Scheme I is the so-called Twisted Internal Charge Transfer (TICT) model for the anomalous dual fluorescence of DMABN in polar solvents.[1]

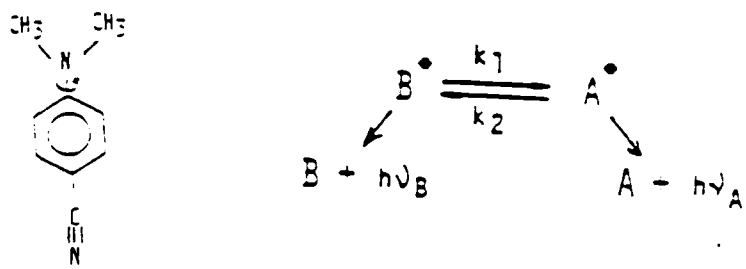

SCHEME I

The B state corresponds to the planar form (twist of angle of 0°), while A refers to the twisted (90°) charge transfer state. In alkanes, only the B fluorescence is observed, whch indicates that the excited state potential surface connecting the planar and twisted forms is dependent on solvent polarity.[2] Despite numerous kinetic studies,[3-6] the role that the solvent plays in determining the dynamics of TICT is still the subject of controversy.

We found that the height of the barrier to this transition for DMABN in normal nitriles depends linearly on the solvent polarity, as measured by the Dimroth $E_T(30)$ value.[7] This polarity dependence of the rate, as given in equation 1, then accounted for the variation of isomerization rates of DMABN observed in the series of neat nitriles.

$$k = C \times \exp(A(E_T(30)-30)/RT) \times \exp(-E_a^{o}/RT) \qquad (1)$$

Here, C is the Arrhenius frequency factor, A is a constant independent viscosity and temperature, and E_a^{o} is the activation energy of the TICT process in an alkane solvent having an $E_T(30)$ of 30 kcal/mole. The viscosity differences through the nitrile series, from .5 to 1.8 cP, did not seem to affect the rate. However, in our previous study, we were not able to determine with confidence the role of solvent viscosity in the TICT process because the correction to the barrier height for polarity changes introduced too much uncertainty. In this study, we have extended the viscosity range of the solvents by using n-alcohols. We wish to clarify the role of the solvent in TICT by separating the effects on k_1 by solvent polarity, viscosity and hydrogen bonding. To accomplish this the rate constants in Scheme I were measured for DMABN in a wide range of neat, normal alcohols at various temperatures. The value of k_1 is calculated for each solvent at a given temperature from the observables k_{obs} (the rate of fast decay of the B emission and the rise of the A emission) and F, the fraction of fluorescence at time zero in the slowly decaying component of the short wavelength band (the planar B state). Based on our observation that the sum of the excited states rates, $k_1 + k_2$, is large compared to the population decay rates of the two excited states, k_A and k_B, equation 2 is obtained (see

reference 4).

$$k_1 = k_{obs}\ (1-F) = (k_1 + k_2)\ (1-F) \qquad (2)$$

To illuminate the differences between protic and aprotic solvation of DMABN, the data for DMABN in alcohols and nitriles are directly compared.

For all of the neat samples studied, the dynamical processes of the DMABN isomerization shown in Scheme I have been verified. Table I gives the results of experiments conducted on the fast components of the fluorescence of DMABN in neat normal alcohols and nitriles. The observed formation and decay rates (k_{obs}) are equal within experimental error, which confirms that the A population originates from the B population.

First it should be noted that, through the series of nitriles and alcohols, solvent dielectric relaxation times vary. If the rate of TICT is limited by the rate of solvent rearrangement, the TICT times should follow the solvent dielectric relaxation times.[8-10] In Table I the first two dielectric relaxation times are shown for the alcohols. It is observed that there is no agreement between these values and TICT times, even when the dielectric relaxation times are corrected for the presence of a constant charge.[12,13] Thus, the TICT process does not seem to be rate-limited by any of the characteristic reorientational motions of the solvent.

To separate the effects of solvent polarity and viscosity on the isomerization dynamics, we have used two techniques: (i) k_{obs} was measured at room temperature in isoviscous mixtures of an alcohol and an alkane, where the polarity of the mixture was controlled by the concentration of the alcohol, and (ii) the temperature was varied for the neat solvents so that the solutions had the same viscosity but different polarity values. In the isoviscosity experiment with butanol/hexadecane mixtures (data from reference 3), it is found that there is a linear relationship between the logarithm of k_1 and the solvent polarity parameter, $E_T(30)$ (see Fig. 1). It is observed that the slopes of the lines, the constant A in equation 1, are equal, but the rates of formation of the charge transfer state at a given $E_T(30)$ value are in fact smaller for DMABN in alcohols than in nitriles.

From the isoviscosity experiments performed in neat alcohols at

different temperatures, it is possible to calculate the Arrhenius parameters of DMABN in alcohols. An inverse temperature dependence of k_1 in isoviscous alcohols is obsereved. Without the polarity factor in equation 1, a negative activation energy is obtained. The effect can be traced to the fact that the polarity of the liquids increases as the temperature is lowered, making the barrier to the isomerization lower. Upon correction of k_1 for changes in solvent polarity, a positive activation energy is obtained for both nitriles and alcohols. Figure 2 is an Arrhenius plot of the polarity-corrected rate, K , where K is given by equation 3.

$$K = k_1 \times \exp(-A(E_T(30)-30)/RT) \qquad (3)$$

While for the nitriles the observed slope corresponds to a barrier height in an alkane of 8.0 ± .7 kcal/mole, for alcohols, the value is 14.3 ± .7 kcal/mole. At a given $E_T(30)$, the height of the barrier to TICT in alcohols is higher than that in nitriles, by about 6.3 ± 1.4 kcal/mole. The barrier raising effect caused by the hydrogen bonding explains why, for an isopolar alcohol and nitrile, the TICT rate is faster in the nitrile. The hydrogen bonding, which withdraws electrons from the donating end of the molecule, opposes the charge transfer and thus must be broken before TICT can take place. The additional energy needed to do the bond breaking, 6.3 kcal/mole, is on the order of typical hydrogen bond strengths.

The viscosity of the DMABN solution has been varied in two ways in order to investigate the viscosity dependence of the rate expression (Eq. 1). First, the series of n-alcohols was used (Table I), and the rate k_1 of TICT of DMABN was corrected for changes in the $E_T(30)$ values. Then, the temperature was varied for DMABN in hexanol and corrections were made to these k_1 values for polarity and temperature changes.

The viscosity dependence of the rate is usually expressed as $1/\eta^{a}$ (Ref. 14). In Figure 3, the logarithm of the polarity-corrected rate, K, as defined by eq. 3, is plotted vs. the logarithm of the viscosity for DMABN in n-nitriles and n-alcohols at room temperature, and for hexanol at different temperatures. The best fit line suggests that there is little or no viscosity dependence on the TICT rate of DMABN in the viscosity range .5 to

TABLE I

RATES FOR TICT OF DMABN IN NORMAL ALCOHOLS AND NITRILES AT 20 DEG C

SOLVENT	η	$E_T(30)$	τ_1	τ_2	τ_1'	F	k_{obs}	k_1	$1/k_1$	k_2	K_{eq}	E_η
n. C_3H_7OH	2.23	50.7	430	21.9	81	.03±.01	3.70±.30	3.59±.35	28±3	.11±.05	32±11	4.2
n. C_4H_9OH	2.98	50.2	668	27.0	127	.06±.01	2.86±.17	2.74±.21	36±3	.11±.04	16± 4	4.6
n. $C_6H_{13}OH$	5.23	48.8	1210	31.0	300	.10±.01	1.41±.08	1.27±.12	79±7	.14±.04	9± 1	5.1
n. $C_8H_{17}OH$	8.95	48.3	1700	38.7	484	.10±.02	1.23±.07	1.11±.10	90±9	.12±.03	9± 1	6.0
n. $C_{10}H_{21}OH$	14.3	47.6	2019	47.5	699		.74±.02					6.3
n. C_4H_7N	.586	43.0		7		.075±.01	7.1±1.2	6.6±1.4	15±2	.54±.17	12± 2	2.0
n. C_5H_9N	.741	42.8				.078±.01	6.7±1.0	6.1±1.2	16±2	.52±.16	12± 2	2.2
n. $C_6H_{11}N$	.975	42.2				.08±.01	6.25±.89	5.8±1.0	17±2	.50±.14	12± 2	2.6
n. $C_8H_{15}N$	1.632	41.8				.10±.01	4.35±.91	3.9±1.1	26±3	.44±.14	9± 1	3.6
n. $C_9H_{17}N$	2.092	41.3				.17±.01	3.57±.28	2.96±.37	34±4	.61±.09	5±.4	3.8

Viscosity is in cP at 20 deg C.

E_η is the activation energy of viscous flow, from the least squares fit of data (ref. 15) (kcal/mole).

$E_T(30)$ values in kcal/mole.

τ_1 and τ_2 are the first and second dielectric relaxation times of alcohols at 20 deg C (ref. 11). For butyronitrile, see ref. 16. All times are in psec.

τ_1 is the first dielectric relaxation time of alcohols corrected for constant charge ($\tau'_1 = \tau_1 \times (\varepsilon_{1\infty}/\varepsilon_{10})$). ε_{10} is the static dielectric constant ($\varepsilon_{1\infty}$ is taken from Cole plots of data in ref. 11.

All rates are given in units of 10^{10} sec^{-1}.

k_{obs} is the average of the fast rise and decay components of the fluorescence at 475 nm and 400 nm, respectively.

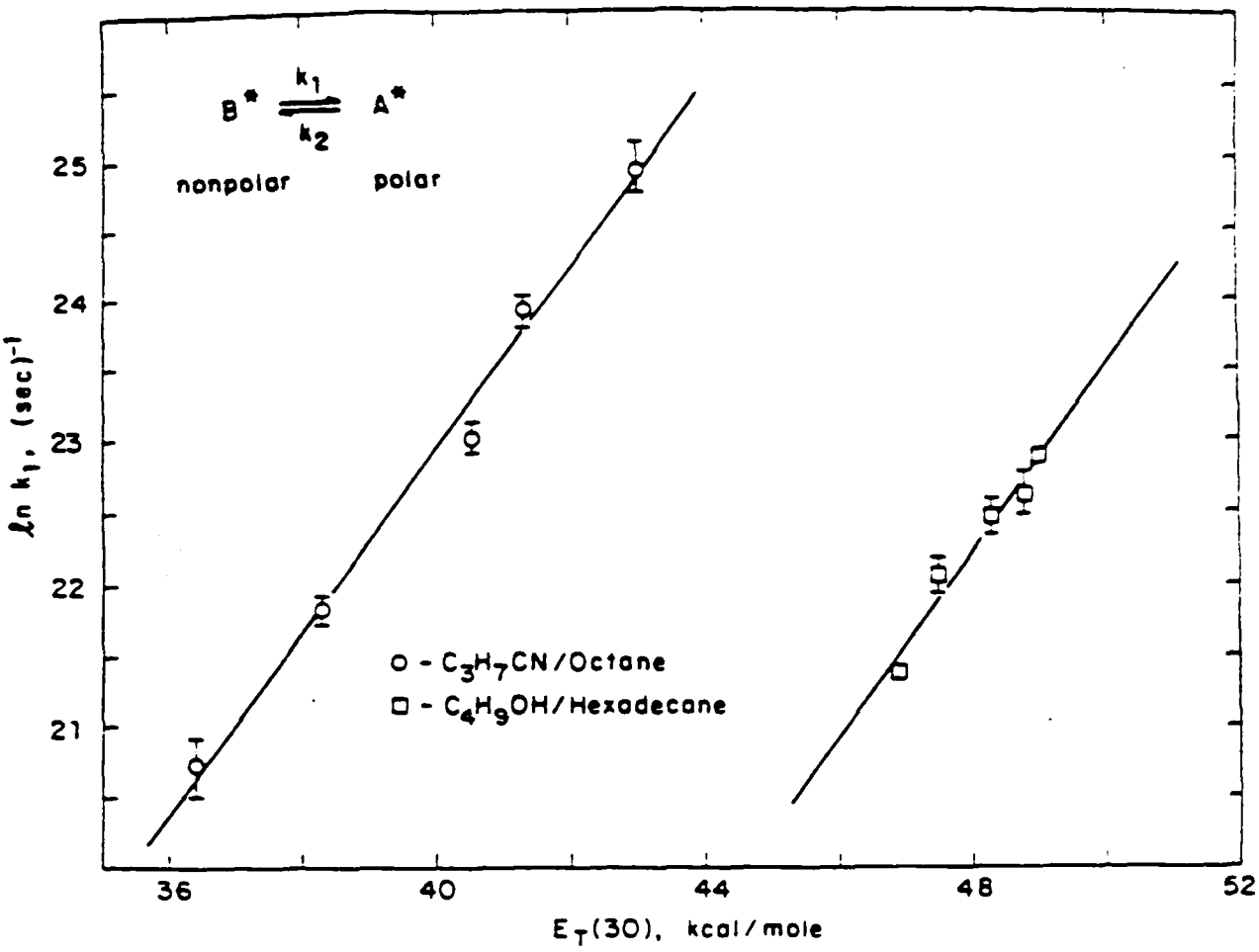

Figure 1: Plot of $\ln k_1$ vs. $E_T(30)$ for DMABN in: Circles -- nitrile/alkane mixtures, slope = .64 ± .04, intercept = -2.7 ± 1.5, corr. = .990. Boxes -- butanol/hexadecane mixtures, slope = .65 ± .08, intercept = -8.9 ± 4.0, corr. = .953.

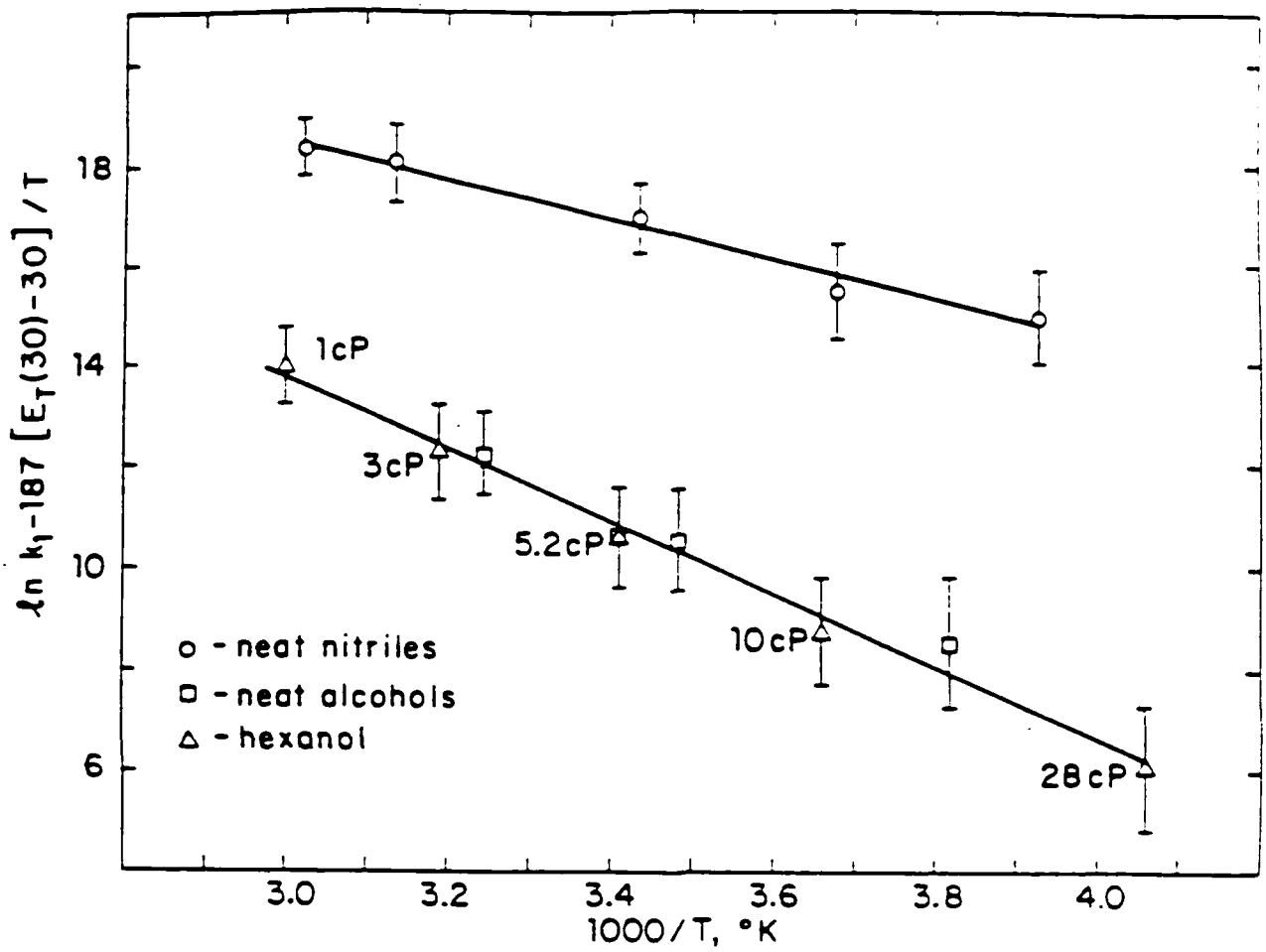

Figure 2: Arrhenius plot of polarity-corrected rate for TICT in: Circles -- neat nitriles, viscosity for all nitriles is .6 cP, slope = -4.02 ± .35, intercept = 30.6 ± 1.2. Boxes -- neat alcohols, viscosity for these alcohols is 5.2 cP. Deltas -- hexanol, slope for alcohols, -7.15 ± .35, intercept = 35.2 ± 1.2.

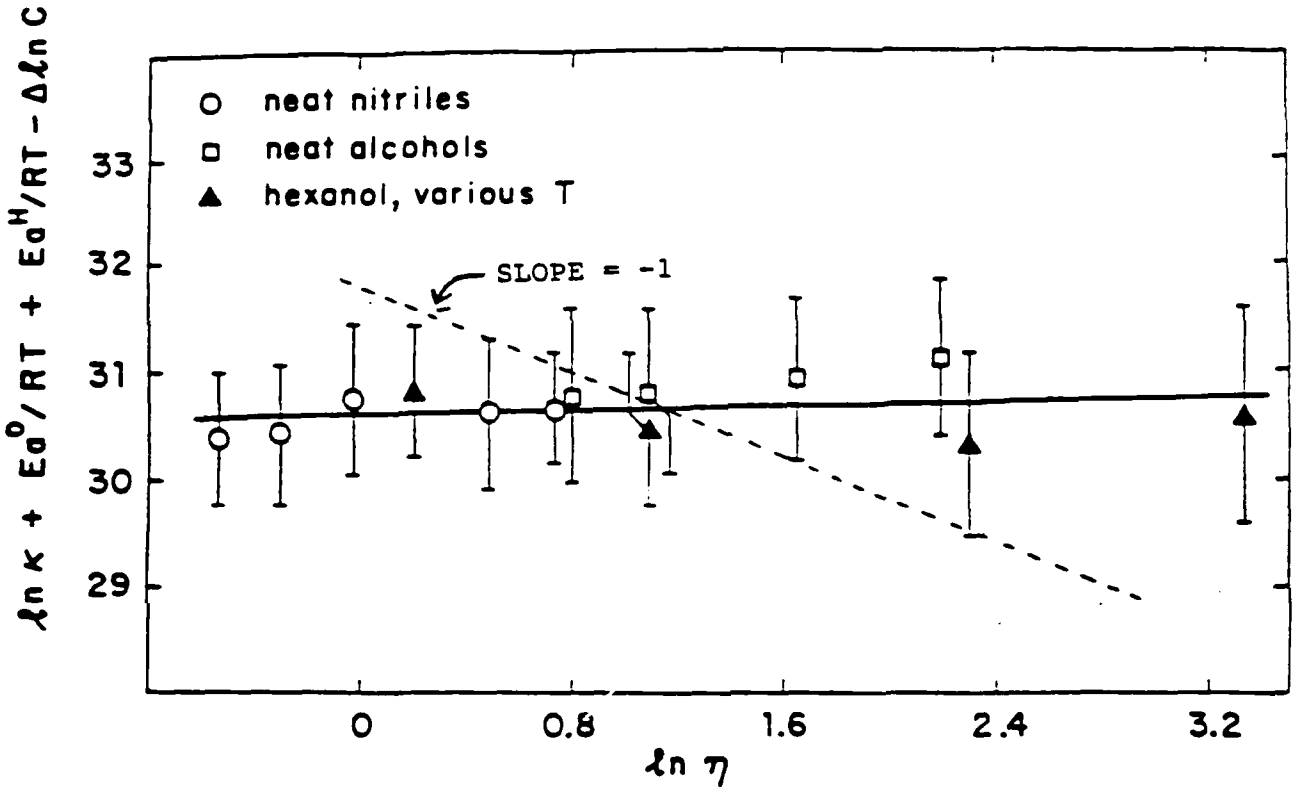

Figure 3: Plot of the polarity-corrected rate vs. the logarithm of the viscosity for n-nitriles (circles), n-alcohols (boxes) and hexanol (deltas). Alcohol data normalized to nitile data by adding $E_a^{o}/RT - \Delta \ln C$. Slope = .05 ± .06 (standard deviation of points), including error bars, slope on a range from -.2 to .4, intercept = 30.6 ± .1.

28 cP. A line with slope = -1, which is predicted by the Smoluchowski limit for a rate inversely proportional to viscosity, is drawn for purposes of comparison. While large errors remain after the correction for polarity (due to the error in A, which is propagated exponentially), it is clear that by extending the viscosity range by an order of magnitude, we have strengthened the argument that the major role played by the solvent in the isomerization of DMABN is in stabilizing the more polar twisted form via dielectric interactions, and not in providing friction against which the dimethylamino group must twist.

In conclusion, using the example of DMABN to test the effects of polar solvents on excited state isomerizations involving charge transfer, we have found that, in addition to solvent polarity-induced barrier height changes, the rate of isomerization can also be affected by hydrogen bonding between the solute and the protic solvent. These factors enter into the determination of the height of the potential energy barrier between the two states, and it is this that controls the kinetics rather than dynamical factors like solvent dielectric relaxation and viscosity. Finally, we have found that the Twisted Internal Charge Transfer model is valid for DMABN in a wide range of alcohols and nitriles over a fairly broad range of temperatures.

This work was also supported by the Air Force Office of Scientific Research under Grant AFOSR-84-0013B and the National Science Foundation under Grant NSF-CHE82-11593.

(1) Z.R. Grabowski, K. Rotkiewica, W. Rubaszewska and E. Kirkor-Kaminska, Acta Physica Polonica, A54, 6 (1978) 767.

(2) E. Lippert, W. Luder and H. Boos, in Advances in Molecular Spectroscopy, A. Mangini, ed., Pergamon Press, Oxford, 1962, p. 443.

(3) Y. Wang and K.B. Eisenthal, J. Chem. Phys. 77, (1982) 6076.

(4) Y. Wang, M. McAuliffe, F. Novak and K.B. Eisenthal, J. Phys. Chem. 85, (1981) 3736.

(5) D. Huppert, S.D. Rand, P.M. Rentzepis, P.F. Barbara, W.S. Struve and Z.R. Grabowski, J. Chem. Phys. 75 (1981) 5714.

(6) F. Heisel and J.A. Miehe, Chem. Phys. Lett., 100, (1983) 183.

(7) J.M. Hicks, M.T. Vandersall, Z. Babarogic and K.B. Eisenthal, Chem. Phys. Lett. (1985).

(8) E.M. Kosower and D. Huppert, Chem. Phys. Lett. 96, (1983) 433.

(9) E.M. Kosower, J. Am. Chem. Soc. 107, (1985) 1114.

(10) D.F. Calef and P.G. Wolynes, J. Phys. Chem. 87 (1983) 3387.

(11) S.K. Garg nd C.P. Smyth, J. Phys. Chem. 69 (1965) 1294.

(12) A. Mozumder, J. Chem. Phys. 50 (1969) 3153.

(13) W.J. Chase and J.W. Hunt, J. Phys. Chem., 79 (1973) 2835.

(14) A.H. Alwattar, M.D. Lumb and J.B. Birks, in Organic Molecular Photophysics, J. Birks, ed., John Wiley and Sons, New York, 1973.

(15) Landolt-Bornstein, Zahlenwerte und Funktionen, Band II, Twil 5a.

(16) A. Mansingh, Bull. Nat. Sci. Inst., India, 30 (1965) 106.

C. SECOND HARMONIC GENERATION FROM LIQUID SURFACES

(J.M. Hicks, K. Kemnitz, T.F. Heinz and K.B. Eisenthal)
(JSEP work unit 6, 1985 - 1988)
(Principal Investigator: K.B. Eisenthal (212)280-3175)

1. Adsorption and Orientation of Phenol Derivatives at the Air/Water Interface Studies by Surface Second Harmonic Generation — A new application of second harmonic generation techniques, which are sensitive to the asymmetry of boundaries, has allowed the direct study of the structure of surfaces of neat liquids and solutions. These techniques have recently been shown to yield detailed information about the orientation and number density of second harmonic active molecules at liquid/solid,[1-3] vapor/solid[4-5] and vapor/liquid[6] interfaces, where the latter interface consisted of insoluble surfactant molecules spread onto the surface of water. We wish to extend these studies to include the vapor/liquid interfaces of neat liquids and aqueous solutions of simple benzene derivatives. We approximate that the second order polarizability of the surface layer is given by equation 1:

$$P^{NL} = N_s < \alpha^{(2)} > (E)^2 \qquad (1)$$

where N_s is the number of surface active molecules, and $\alpha^{(2)}$ is the second order polarizability of the individual molecule.[2] By measuring the polarization of the second harmonic output, we can determine the average angle of the surface molecules with respect to the surface plane. From the intensity of the signal, the relative concentration of the adsorbates on the surface is determined.

Surface second harmonic signals from phenol/water and cresol/water mixtures of varying concentration were measured. Figure 1 shows the second harmonic intensity as a function of polarization angle for phenol/water mixtures of four different bulk concentrations. From the null angle, it is determined that the average orientation of phenol at the surface is 60° from the surface normal. Furthermore, the orientation does not change with

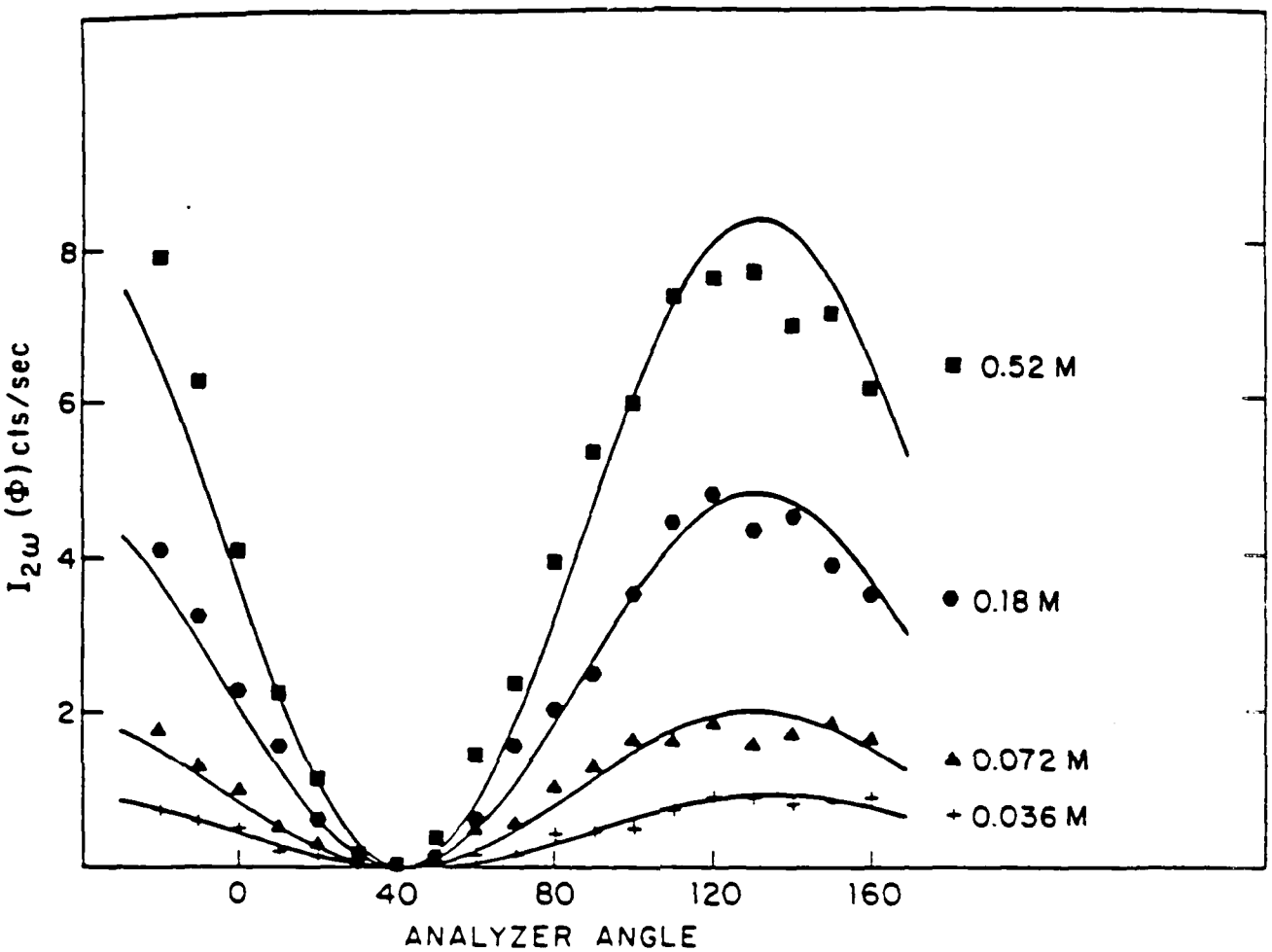

Figure 1: Polarization of the second harmonic signal from phenol/water mixtures: Boxes = .52M phenol, Circles = .18M phenol, Triangles = .072M phenol, Crosses = .036M phenol vs. analyzer angle. Data are corrected for the monochromator response function and fit to a $\cos^2$ function. Null angle is $42 \pm 2^{\circ}$.

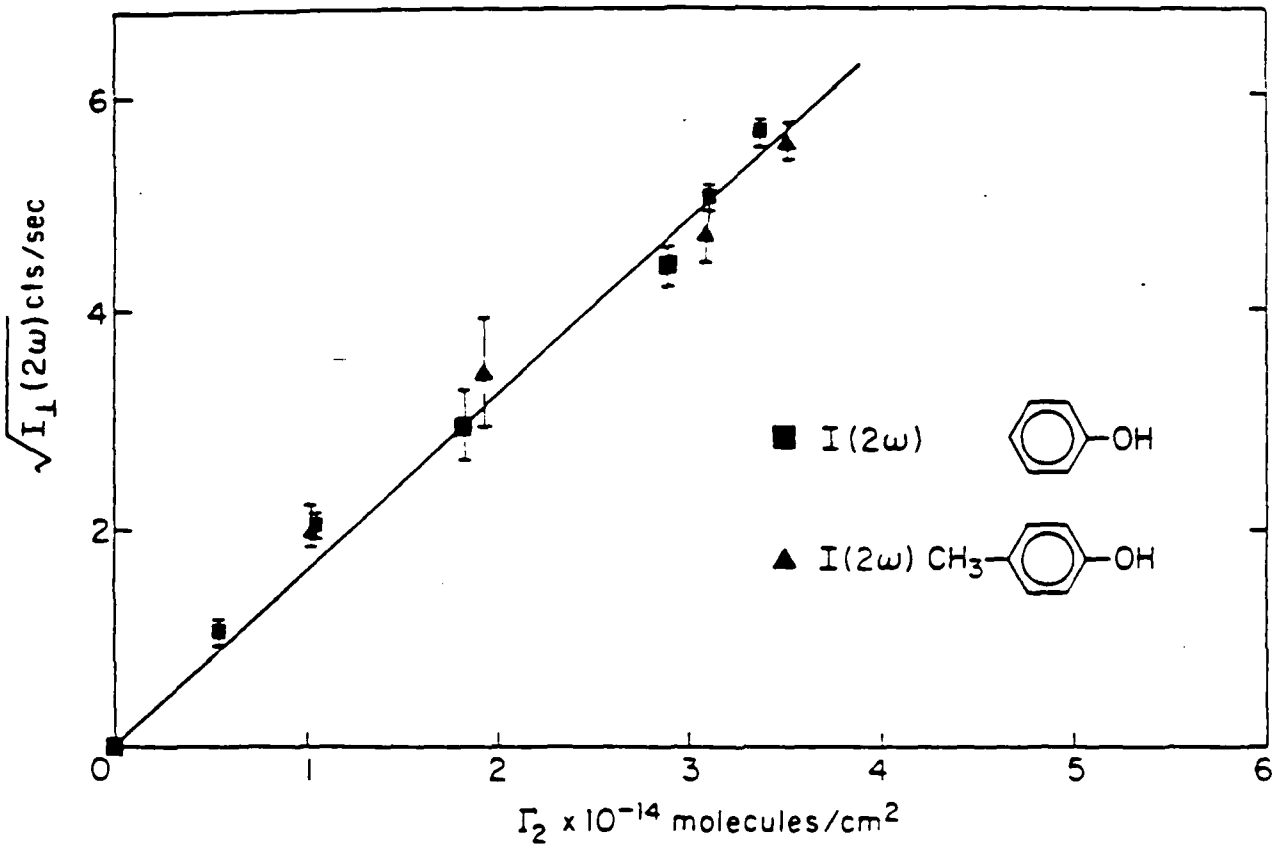

Figure 2: Intensity of s component of second harmonic signal vs. surface coverage of phenol and cresol in water. Boxes = phenol/water solutions, Triangles = cresol/water solutions.

surface concentration.

Now that it is known that the orientation of the molecule's main axis does not change with concentration, changes in the intensity of the signal can be attributed mainly to changes in the surface solute concentration. Figure 2 shows the polarized component of the signal for different phenol and cresol concentrations plotted against the surface coverage calculated from the surface tension data[7,8] via the Gibbs adsorption isotherm.[9] For submonolayer coverages, the second harmonic signal is a linear function of the surface concentration, as predicted by equation 1.

In conclusion, we have shown that it is possible to detect second harmonic signals from the surface molecules of ordinary liquids, even without the benefit of resonance enhancement. We have obtained information about the orientation of adsorbates in the liquid surface for coverages as low as 5% of a monolayer. For phenol molecules adsorbed at the water/air interface, we have shown that they are oriented with their long axis tilted 60° from the surface normal.

This work was also supported by the Air Force Office of Scientific Research under Grant AFOSR-84-0013B and the National Science Foundation under Grant NSF-CHE82-11593.

(1) H.W.K. Tom, T.F. Heinz, and Y.R. Shen, Laser Chemistry 3 (1983) 279.

(2) T.F. Heinz, H.W. K. Tom and Y.R. Shen, Phys. Rev. A 28 (1983) 1883.

(3) Y.R. Shen, in Novel Materials and Techniques in Condensed Matter, G.W. Crabtree and P. Vashishta, eds., Elsevier Sciene Publishing, Amsterdam, 1982, p. 193.

(4) T.F. Heinz, C.K. Chen, and D. Ricard, Y.R. Shen, Phys. Rev. Lett. 48 (1982) 478.

(5) T.F. Heinz, M.M.T. Loy, W.A. Thompson, Phys. Rev. Lett. 54 (1985) 63.

(6) Th. Rasing, Y.R. Shen, M.W. Kim, P. Valint, Jr., and J. Bock, Phys. Rev. A 31 (1985) 537.

(7) W.D. Harkins and E.H. Grafton, J. Am. Chem. Soc. (1925) 1329.

(8) M. Paluch and M. Filek, J. Coll. Int. Sci. 73 (1980) 282.

(9) D.K. Chattoraj and K.S. Birdi, Adsorption and the Gibbs Surface Excess, Plenum Press, New York, 1984, ch. 3.

V. OPTICAL TRANSIENT SPECTROSCOPY

A. INTRODUCTION

(S.R. Hartmann)
(JSEP work unit 2, 1985 - 1988)
(Principal Investigator: S.R. Hartmann (212)280-3272)

With the completion of the renovation of our laboratory, all four experimental stations are in an environmentally-controlled climate with the ambient temperature stable year round to $\pm$ 1 ^{o}F. This significantly improves the stability of our instrumentation and thus our ability to do precision experiments.

Investigations are proceeding on previously established experimental programs as well as exploring new spectroscopic techniques. In the following reports we will outline the progress in these investigations.

Traditionally, it has been thought that to study fast phenomena using optical transient techniques one had to use pulses of light with temporal durations shorter than the phenomena under study. In Section B we explain the important new technique of Time Delayed Four Wave Mixing (TDFWM) using incoherent light in which we show that one can take advantage of the short coherence time of broadband light in investigations of femtosecond phenomena.

In Section C we discuss the extension of Photon Echo Modulation Spectroscopy (PEMS) into a new regime allowing studies of coherences between states that are widely separated in frequency compared to the bandwidth of the exciting laser pulses.

Section D contains results of our spectroscopic and relaxation studies in Pr^{3+}:LaF_3 for the excited $^3H_5$ and $^3H_6$ states. We also present the first satellite echo data taken on a satellite line of $^3P_0$ - $^3H_4$ transition in this sample. We have also observed visible lasing on three transition in this sample. Some preliminary results on laser action in this sample is presented.

We have completed a study of the relaxation of superposition states of

similar parity in Lithium vapor using the trilevel echo technique. This experiment is discussed in Section E and concludes the investigation which was discussed in last year's progress report.

In Section F we discuss a novel experiment in Sodium vapor in which a new photon echo technique is developed. This is the first time a photon echo has been observed in which one of the excitation pulses involves a two-photon transition. This echo was used to measure the total scattering cross section with Argon of Sodium in a 3S-3D superposition.

In conclusion, we will mention in Section G future directions of work in our laboratory.

B. TIME-DELAYED FOUR-WAVE MIXING USING INTENSE INCOHERENT LIGHT

(R. Beach, D. DeBeer and S.R. Hartmann)
(JSEP work unit 2, 1985 - 1988)
(Principal Investigator: S.R. Hartmann (212)280-3272)

1. Introduction — Although there have been photon-echo and four-wave-mixing studies since the early 1960s,[1,2] it is only recently through the work of Ye and Shen[3] that the intimate connection between the two has been recognized. The key to bridging the gap and exploiting this connection is to use incoherent light.

In separate experiments done by Asaka et al.[4] and Beach and Hartmann,[5] incoherent light has been used to generate time-delayed four-wave-mixing (TDFWM) signals. Asaka et al. used a broadened cw laser to generate TDFWM and were thereby able to measure relaxation on a picosecond scale. Beach and Hartmann, using pulsed incoherent light, saw structure in the picosecond regime where the excitation pulses overlapped, while still being able to generate ordinary photon echoes when there was no pulse overlap. More recent work with a pulsed excitation source has pushed relaxation measurements into the subpicosecond regime.[6] Theoretical analyses of relaxation effects have yielded significant agreement with data. Taking the view that TDFWM signals are essentially accumulated echoes, the analysis of Asaka et al. posits that a grating proportional to the power spectrum of the applied fields is formed and then interrogated by the selfsame fields.[4] A more general analysis hasa been presented by Morita and Yajima[7] which is valid for arbitrary values of T_1, T_2, and $\delta\omega$ where T_1 and T_2 are the longitudinal and transverse relaxation times and $\delta\omega$ is the 1/e half-width of the inhomogeneous line.

Both of these last theories are steady state in character and assume the excitation fields are weak. The TDFWM results of Beach and Hartmann cannot be explained by either of these theories because of the large excitation intensities used: what is needed is a nonperturbative analysis. Such an

analysis, valid only when the excitation pulses do not overlap, has recently been presented to explain the generation of incoherent photon echoes.[5] An extension of this analysis is presented herein to explain the TDFWM behavior. New experimental results are also presented.

2. Theory -- In the weak excitation regime for the case of T_1 and T_2 both large in comparison to $\delta\omega^{-1}$, Morita and Yajima's general formulas for the TDFWM signal reduce to the simple form

$$S = \int_{-\delta\omega\tau/\sqrt{2}}^{\infty} dy \; \exp(-y^2) \qquad (1)$$

where τ is the delay between the excitation pulses. The TDFWM signal is observed along $2k_2 - k_1$ where k_1 and k_2 are the wave vectors of the excitation pulses and positive τ corresponds to the pulse with wave vector k_1 preceding the pulse with wave vector k_2. The above formula is plotted in Fig. 1 and should be compared with Fig. 2(a), a recent result from our laboratory. Our experimental result was obtained in a Na cell at 445 K where the shortest relevant relaxation time is the 16-nsec fluorescence lifetime of the 3P state. The inhomogeneous width of the Na D line on which we work is of the order of $\delta\omega = 6.4 \times 10^9$ rad/sec, so that our result is obtained under the condition that T_1 and T_2 are large in comparison to $\delta\omega^{-1}$. Our excitation pulses were such that each Na atom experiences a pulse of effective area on the order of π so that except as regards the intensity of the excitation pulses the data shown in Fig. 2 corresponds to the conditions under which the response shown in Fig. 1 was calculated. The most striking effect of the high-intensity excitation is thus seen to be the degradation of the TDFWM signal for large values of τ. Before we explain how this comes about we give a qualitative explanation of the weak-excitation result shown in Fig. 1.

Excitation pulses made from broadband laser light can be regarded as a train of incoherently phased noise spikes. We consider the case in which the output of a single such laser is divided, delayed, and recombined to provide one pulse with wave vector k_1 and a second pulse delayed by τ and in a slightly different direction with wave vector k_2. Thus we have two trains of

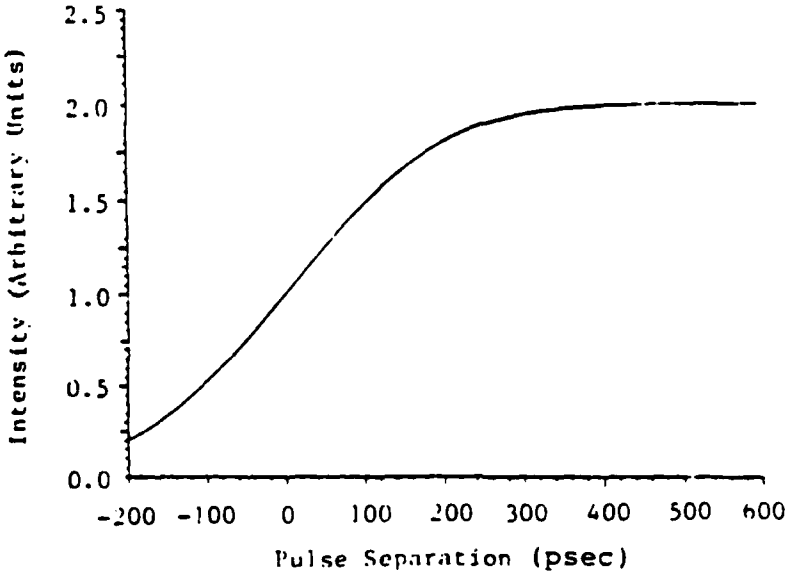

Figure 1: Signal intensity vs. excitation pulse separation after Morita and Yajima (Ref. 7) for the case in which T_1 and T_2 are both large in comparison to $\delta\omega^{-1}$.

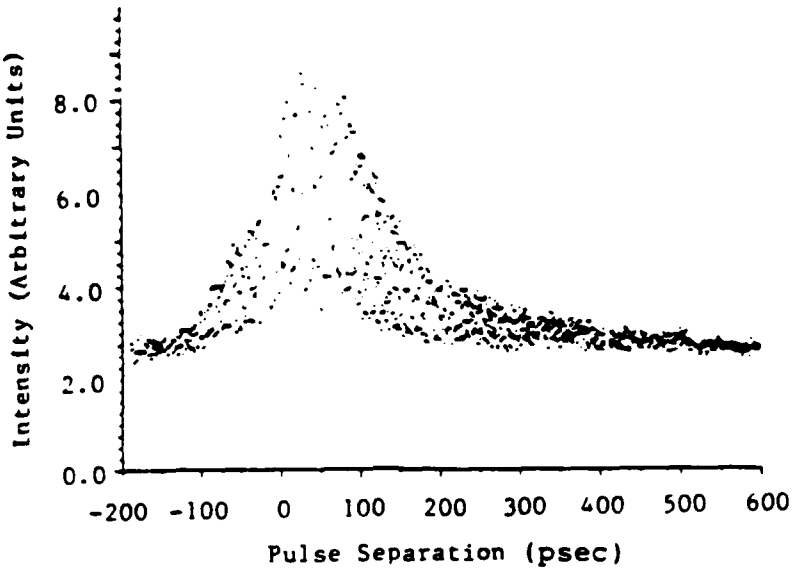

(a)

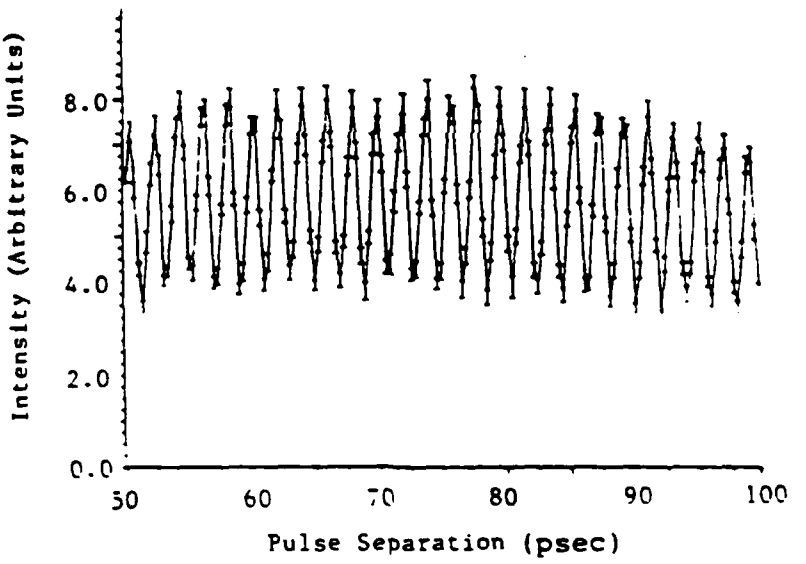

(b)

Figure 2: (a) Experimentally measured signal intensity vs. excitation pulse separation in a 10-cm long Na cell at 445 K. (b) The same data for pulse separation of 50-100 psec with error bars and lines connecting the data. The 1.9-psec modulation is due to the Na 3P fine-structure beating.

correlated noise spikes. Although the phase of each noise spike is random, each correlated noise-spike pair having wave vector k_1 and k_2 has the same relative phase and therefore contributes coherently to a k_1-k_2 momentum component of the ground-state amplitude. We illustrate this in Fig. 3 by drawing only that part of the recoil diagram which shows the elements leading to this ground-state momentum buildup.[8,9] Each spike with wave vector k_1 generates an excited-state component with momentum k_1 which recoils as indicated by the dashed line. After a time τ the correlated noise spike with wave vector k_2 appears and regenerates the ground state except that its momentum k_1-k_2 is not exactly zero since $k_2 \neq k_1$. For $k_2 \simeq k_1$ the resulting ground-state trajectory for the $k_1 - k_2$ state is effectively parallel to the original ground state with $k = 0$. The macroscopic ground-state component with $k = k_1$-k_2 thus develops.

Given a system in a macroscopic superposition of two ground states as described above it is a simple matter to find how it will radiate after subsequent irradiation. Consider, as in Fig. 4, excitation by a noise spike with wave vector k_2 of the ground-state amplitude component with $k = 0$. This state recoils with momentum k_2 and crosses the ground-state component with $k = k_1 - k_2$ a time τ later. This is the classical echo formation process. The echo so produced has momentum $k_2 - (k_1-k_2) = 2k_2 - k_1$. Each noise spike with $k = k_2$ produces such an echo (in addition to aiding in the macroscopic ground-state formation shown in Fig. 3). These echoes add incoherently to provide the TDFWM signal. While we have called the radiated signals "echoes," this identification is not so clear when τ becomes smaller than the inverse inhomogeneous width. Echoes generally appear as a rephasing of a dephased system and radiate throughout the rephasing nad dephasing process. but when τ is too small, the initial dephasing in incomplete and consequently the interval during which appreciable radiation takes place is reduced, with a corresponding reduction in signal intensity. For $\tau = 0$ there is no initial dephasing and half the potential echo signal is lost. For τ negative the macroscopically produced ground-state component has wave vector $k = k_2$-k_1. A noise spike with wave vector k_2 generates from this state an excited state with wave vector $2k_2 - k_1$ as indicated in Fig. 5. This state and the ground-state component with $k = 0$ again combine to radiate along $2k_2$-k_1.

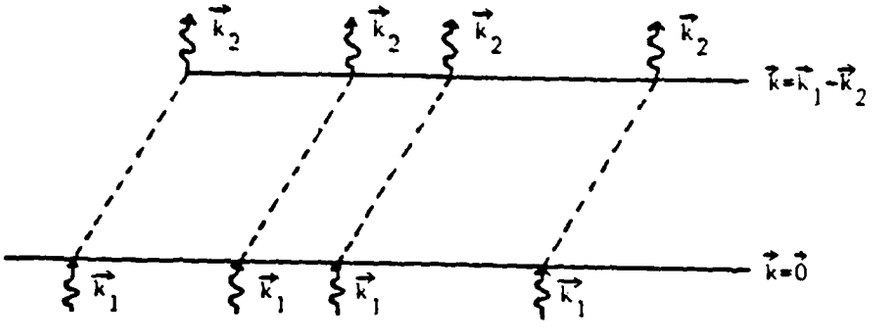

Figure 3: Recoil diagram showing those vertices that contribute to the k_1-k_2 momentum component of the ground-state amplitude. Ground- and excited-state trajectories are denoted by solid and dashed lines, respectively.

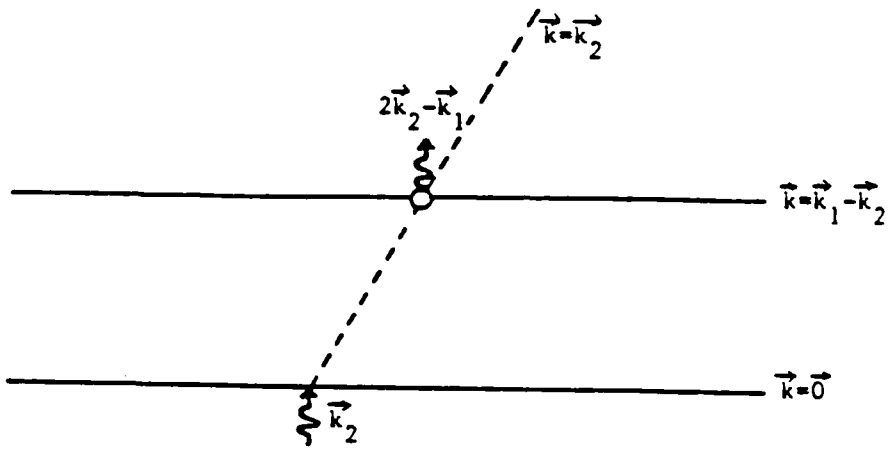

Figure 4: Recoil diagram showing the lowest-order contribution to the signal emitted in the $2k_2-k_1$ direction.

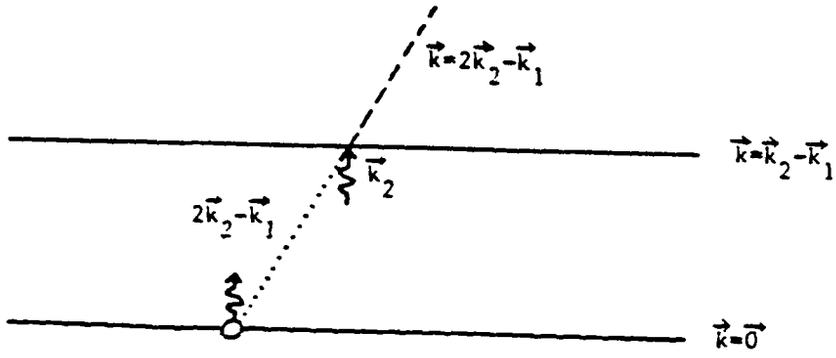

Figure 5: Recoil diagram for the case in which τ is negative, i.e., pulse 2 precedes pulse 1 by τ. Extending the excited-state amplitude generated by the k_2 noise spike backwards in time leads to a virtual crossing a time τ earlier giving rise to signal emission in the $2k_2-k_1$ direction.

This signal is large only for τ small; for nonzero τ it is a normal free decay less that part which would have been radiated between $t = 0$ and τ. In terms of the diagrams we would say this situation corresponds to having a virtual crossing a time τ before the noise spike appears.

The discussion of the recoil diagrams can be summarized by observing that superposition states with relative wave vector $2k_2-k_1$ always radiate but do so with an intensity proportional to $\exp -(\Delta t^2\ \delta\omega^2 \beta z)$ where Δt is the time to the (real or virtual) crossing. In the "billiard-ball" model this exponential factor gives the overlap between the superposition states.[9] In classical analysis the exponential factor represents Doppler dephasing. In any event each noise spike wiht wave vector k_2 generates a signal along $2k_2-k_1$ proportional to $\exp[-(t - \tau)^2\ \delta\omega^2/2]$ where t is the interval between the arrival time of the spike with wave vector k_2 and the time at which the signal is observed. Integrating over all t yields

$$S = \int_0^\infty dt\ \exp[-(t-\tau)^2\ \delta\omega^2/2] \qquad (2)$$

which is identical to the result of Morita and Yajima in Eq. (1). Out picture thus shows that TDFWM signals for positive τ are best thought of as accumulated echoes while for negative τ they arise from accumulated free decays.

In order to go beyond the low-intensity limit we need to consider those diagrams which give rise to the ground-state amplitudes suggested in Fig. 6. With this more-involved grating structure a second kind of contribution to the tDFWM signal along $2k_2-k_1$ appears, as shown in Fig. 7. Now excitation pulses along k_1 produce echoes along $2k_2-k_1$. These echoes are in a different class from those depicted in Fig. 4 inasmuch as they peak at 2τ, instead of τ, after the excitation noise spike. For τ negative we obtain the analog to Fig. 5 which is depicted in Fig. 8.

This differs from the situation depicted in Fig. 5 in that the virtual crossing appears 2τ, instead of τ, before the excitation noise spike. The appearance of terms with crossings 2τ away from the associated noise spikes modifies the relaxation behavior since the sensitivity to relaxation is changed. It should also be noted that as the excitation level increases, the

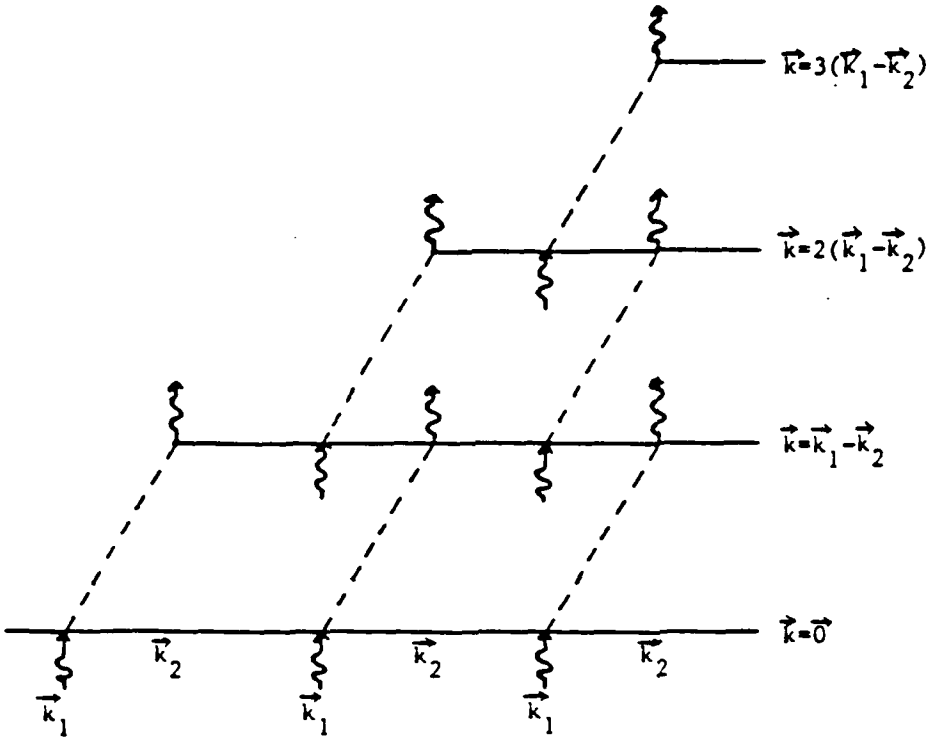

Figure 6: Recoil diagram showing several of the various momentum components of the ground-state amplitude that are generated by intense excitation pulses.

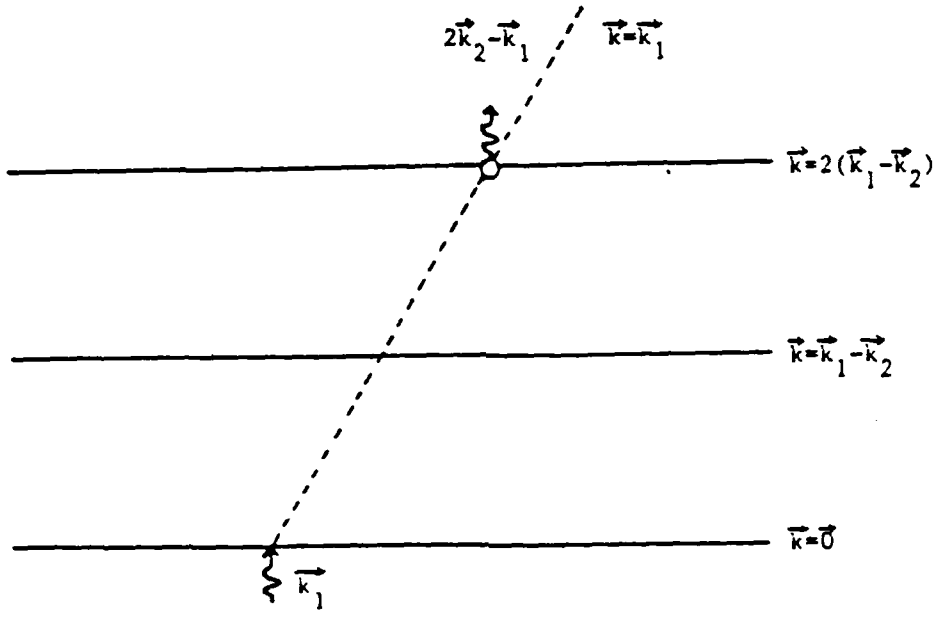

Figure 7: A new class of recoil diagram that can contribute to the $2k_2-k_1$ emitted signal when the ground-state grating structure depicted in Fig. 6 is present.

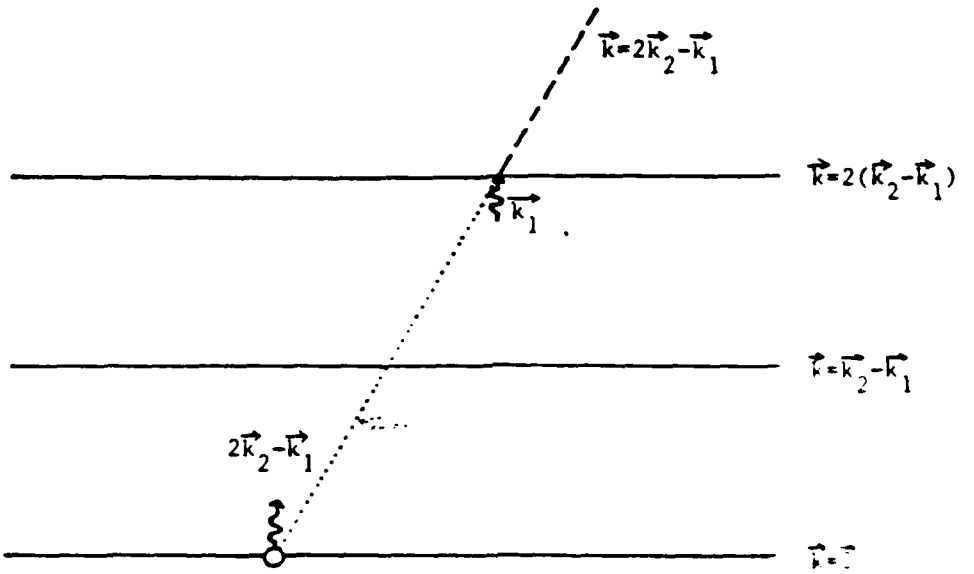

Figure 8: Recoil diagram analogous to that depicted in Fig. 5 for the case of negative pulse separation and higher-intensity pulses. Extending the excited state generated by the k_1 noise spike backwards in time leads to virtual crossing a time 2τ earlier, giving rise to signal emission in the $2k_2-k_1$ direction.

number of terms in each of the classes presented in Fig. 4, 5, 7, and 8 increases.

Our model up to now consists of two parts. First, correlated noise-spike pairs act in unison to set up accumulated gratings and then, these gratings are interrogated by the selfsame fields to generate the TDFWM signal along $2k_2-k_1$. With high-intensity excitation we must also consider how the excitations affect the generated superposition states themselves, degrading the grating and radiated signal both directly and indirectly. For the purpose of this paper we consider only those signal degradation effects which depend on τ. These involve grating formation and grating interrogation and we believe they are comparable. A calculation leads to a noise-spike induced relaxation time and is the reason for the qualitative difference between our result of Fig. 2 and the theoretical curve in Fig. 1.

For large τ, noise-spike signal degradation dominates and the TDFWM signal should diminish as we observe. As we have noted, it is important to take into account high order effects when calculating the pulse-induced grating. This we did by performing a modal analysis which treats the interaction of each atomic group with its resonant mode exactly. All classes of echoes appear in the analysis and agreement with experiment is obtained within the limits of our experimental accuracy.

3. Experiment — Our experimental apparatus generated 7-nsec-long incoherent excitation pulses from a dye solution consisting by volume of 50% R610 (10^{-3}M in CH_3OH) and 50% Kiton Red (3×10^{-4}M in CH_3OH) in a stirred dye cell, pumped by the second harmonic of a Quanta Ray DCR-1A yttrium-aluminum-garnet (YAG) laser. The dye cell was placed in an open-ended cavity with a diffraction grating in the Littrow configuration at the closed end to provide bandwidth narrowing. The output was amplified twice in two longitudinally pumped flowing dye cells containing a solution of R590 (5×10^{-5}M in CH_3OH) as shown in Fig. 9. A spectroscopic analysis of these output pulses showed them to have a central wavelength of 5893 Å and a full width at half maximum (FWHM) of between 6 and 12 Å depending on the grating used in the closed end of the cavity. Using the apparatus shown in Fig. 10 each output pulse was split in two and

recombined to provide two well-defined almost parallel light pulses. We generally made the angle between the light pulses of the order of a few milliradians. The mirror M1 in Fig. 10 was on a translational mount driven by a computer-controlled stepper motor so that a variable delay could be inserted between the two pulses. Beyond a 10-cm-long sample cell containing Na vapor, a signal was detected in the $2k_2-k_1$ phase-matching direction using a spatial filtering technique. The signal intensity was detected by an EG & G FND 100 photodiode and after being integrated over the pulse duration was stored by a computer. A typical data run consisted of measuring integrated signal intensity as a function of delay as mirror M1 was moved through a range corresponding to ~1 nsec in delay time. Care was taken to insure that both the immediate and delayed components of the excitation beam saw the same dispersive optical elements after being split off from the single incoming pulse.

The data shown in Fig. 2 were obtained in a 10-cm cell at 445 K where the Na vapor density was $3\times10^{12}/cm^3$. At line center the sample is optically thick so the theory we have presented is strictly valid only in the wings of the resonance line. Nevertheless, it is still instructive to apply the theory to this case.

Before proceeding we note that the oscillatory behavior revealed on the expanded segment shown in Fig. 2(b) is due to the coherent beating of the sodium D lines at 5889.95 and 5895.92 Å. Our laser bandwidth of 12 Å completely covers these lines which are separated by 6 Å. The beating has a period of 1.9 psec which corresponds to this wavelength separation.

For broadband laser pulse considered as a train of incoherent noise spikes, these spikes have a nominal duration determined by the relation $\Delta\omega t_c = 2\pi$ where $\Delta\omega = 2\pi c\Delta\lambda/\lambda^2$ is the bandwidth $\Delta\omega$ corresponding to $\Delta\lambda$. For $\Delta\lambda$ = 12 Å we find the noise-spike duration is t_c = 1 psec. The laser pulses were 7 nsec long and had an average intensity of 53 $kWcm^{-2}$ over a cross-sectional area of 0.5 cm^2. The effective area of these pulses is 3.2π while the effective noise-spike area is a factor of $\sqrt{t_c/\tau_p}$ smaller, $\Theta_s = 0.038\pi$. Using this value of Θ_s we calculate from Eq. (25) the TDFWM signal as shown in Fig. 11. The vertical scale is arbitrary but we have used the same scale for the abscissa as in Fig. 2 to aid in comparison. The qualitative features

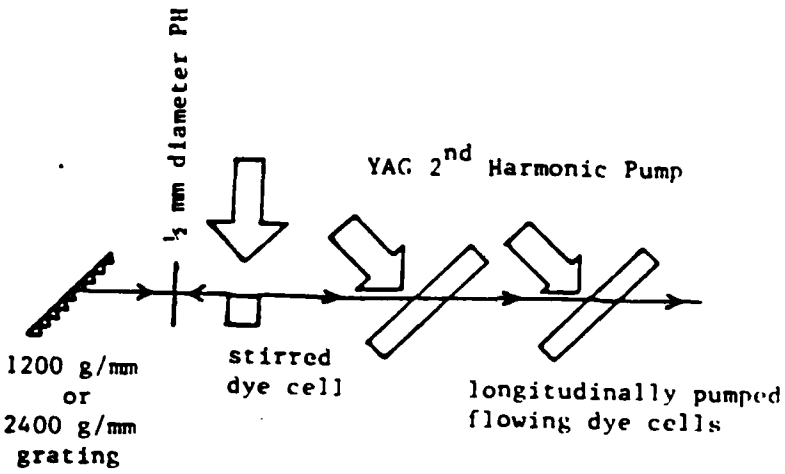

Figure 9: Schematic diagram of apparatus used to generate the incoherent excitation pulses used in our experiment. The large arrows denote the YAG second-harmonic pump beams and PH stands for Pinhole.

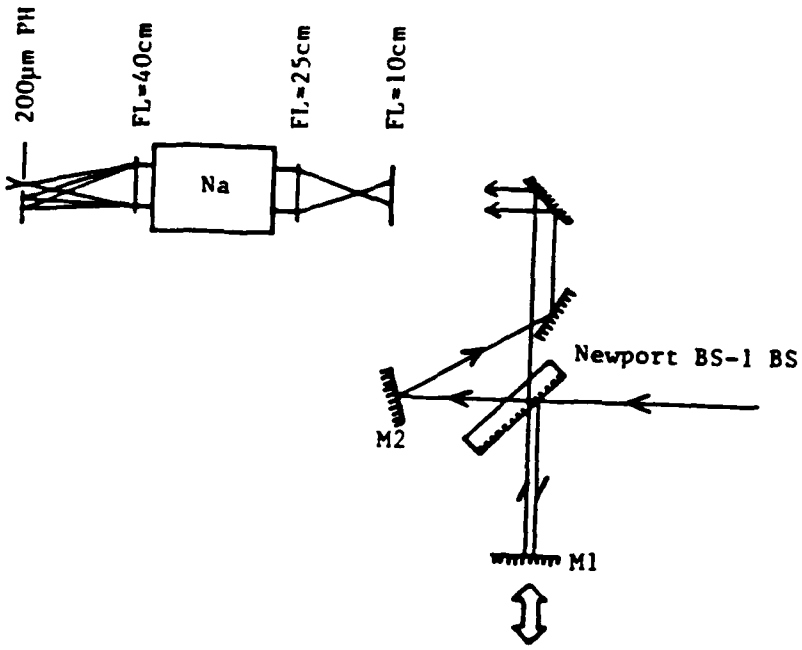

Figure 10: Apparatus used to split apart and recombine the excitations. Mirror M2 is fixed while mirror M1 is moveable in the direction of the arrow so that a variable delay can be inserted in the beams. All mirrors in the diagram are front surface aluminum. BS stands for beam-splitter and the solid line is the reflective side. FL stands for focal length and all such indicated lenses are achromats. The 200-μm PH was placed in the focal plane of the 40-cm lens and positioned to pass the signal emitted in the $2k_2-k_1$ direction while blocking the signal in the k_1 and k_2 directions.

of our data are clearly present in our calculated response. Note that we have calculated only that part of the TDFWM signal which depends on the relative decay τ; an incoherent background, independent of τ, should be added to our result.

The effect of noise-spike degradation can be appreciated if we plot the result shown in Fig. 11 together with the corresponding result when noise-spike degradation is neglected. Again we use $\theta_s - 0.038\pi$ and make the comparison with the two solid traces in Fig. 12. If we use Eq. (25) in the small-pulse area limit which leads to Eq. 91) and set $\theta_s = 0.038\pi$, we obtain the dashed-line response shown in Fig. 12. This response is large inasmuch as saturation effects are not included and inherently less steep since the higher-order diagrams of Figs. 5 and 8 are not included.

A more critical test of our calculation is obtained by working with data obtained in a smaple that is not optically thick. In Fig. 13(a) we plot the TDFWM signal obtained in Na vapor at 425 K when the number density is $\approx 10^{11} cm^{-3}$. In this run we incremented the delay of the excitation pulses by approximately 5 psec between successive data points. Lack of exact synchronization with the fine-structure beating period results in the ragged appearance. If we increase the resolution we obtain the smoother response shown in Fig. 13(b). Here again the beating of the D lines is very strong. In optically thin samples we expect better agreement with our theory and indeed we find that by choosing $\theta = 0.064$, which is within the uncertainty of what we would obtain from our measurements of pulse intensity, we obtain the solid curve which passes through the data. We should note that we have also added a constant incoherent background so this curve represents a two-parameter fit.

Finally, in Fig. 14 we present data taken in a cell with temperature held fixed at 545 K, corresponding to a sodium number density of almost $\simeq 10^{14}/cm^3$. There was also 1.6 torr of AR present in the sample cell to keep the sodium from contacting and condensing on the cool end windows. The excitation pulses had a FWHM of ~ 12 Å centered at 5893 Å and intensities giving noise spikes with rms area of approximately 0.3. The remarkable feature of these data is the abrupt change in character at 0 delay. In a change of excitation delay time on the order of the field correlation time

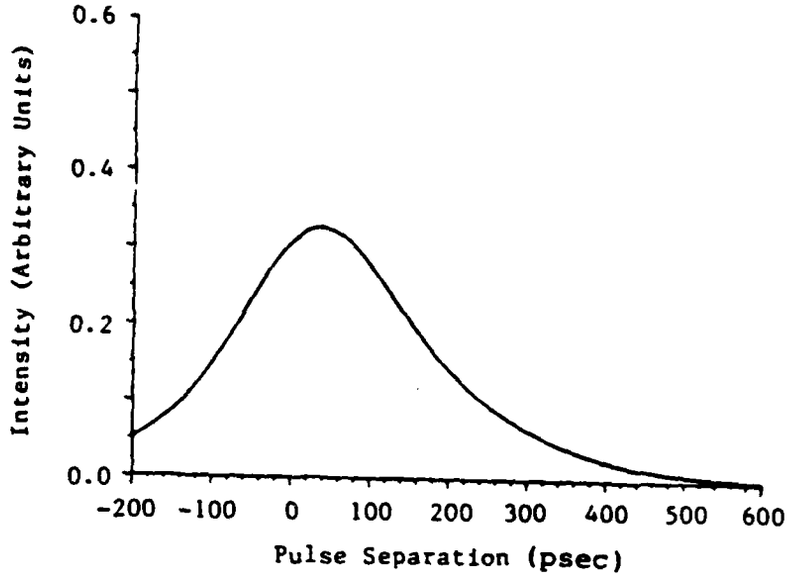

Figure 11: A plot of our theoretical intensity vs pulse separation as given in Eq. (25) using the same parameters that describe the experimental data plotted in Fig. 2.

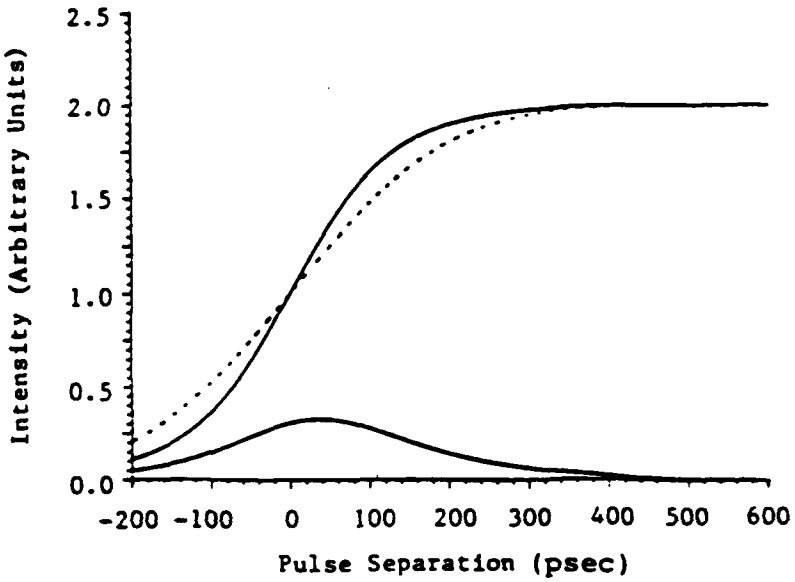

Figure 12: Theoretical curve of Fig. 11 is replotted here along with the same theoretical calculation when the effects of noise-spike degradation are ignored; both of these curves are plotted as solid lines. For comparison we also plot Yajima's formula given in Eq. (1) and normalized to the same maximum value as our result in which noise-spike degradation has been neglected; this curve is drawn as a dashed line.

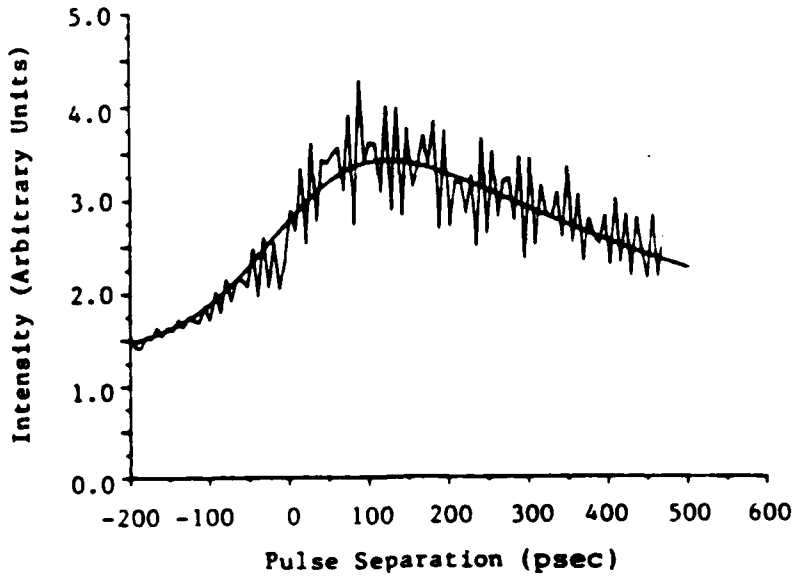

(a)

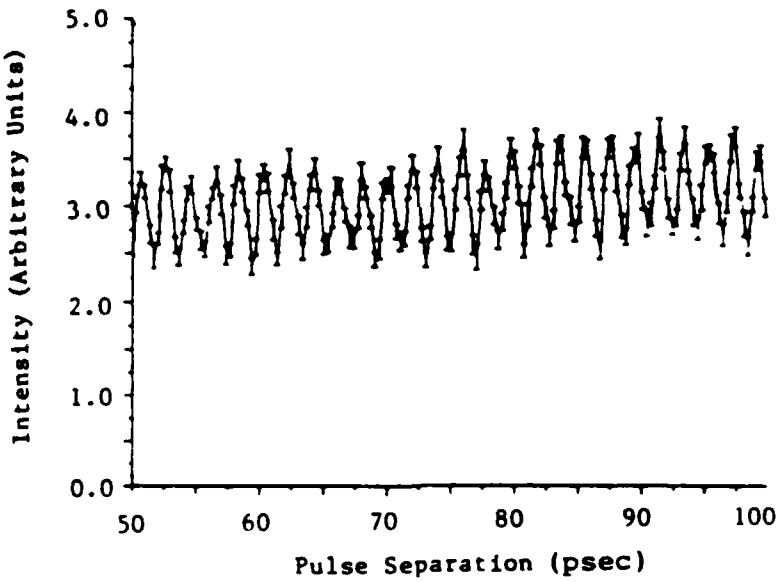

(b)

Figure 13: (a) Experimentally measured signal intensity vs excitation pulse separation in a 10-cm-long Na cell a425 K. In this experiment the pulse separation was stepped in approximately 5-psec increments and the excitations had a FWHM of 6 Å. Solid line represents a two-parameter fit of our theoretical expression for signal intensity given in Eq. (25). (b) Data taken under the same experimental conditions as that shown in part (a) but with a finer incremental change in the excitation pulse separation. The 1.9 psec beating of the 3P state fine structure is clearly visible here.

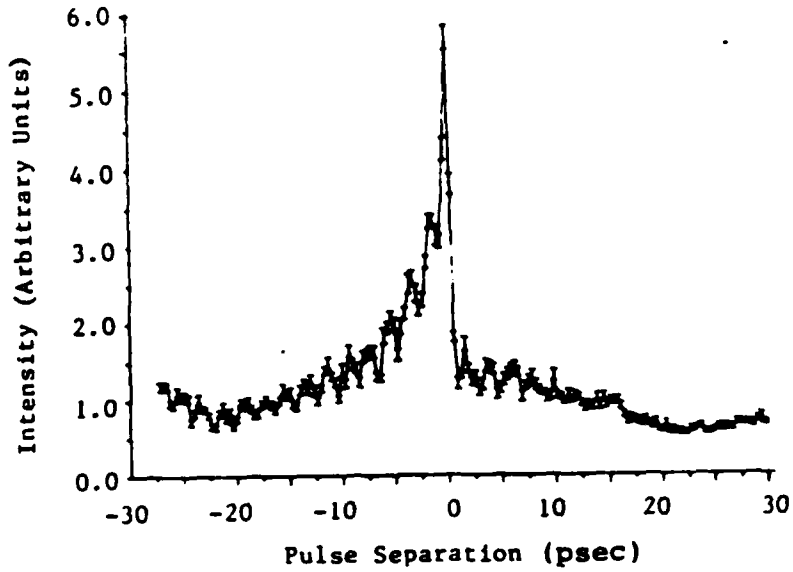

(a)

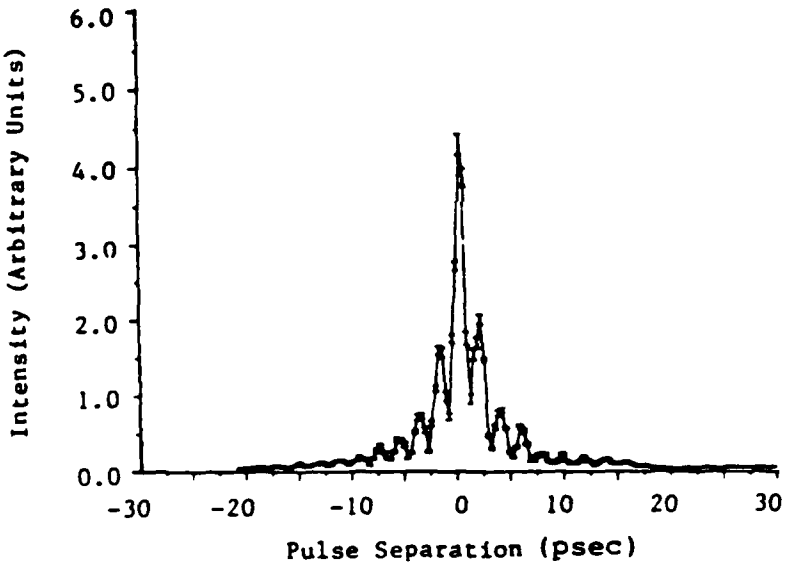

(b)

Figure 14: (a) Data taken in a 10-cm Na cell at 545 K and an excitation pulse intensity leading to noise spikes having an rms pulse area of 0.3. In addition 1.6 torr of argon was present in the sample cell when this data was taken. (b) Data taken under the same conditions as that shown in part (a) except here the argon buffer-gas pressure in increased to 600 torr.

the character of the signal changes drastically in going from negative τ, where the signal is the result of accumulated free decays, to positive τ, where the signal is the result of accumulated photon echoes. When the Ar buffer-gas pressure in increased to 600 torr, the signal envelope becomes symmetric around 0 delay and the background signal that was approximately independent of τ disappears. At this point we have no explanation for the anomalous behavior of the signal near $\tau = 0$ taken with low perturber as pressure.

4. Conclusion — We have presented TDFWM experimental data acquired with excitation pulse intensities at which we do not expect perturbation theory to be valid. Using a model that is similar to one already introduced to explain the photon-echo formation process[5] with excitation pulses of intense, time-separated, incoherent light, we are able to explain the general characteristics of signal versus τ curves even when pulse-induced relaxation becomes important.

Data taken at sodium number densities spanning 3 orders of magnitude is presented and the 1.9-psec fine-structure splitting of the 3P state of sodium is resolved. The simplicity of the technique and its applicability over such a large range of number densities suggest applications in measuring self-broadening and in plasma diagnostics.

Finally, we have presented data acquired at high sodium number density which shows anomalous behavior near $\tau = 0$. Experimental and theoretical work on this problem is continuing.

This work was also supported by the Office of Naval Research under Contract No. N00014-78-C-0517.

(1) N.A. Kurnit, I.D. Abella, and S.R. Hartmann, Phys. Rev. Lett. 13, 567 (1964).

(2) P.D. Maker and R.W. Terhune, Phys. Rev. 137, A801 (1965).

(3) P. Ye and Y.R. Shen, Phys. Rev. A25, 2183 (1982).

(4) S. Asaka, H. Nakatsuka, M. Fujiwara, and M. Matsuoka, Phys. Rev. A29, 2286 (1984).

(5) R. Beach and S.R. Hartmann, Phys. Rev. Lett. 53, 663 (1984).

(6) H. Nakasuka, M. Tomita, M. Fujiwara, and S. Asaka, Opt. Commun. 52 150 (1984).

(7) N. Morita and T. Yajima, Phys. Rev. A30, 2525 (1984).

(8) The language used here is that of the "billiard-ball echo" model of Ref. 9.

(9) N. Beach. S.R. Hartmann, and R. Friedberg, Phys. Rev. A. 25, 2658 (1982).

C. ULTRAFAST PHOTON ECHO MODULATION SPECTROSCOPY

(D. DeBeer, L. WanWagenen, R. Beach and S.R. Hartmann)
(JSEP work unit 2, 1985 - 1988)
(Principal Investigator: S.R. Hartmann (212)280-3272)

1. Introduction — Time Delayed Four Wave Mixing (TDFWM) using two-frequency beams, separately resonant with each of the Na D lines, is performed in dilute Na vapor. The time integrated four wave mixed signal modulates with increasing excitation delay with a period of 1.9 psec corresponding to the 6Å splitting of the D lines. The modulation persists well into the region where the 7 nsec excitation pulses no longer overlap and far beyond the 100 psec correlation time of the either laser.

The notion of exploiting the short correlation time associated with noise spikes in broadband (incoherent) laser light in order to study Ultra Fast phenomena becomes viable via Time Delayed Four Wave Mixing (TDFWM). This technique offers the opportunity of performing picosecond and femtosecond experiments with conventional laser sources which are neither spectrally very narrow nor designed to provide short excitation pulses.[1-4] A second feature of this technique is that it simultaneously provides spectral information contained within the bandwidth of the excitation fields. Recent work in this laboratory using 12Å wide 7 nsec long excitation pulses covering both Na D line transitions showed that the integrated TDFWM signals measured as a function of the relative delay of the excitation pulses was deeply modulated with the 1.9 psec period corresponding to the inverse of the 3P fine structure splitting.[5] As these pulses were greater in length than the period of the modulation they induced, we call them "long". The noise components in the light however give rise to noise spikes which are short. These have a correlation time of the order of a picosecond and allow the measurement of relaxation times of this order. On the other hand, one only expects light which is on or near resonance to effectively interact with any long-lived atomic state. We therefore modified our source so that it peaked

separately at each of the Na D lines and repeated our experiment. We again saw a modulated signal. The 1.9 psec modulation we observe in fact persists well beyond the regime where the excitation pulses overlap. Previous photon echo work using 7 nsec excitation pulses has shown that echoes may be observed twenty excitation lifetimes and longer after the initial excitation pulse.[6] The same should obtain here leading to the possibility for an expanded use of Photon Echo Modulation Spectroscopy (PEMS) to perform high resolution spectroscopic studies.

2. Experiment -- The simultaneous outputs of two pulsed-YAG-pumped dye lasers were combined into a single beam and used to generate a time delayed four wave mixing signal in atomic sodium vapor. The laser pulses were 7 nsec long and centered at 5896Å and 5890Å, the wavelengths corresponding to the $3S_{1/2} - 3P_{1/2}$ and the $3S_{1/2} - 3P_{3/2}$ transitions respectively. Each laser ran in 4 to 5 longitudinal modes yielding an overall bandwidth of 5 GHz.

The double frequency pulse was split and recombined to provide two double frequency pulses directed along k_1 and k_2 and angled at $\theta \simeq 2$ mrad to each other (See Fig 1). Mirror M1 was mounted on a translation mount to provide a variable delay. These pulses overlapped spatially throughout a 10 cm long sodium cell. Signal intensity was measured, away from the excitation pulses, along the phased matched $2k_2 - k_1$ direction. All lenses are achromats with the indicated focal length, FL, a 100μm pinhole, PH, was placed in the focal plane of the 45cm lens to isolate the signal. In order to generate large offset delays mirror M2 was repositioned. Measurements were made using either an EG G FND-100 photodiode or an RCA C31034 PMT. In all cases the signal was integrated over its full 7 nsec pulse duration.

In the regime where there is considerable excitation pulse overlap, we obtain the results shown in Fig. 2. For three positions of M2, stepped displacements of M1 generated delays of several tens of picoseconds around 0, 230, and -300 picoseconds. The three traces are essentially the same; any differences can be ascribed to laser fluctuations and other instabilities. The common important feature is the 1.9 psec modulation corresponding to the inverse of the 3P fine structure splitting. The origin of this beating is clarified by using a spectrometer to look separately at each of the 5896Å and

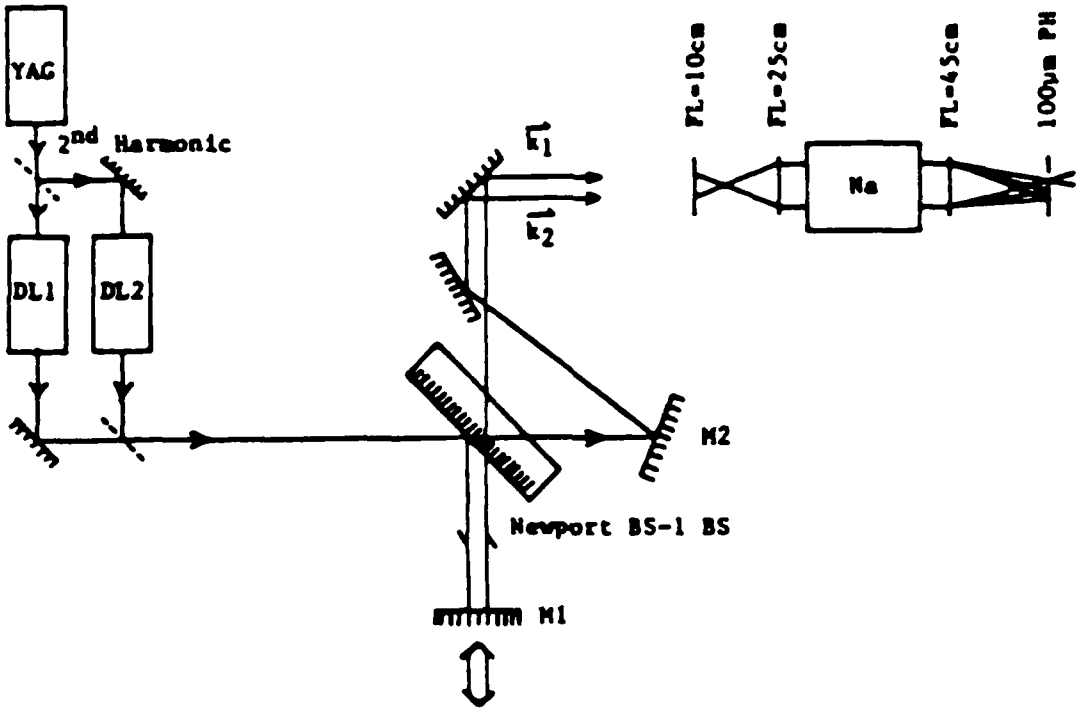

Figure 1: Schematic diagram of the experimental apparatus used to generate TDFWM. The outputs of lasers DL1 and DL2 are combined and then split into double wavelength beams by BS. Time delay is achieved by moving mirror M1.

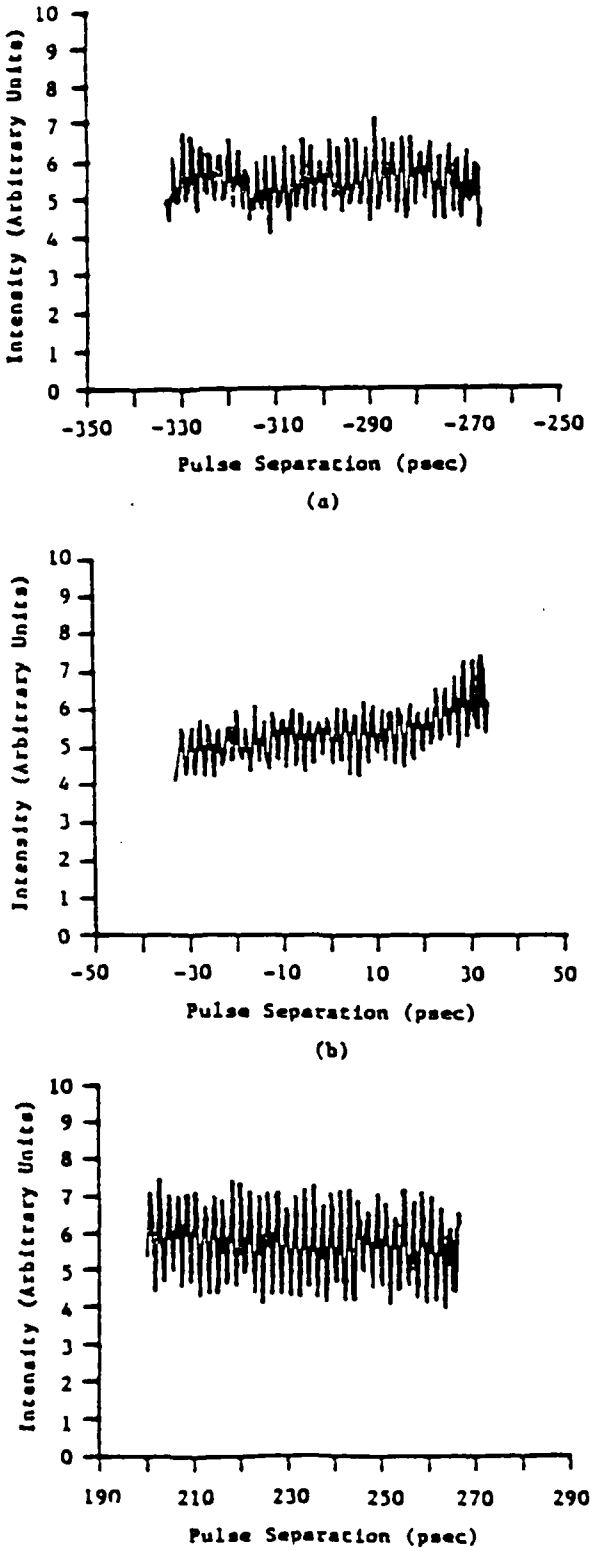

Figure 2: TDFWM signal intensity vs. pulse delay at several delay offsets: (a) -300 psec, (b) 0 psec, and (c) 230 psec.

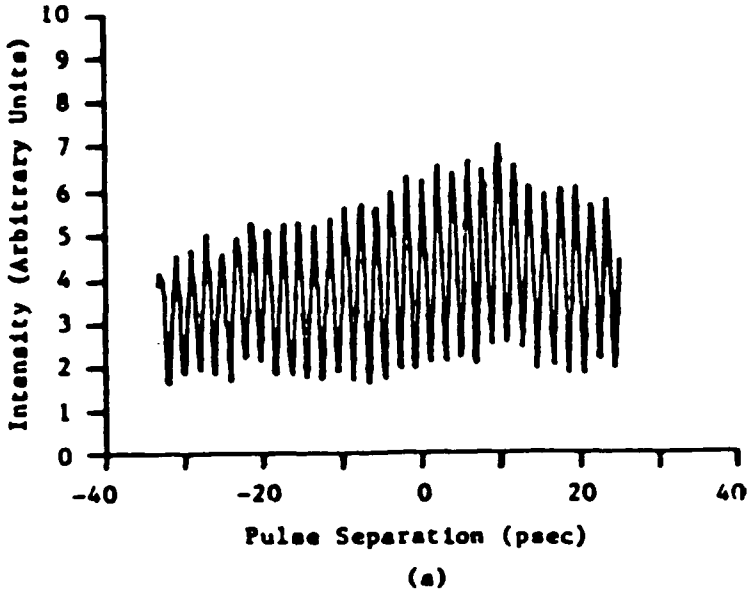

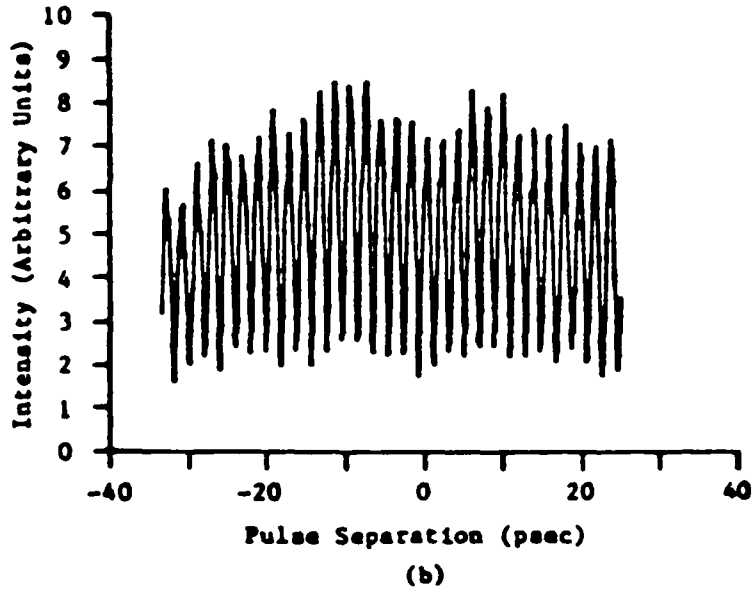

Figure 3: TDFWM signal intensity vs. pulse delay at (a) 5896Å and (b) 5890Å.

5890Å transitions instead of looking at them together. These signals are shown in Fig. 3 and show no significant differences. The depth of modulation has increased but that is only because we took much greater care in alignment and setup. A run we made without the spectrometer displayed equally deep modulation.

Our results imply that the modulation comes simply from a modulation of the atomic state amplitudes. As this obtains when two states are coherently excited through a third, it would seem that the problem is best understood by considering our lasers to be resonant, single mode, and transform limited. The sodium atoms are modeled as three level atoms whose $3S_{1/2}$, $3P_{1/2}$, and $3P_{3/2}$ levels we label as 1, 2, and 3 respectively. For this system the hamiltonian is given by

$$H = \begin{pmatrix} 0 & A & A' \\ A^* & \Omega & 0 \\ A'^* & 0 & \Omega' \end{pmatrix} \qquad (1)$$

where $A = -\Omega_R\{\cos[\Omega t - \mathbf{k}_1\cdot\mathbf{r}] + \cos[\Omega(t-\tau) - \mathbf{k}_2\cdot\mathbf{r}]\}$, Ω_R is the Rabi frequency of the dipole interaction coupling of the 1 and 2 levels, and k_1 and k_2 are the k vectors of the prompt and delayed pulses at frequency $\Omega = ck = 2\pi c/\lambda$ respectively. (The corresponding quantities relating to level 3 are primed.) Working in perturbation theory, we find that the leading order contribution to the dipole moment is phased to radiate in the $2k_2 - k_1$ or $2k'_2 - k'_1$ directions is

$$\mathbf{P} = [it^3/12]\{P\Omega_R\exp[i\Omega(t-\tau)-i\mathbf{k}_2\cdot\mathbf{r}] + P'\Omega'_R\exp[i\Omega'(t-\tau)-i\mathbf{k}'_2\cdot\mathbf{r}]\}\cdot$$
$$\{\Omega_R^2\exp[-i\Omega\tau-i(\mathbf{k}_2-\mathbf{k}_1)\cdot\mathbf{r}] + \Omega'^2_R\exp[-i\Omega'\tau-i(\mathbf{k}'_2-\mathbf{k}'_1)\cdot\mathbf{r}]\} + \text{c.c.}$$

(2)

This equation simplified by setting $k_2-k_1 = k'_2-k'_1$. This is, however, inconsistent with $k_1 \parallel k'_1$ and $k_2 \parallel k'_2$. But the minimum angular separation of the primed and unprimed k vectors imposed solely by the condition $k_2-k_1 = k'_2-k'_1$ is $\Delta\theta = ((\lambda-\lambda')/\lambda)\theta$. For our experiment $\Delta\theta = 10^{-6}$ and is much smaller than the 3×10^{-5} beam divergence in the interaction region so that the error introduced by this simplification is negligible. Using this condition P is better expressed as

$$\mathbf{P} = [i\Omega_R{}^3 t^3/6]\{P\exp[i\Omega(t-\tau)-i(2\mathbf{k}_2-\mathbf{k}_1)\cdot\mathbf{r}] + P'\exp[i\Omega'(t-\tau)-i(2\mathbf{k}'_2-\mathbf{k}'_1)\cdot\mathbf{r}]\}\cdot \{\exp[-i(\Omega+\Omega')\tau/2]\}\{\cos[(\Omega-\Omega')\tau/2]\} + \text{c.c.} \qquad (3)$$

where for simplicity we have set $\Omega_R = \Omega'_R$. This shows that one obtains the same result whether one looks at Ω, Ω' or at both. For frequencies which are not close the $2k_2-k_1$ and $2k'_2-k'_1$ directions will not be parallel to within the laser beam divergence and separate signals will always be observed at Ω and Ω'. These signals will be modulated as long as the condition $k_2-k_1 = k'_2-k'_1$ is maintained. In all cases, the intensity I which varies as $\int dt(P^* \cdot P)$ will depend on τ according to

$$I = (\text{constant}) \cdot [1 + \cos(\Omega - \Omega')\tau]. \qquad (4)$$

The 1.9 psec modulation we observe is thus understood as originating from a modulation of the dipole density and not from an interference of the atomic radiators. All the results displayed in Figs. 2 and 3 are accounted for except the depth of modulation. We believe this is due to jitter in the temporal delay we mechanically introduce.

In addition to looking at a signal in the vicinity of zero delay where both excitation pulses overlap in time, we also investigated the regime where the excitation pulses were well separated. The signals we observed here are more commonly known as photon echoes. We show in Fig. 4 the integrated

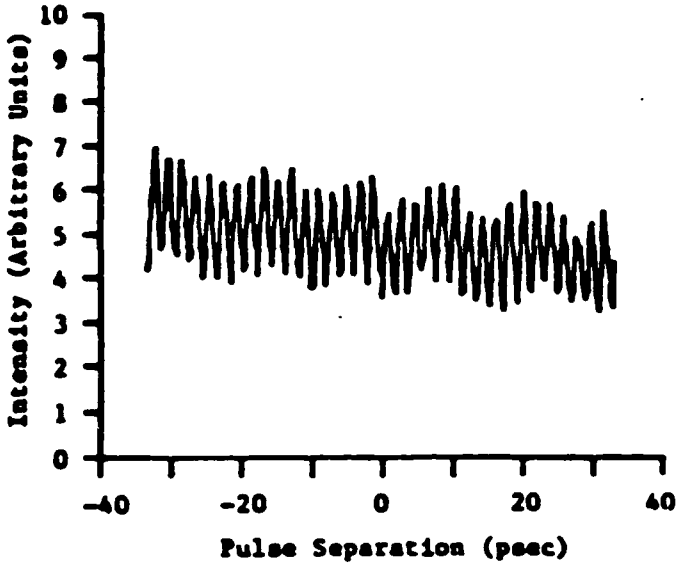

Figure 4: TEFWM signal intensity vs. pulse delay with a 20 nsec delay offset (the photon echo regime).

signal intensity for an excitation pulse separation of approximately 20 nsec. The time scale is in psec measured with the 20 nsec delay as the zero reference. The 1.9 modulation is still present but the depth of modulation has decreased.

For simplicity, we analyse these modulated echoes in the parallel pulse configuration, again assuming single mode laser excitation but allowing for laser detuning from the exact atomic resonances at Ω and Ω'. This is done by letting the excitation pulses act as delta functions on a Doppler distribution shifted according to the laser detuning and having a width corresponding to the actual length of the excitation pulses.

The wavefunction of an atom which experiences two-frequency excitations at t_1 and t_2 is given by

$$|\psi\rangle = \exp[-i\Omega(t-t_2)]\,|2\rangle + \exp[-i\Omega'(t-t_2)]\,|3\rangle + \{\exp[-i\Omega(t_2-t_1)] + \exp[-i\Omega'(t_2-t_1)]\}\,|1\rangle \qquad (5)$$

where in order to keep the presentation clear we have omitted terms which don't contribute to the echo and have kept the numerical coefficients of the state vectors equal to unity. The associated dipole moment oscillating at Ω is

$$P_j(t) \sim \exp[i\Omega(t-t_2)]\,\exp[-i\Omega(t_2-t_1)]\,\{\,1 + \exp[-i(\Omega'-\Omega)(t_2-t_1)]\,\}. \qquad (6)$$

The subscript j is introduced as P depends implicitly on the trajectory $x = x_j + v_j t$ of the atom (labeled by j) being followed. We have assumed the lasers are directed essentially along the x direction and v_j is the velocity component along x. The dipole density is obtained from $P(x,t) = \Sigma_j P_j(x,t) = \Sigma_j P_j(t)\ \ (x-x_j-v_j t)$. The summation is over all atoms and can be replaced by an integral over an effective velocity distribution. The radiated field is obtained by integrating the dipole density evaluated at the retarded time according to $E \sim \tau dx\ P(x,t+x/c)$. We allow for laser detuning and the non

zero length of the excitation pulses by expressing the effective velocity distribution by $g(v) = [1/v_p \quad 2\pi] \exp[-(v-v_s)^2/v_p^2]$. The shifted velocity is determined by the laser detuning Δ according to $v_s = (\Delta \ \Omega / \Omega)c$ while the effective Doppler velocity is $v_p = (\tau_D/ \tau_p)v_D$, where $v_D = \sqrt{(2k_BT/m)}$, k_B is Boltzman's constant, T is the temperature, and m is the atomic mass. Here is the normal Doppler dephasing time and $_p$ is the excitation pulse width.[7] Evaluating the electric field and calculating the integrated intensity we find

$$\int dt\, I_{echo} \sim 1 + \exp\{(-1/8)[\tau v_D(\Omega'-\Omega)/c]^2\} \cos[(\Omega-\Omega')\tau(1+v_s/c)]. \tag{7}$$

We note the 1.9 psec beat is again predicted but it is not Doppler free. The error however is of order $(\Omega-\Omega')v_s/c$ and not $\Omega\, v_s/c$ and it disappears in the limit of short excitation pulses ($\tau_p/ \tau_D \longrightarrow 0$). Also to be noted is the Gaussian degradation term. For our laser which was multimode and covers most of the Doppler line, v_D must replace v_p. But even so, for our sodium echoes the modulation depth would only be reduced by a factor of 1/e at τ = 760 nsec corresponding to echoes that appear 95 lifetimes after the first excitation pulse.

We noted earlier that the depth of modulation we found in the echo experiment was not as great as we had observed in the four wave mixing experiments where the excitation pulses overlapped. In subsequent experiments performed with parallel excitation pulses delayed by 30 nsec, we found the modulation was again weaker. As the tables on which we work are not acoustically isolated, we checked to determine if vibrations posed a problem by repeating our initial four wave mixing experiments, again with small delay but with extended optical paths. By appropriately moving mirrors M1 and M2 we extended the optical paths so that the perpendicular travel was comparable to that in the echo epxeriments. The result was that the depth of modulation was reduced to that observed in the associated echo experiment. We believe that with care many orders of improvement are possible.

In this report PEMS is extended into a new regime to study transitions between states that are widely separated in frequency compared to the

bandwidth of the exciting laser pulses. The accuracy to which a splitting can be measured using this technique depends on how many beats can be observed. The spectroscopic advantage here arises because the beats are long-lived; they last much longer than the coherence time of the lasers. If we block the entrance window of the sodium cell with a white card, the two overlapping excitation pulses form an interference pattern on this card only for pulse delays of the order of a hundred picoseconds or less. Echo beats on the other hand last well into the nanosecond regime.

This work was also supported by the U.S. Office of Naval Research under Contract No. N00014-78-C-0517.

(1) R. Beach and S.R. Hartmann, Phys. Rev. Lett. 53, 663 (1984).

(2) S. Asaka, H. Nakatsuka, M. Fujiwara, and M. Matsuoka, Phys. Rev. A 29, 2286 (1984).

(3) N. Morita and T. Yajima, Phys Rev A 30, 2525 (1984).

(4) H. Nakatsuka, M. Tomita, M. Fujiwara, and S. Asaka, Opt. Comm. 52, 150 (1984).

(5) R. Beach, D. DeBeer, and S.R. Hartmann, Phys. Rev. A to be published.

(6) R. Beach, B. Brody, and S.R. Hartmann, J. Opt. Soc. Am. B 1, 189 (1984).

(7) R. Beach, B. Brody, and S.R. Hartmann, Phys. Rev. A 27, 2537 (1983).

D. SPECTROSCOPY, RELAXATION, AND LASER ACTION IN $LaF_3:Pr^{3+}$

(R. Kichinski, F. Moshary and S.R. Hartmann)
(JSEP work unit 2, 1985 - 1988)
(Principal Investigator: S.R. Hartmann (212)280-3272)

1. Introduction — In this report we describe photon echo experiments performed on the strong σ polarized $^3P_0$-$(^3H_6)_1$ transition at 5985 Å and the $^3P_0$-$(^3H_5)_{1,2}$ transitions at 5333 Å and 5333.5 Å. This is a well-known technique and have been described in detail elsewhere.(1) The photon echo represents the coherent rephasing of a collection of oscillating electric dipoles that have been produced by the application of two consecutive laser pulses. The advantage of the photon echo technique is that the decay of the echo as a function of excitation pulse separation is determined by homogeneous effects alone. Therefore it allows one to study a homogeneous linewidth in the presence of a large inhomogeneous linewidth and is very suitable to linewidth studies in solids. In particular, this technique was used by Chen, et al. to study the $^3P_0$-$^3H_4$ transition(2,3) and by Whittaker et al. to investigate the $^1D_2$ - $^3H_4$ transition(4) in Pr^{3+}:LaF_3.

By first populating $^3P_0$ via the $^3H_4$ ground state with a excitation pulse at 4778 Å, we obtain a prepared excited state which now acts as the ground state for our echo experiment. Another dye laser would allow us to coherently excite any level which is connected to $^3P_0$ by an electric diplole transition. There are many such transitinos available(5) but because of the spontaneous phonon emission, the narrowest linewidths accompany transitions to the lowest levels of other manifolds. This technique allows us to study the lowest crystal field split levels of multiplets ($^3H_5$, $^3H_6$, etc...) which are not easily accessible from the ground state through an optical transition.

Photon echoes were also observed on a satelite line of the $^3P_0$-$^3H_4$ transition. In this report, we present the first statelite echo data. Echoes on a least a dozen satelite lines on the longer and short wavelength side of the $^3P_0$-$^3H_4$ transition were observed. These lines seem to be

symmetric about the $^3P_0$-$^3H_4$ transition.

Stimulated emission in Pr^{3+}:LaF_3 was first observed by Solomon et al. on the $^3P_0$-$^3H_6$ transition at 5985 Å at LN temperature.[6] Kaminskii et al. recently reported stimulated emission in a rod of Pr^{3+}:LaF_3, excited by Xe flash lamps, on the $^3P_0$-$^3H_6$ transitions at 5985 Å and 6000 Å and on the $^3P_0$-$^3F_4$ transition at 7195 Å at LN and room temperature.[7] Laser action on the 5985 Å transition has also been reported by Hegarty et al. in PrF_3 following laser excitation of the $^3P_0$-$^3H_4$ transition at temperatures up to 40° K.[8] We report observation of laser action and stimulated emission in Pr^{3+}:LaF_3 following laser excitation of the $^3P_0$ state at LHe and LN temperatures.

2. Experimental Procedure — The sample used was a 0.1% Pr^{3+}:LaF_3 of dimensions 1.0 cm diameter and 0.5 cm length. The value of αL for the $^3P_0$-$^3H_4$ transition in this sample at 4.6 °K is approximately 1. The sample is mounted in a Janis Supertran refrigerator so that its temperature may be varied smoothly from 2.5 °K to 15 °K.

Two independently triggered Quanta Ray YAG lasers were used to pump three Littman type dye lasers and six transverse amplifiers. The dye laser pulse width was about 7 nsec and the power .25 mJ/pulse. Dye laser linewidth was about 1-2 GHZ with about 4-5 modes (as measured with a Fabry-Perot etalon). The third Harmonic output from one YAG pumped a dye laser with two states of amplification at 4778 Å. The output of this dye laser was used to excite the $^3P_0$-$^3H_4$ transition and populate the $^3P_0$ state. The second and third harmonic of the YAG's were used to pump other dye lasers and amplifiers at 5985 Å (for the $^3P_0$-$^3H_6$ experiment) and 5333 Å (for the $^3P_0$-$^3H_5$ experiments). The relevant energy level diagram is shown in Fig. 1.

(a) $^3P_0$-$^3H_6$ Experiment — For the Photon echo, less than 40 nsec after transfering the population to $^3P_0$ state, two pulses at 5985 Å and wavevectors k_1 and k_2 entered the sample separated by a time τ and an angle of 50 mrad. Pulse 2 was reflected immediately back into the sample and the echo emerged in the direction opposite to pulse 1 ($k_e=-k_1$) and a time 2τ after the first pulse. The large angle between the beams greatly improved

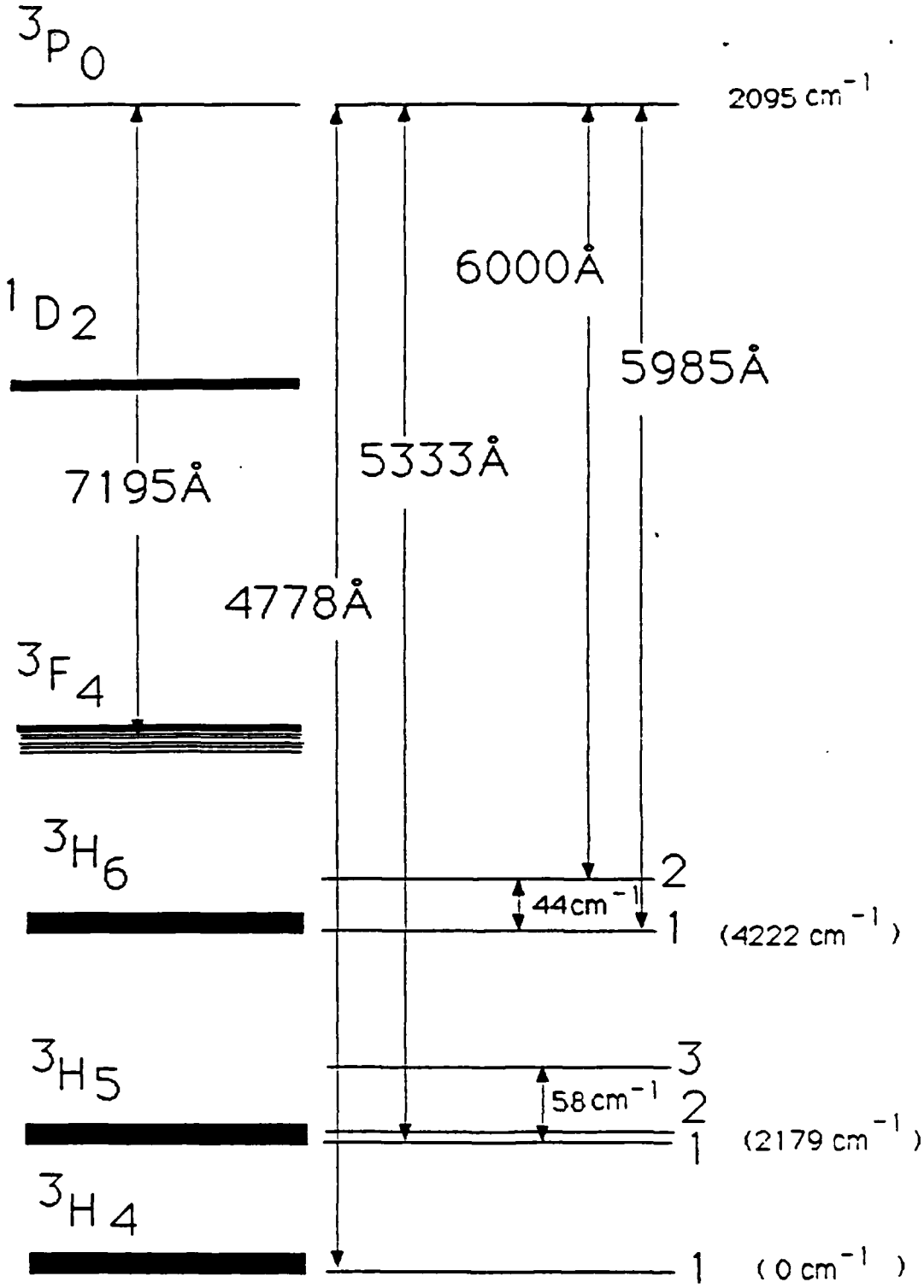
$^3P_0$
2095 cm^{-1}
6000Å
$^1D_2$
5985Å
5333Å
7195Å
4778Å
$^3F_4$
$^3H_6$
2
44cm^{-1}
1
(4222 cm^{-1})
$^3H_5$
3
58 cm^{-1}
2
1
(2179 cm^{-1})
$^3H_4$
1
(0 cm^{-1})

Figure 1

the signal to noise ratio while the backward wave configuration guaranteed perfect phase matching and thus no degradation of the signal resulted from angling k_1 and k_2.

For the stimulated echo three pulses at 5985 Å were used with a fixed delay of 80 nsec between the first and the second pulses. The beam arrangement was similar to that of the ordinary echo. Pulses 1 and 2 were split off from the same dye laser and the delay was introduced by a white cell. A third pulse at time τ after the second pulse and travelling opposite to the second pulse ($k_3=-k_2$) produced an echo signal 80 nsec laster with $k_3=-k_1$.

(b) $^3P_0$-$^3H_5$ Experiments -- We have observed $^3P_0$ fluorescence to both $(^3H_5)_1$ and $(^3H_5)_2$ on a Spex spectrometer at 5333 Å and 5333.5 Å. The experimental arrangements for the photon echoes were slightly different from that of $^3P_0$-$^3H_6$. The excitation pulses were colinear and parallel. The pulses were focused into the sampler with a f=25 cm lenz to produce the required pulse-area for an echo. As a result, the pump beam at 4778 Å is focused into the sample as well producing a greater population in the $^3P_0$ state. The observed fluorescence intensity from $^3P_0$ to $(^3H_6)_1$ is an order of magnitude larger than that to $(^3H_5)_{1,2}$ and therefore the pulse intensities needed are at least 10x larger than that of the previous experiment.

(c) Satellite Echoes -- A similar arrangement to that of $^3P_0$-$^3H_5$ experiment was used here but the beams were not focused into the sample. First we used one dye laser and whilte cell to produce two pulses with a fixed delay of 60 nsec to look for echoes on the satellite lines of the $^3P_0$-$^3H_4$ transition. After locating the strong satellite line at 4768 Å, we used two separate dye lasers during data acquisition so that we could vary the excitation pulse separation.

For all the above experiments, the signal is sent through three Pockels Cells and a spatial filter to further reduce the noise. An RCA C31034 photomultiplier tube is used to detect the signal. A suitable narrowband filter is placed in front of the PMT to reduce the long lived fluorescence from the $^3P_0$ state radiated into the solid angle of the echo with a lifetime of 50

μsec.

The PMT output is fed into a gated stretcher and then passed to a lab built sample/hold unit. From there, it is sent to an A/D converter and stored by an LSI 11/23 computer which also controls the YAG firing timing and therefore the excitation pulse separation. Both the laser timing jitter and the background were monitored and corrected for by the computer. The schematic diagram of the apparatus is shown in Fig. 2

(d) Fluorescence Spectroscopy, Laser Action, and Stimulated Emission -- A Spex 1702 spectrometer was used to analyze the fluorescence from the $^3P_0$ level to the $^3F_4$, $^3H_6$, $^3H_5$, and $^3H_4$ manifolds. Visible lasing was stimulated by focusing a laser pump pulse at 4778 Å ($^3P_0$-$^3H_4$) with a peak power of over 50 KW into the c=5% sample at 77°K and the c=0.1% sample for the temperature range of 4.6 °K to 38 °K. Lasing was also observed when the sample was pumped by a pulse at 4633 Å ($^3P_1$-($^3H_4$)in the c=5% sample at 77°K. The character of the lasing was analized using the Pockels Cell assembly of the photon echo experiments and the Spex spectrometer. The Pockels Cells gave us the ability to gate the lasing signal and therefore enabled us to study the tail of the signal.

3. Experimental Results

(a) $^3P_0$-$^3H_6$ -- For the two pulse echo, data was taken at 4.6 °K from τ=40 nsec to τ=1.2 μsec and is displayed in the upper trace of Fig. 3. The lower trace shows a theoretically calculated curve which will be discussed later. The echo intensity spans nine decades in magnitude. The overall exponential decay is effectively removed by multiplying the data by the factor exp(4τ/250 nsec). This factor is chosen to raise the smallest signal at τ = 1.2 μsec to the same level as the largest signal at τ = 40 nsec. The strong modulation is due to the hyperfine splitting frequencies of the terminal $^3H_6$ level which are of the order of 10 MHZ.

For the stimulated echo, data was taken in the range of τ' = 80 nsec to τ' = 70 μsec and at 4.6 °K. The experimental trace is displayed in Fig. 4a and the theoretical trace is displayed in Fig. 4b. The data ia characterized

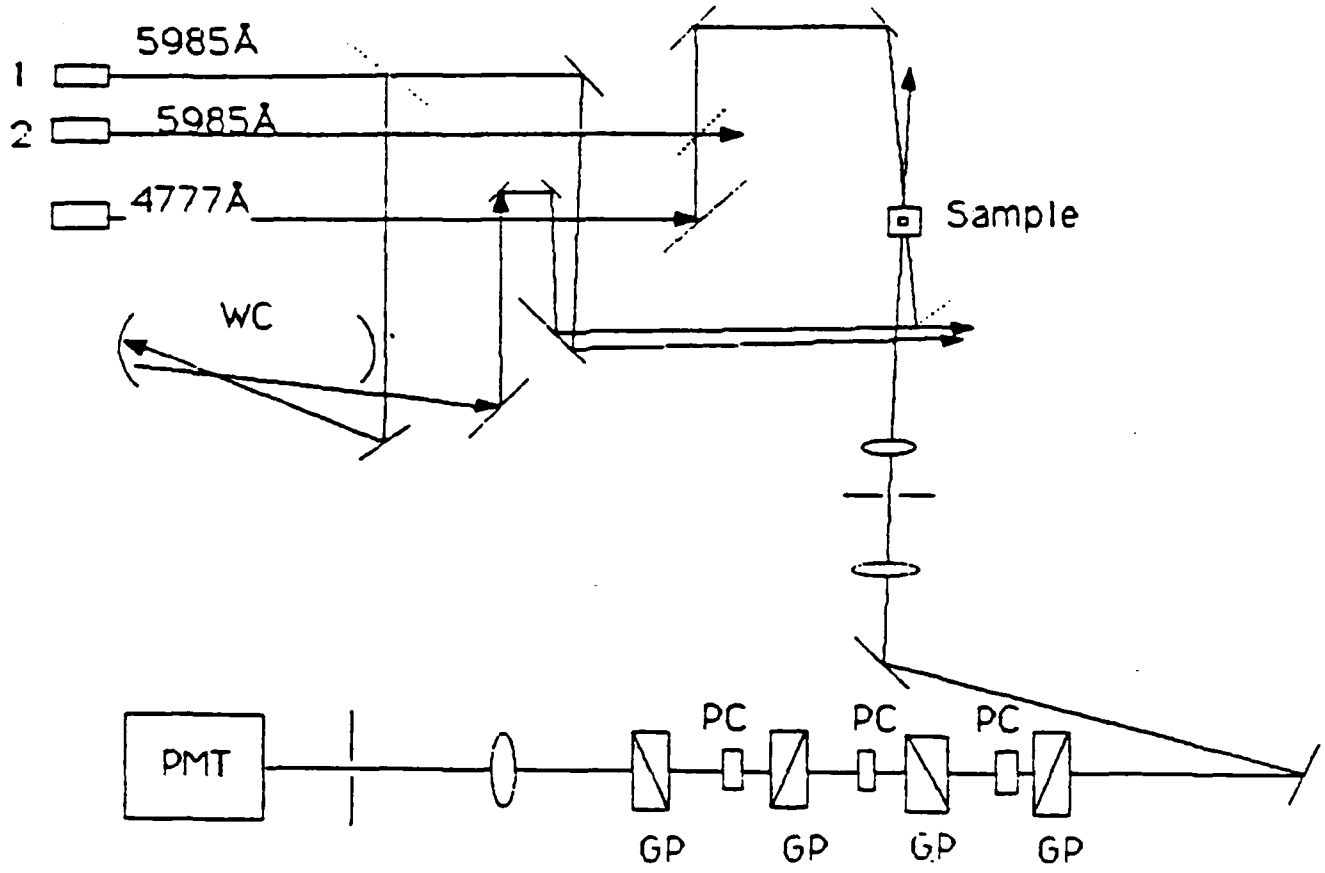

Figure 2

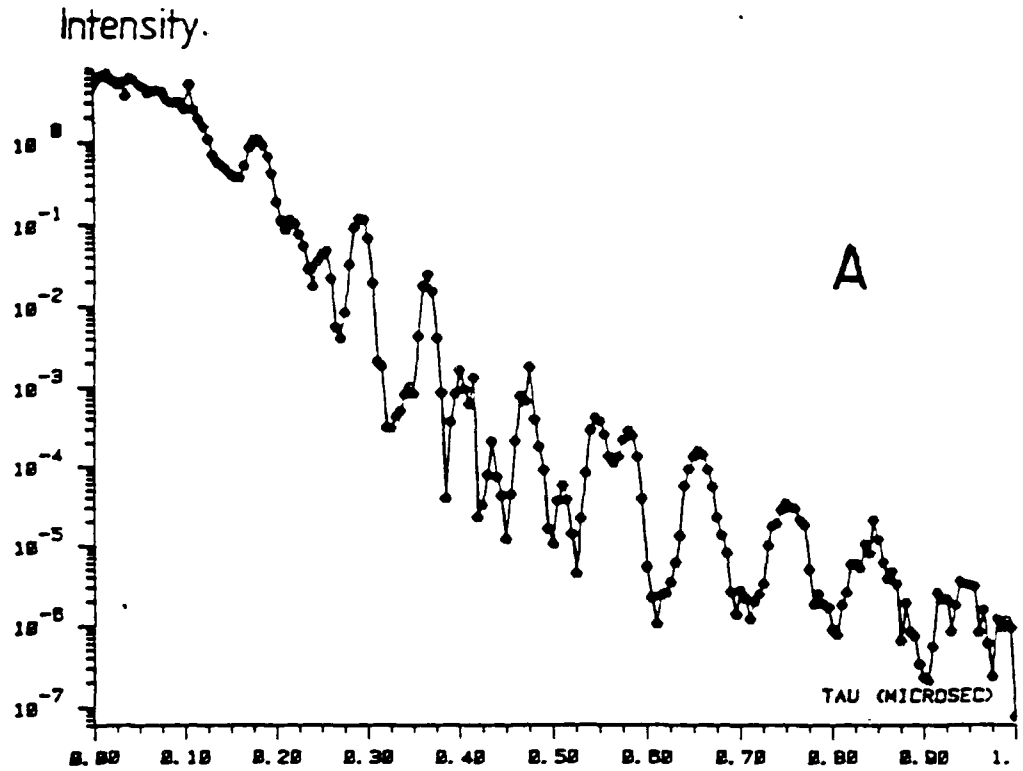
Intensity
A
TAU (MICROSEC)
0.00
0.10
0.20
0.30
0.40
0.50
0.60
0.70
0.80
0.90
1.

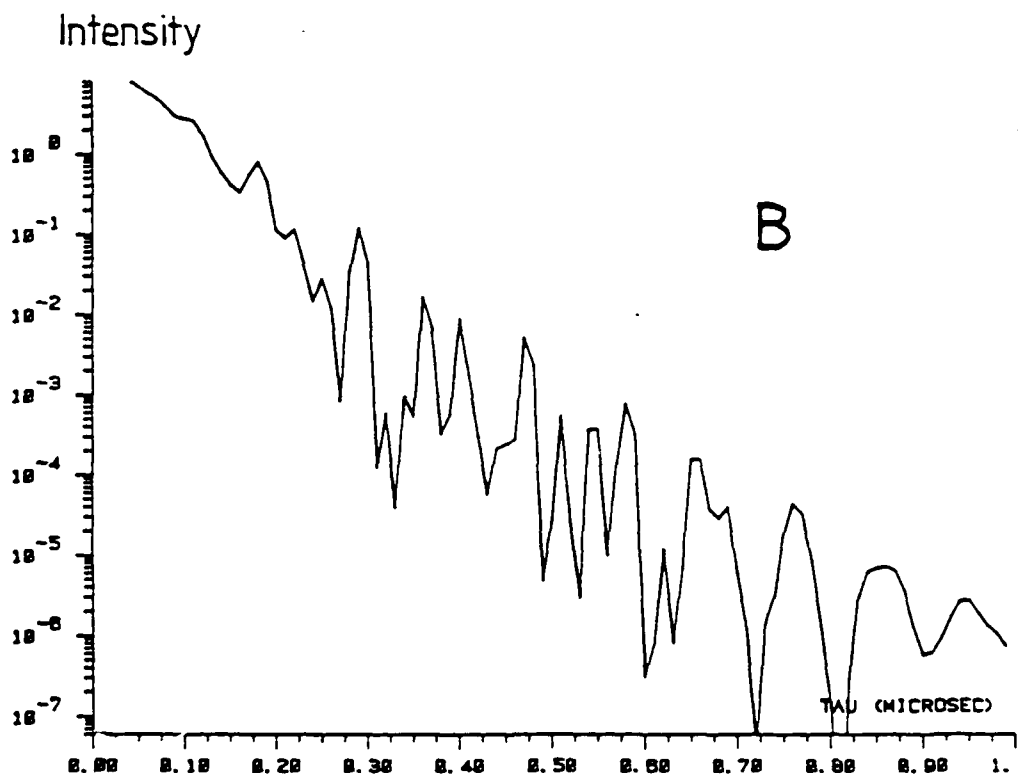
Intensity
B
TAU (MICROSEC)
0.00
0.10
0.20
0.30
0.40
0.50
0.60
0.70
0.80
0.90
1.

Figure 3

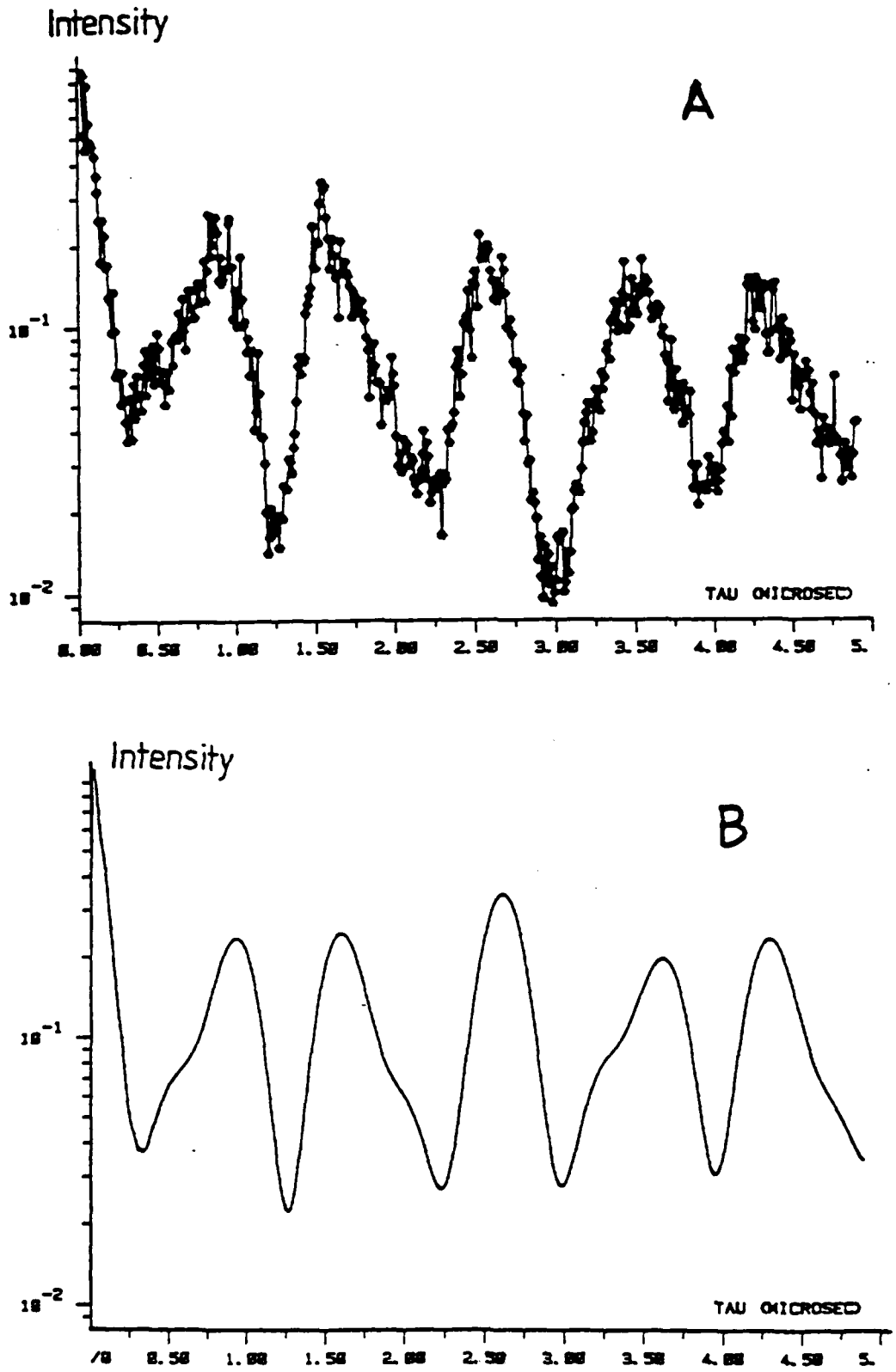
Intensity
A
10^{-1}
10^{-2}
TAU (MICROSEC)
0.00
0.50
1.00
1.50
2.00
2.50
3.00
3.50
4.00
4.50
5.
Intensity
B
10^{-1}
10^{-2}
TAU (MICROSEC)
0.00
0.50
1.00
1.50
2.00
2.50
3.00
3.50
4.00
4.50
5.

Figure 4

by a fast initial decay followed by a long lived signal which seems to decay with a time constant of the order of the $^3P_0$ lifetime. The $^3H_6$ hyperfine splitting modulatin is absent while that due to $^3P_0$ is evident out to $\tau = 15$ μsec.

An unambiguous determination of hyperfine splitting frequencies of the $(^3H_6)_1$ level is obtained by Fourier analysing of the data of Fig. 3. This approach is based on the theory of modulated echoes discussed elsewhere.[9] The result is displayed in Fig. 5. Distinct peaks occur at $v_1 = 10.0$ MHZ, $v_2 = 17.4$ MHZ and $v_3 = 27.4$ MHZ $= v_1 + v_2$. v_1 amd v_2 represent the hyperfine splittings of the $^3H_6$ level.

Temperature relaxation data for the $^3P_0 - {}^3H_6$ transition was taken by observing the two pulse echo at a fixed τ while the temperature of the sample was varied from 2.5 ^oK. Data was taken for $\tau = 150$ nsec and 250 nsec. The data for $\tau = 150$ nsec is displayed in Fig. 6. The solid curve is a best fit curve calculated based on the phonon relaxation mechanism to be described later.

(b) $^3P_0 - {}^3H_5$ — The $^3P_0 - (^3H_5)_1$ transition at 5333 Å is both σ and π polarized while the $^3P_0 - (^3H_5)_2$ transition at 5333.5 Å is only σ polarized. Both σ and π polarized photon echoes were observed on the 5333 Å transition. The σ polarized echo on the first transition is five times stronger than that of the second transition. Data was taken on the two σ polarized echoes in the range of $\tau = 50$ nsec to $\tau = 450$ nsec at 4.6 ^oK. No modulation was apparent on either of the two echoes. A sample experimental run on the $^3P_0 - (^3H_5)_1$ echo and one on $^3P_0 - (^3H_5)_2$ are shown in Figs. 7a and 7b respectively. The time constant deduced from the data for the 5333 Å echo is $T_2 = 100$ ($\pm$ 10) nsec and that for the 5333.5 Å echo is $T_2 = 93$ ($\pm$5) nsec. Absence of modulation is possibly due to the fact that the hyperfine splittings of the $^3H_5$ levels under investigation are smaller than 0.7 MHZ and because of the fast decay rates the low frequency modulation is not observable. We have noticed a slight curvature in the data taken on the $^3P_0 - (^3H_5)_1$ echo which may be due to this low frequency modulation.

Fig. 8 is the stimulated echo data taken on the $^3P_0 - (^3H_5)_1$ transition. A fast initial slope similar to that of the stimulated echo on the $^3P_0$-$(^3H_6)_1$

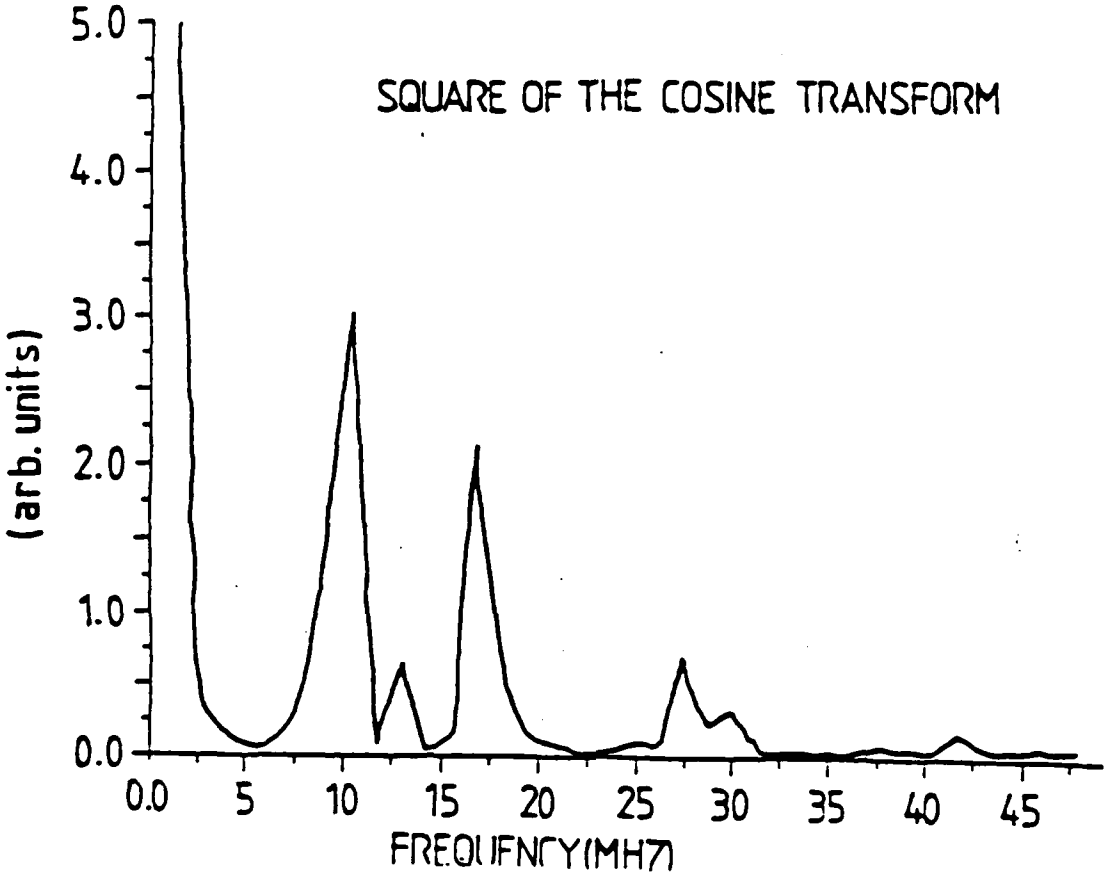
SQUARE OF THE COSINE TRANSFORM
(arb. units)
5.0
4.0
3.0
2.0
1.0
0.0
0.0
5
10
15
20
25
30
35
40
45
FREQUENCY(MHZ)

Figure 5

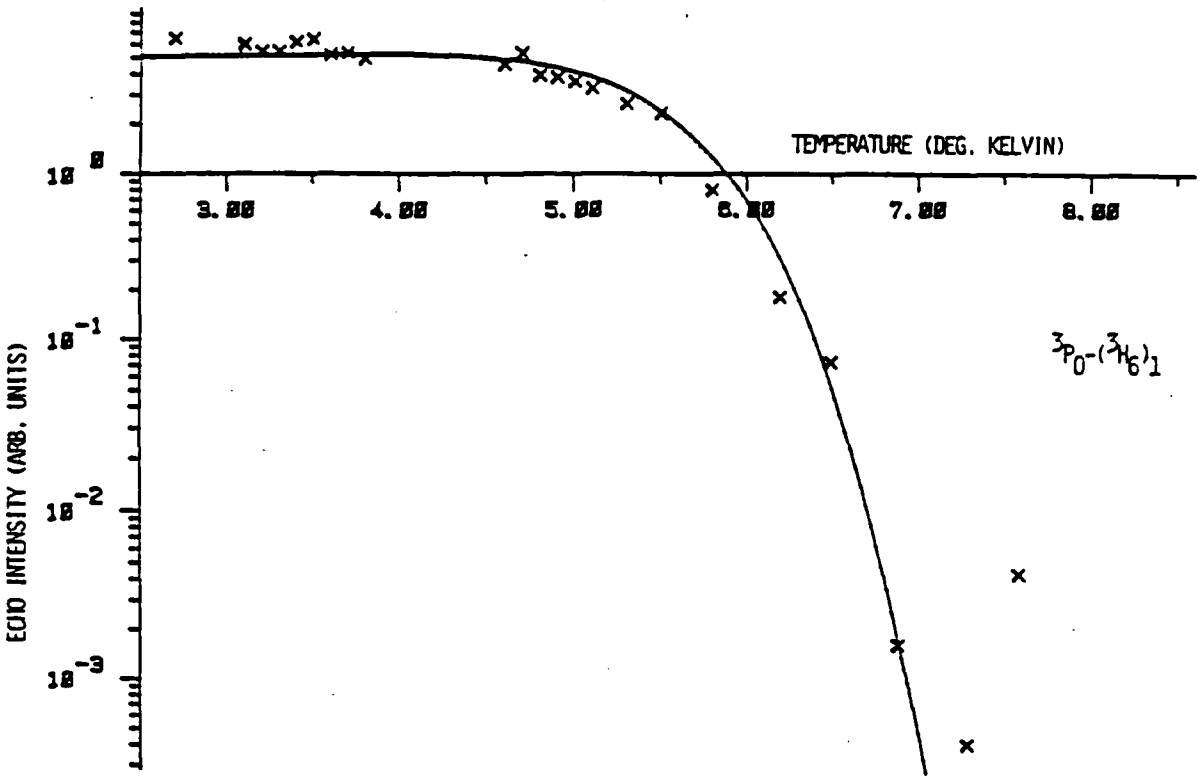
TEMPERATURE (DEG. KELVIN)
3.00
4.00
5.00
6.00
7.00
8.00
10 0
10 -1
10 -2
10 -3
ECID INTENSITY (ARB. UNITS)
$^3P_0-(^3H_6)_1$

Figure 6

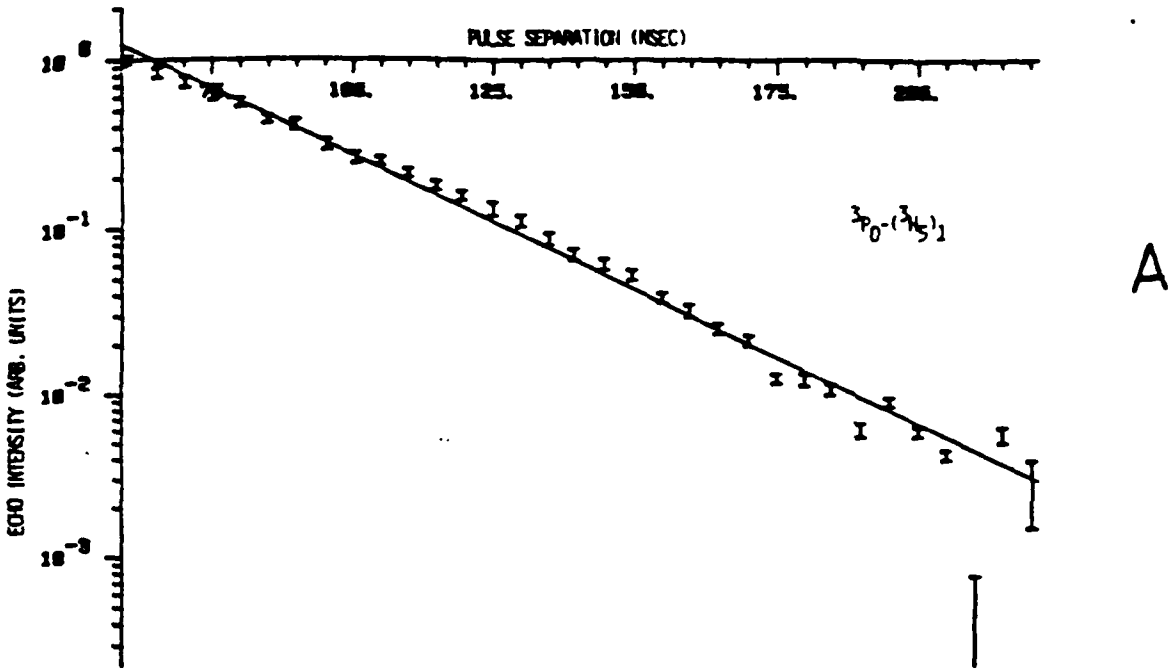
PULSE SEPARATION (NSEC)
ECHO INTENSITY (ARB. UNITS)
$^3P_0$-($^3H_5$)$_1$
A

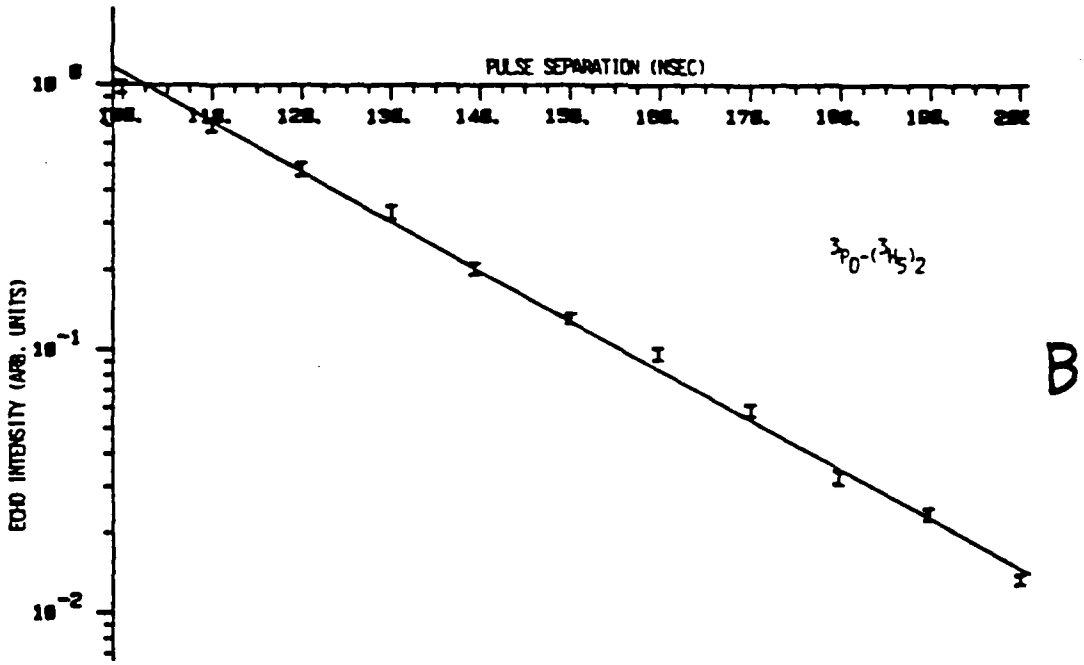
PULSE SEPARATION (NSEC)
ECHO INTENSITY (ARB. UNITS)
$^3P_0$-($^3H_5$)$_2$
B

Figure 7

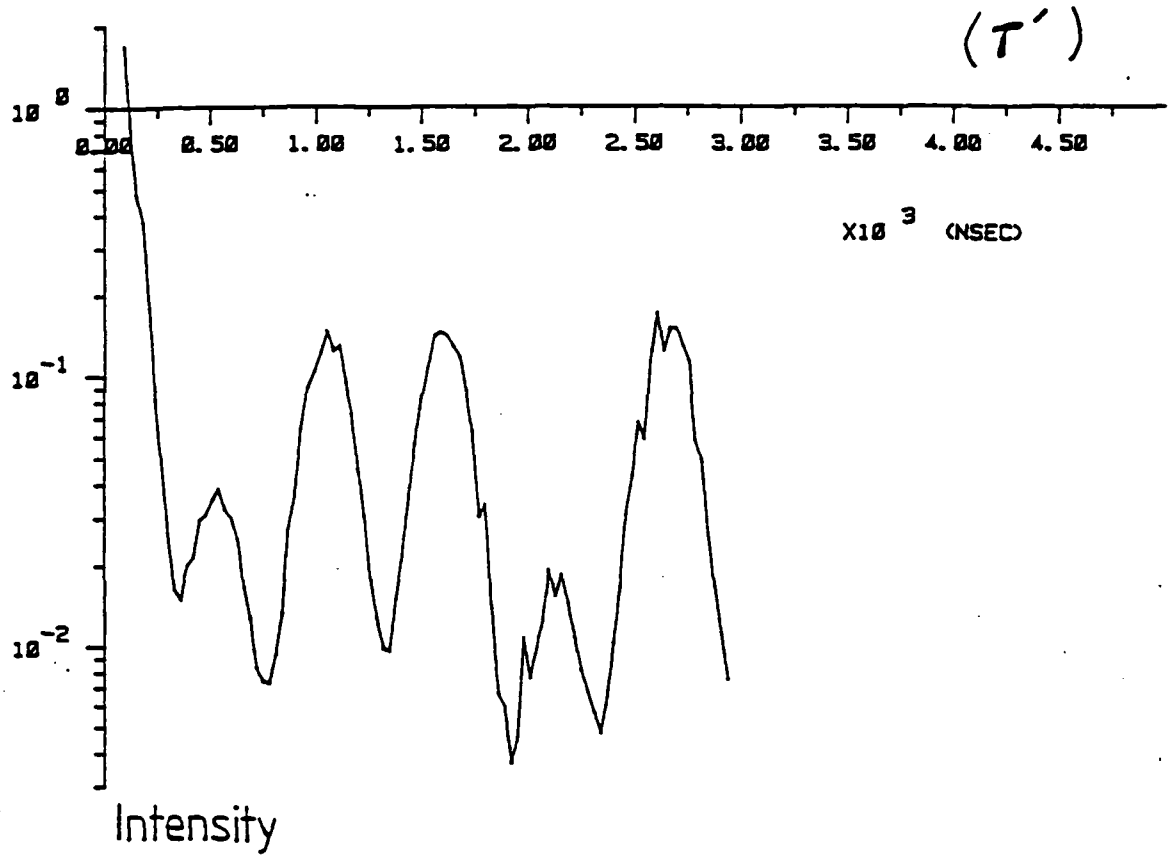
(T′)
10 0
0.00
0.50
1.00
1.50
2.00
2.50
3.00
3.50
4.00
4.50
X10 3 (NSEC)
10-1
10-2
Intensity

Figure 8

transition is apparent. The modulation present is due to the hyperfine splittings of the $^3P_0$ level.

Temperature relaxation data on the two echoes were taken by measuring the value of T_2 from experimental runs performed between 2 ^oK to 8 ^oK. The traces shown in Fig. 9 are obtained by plotting the homogeneous linewidth $\Delta v(T) = [\pi\ T_2(T)]^{-1}$ as a function of temperature. For both of the transitions under investigation, these curves illustrate the existence of residual homogeneous line-broadenings of approximatley 2.2 MHZ which from the stimulated echo results is due to fast population decay out of the $(^3H_5)_1$ and $(^3H_5)_2$ levels.

(b) Satellite Echoes — Photon echo data was taken on the $^3P_0$ - $^3H_4$ transition at 4778 Å and on the satellite line at 4768 Å in the range of τ = 60 nsec to τ = 1.1 μsec. The data is displayed in Fig. 10, with the lower trace being the satellite echo data. As apparent from the two curves, the nature of the modulation of the satellite echo data as well as its relaxation rate is different from that of the central transition. The time constant T_2 observed for the satellite echo is 2.74 μsec while T_2 on the main transition is 7.2 μsec. Future studies of other satellite lines as well as investigation on the nature of the apparent modulation pattern and the relaxation rate will provide valuable information on the character and origins of these lines.

(c) Laser action — The upper trace in Fig. 11 displays a picture taken from the pump pulse exciting the sample at 4778 Å with the total peak power of 50 KW. The next picutre in Fig. 11 is the lasing observed during he excitation pulse. The pump pulse is 7 nsec long and the lasing is 2 to 3 nsec long and slightly delayed with respect to othe pump pulse (about 2 nsec). This lasing is collimated and follows the pump pulse. Since this laser action is observed regardless of the angle the pump pulse makes with respect to the surface of the crystal, it is due to amplified spontaneous emission. The two pictures shown were taken at LHe temperatures in a c=1% sample. The lasing at this temperature is at the $^3P_0$ - $(^3H_6)_1$ transition (5985 Å). This lasing was also observed in a c=0.1% sample at temperatures

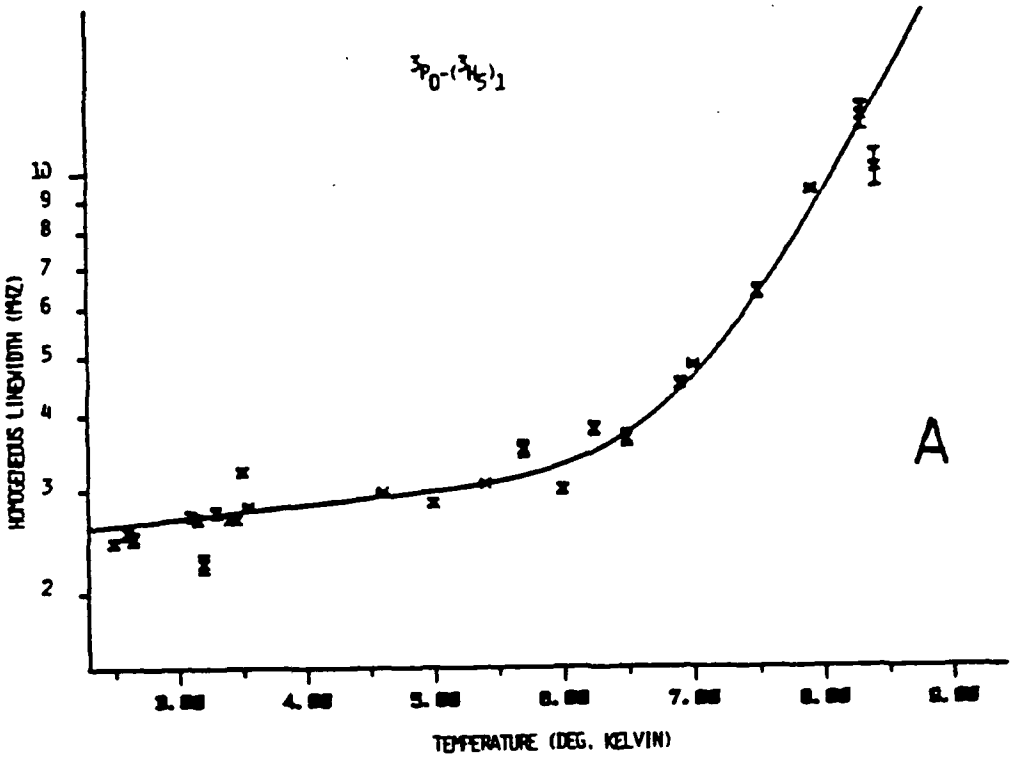
$^3P_0-(^3H_5)_1$
A
HOMOGENEOUS LINEWIDTH (MHZ)
TEMPERATURE (DEG. KELVIN)

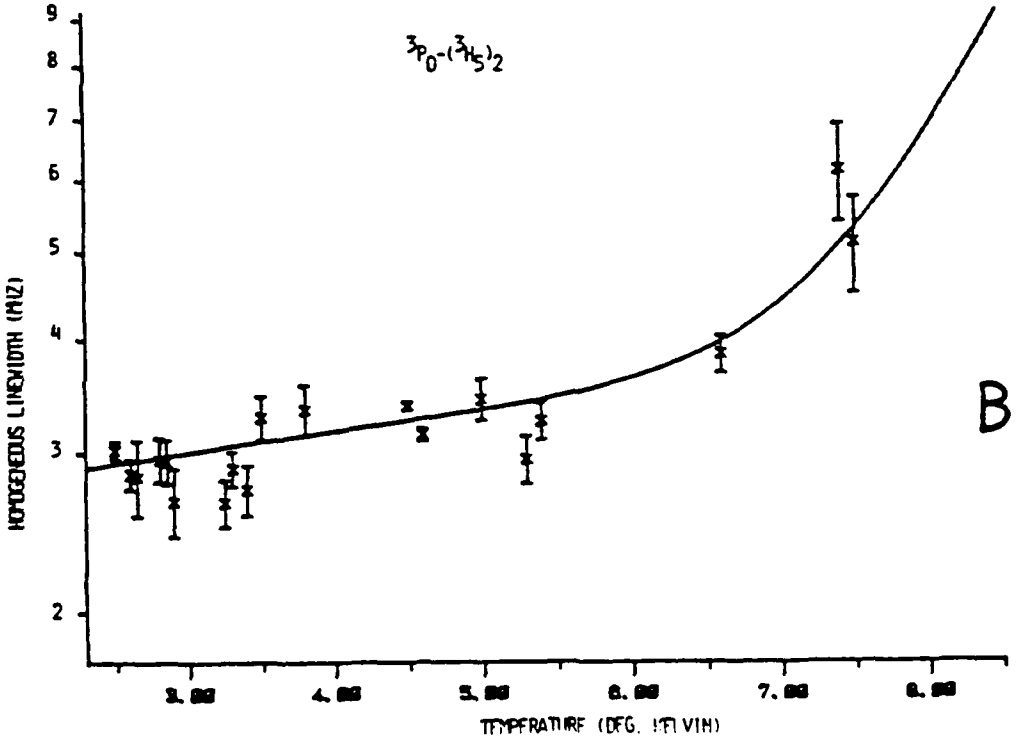
$^3P_0-(^3H_5)_2$
B
HOMOGENEOUS LINEWIDTH (MHZ)
TEMPERATURE (DEG. KELVIN)

Figure 9

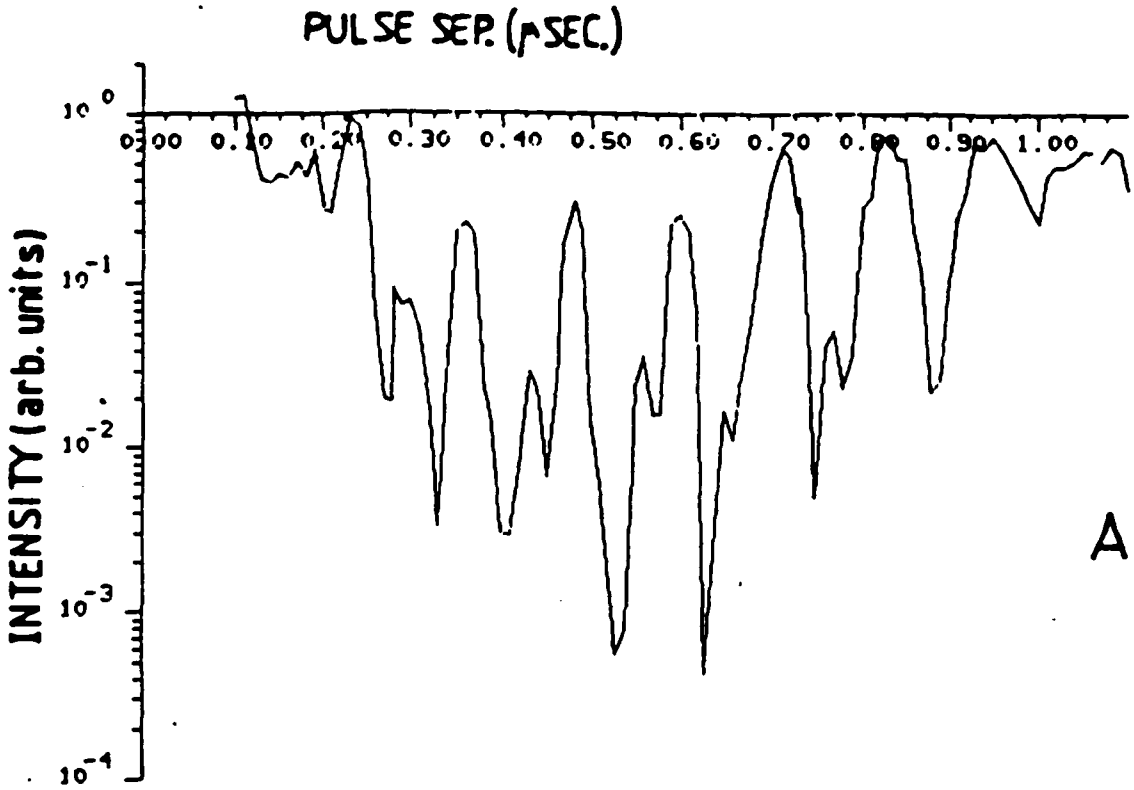
PULSE SEP. (μSEC.)
INTENSITY (arb. units)
A

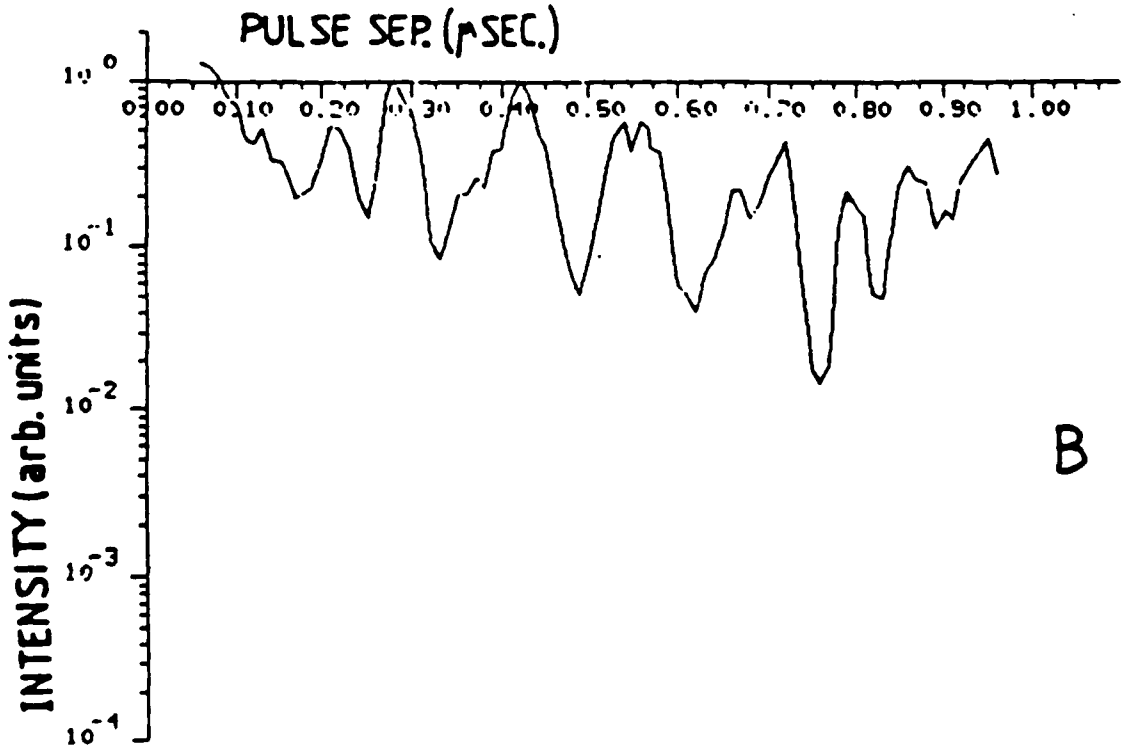
PULSE SEP. (μSEC.)
INTENSITY (arb. units)
B

Figure 10

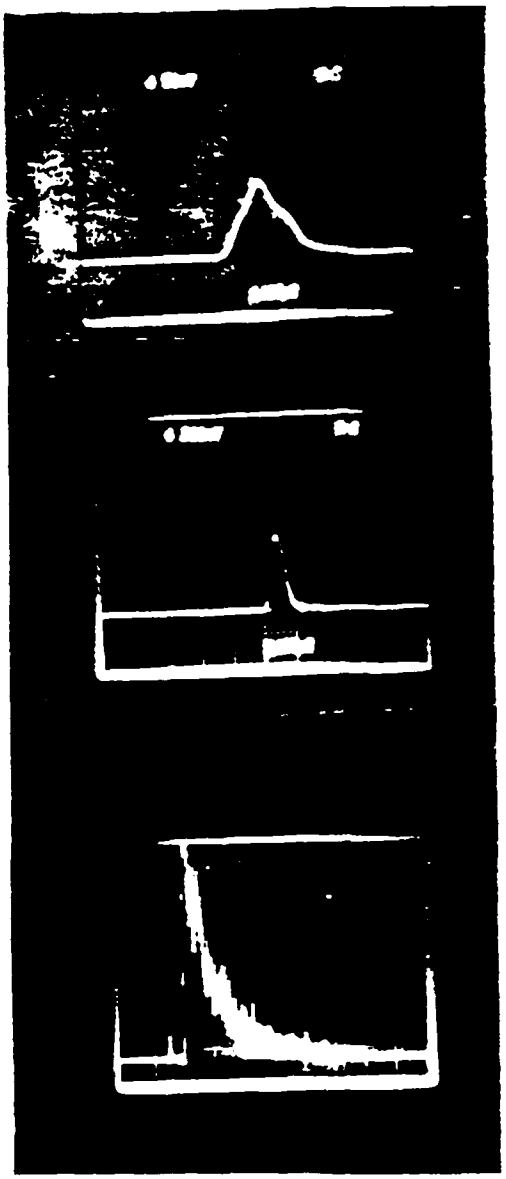

Figure 11

as high as 38 °K. Visible lasing was also observed at 77 °K in a c=5% sample at three lines: $^3P_0 - (^3H_6)_1$(5895Å), $^3P_0 - (^3H_6)_2$ (6000 Å), and $^3P_0 - (^3F_4)_5$ (7195 Å). The lasing efficiency was measured to be 1% in this sample. We measured the value of αL for the pump transition ($^3P_0 - {}^3H_4$) to be 6 in this sample at 77 °K. The relative decay of the lasing with respect to the excitation pulse is difficult to determine due to pulse delay and breakup of the pump pulse while the pulse-width of the lasing was similar to that previously observed at LHe temperatures. In either case, the lasing is followed by an apparently exponential tail with a time constant of about 300 nsec which is collimated and in the direction of the pump pulse (third picture in Fig. 11). It is interesting to note that the fluorescence decay time of the $^3P_0$ state is approximately 6 μsec at 77 °K in the c = 5% sample and is observable during the lasing. The time constant of the exponential tail seems to be the same on all the transitions. The emission is primarily to the 6000 Å line. As the pump power is increased, prior to the onset of lasing at a given line, the aforementioned collimated exponential emission (with τ = 300 nsec) appears. We estimate that the amount of energy in the initial lasing pulse is of the same order as the energy in the tail of the pulse.

Using a weak probe, we were able to stimulate emission into a single line at 77 °K in the c = 5% sample, quenching emission to the other two lines. We have observed gain of over 400x on a weak probe at 5985 Å line.

The above lasing action was also observed when we pumped the c=5% sample at the $^3P_1(^1I_6) - {}^3H_4$ transition at 4633 Å. The $^3P_1(^1I_6)$ levels are very braod at 77 °K and the lasing is observable over a large tuning range of several hundred GHZ.

4. Discussion

(a) Echo Modulation Maps — As in the works of Whittaker[4] and Chen,[3] it is possible to produce a theoretically calculated modulation pattern for the $^3P_0 - {}^3H_6$ echo. We start with the ground and excited state hamiltonians for our two pulse echo which may be written as:[3]

$$H_g(e) = P_{g(e)}[I_{z(Z)} + \eta_{g(e)}(I_{x(X)} - I_{y(Y)})] \qquad (1)$$

These hamiltonians re diagonalized by matrices $U_{g(e)}$. If we define $W = U_e U_g^{-1}$, the rephased dipolemoment at $t = 2\tau$ may be written as:

$$P(2\tau) = P(0)(2I+1)^{-1} \sum_{\alpha,\beta,\gamma,\varepsilon=1}^{2I+1} (W)_{\alpha\beta}(W^{-1})_{\beta\gamma}(W)_{\gamma\varepsilon}(W^{-1})_{\varepsilon\alpha} \exp[-(\Omega^e_{\alpha\gamma} - \Omega^g_{\beta\varepsilon})\tau] \cos[(\omega^e_{\alpha\gamma} - \omega^g_{\beta\varepsilon})\tau] \exp(-2\tau/T_2) \qquad (2)$$

where for Pr^{3+} in LaF_3, $I = 5/2$. The ω's are the hyperfine frequencies of the ground and the excited sates, and the Ω's are the nuclear hyperfine transition linewidths.

However, it need not be true that the principal axes of the ground and excited state hamiltonians are identical (x, y, z and X, Y, Z respectively). In fact, the relative orientation of these two systems will strongly influence the calculated results. Thus, a rotation of the excited state principal axes by θ has the effect of producing a new excited state hamiltonian H'_e where:

$$H'_e = R^{-1} H_e R \qquad (3).$$

This new hamiltonian may be diagonalized and the appropriate W matix elements found and using Eq. (2), and $P(2\tau)$ calculated. In this way we generate traces that can be compared to the data. The best fit is taken to yield the correct parameters n and θ. In our case the best fit to the two pulse echo $^3P_0 - {}^3H_6$ data is shown in Fig. 3b and represents a rotation of $\theta = 35^o$ around Y with z ||Y. We obtained $P_e = 4.4$ MHZ and $\eta_e = 0.44$ from the fourier transform data ($P_g = .293$ MHZ and $_g$ - .516 were taken from Chen et al.). We used $\Omega = 200$ KHZ for all three $(^3H_6)_1$ hyperfine nuclear linewidths.

This result is corroborated by a similar set of traces which we generated for the stimulatd echo. To do this we use a slightly different equation for $P(\tau + \tau)$ and follow a similar procedure to that of the two

pulse echo. The theoretical trace is shown in Fib. 4b. We were able to confirm, using the $^3P_0$ - $^3H_6$ stimulated echo data, for the first time that theoretical agreement is produced for both the normal and stimulated echo independently for the same parameters.

(b) Echo Relaxation — The overall decay of the echoes on the transitions investigated here appear anomalous in view of the other relaxation measurements made in this sample (e.g. the $^3P_0$ - $^3H_4$ and the $^1D_2$-$^3H_4$ echoes decay with the time constants $T_2 > 4\mu sec$). The radiative lifetime of $^3P_0$ is 50 μsec while the radiative lifetime of $^3H_6$ and $^3H_5$ are 56 msec and 100 msec respectively.[10]

Multiphonon decay from $^3H_6$ to the heighest level of $^3H_5$ can be estimated to yield a lifetime of 50 μsec from the work of Riseberg et al.[11] A similar estimate for the multiphonon relaxation from $^3H_5$ to the highest level of $^3H_4$ yields a relaxation rate of 25 μsec. Thus multiphonon processes are too slow to account for our observed decay rates.

We expect the temperature relaxation of the echo to be given by:[12]

$$I(T) = I_0 \exp(-4\tau/T_2(T)) \qquad (4)$$

$T_2(T)$ is related to the homogeneous linewidth by

$$T_2(T) = [\pi\Delta\nu(T)]^{-1} \qquad (5)$$

Considering the phonon relaxation within a manifold, Δ for the ith level within the manifold may be written as:[5]

$$\Delta\nu_i(T) = \Delta\nu'_i(T) + \sum_{e_j<e_i} A_{ji}[1+P(\Delta_{ij})] + \sum_{e_j>e_i} A_{ij}P(\Delta_{ij}) \qquad (6)$$

where $\Delta_{ij} = |E_i - E_j|$, $P(\Delta_{ij}) = [\exp(\Delta_{ij}/k_BT) - 1]^{-1}$, and A_{ij} is the spontaneous phonon emission rate from level i to j. If we assume that $\Delta\nu'_i$ is temperature independent, or the temperature dependence of this term is much weaker than that due to phonon relaxation, we can try to obtain a fit to our data by using the above equations. Considering Phonon absorption from

$(^3H_6)_1$ to $(^3H_6)_2$ (Δ = 44 cm^{-1}), the value of A_{12} obtained from fitting our data sets is: A_{12} = 44 $\pm$ 3 GHZ. The solid curve in Fig. 6 is a fit obtained to the data set displayed. This curve exhibits a temperature dependence similar to that of our data. By using the values obtained for T_2(4.6 ^oK) = 250 nsec and A_{12}, we find Δ ' = 1.2 MHZ.

A similar analysis on the temperature relaxation data obtained on the $^3P_0$ - $(^3H_5)_{1,2}$ transitions by considering the phonon absorption to the $(^3H_5)_3$ level with Δ_{1-3} = 58 cm^{-1} and the phonon coupling of $(^3H_5)_1$ and $(^3H_5)_2$ levels with Δ_{12} = 2 cm^{-1} yields the following results:

$$\Delta\nu[^3P_0-(^3H_5)_1]=2.2\times10^{-3}+4\times10^{-4}P(2\ cm^{-1})+260\ P(58\ cm^{-1})\quad GHZ$$
$$\Delta\nu[^3P_0-(^3H_5)_2]=2.2\times10^{-3}+4\times10^{-4}[1+P(2\ cm^{-1})]+74P(56\ cm^{-1})\quad GHZ$$

(7)

Theoretical fits are plotted along with the data in Fig. 9. From these plots it is clear that the assumption that Δ '$_i$ is temperature independent is reasonable and the temperature dependence of the linewidths is due to phonon relaxation.

In investigating the origins of this residual homogeneous linewidth observed, we considered Pr^{3+} ion - ion interaction. In particular, based on fluorescence studies we have performed, we estimate the dipole moment for the $^3P_0$ - $(^3H_6)_1$ transition to be an order of magnitude larger than that for $^3P_0$ - $(^3H_4)_1$. Therefore, we performed a two pulse echo experiment in a c = 0.01 sample. If the residual linewidth was due to dipole-dipole interaction, T_2 should increase with decreasing concentration. However, we observe a decrease in the value of T_2 when the concentration was decreased by a factor of ten. The estimated value of T_2 for the c = 0.01% sample is 80 nsec which is three times smaller than that in c=0.1% sample. This suggests that the variation in the relaxation rate observed, and possibly the anomoly in relaxation rate itself, is due to different amounts of impurities present in the two samples used. The possibility of Pr^{3+} - Impurity Ion interaction as the source of homogeneous broadening for the $(^3H_6)_1$ level was first suggested

by Yen et al.[13] They considered broadening of Pr^{3+} $^3P_0$ -$(^3H_6)_1$ transition by Nd^{3+} impurities in LaF_3 crystal. They demonstrated that a Pr^{3+}-Nd^{3+} ion pair in the initial state

$$|i\rangle = |\ (^3H_6)_1;\ (^4I_{9/2})_1\rangle \tag{8}$$

can relax to the final state

$$|f\rangle = |(^3H_5)_1;\ (^4I_{11/2})_1\rangle \tag{9}$$

through some intermediate near resonant state like:

$$|j\rangle = |(^3H_5)_1;\ (^4I_{11/2})_2\rangle \tag{10}$$

emitting a phonon of energy $E = 61\ cm^{-1}$ to conserve energy. Yen et al suggest two possible mechanisms for this direct transfer of energy between spatially separated Pr and Nd ions: (1) electric dipole interaction, and (2) Spin exchange interaction. The lifetimes of the $^3P_0$, and $^3F_3$ states as a function of Nd concentration have been studied in LaF_3 and $LaCl_3$,[14-16] and a decrease in lifetime of the $^3H_6$ state due to energy transfer to Nd^{3+} ion in $LaCl_3$ has been suggested by Kraustsky et al.[15]

Using the approach outlined above, one can find many near resonant intermediate states through which the $(^3H_6)_1$ and $(^3H_5)_{1,2}$ excited states of Pr^{3+} can relax via transfer of energy to Nd^{3+} $^4I_{13/2}$ and $^4I_{11/2}$ manifolds. Currently we are spectroanalyzing our samples to determine the relative Nd^{3+} concentrations in the samples used.

This work was also supported by the National Science Foundation under Grant No. NSF DMR-80-06966.

(1) I.D. Abella, N.A. Kurnit and S.R.Hartmann, Phys. Rev. 141, 391 (1966).

(2) Y.C. Chen, K. Chiang, and S.R. Hartmann, Opt. Comm. 29, 181 (1979).

(3) Y.C. Chen, K. Chiang and S.R. Hartmann, Phys. Rev. B 21, 40 (1980).

(4) E.A. Whittaker and S.R. Hartmann, Phys. Rev. B 26 3617 (1982).

(5) W.M. Yen, W.C. Scott and A.L. Schawlow, Phys. Rev. 136, 27 (1964).

(6) R. Solomon and L. Mueller, Appl. Phys. Lett. 3, 135 (1963).

(7) A.A. Kaminskii, Int. Conf. on Lasers '80, New Orleans, LA, USA Soc. Opt. Quant. Elec., McClean, VA, USA 328-342 (1980).

(8) J. Hegarty and W.M. Yen, J. Appl. Phys. 51, 3545 (1981).

(9) D. Grischkowsky and S.R. Hartmann, Phys. Rev. B 2, 60 (1970).

(10) M.J. Weber, J. Chem. Phys. 48, 4774 (1968).

(11) L.A. Riseberg and H.W. Moos, Phys. Rev. Lett. 19, 1423 (1967).

(12) T. Kohmoto, H. Nakatsuka and M. Matsuoka, Jap. J. App. Phys. 22, 1571 (1983).

(13) W.M. Yen, R.L. Greene, W.C. Scott and D.L. Huber, Phys. Rev. 140, A1188 (1965).

(14) D.S. Hamilton, P.M. Selzer, and D.L. Huber, and W.M. Yen, Phys. Rev. B 14, 2183 (1976).

(15) N. Kraustsky and H.W. Moos, Phys. Rev. B 8, 1010 (1973).

(16) B.R. Reddy, J. Chem. Phys. 77, 2862 (1982).

E. NOBLE GAS-INDUCED COLLISIONAL LINE BROADENING OF ATOMIC Li RYDBERG SUPERPOSITION STATES 2S–nS AND 2S–nD (n = 4 to 30) MEASURED BY TRILEVEL ECHOES

(E. Yu, F. Moshary, and S.R. Hartmann)
(JSEP work unit 2, 1985 - 1988)
(Principal Investigator: S.R. Hartmann (212) 280-3272)

1. Introduction — The development of the trilevel echo technique facilitated the first comprehensive study of foreigh gas-induced broadening of superposition states of the same parity. In Na vapor the collisional broadening of 3S–nS (3S–nD) superposition states due to He, Ne, Ar, Kr and Xe has been measured over the range of n = 5 to 38 (n = 4 to 40).[1,2]

Using the trilevel echo technique in our experiments, we measure the effect of collision induced phase changes by monitoring the echo decay as a function of perturber gas pressure. The decay factor, obtained in this manner is directly proportional to the collisional cross-section.

Among alkali elements, lithium has the simplest structure: it has one valence electron with two inner electrons forming a closed shell, and is more closely approximated by hydrogenic wave function than other alkali elements. Our experiment is the first to measure the line broadening of Li Rydberg superposition states 2S–nS and 2S–nD with n = 4 to 30.

2. Trilevel echo in gases — The atomic system involved in our Li trilevel echo experiment has three energy levels: $|2S\rangle$, $|2P\rangle$, and $|nS\rangle$ (or $|nD\rangle$) as in Fig. 1a. The levels $|2S\rangle$ and $|2P\rangle$ and the levels $|2P\rangle$ and $|nS\rangle$(or $|nD\rangle$) are coupled by electric dipole moments. Fig. 1b displays the excitation pulse sequence and the expected position of the echo. Fig. 1c shows the recoil diagram using the Billard Ball Model.[3] The solid line represents the ground state ($|2S\rangle$)
trajectory. As shown in Fig. 1c, the first pulse, at the t_1, frequency ω_1, and wave vector K_1, excites a $|2P\rangle$ state component which recoils along the

dotted line until the arrival of the oppositely directed second pulse at the time t_2, frequency ω_2, and wave vector K_2. This second pulse excites the $|2P\rangle$ state component into a $|nS\rangle$ (or $|nD\rangle$) state component which recoils along the dashed line trajectory. A third pulse at the time t_3, frequency ω_2, and wave vector $K_3(K_3=K_2)$ regenerates the $|2P\rangle$ state component which recoils towards the ground state ($|2S\rangle$) component. These trajectories cross to produce the echo at

$$t_e = t_1 + (t_3-t_2)K_2/K_1 \qquad (1)$$

with wave vector

$$K_e = K_1-K_2 + K_3 \qquad (2)$$

The trivelel echo emerges along the same direction as pulse 1 and with the frequency $\omega_{2P-2S} = \omega_1$. In the interval between pulse 2 and pulse 3, the atoms are in a 2S–nS(nD) superposition state. During this time, the phase changing collisions between the Li atoms (in 2S–nS(nD) superposition state) and the perturber atoms contribute to the overall decay of the echo.

3. Experiment — Three laser pulses, the first and second simultaneous ($t_1=t_2=0$), and the third one delayed by $t_3-t_2 = \tau$, traversed a sample of Li vapor. The echo signal was formed as described. The echo intensity signal was detected by a computer controlled data acquisition system and was registered as a function of perturber gas pressure. The data so collected was stored and analyzed on the computer. Data for five noble gases were collected, one at a time, for each nS or nD state as the state was changed from n = 4 to 30 sequentially.

Two Nd:YAG lasers are used to pump our dye laser oscillators and dye laser amplifiers. The firing of the YAGs was externally controlled by a digital delay generator (DDG) which was set by the computer.

Fig. 2a shows the direction of the pulses approaching the Li cell in the experiment. The pulse polarization was arranged (see Fig. 2b) so that the echo was oppositely polarized from pulse one. This arrangement gave us a

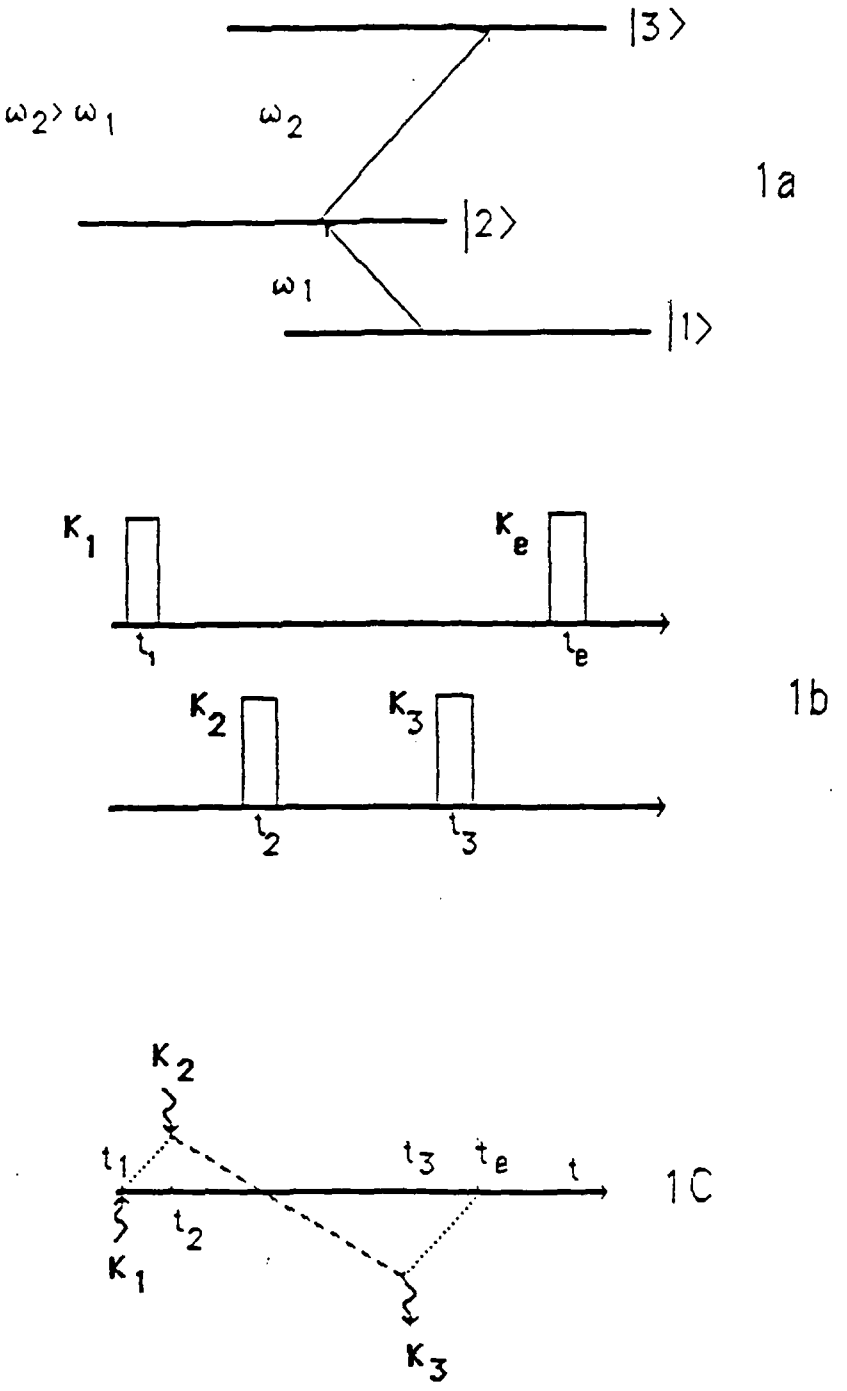

Figure 1(a), (b), (c): Energy level in the trilevel echo experiment.

2a

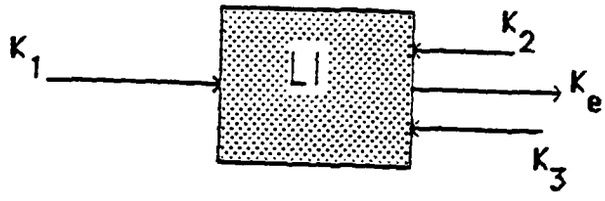

2b

K_1	K_2	K_3	K_e
→	→	↑	↑

Figure 2 (a) and (b): Pulse propagation direction for the trilevel echo experiment.

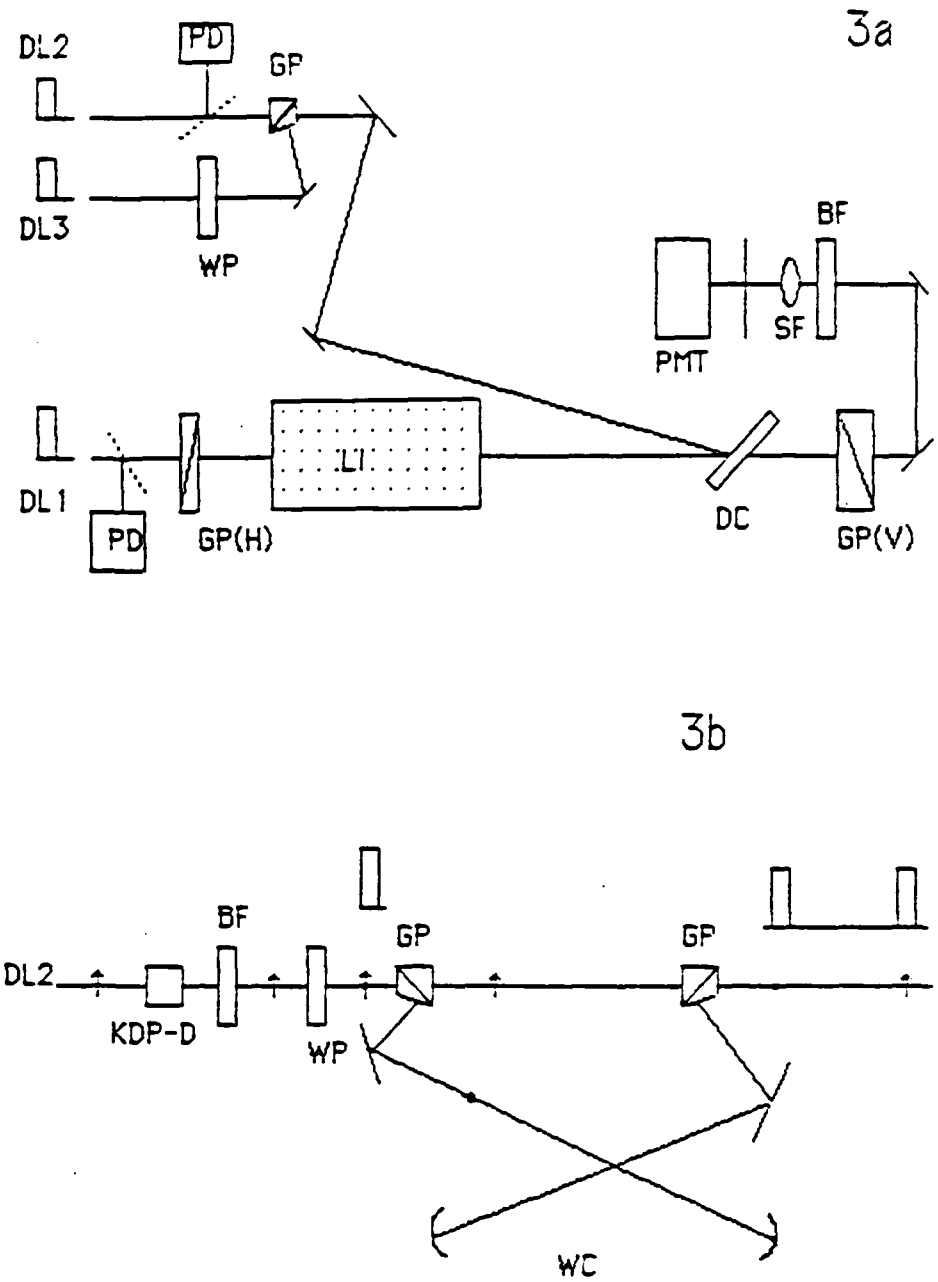

Figure 3(a) and (b): Schematic diagram of experimental apparatus for n < 7. PD = photodiode; WP = wave plate; GP = Glan prism; DC = dichroic; BF = Band filter; SF = Spatial filter.

large signal to noise ratio.

Dye laser 1 was tuned in resonance with the Li 2S-2P(λ_1 = 6708 Å) transition. For n < 7 states (see Fig. 3a), two separate dye lasers were used to generate pulse 2 and pulse 3. Dye lasers 2 and 3 were tuned to the 2P-nS (nD) transition, and one stage of amplification was used to get suitable π pulses.

The scattered light from dye lasers 2 and 3 was fed into two photodiodes whose outputs served as the start and stop signals for a time-to-amplitude converter (TAC) to measure and correct he offset in the DDG time delay setting throughout the experiment.

The experimental set up for n > 7 was slightly different in that pulses 2 and 3 were both obtained from the same source as shown in Fig. 3b. One dye laser plus three stages of amplification produced a 220 kw peak power beam below 7800 Å. This beam was focused into an Inrad KDP-D doubling crystal to provide excitation pulses below 3800 Å. The SHG beam was initially vertically polarized after the crystal, but its polarization orientation was subsequently changed by passing it through a waveplate. Two different polarizations were then separated by a Glan prism. The vertically polarized pulse 3 went through a White cell for a 29 nanosecond delay and recombined with the horizontally polarized pulses at the second Glan prism. The set up after that was the same as in Fig. 3a.

Li vapor was contained in a 4-inch diameter stainless steel pipe sealed with quartz windows, wrapped with heating coils, and maintained at 700 $\pm$ 2 ^{o}K. The Li vapor pressure was 10^{-4} Torr (corresponding to a number density of $10^{13}/cm^3$). A needle valve controlled the leak rate of perturber gas into the heat pipe, and MKS capacitance manometer Baratron monitored the gas pressure to within 1 mTorr.

The experiment was controlled by a PDP 11/23 computer. The output of the PMT was read into the computer through one channel of an analog-to-digital converter (ADC). Into a separate ADC channel was fed the output of TAC and another ADC channel read the Baratron, thus recording the noble gas pressure in the Li oven.

4. <u>Data Analysis</u> -- The phenomenological decay constant which

represents the total relaxation rate of the $|i\rangle - |j\rangle$ superposition state, Γ_{ij} decomposed into two parts; one representing the effect of atomic collisions and the other representing the effects of all other decay processes. We may write

$$\Gamma_{ij} = \Gamma_{ij}^{o} + \eta_{ij}P \qquad (3)$$

where P is the foreign gas perssure, Γ_{ij}^{o} is the relaxation rate of $|i\rangle - |j\rangle$ superposition state in the absence of collisions. The echo intensity as a function of pressure is given by:

$$I(p) = I_e(P=0)\exp(-\beta P) = I_e(0)\exp(-2\sigma_{eff}vt_eN) \qquad (4)$$

where σ_{eff} is the effective cross section for the total period, $v = [8k_BT/(\pi\mu)]^{1/2}$ is the average relative speed of the perturber and the radiator, μ is their reduced mass, k_B is the Boltzmann constant, T is the absolute temperature, and N is the noble gas number density. We use the relation $P = NK_BT$. σ_{eff} may be written as:

$$\sigma_{eff} = \sigma_{23}(\tau / t_e) + \sigma_{12}[(t_e - \tau)/t_e] \qquad (5)$$

where σ_{ij} is the collisional cross section of the Li-perturber gas atoms with Li atoms in the $|i\rangle - |j\rangle$ superposition state. Therefore, using equation (1):

$$\sigma_{2S-n} = \sigma_{eff}(K_2/K_1) - \sigma_{2S-2P}[(K_2/K_1)-1] \qquad (6)$$

Using the value for σ_{2S-2P} measured by Kachru et.al.[4] σ_{2S-nP} can be obtained from σ_{eff}.

The echo intensity was measured as a function of noble gas pressure P. From a least-squares fit to the data β was obtained. Thus, using Eq. (4), a value for σ_{eff} was calculated and used in Eq. (6) to give a value for σ_{2S-n}. The resulting values for σ_{2S-ns} and σ_{2S-nD} are presented in Tables 1 and 2. These are the collisional cross sections of Rydberg states perturbed by five

Table 1

Cross sections (x 10^{-16} cm^2)

Angstroms. The statistical uncertainties are presented in the parentheses following the cross sections.

Superposition state	Helium	Neon	Argon	Krypton	Xenon
2S- 4S	722(75)	403(19)	933(50)	1700(129)	2083(242)
- 5S	907(121)	347(25)	1635(227)	2385(226)	2492(242)
- 6S	721(73)	441(64)	1802(206)	4785(472)	4361(464)
- 8S	522(24)	252(12)	1483(84)	4030(207)	9895(475)
- 9S	463(17)	314(13)	1360(71)	3025(157)	7336(411)
-10S	518(19)	381(15)	1380(72)	3438(165)	7433(282)
-11S	369(13)	511(20)	1514(80)	2927(163)	6273(438)
-12S	379(15)	509(21)	1435(78)	2701(177)	4943(265)
-13S	309(16)	407(17)	1153(58)	2082(98)	4029(273)
-14S	281(12)	386(16)	1156(64)	2019(109)	3830(191)
-15S	319(19)	473(20)	1329(113)	2015(101)	3239(180)
-16S	362(24)	356(14)	1417(71)	1968(102)	3902(194)
-17S	515(20)	601(41)	1490(77)	2112(95)	3806(190)
-18S	437(33)	796(36)	1455(77)	2164(114)	3736(177)
-19S	411(20)	375(15)	1087(57)	1906(87)	3360(217)
-20S	384(19)	417(25)	1015(51)	1876(82)	2995(234)
-25S	260(10)	474(19)	1268(165)	2169(101)	2510(119)
-30S	331(15)	-	1348(104)	1665(75)	2500(174)

Table 2

Cross sections (x 10^{-16} cm^2)

Angstroms. The statistical uncertainties are presented in the parentheses following the cross sections.

Superposition state	Helium	Neon	Argon	Krypton	Xenon
2S- 4D	684(63)	663(72)	1449(170)	1555(149)	1568(172)
- 5D	545(64)	1199(146)	1343(152)	2227(285)	2618(243)
- 6D	1003(87)	684(68)	2026(192)	3137(310)	2605(249)
- 8D	1237(46)	486(33)	2206(117)	3064(144)	3877(159)
- 9D	1385(40)	648(26)	2845(156)	3719(178)	5453(229)
-10D	1281(49)	566(22)	2426(126)	4000(195)	4921(217)
-11D	1051(41)	479(20)	2411(121)	4699(219)	8594(383)
-12D	919(35)	536(22)	2372(154)	5678(267)	7347(411)
-13D	798(32)	420(17)	2249(124)	5375(262)	7559(352)
-14D	715(29)	402(17)	1750(87)	4753(240)	7541(382)
-15D	619(24)	451(20)	1454(74)	4415(211)	7317(413)
-16D	631(26)	388(19)	1681(89)	4248(206)	9505(475)
-17D	484(18)	441(30)	1880(101)	4946(247)	8736(399)
-18D	592(25)	376(15)	1586(84)	4025(185)	8194(516)
-19D	634(23)	641(26)	1768(92)	4398(202)	9762(446)
-20D	-	-	-	-	10791(611)
-25D	498(21)	571(25)	1748(91)	3489(249)	6298(283)
-30D	572(25)	606(34)	1650(107)	3127(146)	5202(239)

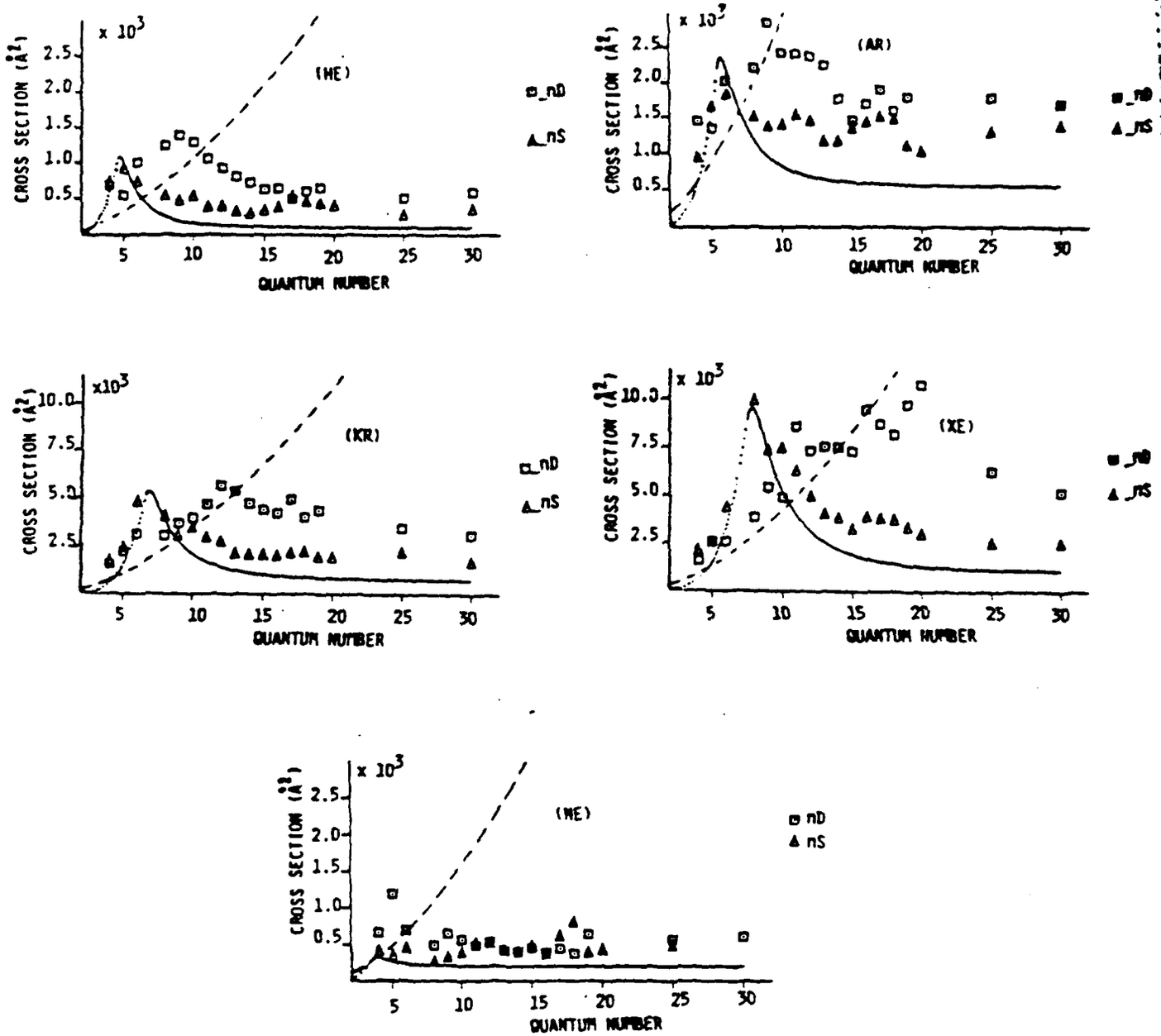

Figure 4: Li 2S - nS (nD) collisional cross section versus principle quantum number n or He, Ne, Ar, Kr and Xe. The dashed line is ven der Waals' cross section given by the Lindholm approach. The solid curevs are Omont's theory and the dotted curbes are the extension of Omont's theory to low n regime.

noble gases: He, Ne, Ar, Kr and Xe. The results are given in units of 10^{-16} cm^2, i.e. of square Angstroms. The statistical uncertainties are presented in the parenthesis following the cross sections. The experimental results are also ploteed in Fig. 4 with the theoretical calculations which will be described next.

4. Discussion -- Calculated atomic scattering cross sections are in general sensitive to the potential assumed. For the excited Li-noble gas system under consideration, realistic potentials are not known. For sufficiently large values of n (the Rydberg atom regime), the foundation of theoretical treatment was laid by Fermi.[5] According to Fermi, two mechanisms are responsible for the broadening and shift of the spectral lines involving highly excited states. The first is the scattering of the atomic electrons by the perturber atoms and the second is the effect of the polarization of the perturbing atom by the ionic core-perturber interaction. In the Fermi model these two physical processes are treated as statistically independent.

A theory for the intermediate n regime was developed by A. Omont.[6] Using Omont's theory, the total cross sections are:

$$\sigma = \pi(4b_2 n^2 - b_2^2) \qquad 2n^2 > b_2 > b_1 \qquad (7)$$

$$\sigma = \pi b_2(2n^{*2} - b_1) + \pi b_1^2 \qquad b_2 < b_1 \qquad (8)$$

where n* is the effective quantum number, $b_2 = 1/2[0.53L/(n^{*3}v)^2$, and $b_1 = 1.225[\pi\alpha/(4v\sqrt{2})]^{1/3}$. Omont's calaulcation may be extended to the small n regime, where σ is a rapidly increasing function of n:

$$\sigma = \pi \int_0^{2n^{*2}} W^2 b \, db = \pi \int_0^{2n^{*2}} 2b \, db = 4\pi n^{*4} \qquad (9)$$

The result is proportional to the geometric cross section. This is an approximate and simplified result derived here only for the completeness of the model.

This result is plotted in Fig. 4 along with our experimental data.

Equation (9) is plotted as the dotted curve and (7) and (8) are the solid curve. Note that the cross section σ given by these equations is a continuous function of n. The Ls and αs used here are from references 7 and 8.

5. nS Data -- Since Omont's calculations assume a spherically symmetric potential, it is expected that his results apply principally to the 2S-nS state scattering. Inelastic scattering mechanisms such as population degrading, ℓ changing collisions, etc., have not been included in this analysis. It follows that cross sections associated with the 2S-nS and especially the 2S-nD states are in general underestimated. The observed qualitative agreement of Omont's pseudo- potential theory and our data in the intermediate n regime provides support that the model of two statistically independent binary interactions, the electron-perturber and the core-perturber, is reasonable in this range. However, there are many discrepancies between the theory and our data. For the 4S state, argon, krypton and xenon have cross sections approximately twice as large as the geometric cross sections. With increasing n our results approach the geometric cross sections until the maxima are reached. Because $4\pi a_0^2 n^4$ is the quantum mechanical result for a hard-sphere collisional cross section, the experimental data imply a much more complicated interaction between the two atoms for low excited states. In other words, a multi-electron interaction instead of a pure binary collision exists between the low excited Li and the rare gas atoms.

At large n our experimental cross sections approach asymptotic values which are independent of the quantum numbers n and ℓ. For highly excited Li atoms, the atomic wave function is so dilute that it could hardly be effected by the penetration of a perturber through its orbit. Therefore, the collisional effect is predominantly Li core-noble gas interaction which is independent of the electronic states, as is observed experimentally (Fig. 4).

The theoretical predictinos for high n lie significantly below our experimental results. Although the disagreement varies from gas to gas, Omont's cross sections are in general 50% lower than our data at the large n limit.

AD-A163 402 RESEARCH INVESTIGATION DIRECTED TOWARD EXTENDING THE USEFUL RANGE OF THE ELECTROMAGNETIC SPECTRUM(U) COLUMBIA RADIATION LAB NEW YORK G W FLYNN ET AL. 4/4

UNCLASSIFIED 31 DEC 85 DAAG29-85-K-0049 F/G 20/6 NL

END

FILMED

DTIC

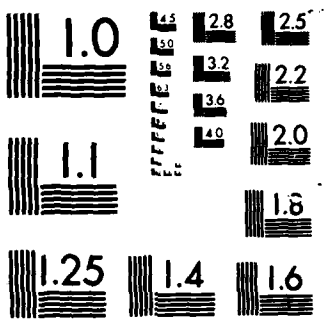

MICROCOPY RESOLUTION TEST CHART
NATIONAL BUREAU OF STANDARDS 1963-A

6. nD Data and Collisional ℓ Mixing -- The main contribution to the difference between nD and nS is the collisional ℓ-mixing effect which causes nD state population depletion during the 2S-nD superposition time in the trilevel echo experiment. At the present time no theory is available to explain the nD data quantitatively.

The Li nS states are energetically isolated from the hydrogenic energy levels, while the nD states are quite close to the hydrogenic levels and are almost degenerate with nF and other $\ell > 2$ states. T.F. Gallagher et al,[9] measured Li nD-nF and nD-nG splitting in the range $7 < n < 11$. Comparing our collisional broadening data for nD states from Table 2 with the energy separation data in reference 9, one can see that the nD state broadening matches the energy separation $\Delta E(D-F)$ to the same order of magnitude in the large n regime especially for heavy gases such as Ar, Kr, and Xe. This indicates the presence of collitional i-mixing effects in nD states.

7. Comparison with the Na Data -- The trilevel echo technique was applied to the measurement of collisional broadening of Na(3S - nS) and (3S - nD) lines from collisions with He, Ne, Ar, Kr, and Xe from n = 5 to 38 (S states) and n = 4 to 40 (D states).[1,2] Na nS data are successfully predicted by Omont's theory (see Fig. 6). The theory reproduces the general features of the observed cross sections. Li data have some similar characteristics to the Na data. For instance, they both have the same rapid increase of σ in the small n regime, similar relative broadenings induced by different noble gases in the asymptotic limit, and parallel behavior of the nD data relatiave to the nS data.

The Li data show some apparent differences from the Na data as follows:

1) In the intermediate n range, Li cross sections reach their maximum values slightly lower than Na by a difference of 1 to 3 in n; Li's maxima are smaller than Na's.

2) In the high n regime, the asymptotic cross section values for Li-He, Li-Ne, and Li-Ar are about 50% larger than those for Na-He, Na-Ne, and Na-Ar. Also, while Li-Kr and Na-Kr reach the same limit, Li-Xe is 20% lower than Na-Xe.

3) At the high n limit, Omont's theory predicts cross sections which

are 50% smaller than those observed in our Li(nS) experiment (except about 30% lower in the case of Ne). However, the Na data agree more closely with Omont's theory, they lie slightly above the theory for all the gases except for neon where the data lie lower than than the theory.

According to Omont's calculation, difference (1) is preducted, but differences (2) and (3) for the high n limit are in contradiction with the theory. The dominant contribution to the cross section in the high n regime, comes from the Li core-noble gas atom interaction and is proportional to:

$$\sigma \sim (\alpha/v)^{2/3} \sim \alpha^{2/3}(\mu/T)^{1/3} \qquad (10)$$

A Li-noble gas pair has a smaller μ than the Na-noble gas pair and the Li experiment ran at a higher temperature (700 K) than the Na (525 K), therefore σ (li) should be smaller than σ (Na). Therefore, the difference between the measurements on Li and on Na remains unexplained by the theory.

8. Conclusions -- Our Li data have shown the general features of Rydberg atoms. Although the Li data can be interpreted by Omont's pseudo-potential theory qualitatively, the quantitative discrepancies are quite noticeable in the intermediate and high n regimes. Compared with the trilevel echo Na data which are in good agreement with omont's theory, an improvement to generalize the theory is necessary on the basis of all the information provided by this experiment.

This work was also supported by the U.S. Office of Naval Research under Contract No. N00014-78-C-0317.

(1) A. Flusberg, R. Kachru, T. Mossberg, and S.R. Hartmann, Phys. Rev. A. 19, 1607 (1979).

(2) R. Kachru, T.W. Mossberg, and S.R. Hartmann, Phys. Rev. A 21, 4, 1124 (1980).

(3) R. Beach, S.R. Hartmann and R. friedberg, Phys. Rev. A 25, 2658 (1982).

(4) R. Kachru, R.J. Chen, S.R. Hartmann, T.W. Mossberg and P.R. Berman, Phys. Rev. Lett. 47, 13 (1981).

(5) E. Fermi, Nuovo Cementao 11, 157 (1934).

(6) A. Omont, J. de Physique, Tome 38, November 1977, 1343.

(7) A. Dalgarno and R.E. Kingston, Proc. R. Soc. London Ser. A 259, 424 (1960).

(8) H.S. W. Massey and E.H.S. Burhop, Electronics Impact Phenomena, Vol. 1, Claredon Press, Oxford, 1969.

(9) W.E. Cooke, T.F. Gallagher, R.M. Hill and S.A. Edelstein, Phys. Rev. A 16, 3, 1141 (1977).

F. OBSERVATION AND RELAXATION OF THE TWO-PHOTON-EXCITED-STATE TRILEVEL ECHO IN SODIUM VAPOR

(T.J. Chen, D. DeBeer, and S.R. Hartmann)
(JSEP work unit 2, 1985 - 1988)
(Principal Investigator: S.R. Hartmann (212)280-3272)

1. Introduction -- In 1978, relaxation measurements of the excited nD-3P superposition states in Na vapor perturbed by Ar were made for n = 4, 5, 6, and 7 by means of the excited state photon echo technique.[1] This study showed a very fast increase of the collisional cross section σ with increasing principal qunatum number n similar to that first observed by Fuchtbauer et al.[2] in studies of nP-3S superposition state broadening in Na perturbed by Ar. Excited state relaxation measurements for the lowest lying D state with n = 3 were not made because of the difficulty of generating the long wavelength (λ = 8183Å) excitation pulses which would have been necessary to coherently excite the 3D-3P transition. We have circumvented this difficulty by using a variation of the trilevel echo technique[3] that allows us to excite a coherent 3D-3P superposition state indirectly: we first resonantly excite a 3S-3P coherence then time τ later resonantly excite (via a two-photon process) a 3S-3D coherence. This procedure coherently related the 3P and 3D states so that an echo is subsequently formed; this echo can then be monitored to study 3D-3P superposition state relaxation.

2. Theory -- The two-photon-excited-state trilevel echo can be understood by treating each atom as a three level system (see Fig. 1) with energy levels $\hbar\Omega_a < \hbar\Omega_b < \hbar\Omega_c$ such that the $|a\rangle - |b\rangle$ and $|b\rangle - |c\rangle$ transitions are electric dipole allowed while the $|a\rangle - |c\rangle$ transition is not. We use the Billiard Ball Model[4] to describe the echo formation process for which the atomic recoil diagram is shown in Fig. 2. At time t_1 the atoms in ground state $|a\rangle$ are excited by a laser pulse of angular frequency $\omega_1 = \Omega_b - \Omega_a$. This generates a $|b\rangle$ excited state amplitude

which recoils away from the ground state amplitude with velocity $\hbar k_1/m$ where $k_1 = \omega_1 n_1/c$ is the wavevector of the excitation pulse and m is the mass of the Na atom. Similarly, at time $t_2 = t_1 + \tau$ the second excitation pulse, with wavevector $k_2 = \omega_2 n_2/c$ ($\omega_2 = (\Omega_c - \Omega_a)/2$), generates a $|c\rangle$ excited state amplitude, indicated in Fig. 2 by dashed dotted lines which recoils with velocity $2nk_2/m$. At subsequent time t_e such that

$$t_e = \frac{2k_2}{2k_2 - k_1} \tag{1}$$

the $|c\rangle$ excited state amplitude overtakes the $|b\rangle$ amplitude and the echo is radiated on the $|b\rangle - |c\rangle$ transition with the wavevector k_e,

$$\vec{k}_e = 2\,\vec{k}_2 - \vec{k}_1 \tag{2}$$

Optimum echoes arise when the two excitations have pulse areas of $\pi/2$ and π, respectively. The laser electric field amplitude necessary for the first excitation pulse to have an area of $\pi/2$ is[5]

$$E_1(\Theta = \tfrac{\pi}{2}) = \frac{\pi\hbar}{2P_{12}\tau_p} \tag{3}$$

where P_{12} is the dipole moment matrix element and $_p$ is the pulse duration.

Similarly, the optimum electric field amplitude of the second excitation pulse is[6]

$$E_2(\Theta = \pi) = \left(\frac{\gamma\pi\ {}^2\Delta}{(P_{12}{}^2 + P_{23}{}^2)\tau_p}\right)^{1/2} \tag{4}$$

where $\Delta = (\Omega_2 - \Omega_1) - \omega_2$.

The corresponding pulse intensities are:

$$I_1(\Theta = \tfrac{\pi}{2}) = \frac{\pi\hbar}{24C^2\ \tau_p{}^2} \Big/ \left(\frac{A_{12}}{(\Omega_2 - \Omega_1)^3}\right) \tag{5}$$

$$I_2(\Theta = \pi) = \frac{2\hbar}{3C^2\ \tau_p} \Big/ \left(\frac{A_{12}}{(\Omega_2 - \Omega_3)^3} + \frac{A_{23}}{(\Omega_3 - \Omega_2)^3}\right) \tag{6}$$

where the A_{ij} are the Einstein A coefficients. For the 3S, 3P, and 3D levels in Na these are $I_1(\Theta = \pi/2) = .16\ W/cm^2$ and $I_2(\Theta = \pi) = 840 kW/cm^2$.

3. Experiment -- We have observed two-photon-excited-state trilevel echoes on the 3S-3P-3D levels in Na or both $3^2P_{1/2}$ and $3^2P_{3/2}$ states. The echoes are generated using two pulsed dye lasers pumped by a single Nd:YAG laser. The first dye laser is tuned to a 3S-3P transition, 5896Å for the $3^2P_{1/2}$ state and 5890Å for the $3^2P_{3/2}$ state, while the second dye laser is tuned to 6854Å so as to be two photon resonant with the 3S-3D transition.

Both dye laser pulses have spectral widths of 3 GHz and temporal durations of 7 ns. The output of the second laser is delayed optically by 24 ns and then superimposed collinearly with the first pulse using a piece of uncoated glass, preserving more than 90% of the light in the second pulse. The resultant beam is directed through the Na sample cell, a stainless-steel heat pipe type oven. The oven is maintained at 422 $\pm$ 5 K to give a Na number density such that $\alpha L \sim 1$ for the 3S-3P transition where α is the absorption coefficient and L is the sample length (about 10 cm). In the sample the two excitation pulses have diameters of 10 mm, peak powers of 5W and 12kW, respectively, and a relative delay of 24 $\pm$ 1 ns. From eqs. 1 and 2, we see that the echo is generated on the 3P-3D transition, 8183 Å for $3^2P_{1/2}$ or 8194 Å for $3^2P_{3/2}$, 33 ns after the second excitation pulse. The echo is collinear with both excitations and is separated from them using an interference filter and a monochromator, and then detected with an RCA C31034 photomultiplier tube. The intensity of the echo for the $3_2P_{3/2}$ intermediate state is $7 \times 10^{-5}\ W/cm^2$ or .001 % of the intensity of the first excitation pulse.

In the absence of any collisional relaxation the echo intensity decays with a 4.6 ns time constant as the pulse separation τ is increased. This short relaxation time is a consequence of the relatively short 20.2 ns and 15.9 ns lifetimes of the 3D and 3P states involved in forming the echo. Because of the short inherent relaxation time constant associated with this echo it was imperative that the temporal jitter in τ be substantially less than a nanosecond. This was easily achieved by using an optical delay line to delay the 6854Å light. However, the echo still occurred about 1 ns early

since the pulse durations were comparable to the relaxation time constant.

The measurement of the collisional relaxation cross section with Ar of Na in a 3P-3D superposition begins by monitoring the echo intensity as an Ar buffer gas is introduced up to a partial pressure of 1 torr as measured by a MKS Baratron capacitance manometer. The echo intensity decays exponentially with buffer gas pressure, P, as:[7]

$$I = I_o \exp(-\beta P) \tag{7}$$

where

$$\beta = 2 \frac{N}{P} \bar{v}[\sigma_1 \tau + \sigma_2 (A_e - A_2)], \tag{8}$$

σ and σ_2 are the collisional cross sections betweeen Ar atoms and the Na atoms in 3S-3P and 3P-3D superpositions, respectively, N is the Ar number density, and v is the average relative speed between Na and Ar atoms which is given by $(8k_BT/\pi\mu)^{1/2}$, where k_B is Boltzmann's constant, T is the absolute temperature and μ is the reduced mass of the Na/Ar pair. For an ideal gas $2Nv/P = 2(8\tau k_B T\pi\mu)^{1/2}$.

Data from a typical experimental run are shown in Fig. 3. The data conform well to the expected exponential decay. Performing a least squares fit and averaging over several runs, we obtain decay rates of 7.25 (10) and 7.42 (10) $torr^{-1}$ for the $3^2P_{1/2}$ and $3^2P_{3/2}$ intermediate states, respectively. The 3S-3P collisional cross sections, σ_1, have been measured previously[8] and were found to be 268 (17) and 267 (17)$Å^2$ for the 3S-$3^2P_{1/2}$ and 3S-$3^2P_{3/2}$ superpositions, respectively, so that using these values in eq. 8 we find

$$\sigma(3^2P_{1/2}\text{-}3D) = 414(30)A^2$$

$$\sigma(3^2P_{3/2}\text{-}3D) = 429(30)A^2$$

This is the first time these 3P-3D cross sections have been determined.

4. Conclusion -- We have demonstrated a novel coherent transient

technique and have used it to extend relaxation data to a regime which was previously avoided because of experimental difficulty. In Fig. 4 we show the current determination of the $3^2P_{1/2}$-$3^2D_{3/2}$ collisional cross section along with the previous measurements of the $3^2P_{1/2}$-$n^2D_{3/2}$ (n = 4, 5, 6, 7) collisional cross sections obtained using the more conventional excited state photon echo technique.[1] The dependence of cross section on principal quantum number is almost linear.

The collisional cross sections associated with both the $3^2P_{1/2}$-3D and $3^2P_{3/2}$-3D superposition states were equal to within experimental error. Similar behavior has been found for the relaxation of the 3S-$3^2P_{1/2}$ and 3S-$3^2P_{3/2}$ superposition states when measured by the two pulse photon echo technique.[8] When conventional cw techniques were used they differed by about 20%, with the 3S-$3^2P_{1/2}$ cross section being larger.[10, 11]

This work was also supported by the U.S. Office of Naval Research under Contract No. N00014-78-C-0517.

(1) A. Flusberg, T. Mossberg, and S.R. Hartmann, Opt. Commun. 24, 207 (1978).

(2) C. Fuchtbauer and P. Schulz, Z. Phys. 97, 699 (1935).

(3) T. Mossberg, A. Flusberg, R. Kachru, and S.R. Hartmann, Phys. Rev. Lett. 39, 1523 (1977).

(4) R. Beach, S.R. Hartmann, and R. Friedberg, Phys. Rev. A 25, 2658 (1982).

(5) T.W. Mossberg, R. Kachru, S.R. Hartmann, and A.M. Flusberg, Phys. Rev. A 20, 1976 (1979).

(6) M. Sargent III, M.O. Scully, and W.E. Lamb, Jr., Laser Physics (Addison-Wesley, Reading, 1974), chap. 2.

(7) M. Sargent III and P. Horwitz, Phys. Rev. A 13, 1962 (1976).

(8) A. Flusberg, R. Kachru, T. Mossberg, and S.R. Hartmann, Phys. Rev. A 19, 1607 (1979).

(9) R. Kachru, T.W. Mossberg, and S.R. Hartmann, J. Phys. B 13, L363 (1980).

(10) R.H. Chatham, A. Gallagher, and E.L. Lewis, J. Phys. B 13, L7 (1980).

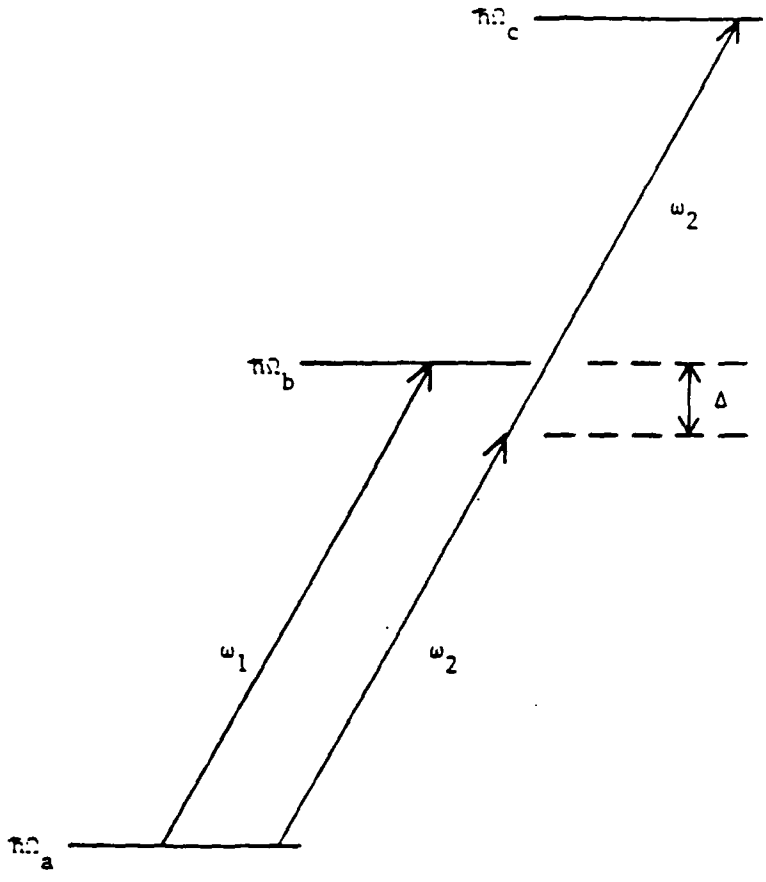

Figure 1: Energy level diagram for two-photon-excited-state trilevel echo. The energy eigenstate levels are indicated with different line types so that the states can be distinguished in Fig. 2.

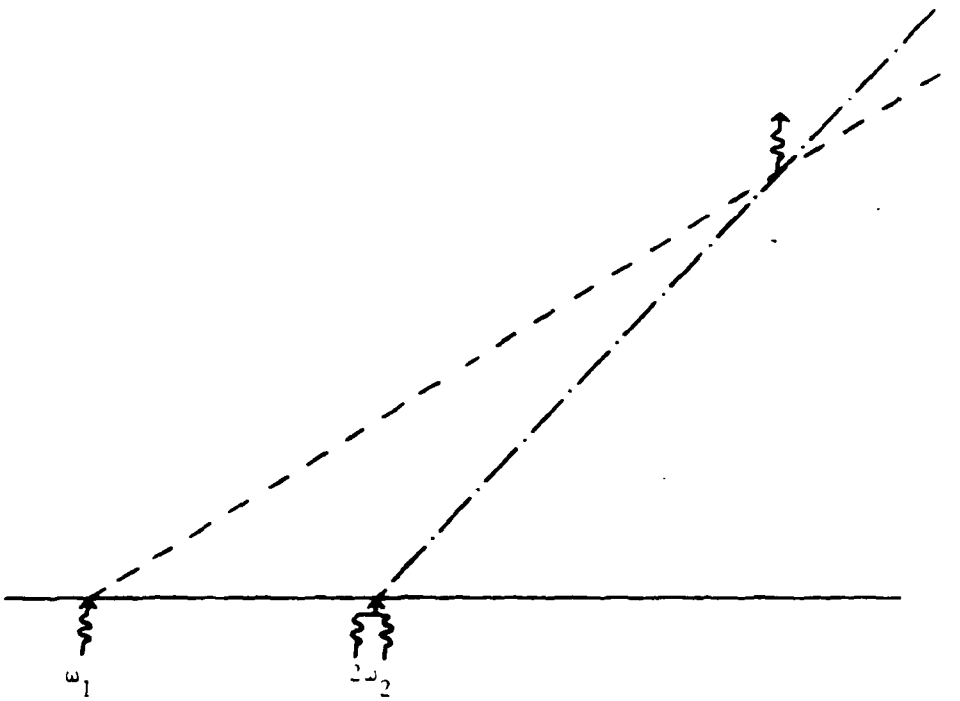

Figure 2: Billiard Ball Model recoil diagram for two-photon-excited state trilevel echo for nearly collinear excitation pulses. The recoil position of the various laser generated states is pdotting versus time with time increasing to the right and the laser directions being upward.

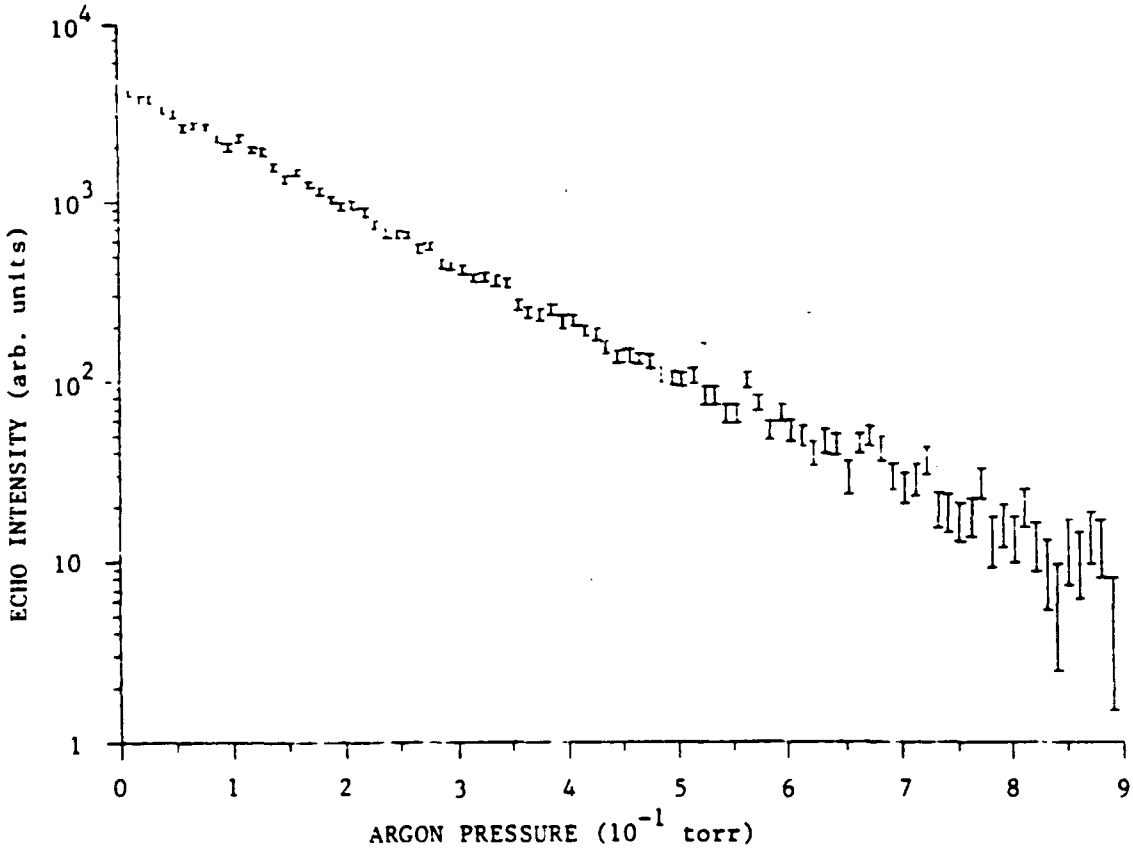

Figure 3: Typical set of data for decay of echo intensity with Ar gas pressure. Each point represents an average over 100 laser pulses.

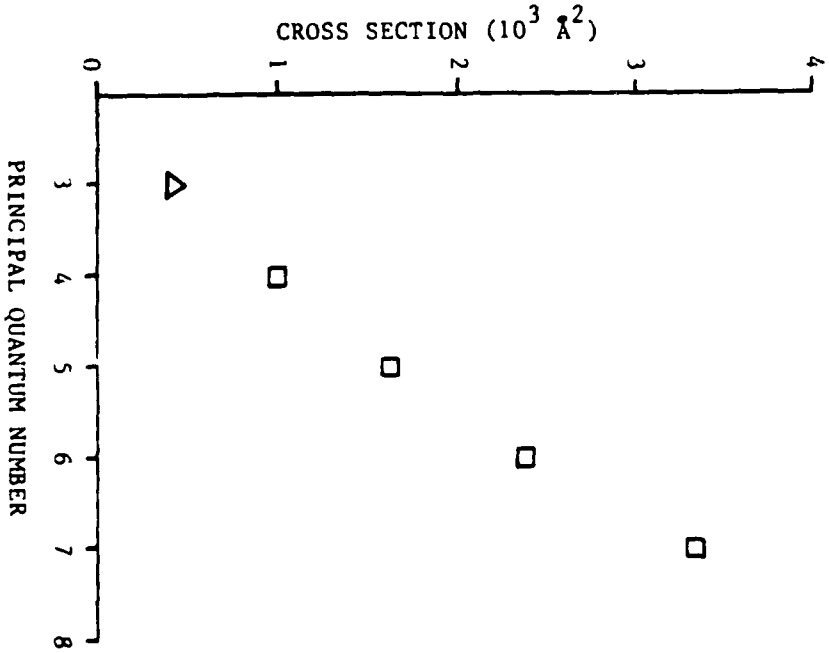

Figure 4: Collisional cross section of Na in a $3^2P_{1/2}$–$n^2D_{3/2}$ superposition with Ar, versus principal quantum number n. The uncertainties in the cross sections are smaller than the symbols used except for n = 7 where the uncertainty is 1500A.

G. CONCLUSIONS AND FUTURE DIRECTIONS OF RESEARCH

(S.R. Hartmann)
(JSEP work unit 2, 1985 - 1988)
(Principal Investigator: S.R. Hartmann (212) 280-3272)

While our laboratory has continued studies of long-standing interest we have also initiated investigations in several new directions. As a spin-off from our two-photon-excited-state photon echo experiment, we are now studying coherences between electric dipole forbidden states. We are continuing TDFWM studies in Sodium vapor to understand further the anomalies we have reported. The possibility of using the short coherence time of broadband light to study femtosecond phenomena shows great promise and could open up a whole new field of study. We shall discuss this last direction in more detail.

The recent development of the Time Delayed Four Wave Mixing (TDFWM) Technique (in this laboratory) shows great promise of being able to effectively study physical phenomena in the ultrafast (femtosecond) regime. This technique exploits the short correlation time of broadband laser radiation to enable the performance of experiments which would otherwise require the generation of femtosecond laser pulses. It is a much simpler matter to generate broadband laser radiation (whose inverse bandwidth is in the femtosecond regime) of moderate pulse length than it is to generate usable femtosecond laser pulses. In addition, these broadband pulses are readily tunable giving them an important advantage over current state-of-the art femtosecond pulses which are not.

Photon Echoes are a special case of the general phenomena which can be produced with the TDFWM technique. In a recent paper (Phys. Rev. Lett, 53, 663 [1984]) we demonstrated that incoherent light serves very well in generating photon echoes and that there are definite advantages in using incoherent light. Photon echoes are produced when the excitation pulses are well separated in time. When the excitation pulses overlap interesting signals are still produced and these signals have important properties when the excitation pulses are incoherent and broadband as discussed in our

report. Recent parallel work in Japan (Opt. Comm. 52, 150 [1984]) supports our work and shows the technique is effective in studying fast relaxation processes. In addition to being able to investigate fast relaxation processes the technique is also an effective spectroscopic tool as demonstrated in our report on ultrafast photon echo modulation spectroscopy. Our experiments so far have been restricted to studying TDFWM in Na vapor simply because we wanted to develop the technique in a familiar regime.

It is a simple matter to generate 300Å wide excitation pulses and we have done so in our laboratory with great ease. We would like to develop and exploit the TDFWM technique by using these pulses to study fast relaxation processes in a wide variety of interesting materials. Relaxation of many organic dyes (i.e. Malachite Green in Aqueous solution) are known to take place in the short end of the femtosecond regime where only limiting rates have been ascertained to date. Relaxation of electronic states of impurity atoms in optical quality laser crystals ($Pr^{3+}:LaF_3$) range from the microsecond regime at low temperatures to the low femtosecond regime at higher temperatures. Relaxation of carriers (ballistics) in semiconductors, e.g. GaAs, is claimed to be of the order of tens of femtoseconds but measurements to date have only been of an incoherent nature. Only recently have coherent transient studies been performed on exciton relaxation in semiconductors (e.g. GaP:n) and these have of necessity been restricted to the picosecond regime. With the TDFWM technique these could be extended to the femtosecond regime. This case is especially noteworthy in that the tunability of the TDFWM technique can be used to advantage. Similar remarks can be made with respect to corresponding processes in multiple quantum wells.

The TDFWM method can also be applied to other coherent transient techniques to enable CARS type experiments. Here again vibrational energy transfer and relaxation studies could be extended into shorter time domains. Another novel application of a generalized TDFWM technique would be in what is called the nonlinear luminescence technique. Strictly speaking, this is an incoherent technique which relies on an flourescence relaxation rate which is carrier density dependent. The implementation of the TDFWM method again allows faster relaxation processes to be studied as well as the all important excitation energy dependence to be determined.

SIGNIFICANT ACCOMPLISHMENTS AND TECHNOLOGY TRANSITION REPORTS

Significant Accomplishments

I. Variance stabilizing transformations have been derived for exponential and Rayleigh random variables. Applying these transforms to noisy images permits the use of classical estimation procedures.

We produced the first source of quiet (nonclassical) light by using a Franck-Hertz apparatus excited by a space-charge-limited electron beam. We also proved a quantum analog of the Burgess variance theorem confirming that the sub-Poisson nature of a light beam is conserved in the presence of absorptive media and additive (Poisson) background light. Thus the quiet light can be used once it is generated.

II. Maskless dry etching of GaAs has been demonstrated. The technique uses a patterned pulsed excimer laser beam to etch the surface of a GaAs wafer by photolyzing etchant precursors near the gas - wafer interface. No separate masking steps are required. This represents the first demonstration of a nonthermal, maskless process for etching semiconductors. High resolution was attained for the process by introducing various buffer gases to the active etching gas. This technique provides a gentle (ion-free) method of etching GaAs without recourse to prior masking.

Thin-oxide layers can be grown on GaAs by illuminating a wafer in distilled water with ultraviolet light. This technique provides the first step in a new method of ultraclean surface preparation of GaAs wafers.

Columbia University, and the Radiation Laboratory, in particular, has acquired the capability to do experimental surface analysis of electronic materials. The surface analysis system has already been used to aid the study of ion-beam assisted oxidation of silicon and ultraviolet oxidation of GaAs (see above). Columbia was assisted in this effort by IBM support of a Postdoctoral Fellow.

A new technique known as the accurate phase capacitance spectroscopy

has been developed to investigate the interface states of Schottky barriers.

For the first time reliable measurements of interface states in metal-semiconductor systems have been made using APCS. Unoccupied electronic states were found inside the band gap at silicide-silicon Schottky barriers. Of particular significance was the correlation of interface states density and microstructural perfection in epitaxial nickel silicide-silicon devices. Less perfect interfaces formed under less than ideal conditions give rise to a larger interface state density and lower Schottky barrier height.

A silicon charge-coupled computer for analog operations in the charge-domain has been designed and fabricated. Gallium arsenide charge-coupled computing structures have been analyzed.

An ultra-thin room temperature gate oxide fabricated using a low energy ion beam has been successfully employed in an MOS transistor.

A novel photodetector formed on the inside wall of a laser etched cavity in silicon for an optical fiber receiver has been fabricated and tested.

III. We have used a U.V. laser-assisted, plasma discharge technique to etch GaAs. Ultraviolet laser radiation provides separate control of ion bombardment energy and chemical species production in a plasma etching reactor.

We have developed an extraordinarily powerful, high resolution, diode laser probe technique which provides a method for monitoring high energy collision and chemical reaction processes with a spectral resolution of 0.001 cm^{-1} and a time resolution faster than 10^{-7} sec.

We have monitored the final states of a bath molecule produced by collisions with an electronically excited metal atom. In the case of mercury and CO_2, the collision produced triplet, bent CO_2 which then slowly relaxes back to the ground singlet state. These studies are prototypes for catalytic metal/molecule interaction processes occuring on surfaces or in metal clusters.

We have developed plasma discharge and collisional energy transfer techniques for identifying high energy vibrational states of molecules.

These methods have already been used to identify the exact quantum states of levels with energies in excess of 0.75 eV, and they have the potential for identification of levels as high as 2.5 eV.

IV. We have determined experimentally the reaction rates as well as the singlet to triplet intersystem crossing rate in a number of carbenes (R_1-C-R_2), which are important short-lived molecular fragments. The intersystem crossing rates, which have remained unknown despite advances in techniques for the study of these chemical intermediates, have important implications in the chemistry and photophysics for this class of molecules.

Long range and short range solvent effects on the dynamics of intramolecular charge-transfer in p-dimethyl-aminobenzonitrile have been determined. Alcohols are shown to enhance the rate of internal charge-transfer through a polarity effect but can also slow the process down via hydrogen bonding. The results are important in showing how the environment can affect intramolecular electronic energy relaxation.

Using a new application of second harmonic generation techniques we have succeeded in the direct study of the structure of surfaces of neat liquids and solutions. This novel technique yielded new information about the orientation of adsorbates at the liquid/air interface.

V. Time-Delayed-Four-Wave-Mixing (TDFWM) using intense broadband laser light has been observed in Na vapor. A nonperturbative theory has been developed and checked experimentally.

Ultrafast modulation spectroscopic measurements have been made on the Na D doublets using a pair of narrow band lasers.

Two photon trilevel echoes have been excited via the 3S-3D Transition on Na vapor and the collisionally-induced relaxation cross section has been measured.

Photon echoes between the excited $^3P_0$ and $_3H_5$ states in La^{3+}:LaF_3 have been detected and analyzed. Evidence of fast population transfer from the $^3H_6$ and $^3H_5$ levels is supported by two and three pulse echo experiments

performed on the $^3P_0$-$^3H_6$ and $^3P_0$-$^3H_5$ transitions.

Technology Transition Reports

1. Nearby industrial colleagues have made many inquiries on our work on dry and light-guided etching of GaAs. The interest stems from obvious applications in processing GaAs ICs and making electrooptical devices. In addition, a number of various unusual applications for light-guided etching have been suggested by industry, including microslicing of TEM samples and clearing laser diodes. Specific industrial contacts on this work have been made with GE: Syracuse and Schenectady; AT&T Bell Labs; IBM: East Fishkill; and Bell Communications Research.

2. A patent was filed by Professors Prucnal, Fossum and Osgood for a novel technique to make optical interconnects to high-density silicon and gallium arsenide IC's. Because of the increased demands for high data rate and dense packing in the coming of IC technoogy, chip-to-chip and board-to-board interconnection must be done optically. IBM, GE, and other companies have been extremely interested in the Columbia approach.

PERSONNEL

Faculty

R. Beach, Assistant Professor of Physics
K. Eisenthal, Professor of Chemistry
G. Flynn, Professor of Chemistry, Co-Director
E. Fossum, Assistant Professor of Electrical Engineering
S. Hartmann, Professor of Physics
R. Osgood, Professor of Electrical Engineering and Applied Physics
P. Prucnal, Associate Professor of Electrical Engineering
M. Teich, Professor of Engineering Science

Visiting Scientists

Dr. Z. Babarogic
Dr. B. Brody
Dr. Ji Ye Cai
Dr. B. Saleh
Dr. D. Stoler
Dr. Chen Xi Wang

Research Associates

Dr. Raymond Beach
Dr. Peter Brewer (now at Hughes Research Labs)
Dr. Julian Chen (now at IBM T.J. Research Center)
Dr. Lucille Chia
Dr. Jack Chu (Joint Postdoctoral Fellow with Profesors Flynn and Osgood)
Dr. H. Evans
Dr. H.H. Gilgen
Dr. Will Hollingsworth
Dr. K. Kemnitz
Dr. Thomas Krutz
Dr. K. Matsuo
Dr. Grace Reksten
Dr. S. Shih
Dr. E. Sitzmann
Dr. Chien Yu (IBM Fellow at Columbia Rad. Lab)

Graduate Research Assistants

R. Ade
R. Bowman
B. Brady
T. Cacouris
L. Chen
R. Colbeth
D. DeBeer
N. Doudoumopoulos
S. Hewitt
J. Hicks
W. Holber
B. Jalali
K. Kasturi
R. Kichinski
R. Krchnavek
J. Langan
K. Luo
P. Meyer
F. Mitlitzky (at Lawrence Livermore National Lab)
F. Moshary
J. O'Neill
G. Pinto
D. Podlesnik
D. Rossi
E. Sanchez
M. Santoro
M. Schmidt
P. Shaw
G. Spector
J. Subbiah
S. Todorov
F. Tong (at MIT Lincoln Lab)
V. Treyz
L. Van Wagenen
A. Willner
E. Xu

Administration

Ms. Cheryl Hampton
Ms. Cynthia Leslie
Ms. Karen Wingate

Technician

Dave Rivera

Undergraduate Technicians

C. Delos-Reyes
D. Gu
N. Joshi
P. Landsberg
N. Ramlagan
S. Ross
S. Seshadri
S. Shillinger
J. Yee
J. Yves
G. Zolotarev

Dr. Jimmie R. Suttle
U. S. Army Research Office
P. O. Box 12211
Research Triangle Park, NC 27709

Mr. Charles Graff
U. S. Army Comm. - Electronics Command
ATTN: DRSEL-COM-RF-Z
Fort Monmouth, NJ 07703

Mr. Edward Herr
U. S. Army Comm. - Electronics Command
ATTN: DRSEL-COM-RX-4
Fort Monmouth, NJ 07703

Mr. Roland Wright
Night Vision & Electro-Optics Labs
Fort Belvoir, VA 22060

Dr. Robert Rohde
Night Vision & Electro-Optics Labs
Fort Belvoir, VA 22060

Dr. Donn V. Campbell
U. S. Army Comm. - Electronics Command
ATTN: DRSEL-COM-RN-4
Fort Monmouth, NJ 07703

Dr. Nick Karayianis
Harry Diamond Laboratories
ATTN: DELHD-RT-CA
2800 Powder Mill Road
Adelphi, MD 20783

Dr. T. N. Chin
U. S. Army ARRADCOM
ATTN: DRDAR-SCF-10
Dover, NJ 07801

Dr. John Malamus
Night Vision & Electro-Optics Labs
Fort Belvoir, VA 22060

Dr. Rudolf G. Buser
Night Vision & Electro-Optics Labs
ATTN: DELNL-L
Fort Belvoir, NJ 22060

Dr. W. Ealy
Night Vision & Electro-Optics Labs
ATTN: DELNV-AC
Fort Monmouth, NJ 22060

Dr. J. Hall
Night Vision & Electro-Optics Labs
ATTN: DELNV-AC
Fort Belvoir, NJ 22060

Dr. J. Burgess
Night Vision & Electro-Optics Labs
ATTN: DELNV-RM-RA
Fort Belvoir, NJ 22060

DEPARMENT OF THE AIR FORCE

Dr. E. Champagne
AFWAL/AADD-I
Wright-Patterson AFB, OH 45433

Mr. W. Edwards, Chief
AFWAL/AAD
Wright-Patterson AFB, OH 45433

Professor R. E. Fontana
Head, Department of Electrical Engineering
AFIT/ENG
Wright-Patterson AFB, OH 45433

Dr. Alan Garscadden
AFWAL/POOC-3
Air Force Aeronautical Labs
Wright-Patterson AFB, OH 45433

Mr. Alan R. Barnum (CO)
Rome Air Development Center
Griffiss AFB, NY 13441

Chief, Electronic Research Branch
AFWAL/AADR
Wright-Patterson AFB, OH 45433

Mr. John Mott-Smith (ESD/ECE)
HQ ESD (AFSC), Stop 36
Hanscom AFB, MA 01731

Dr. J. Ryles
Chief Scientist
AFWAL/AS
Wright-Patterson AFB, OH 45433

Dr. Allan Schell
RADC/EE
Hanscom AFB, MA 01731

Dr. J. Bram
AFOSR/NM
Bolling AFB, DC 20332

Dr. David W. Fox
AFOSR/NM
Bolling AFB, DC 20332

Dr. J. Neff
AFOSR/NE
Bolling AFB, DC 20332

Dr. N. H. DeAngelis
RADC/ESR
Hanscom AFB, MA 01731

Dr. Gerald L. Witt
Program Manager
Electronic & Material Sciences Directorate
Department of the Air Force
AFOSR
Bolling AFB, DC 20332

Mr. Allan Barnum
RADC/IS
Griffiss AFB, N.Y. 13411

Dr. Tom Walsh
AFOSR/NE
Bolling AFB, DC 20332

Dr. Edward Altshuler
RADC/EEP
Hanscom AFB, MA 01731

DEPARTMENT OF THE NAVY

Naval Surface Weapons Center
ATTN: Technical Library
Code DX-21
Dahlgren, VA 22448

Dr. Gernot M. R. Winkler
Director, Time Service
U. S. Naval Observatory
Massachusetts Avenue at 34th Street, NW
Washington, DC 20390

G. C. Dilworth, Jr.
Technical Director
Naval Coastal Systems Center
Panama City, FL 32407

Naval Air Development Center
ATTN: Code - 301 A. Witt
Technical Library
Warminster, PA 18974

R. S. Allgaier, R-45
Naval Surface Weapons Center
Silver Spring, MD 20910

Office of Naval Research
800 North Quincy Street
ATTN: Code 250
Arlington, VA 22217

Office of Naval Research
800 North Quincy Street
ATTN: Code 414
Arlington, VA 22217

Office of Naval Research
800 North Quincy Street
ATTN: Code 411MA
(Dr. Stuart L. Brodsky)
Arlington, VA 22217

Commanding Officer
Naval Research Laboratory
ATTN: Dr. S. Teitler, Code 6801
Washington, DC 20375

Commanding Officer
Naval Research Laboratory
ATTN: Mrs. D. Folen, Code 2627
Washington, DC 20375

Commanding Officer
Naval Research Laboratory
ATTN: Mr. A. Brodzinsky, Code 5200
Washington, DC 20375

Commanding Officer
Naval Research Laboratory
ATTN: Mr. J. E. Davey, Code 6810
Washington, DC 20375

Commanding Officer
Naval Research Laboratory
ATTN: Mr. B. D. McCombe, Code 6800
Washington, DC 20375

Commanding Officer
Naval Research Laboratory
ATTN: Mr. W. L. Faust, Code 6504
Washington, DC 20375

Technical Director
Naval Underwater Systems Center
New London, CT 06320

Naval Research Laboratory
Underwater Sound Reference Detachment
Technical Library
P. O. Box 8337
Orlando, FL 32856

Naval Ocean Systems Center
ATTN: Dr. F. C. Fletcher, Code 92
San Diego, CA 92152

Naval Ocean Systems Center
ATTN: Mr. W. J. Dejka, Code 8302
San Diego, CA 92152

Naval Ocean Systems Center
ATTN: Dr. Alfred K. Nedoluha,
Code 922
San Diego, CA 92152

Naval Weapons Center
ATTN: Dr. G. H. Winkler, Code 381
China Lake, CA 93555

Dr. Donald E. Kirk (62)
Professor and Chairman, Electrical
Engineering
SP-304
Naval Postgraduate School
Monterey, CA 93940

Dr. D. F. Dence
Naval Underwater Systems Center
New London Laboratory
ATTN: Code 34
New London, CT 06320

Director, Technology Assessment
Division (OP-987)
Office of the Chief of Naval Oper.
Navy Department
Washington, DC 20350

Mr. J. W. Willis
Naval Air Systems Command
AIR-310
Washington, DC 20361

Naval Electronics Systems Command
NC #1
ATTN: Code 61R
2511 Jefferson Davis Highway
Arlington, VA 20360

Department of the Navy
Naval Sea Systems Command
ATTN: W. W. Blaine (SEA-62R)
Washington, DC 20362

David Taylor Naval Ship Research
and Development Center
ATTN: Mr. G. H. Gleissner, Code 18
Bethesda, MD 20084

Mr. Martin Mandelberg
Coast Guard R&D Center
Avery Point
Groton, CT 06340

Naval Underwater Systems Center
New London Laboratory
ATTN: 101E (Dr. Edward S. Eby)
New London, CT 06320

Mr. Thomas J. Manuccia, Head
Chemistry and Application Section
Code 6543
Naval Research Laboratory
Washington, DC 20375

Dr. Stephen G. Bishop, Head
Semiconductor Branch
Code 6870
Naval Research Laboratory
Washington, DC 20375

Dr. John W. Rockway
Comm. Technology Prog. Off.
Code 8105
Naval Ocean Systems Center
San Diego, CA 92152

Dr. Barry P. Shay
Joint Program Office,
ODUSD(P)
The Pentagon, Rm 4D825
Washington, DC 20301

Dr. Sydney R. Parker
Professor, Electrical Engineering
Code 62PX
Naval Postgraduate School
Monterey, CA 93940

Dr. George B. Wright
Office of Naval Research
Code 427
Arlington, VA 22217

OTHER GOVERNMENT AGENCIES

Dr. Ronald E. Kagarise
Director
Division of Materials Research
National Science Foundation
1800 G Street
Washington, DC 20550

Director
Division of Electrical, Computer
and Systems Engineering
National Science Foundation
Washington, DC 20550

Dr. Dean L. Mitchell
Section Head
Condensed Matter Sciences Section
Division of Materials Research
National Science Foundation
1800 G Street, N. W.
Washington, DC 20550

Judson C. French, Director
Center for Electronics and Electrical
Engineering
B 358 Metrology Building
National Bureau of Standards
Washington, DC 20234

NON-GOVERNMENT AGENCIES

Director
Columbia Radiation Laboratory
Columbia University
538 West 120th Street
New York, NY 10027

Director
Coordinated Science Laboratory
University of Illinois
Urbana, IL 61801

Associate Director pf Materials
and Electronics Research
Division of Applied Sciences
McKay Laboratory 107
Harvard University
Cambridge, MA 02138

Director
Electronics Research Center
University of Texas
P. O. Box 7728
Austin, TX 78712

Director
Electronics Research Laboratory
University of California
Berkeley, CA 94720

Director
Electronics Sciences Laboratory
University of Southern California
Los Angeles, CA 90007

Director
Microwave Research Institute
Polytechnic Institute of New York
333 Jay Street
Brooklyn, NY 11201

Director
Research Laboratory of Electronics
Massachusetts Institute of Technology
Cambridge, MA 02139

Director
Stanford Electronics Laboratory
Stanford University
Stanford, CA 94305

Director
Edward L. Ginzton Laboratory
Stanford University
Stanford, CA 94305

END

FILMED

3-86

DTIC